The hydrogeological structure of fault zones in poorly lithified sediment, Gulf of Corinth rift.

Sian Eleri Loveless

A thesis submitted for the requirements for the degree of

Doctor of Philosophy

University of East Anglia

School of Environmental Sciences

April 2013

Abstract

Often, the structure of fault zones cutting poorly lithified sediment examined in outcrop indicate such fault zones should behave as hydraulic barriers, but hydrological observations indicate they behave as conduit-barriers. This thesis investigates the hydrogeological structure of fault zones cutting poorly lithified sediment to better understand the observed conduit-barrier behaviour.

The macro- and micro-structure of fault zones was investigated at outcrops of five fault arrays cutting syn-rift sediment of the rapidly extending Gulf of Corinth rift, Central Greece. Fault zone evolution was interpreted from these observations and changes to sediment hydraulic characteristics in fault zones estimated. Based upon the field data, characteristic fault zone hydrogeological structure was represented in two-dimensional numerical fluid-flow models in order to assess likely hydraulic impacts.

Fault zone structure is found to be dominated by a mixed zone and differs to those previously reported. Two models of fault zone evolution are proposed for faults cutting: 1. Only poorly lithified sediment, in which beds are rotated and smeared in the mixed zone, where these can mix at the grain-scale through distributed, controlled particulate flow. 2. Sediment of contrasting competency, with mixed zones comprising blocks and lenses, and fine-grained smears in which strain localisation and fault-tip bifurcation are central to their evolution. Both models apply to fault zones that juxtapose fine and coarse-grained sediment.

Numerical models show that the majority of these fault zones will behave as barriers to fluid-flow due to a reduction in hydraulic conductivity. Fault zones of all sizes influence fluid-flow, but hydraulic impact increases with fault throw. Conduit-barrier behaviour can be explained by anisotropies, particularly from slip-surface cataclasites, in fault zones cutting poorly lithified sediment only. Fault hydraulic behaviour is strongly dependent on structural hetereogeneities and their geometry in the fault zone. The cumulative effects of these faults will be significant for sub-surface fluid-flow.

Table of Contents

List of Figures

List of Tables

Acknowledgements

There are innumerable people to whom I am immensely grateful to for helping me get to this point. First, I would like to express my sincere gratitude to my supervisory team whose abundant scientific knowledge and advice I have relied on. I would like to thank my primary supervisor Victor Bense, for giving me the opportunity to undertake this research and for providing guidance and support throughout. I would also like to thank Victor for encouraging me to make the most of other opportunities that came along. I am grateful for the help and support offered by Jenni Turner who often went above and beyond the call of duty to assist with this project, and Julian Andrews who always offered invaluable and straight forward advice.

None of this work could have happened without help in the field. Victor Bense and Jenni Turner provided much help with this, not only with discussions about the research but also with a great deal of the leg work, for which I am truly grateful. I also was lucky to have three field assistants who put up with the hardships of field work in Greece. My Dad, who never got to rest on retirement; he was not only a great field assistant but also my spare arm after I came off my bike two days before our trip. Thanks also to my Mum who let him come away despite having to work. Richard Walker who really enlightened the world of structural geology to me, and from whom I learnt so much. Stuart Vinen for a great two weeks of field work despite the rain.

Recently I have been indebted to a number of people who have helped me get to this stage. Julian Andrews who gave me confidence in the final stages. Jan Alexander who provided extremely useful comments on chapters that have improved the quality greatly. James Hodson and Johanna Scheidegger who also took time to read chapters and whose comments were incredibly helpful. Yet again, my Dad (and Mum) who dared to read the whole thesis, and provided many valuable (and some wonderfully sarcastic) comments.

At this point I would like to thank Professor Mark Reed from the University of Oregon, without whose suggestion I probably would not have considered doing a PhD and Julian Andrews for initially encouraging me to apply for this project.

There is a whole cohort of people in the School of Environmental Sciences who I have relied upon these last few years. In the laboratory, Emma Hooper, Judith Mayne and Jenny Stevenson, and John Brindle for persisting with, and taking such an interest in my slides. Also to Ashley Sampson and Alan Ovenden who rival my passion for maps – it was always a fun experience finding maps. Fiona who greeted us with a smile every morning without fail, and the IT support who are always cheery despite being at the receiving end of so many frustrations.

The whole EnvGeo group. Especially the 3.16 and previously Norfolk Terrace B families, where would I be without you all? The Gulf of Corinth research group through which I have been exposed to such exciting research, conversations and opportunities, not to mention the enjoyment of field work with this group. In particular, I'd like to thank Mike Leeder for all his encouragement and support, and the interest that he took in my work.

I appreciate the funding from the UK Natural Environment Research Council for this project, and the opportunities that have come with being funded by NERC. Thanks to the Greek Institute of Geology and Mineral Exploration for allowing me to carry out field work in this wonderful field area.

Finally, at this time I feel so lucky to have such wonderful family and friends. In particular, my parents Mike and Maggie Loveless, without their love and support I would never embarked on, and certainly not have finished this project. I have relied on them throughout. This work is dedicated to you both, and my dear friend Rob, who would have found this a hoot if he were here today. Thank you also to my little sister Rhian, for all her support, who just the other day dreamt about rocks after all these years listening to me talk about them. She has been my rock. Nain and Aunty Ann for their support, and keeping my feet on the ground. I have so many friends that I should thank, but Jenny Hodbod and Lisa Thurston have put up with more than most over these last four years. Bastien Queste who supported my coffee habits. There are many more who are dear to me, in Norwich and further afield and to whom I also owe thanks but can't list here so they will have to settle for a beer.

I am also extremely grateful to my examiners Professors John Walsh and Kevin Hiscock for their helpful suggestions and interesting discussion.

1. Introduction

This thesis investigates the hydrogeological structure of fault zones in poorly lithified sediment. It uses outcrop studies and numerical modelling to bridge the fields of structural geology and hydrogeology.

In this chapter the topic of fault zone hydrogeology is introduced. Implications of the ways in which fault zones impact fluid-flow are first presented, providing a rationale for the thesis. The thesis aim is outlined in this context and a hypothesis proposed, together with three main research questions through which the hypothesis will be addressed. This is followed by an overview of the current understanding of the topic, and concluded with an overview of the thesis structure.

1.1 Rationale

1.1.1 Faults and fluid flow

Geological faults are planar discontinuities within a volume of rock, across which there has been displacement of two tectonic blocks by lithospheric stresses (Kearey, 2001; Wibberley *et al.*, 2008). A fault zone describes the total volume of rock deformed either side of the discontinuity (e.g. Caine *et al.*, 1996). Fault zones occupy a small volume of the Earth's crust, yet they have a significant impact on subsurface fluids, influencing both their location and transport pathways (Bredehoeft *et al.*, 1992; Faulkner *et al.*, 2010).

The influence of faults on fluid-fluid flow has impacted society since early civilisation. Faults have long been known to control the locality of springs, which were key to providing fresh drinking water for ancient and historical civilisations (Alfaro and Wallace, 1994; Crouch, 1996). Faults are also considered the most important pathways for fluids flowing in hydrothermal systems (Yang *et al.*, 2004; Barnicoat *et al.*, 2009), causing thermal hot springs, such as in Bath, England (Andrews *et al.*, 1982), and concentrations of valuable metal ore deposits such as gold, zinc and lead, from circulating deep waters (Sibson *et al.*, 1988; Yang *et al.*, 2004; Barnicoat *et al.*, 2009).

The role of faults on subsurface fluids is also important in modern society; for natural resources such as hydrocarbons (Antonellini and Aydin, 1994; 1995; Knipe *et al*., 1998) and geothermal energy (Lambrakis and Kallergis, 2005; Younger *et al*., 2012), and the security of carbon dioxide sequestered underground (Shipton *et al*., 2004; Chadwick *et al*., 2009; Kampman *et al*., 2012). Faults can also influence the quantity and quality of groundwater supplies (Bense *et al*., 2003; Minor and Hudson, 2006), and complicate environmental challenges such as the safe burial of radioactive waste (Bredehoeft, 1997; Flint *et al*., 2001).

The fluid flow properties of faults remain one of the greatest sources of uncertainty in many fields of subsurface fluid research due to their range of potential hydraulic behaviours (Do Nascimento *et al*., 2005). Faults can focus fluid-flow, acting as conduits (Brown and Moore, 1993; Ferrill *et al.*, 2004), hinder fluid flow, acting as barriers (e.g. Gibson *et al*., 1998; Mohamed and Worden, 2006), or a combination of both, termed conduit-barriers (Bredehoeft *et al*., 1992; Caine *et al*., 1996; Bense and Person, 2006).

1.1.2 Faults and groundwater

The conduit, barrier or conduit-barrier behaviour of faults can impact water resources in a number of ways (Figure 1.1). Compartmentalisation of aquifers by fault barriers can limit the extent of accessible groundwater, or prevent the spread of contaminant plumes (Bredehoeft *et al*., 1992; Mohamed and Worden, 2006; Sternlof *et al*., 2006). Fault conduits can allow preferential recharge into aquifers (Sigda and Wilson, 2003; Ferrill *et al*., 2004), act as sources of groundwater from deeper aquifers (Bense *et al*., 2003), or provide pathways for salt water intrusion, or other contaminants, into freshwater aquifers (Stamatis and Voudouris, 2003). An understanding of these processes is important for securing and protecting water supplies in an age of ever-increasing pressures on groundwater resources (e.g. Wada *et al*., 2010).

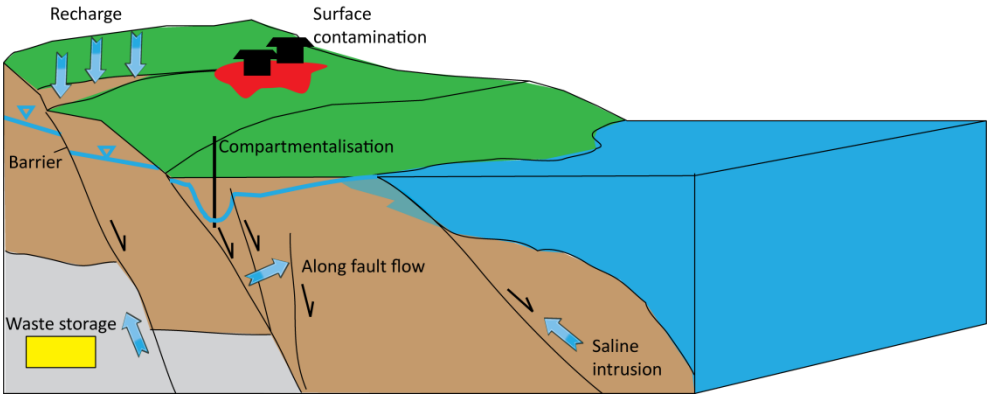

Figure 1.1 Conceptual diagram of possible impacts of faults on groundwater in an unconfined aquifer (brown unit). Black arrows indicate faults and the direction of hangingwall displacement. Thick blue arrows indicate water flow direction. Blue line with triangles indicates the groundwater hydraulic head. The thick black vertical line is a borehole with a limited water supply due to aquifer compartmentalisation by adjacent fault zones. Faults at the coast could provide a barrier, preventing saline intrusion into the freshwater aquifer, or allow leaks or along-fault fluid-flow. Grey unit represents low permeability rock that could be used to store high risk waste adjacent to a fault zone, along which fluid-flow could occur.

Whilst there is now a reasonable understanding of how faults in crystalline or lithified rock impact fluid flow (e.g. Wibberley *et al.*, 2008; Faulkner *et al.*, 2010), less is known about how faults in poorly lithified sediment impact fluid flow. These sediments accommodate major aquifers in the USA (Grauch *et al.*, 2004; Minor and Hudson, 2006) and Europe (Voudouris *et al.*, 2005; Magri *et al.*, 2010), and are commonly primary targets for investigation in the search for groundwater (Davies and DeWeist, 1967; Mathers *et al.*, 1993). Widespread faulting in these aquifers is common (Heynekamp *et al.*, 1999; Grauch *et al.*, 2004) though is frequently overlooked in regional hydrogeological studies, at least in part due to the difficulties identifying faults resulting from poor preservation of fault scarps and traces in highly erodible sediments (e.g. Carter and Winter, 1995; Wilson *et al.*, 2003). Nevertheless, over the last two decades there has been widening recognition of the potential for faults in poorly lithified sediment to have significant hydrological impacts (e.g. Henyekamp *et al.*, 1999; Sigda *et al.*, 1999; Rawling *et al.*, 2001; Rawling and Goodwin, 2003; Bense *et al.*, 2003; Bense and Person, 2006; Minor and Hudson,

2006; Rawling and Goodwin, 2006; Balsamo *et al.*, 2008; Bense *et al*., 2008; Caine and Minor, 2009; Balsamo and Storti, 2010; 2011), and crucially, the considerable risks associated with inaccurate prediction of fault zone hydraulic behaviour (Bense *et al*., 2008).

Current understanding of fault zone hydrogeology has been established through a combination of investigation techniques. The most direct method is through analysis of hydrogeological data. Analysis of hydraulic head either side of a fault zone can infer the seal capacity of a fault (Bense and Van Balen, 2003; Mohamed and Worden, 2006) although additional data such as temperature (Bense *et al*., 2008) or geochemistry (Gumm, 2011) is necessary to delineate flow paths within fault zones (Bense *et al*., *in review*). Whilst hydrogeological studies provide tangible evidence of fault zone hydraulic behaviour, the availability of such data is often limited and rarely reveals the physical basis behind specific fault behaviour.

A more deterministic insight into fault zone behaviour is afforded by investigations of fault zone permeability (or hydraulic conductivity) structure (Caine *et al*., 1996; Rawling *et al*., 2001). These studies can reveal the physical basis behind fault hydraulic behaviours, and enable elucidation of factors that might contribute to controlling these; such as crustal stress conditions, fault age or size, seismicity, fault zone and protolith/protosediment (original undeformed rock or sediment) petrophysical properties, and fault deformation mechanisms (e.g. Antonellini and Aydin, 1994; Rawling *et al*., 2001; Balsamo and Storti, 2011). Fault zone hydraulic conductivity structure can be inferred from field observations (e.g. Heynekamp *et al*., 1999; Rawling *et al*., 2001; Caine and Minor, 2009; Balsamo and Storti, 2010), laboratory experiments on fault core samples (Evans *et al*., 1997; Bense *et al*., 2003; Balsamo *et al*., 2010), shear deformation experiments (Zhang and Tullis, 1998; Sperrevik *et al*., 2000), seismicity (Do Nascimento *et al*., 2005), and analytical and numerical models (Haneberg, 1995; Yang *et al*., 2004; Bense and Person, 2006; Anderson and Bakker, 2008).

Examination of flow tracers, contemporary hydrological data, and numerical modelling of groundwater flow show evidence to support the conduit (Flint *et al*., 2001; Stamatis and Voudouris, 2003; Giurgea *et al*., 2004) or conduit-barrier (Person *et al*., 2000; Bense and Van Balen, 2003; Heffner and Fairley, 2006; Bense and

Person, 2006; Bense *et al*., 2008) behaviour for faults in poorly lithified sediment. Yet outcrop studies of fault zones generally predict that faults in poorly lithified sediment behave as hydraulic barriers, and will prevent cross-fault fluid-flow and potentially compartmentalise regional aquifers (Heyenkamp *et al*., 1999; Rawling *et al*., 2001; Barnicoat *et al*., 2009; Caine and Minor, 2009; Balsamo and Storti, 2010). In outcrop, conduit-barrier behaviour has only been predicted from fault zone structure in low porosity sediments (Balsamo *et al*., 2010), and conduit behaviour in the early stages of faulting (Bense *et al*., 2003; Balsamo *et al*., 2008).

The discrepancies between the expected hydraulic behaviour of faults in poorly lithified sediment, as determined from outcrop studies of fault zone structure, and those ascertained from hydrological data, cause uncertainty in understanding their hydraulic impacts. Heffner and Fairley (2006) suggested that further outcrop investigations could lead to identification of a greater range of possible fault zone hydrogeologic structures than so far reported, which could explain these discrepancies. Indeed, the greater range of fault zone structures reported from outcrop studies by Balsamo and Storti (2010; 2011) supports this position.

1.2 Aim

The aim of this thesis is to examine the reasons behind the discrepancies in predicted and observed fault hydraulic behaviours. The following hypothesis is proposed for investigation:

"The structure of fault zones in poorly lithified sediment can explain the model of conduit-barrier behaviour derived from hydrogeological observations"

Three objectives are used in order to address this hypothesis:

1. Identify the structure and deformation processes of fault zones in poorly lithified sediment of the Gulf of Corinth rift.

2. Ascertain the changes to the hydraulic conductivity of poorly lithified sediment in fault zones.

3. Establish the ways in which fault zones in poorly lithified sediment influence fluid-flow.

Outcrop investigations of syn-rift sediment are used to deduce fault zone hydraulic conductivity structure. The hydraulic impacts of these structures are explored using numerical fluid-flow models. The Gulf of Corinth rift, a rapidly extending basin in central Greece (Figure 1.2), was chosen as the field area for this investigation. Voluminous deposits of poorly lithified syn-rift sediment on the southern flank of the Gulf of Corinth rift form important aquifers and confining units, which are locally highly faulted. The syn-rift sediment (<3.2 Ma) (Leeder *et al*., 2012) is characterised by coarse gravel delta and alluvial conglomerates overlying lacustrine and delta bottomset finer-grained sediment, that can be locally inter-bedded with sand to cobble-sized conglomerates from submarine debris flows (Rohais *et al*., 2007). Syn-rift sediment has been undergoing uplift along the south rift flank since deposition (Ori, 1989; Vita-Finzi, 1993; Ford *et al*., 2012), thus has only experienced shallow burial depths (<200 m) and very modest lithification. Incision of cross axial-drainage channels along the southern flank (Figure 1.2) has resulted in excellent exposures of a number of fault arrays cutting syn-rift sediment. The geological setting is described in greater detail in Chapter 2.

The structure of faults cutting poorly lithified syn-rift sediment of the Gulf of Corinth rift has not previously been examined. This setting provides a novel insight into the structure of fault zones cutting different lithologies, and under different crustal stress conditions to previous outcrop studies, which have been conducted in predominantly sandy continental sediments from a handful of sites in New Mexico (Heynekamp *et al*., 1999; Sigda *et al*., 1999; Rawling *et al*., 2001; Rawling and Goodwin, 2003; Rawling and Goodwin, 2006; Minor and Hudson, 2006; Caine and Minor, 2009), Germany (Bense *et al*., 2003; Bense and Van Balen, 2003; 2004) and Italy (Balsamo *et al*., 2008; Balsamo and Storti, 2010; Balsamo and Storti, 2011). Faults exposed in the Gulf of Corinth syn-rift sediment are likely to be analogous to those where basin subsidence is continuous, but less well exposed (e.g. Maltman, 1988). Furthermore, these faults may have important hydrological impacts on the valuable groundwater resources of the Gulf of Corinth rift region (e.g. Stamatis and Voudouris, 2003; Giurgea *et al*., 2004; Micarelli *et al*., 2006a).

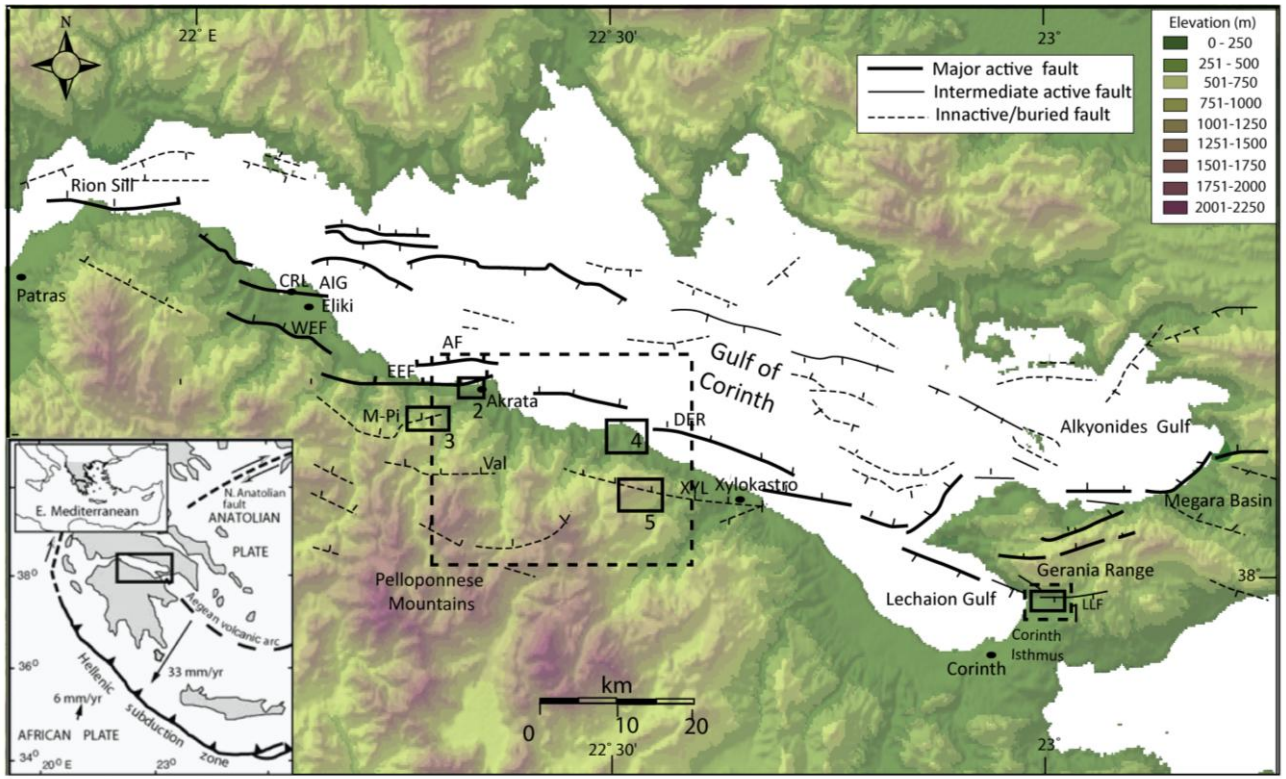

Figure 1.2 Topographical map of the Gulf of Corinth rift, with active and inactive faults (Rohais *et al*., 2007; Bell *et al*., 2008; Leeder *et al*., 2012); West and East Eliki (WEF and EEF); Aigion (AIG); Akrata (AF); Derveni (DER); Xylokastro (XYL). Mamoussia-Pirgaki (M-Pi); Valimi (VAL); Lower Loutraki (LLF). CRL shows the location of the Corinth Rift Laboratory. Outcrop locations used in this work are shown by solid boxes; 1. Loutraki; 2. Akrata; 3. Voutsimos; 4. Mentourgianika; 5. Pirgos. Boxes with dashed lines show regions covered by the geological maps in Figure 2.2. Inset map shows Gulf of Corinth rift setting in mainland Greece and its regional tectonic setting, from Leeder *et al*. (2003).

1.3 Hydrogeological structure of fault zones

Arguably the primary reason that faults impact sub-surface fluid-flow is the change to bed configuration resulting from displacement across a fault, which can result in rocks with contrasting hydraulic properties being juxtaposed either side of the fault zone (Allan, 1989; Haneberg, 1995; Knipe, 1997; Mailloux, *et al*., 1999). Fault displacement (Figure 1.3a), commonly used to describe fault size, is the separation distance of two initially adjoined points either side of the fault. Groundwater flowing in a hydraulically conductive unit encountering a low hydraulic conductivity unit juxtaposed across a fault zone, will generally get diverted along the fault to another aquifer, or to the surface as a spring (Davis and DeWeist, 1967) rather than crossing the fault. "Allan diagrams" can be used to map juxtapositions of key hydrogeologic units and assess the hydrological impacts if fault displacement and stratigraphy (bed composition and thickness) are known (Allan, 1989; Knipe, 1997).

However, faults do not require the juxtaposition of differing hydogeologic units to impact fluid flow, since deformation of rock/ sediment by faults introduces heterogeneity and anisotropy into aquifers by altering their structure (Bredehoeft *et al*., 1992; Caine *et al*., 1996). The specific heterogeneities and anisotropies resulting from fault zones arise from the particular fault zone stucture, often described in terms of its architecture (Caine *et al*., 1996; Rawling *et al*., 2001). Conceptual models of fault zone architecture typically comprise two architectural elements; a fault core and damage zones (Figure 1.3b) (Caine *et al*., 1996). The fault core comprises structural elements (discrete geological units in the fault zone with similar petrophysical properties) that have accommodated the majority of fault displacement. Damage zones flank the fault core and are comprised of structural elements that are mechanically related to the growth of the fault (Sibson, 1977; Caine *et al*., 1996). The structural elements comprising a fault zone vary depending on the mechanism of deformation, i.e. the mechanical process by which a rock or sediment accommodates strain in response to applied stress (Table 1.1). Fault zone structural elements generally alter the protolith or protosediment hydraulic conductivity, as summarised in Table 1.1.

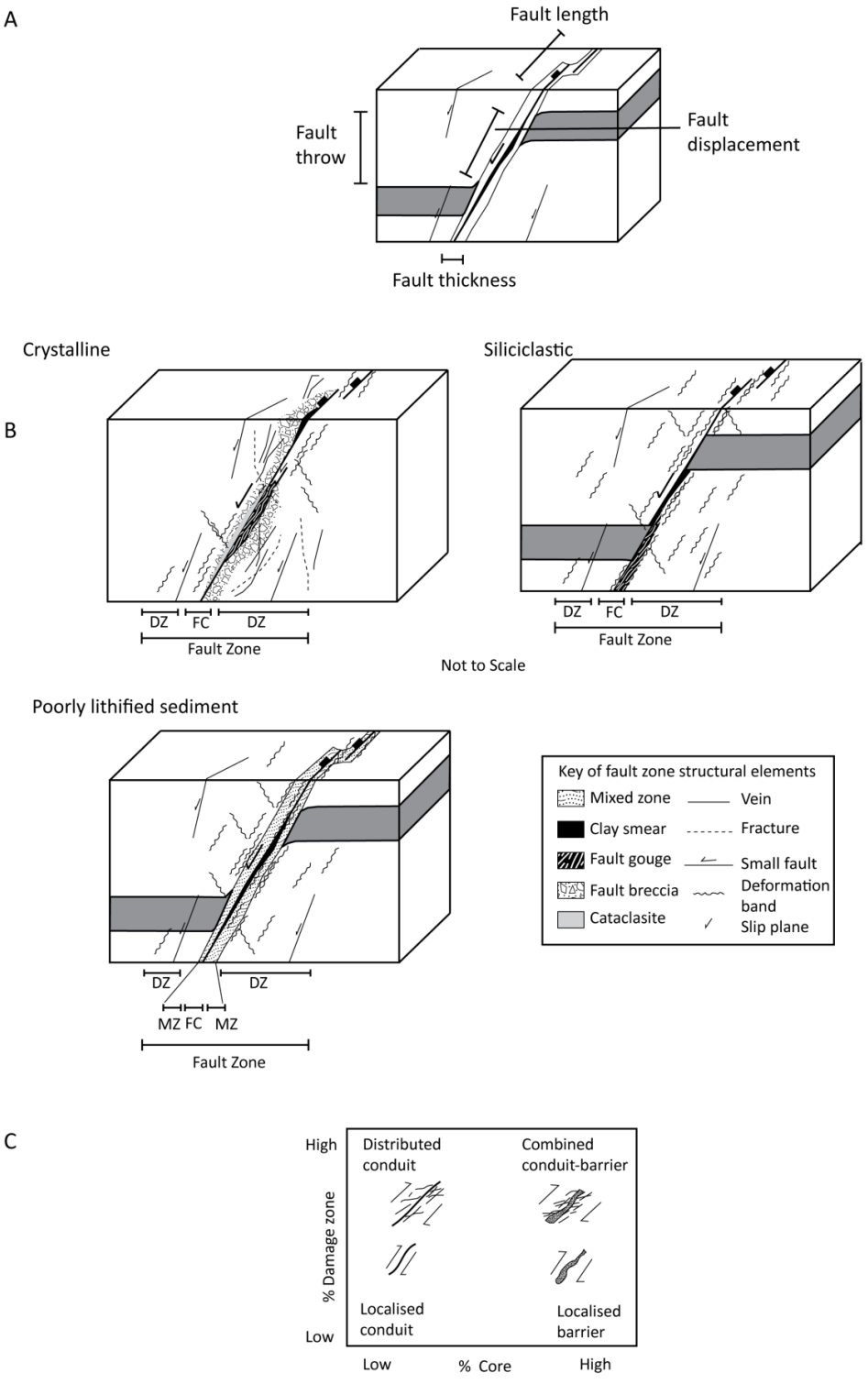

Figure 1.3 Fault zone hydrogeological structure. A) Illustration of fault zone thickness, displacement, throw and length. B) Conceptual models of fault zone structure. Fault zones in crystalline and siliciclastic rocks typically comprise a fault core (FC) and damage zones (DZ). Fault zones in poorly lithified sediment also typically have a mixed zone (MZ). C) Conceptual model of the hydraulic behaviour of fault zones in brittle rocks based on the relative proportion of fault zone structural elements, from Caine *et al*. (1996).

Process	Product	Description	Poorly lithified sediments	Clastic sedimentary	Carbonate sedimentary	Crystalline rock
Fault processes that enhance permeability						
Brecciation	Fault mega breccias, breccias, microbreccia	Rock that has been broken into angular clasts as a result of applied tectonic stresses.		Hippler 1993; Eichhubl *et al.* 2009	Roberts and Stewart 1994; Billi 2005;	Bruhn *et al.* 1994;
Fracturing	Shear fractures, joints	Discrete, roughly planar discontinuity across which there has been rock separation.		Laubach 1988; Eichhubl *et al.* 2009	Roberts and Stewart 1994; Ferrill *et al* . 2004	Caine and Tomusiak 2003; Martel 1990
Particulate/ granular flow	Disaggregation bands, dilation bands	Tabular zones of grain deformation a few mm in width, up to tens of meters in length, each band may accommodate a few cm of slip (Aydin 1978). Grains are neither crushed nor compacted but sediment structure is disaggregated (Du Bernard *et al.* 2002) formed by grain rolling and sliding. Porosity increase is greater in dilation bands.	Du Bernard *et al* . 2002; Exner and Graseman 2010			
	Sediment smear	Entrainment and smear of sediment beds into the fault zone and along the fault zone.	Bense and Person (2006)			
Fault processes that reduce permeability						
Brecciation/ cataclasis	Fault gouge	Fracturing of grains into smaller constituent parts forming fine grained, incohesive rock with > 30 % visible fragments surrounded by matrix .		Engelder 1974; Gibson 1998	Ferrill and Morris 2003; Benedicto *et al.* 2008	Chester and Logan 1987; Schulz and Evans 2000
Cataclasis	Shear/cataclastic deformation bands	As disaggregation bands above, in which grains are also fractured (cataclasis) and/or compacted as a result of shear stresses.	Sigda *et al.* 1999; Cashman and Cashman 2000	Aydin 1978; Antonellini and Aydin 1994 and 1995	Rath *et al.* 2011	
	Cataclasite, ultracataclasite	Cohesive fault rock formed from grains fracturing (cataclasis), 15-20 % fragments in finer grained matrix (Kearey, 2001).	Balsamo and Storti 2010	Labaume *et al.* 2001; Tueckmantel *et al.* 2012	Agosta and Kirschner 2003; Micarrelli *et al.* 2006;	Chester and Logan 1987
Phylosilicate smearing	Phylosilicate band	As disaggregation bands and deformation bands above, in which a significant proportion of clay grains are entrained and aligned along the band		Antonellini *et al.* 1994; Knipe 1997		
	Clay smear	Smearing of clay-sized material along the fault plane, or into the fault zone for which the protolith must have a high proportion of clay.	Rawling *et al.* 2001; Bense and Van Balen 2004	Lindsay *et al.* 1993; Egholm *et al.* 2008	Ferrill *et al* . 2004; Bonson *et al* . 2007	
Frictional melting	Pseudotachylite	Glass-like fine grained rock formed by heating from shear displacement.		Rowe *et al.* 2005	Craddock *et al.* 2012	Lin 1996; Sibson 1977
Particulate/ granular flow	Zone of mixed sediment	Zone in which sediment from different beds are mixed at the grain-scale.	Heynekamp *et al.* 1999; Rawling and Goodwin 2006			
Fault processes that may increase or reduce permeability						
Shear localisation	Slip surface	Localised zone, often a plane along which significant displacement is focused.	Heynekamp *et al.* 1999; De Boever *et al.* 2011	Antonellini and Aydin 1994 and 1995	Roberts and Stewart 1994; Bastesen *et al.* 2009	Bruhn *et al.* 1994; Walker *et al.* 2012
	Lenses or blocks	Blocks of largely undeformed sediment bound by localised shear zones.	Heynekamp *et al.* 1999	Lindanger *et al.* 2007	Bastesen *et al.* 2009; Lindanger *et al.* 2007	Lee and Kim 2005

Table 1.1 Fault zone deformation processes and structural elements (product) with impact on permeability and occurrence. Dark grey and light grey boxes indicate common and uncommon elements for the lithology respectively, with examples found in the literature. Structural elements are thus far not reported where boxes have no fill. Adapted from Bense *et al.* (*under review)*.

Fault zone hydraulic properties are strongly dependent on fault zone structure; the specific structural elements (and their particular hydraulic properties) (Figure 1.3b; Table 1.1), and their geometry and spatial distribution in the fault zone (e.g. Antonellini and Aydin, 1995; Caine *et al.*, 1996; Knipe, 1997; Heynekamp *et al.*, 1999; Lunn *et al*., 2008). These properties can vary significantly throughout the three dimensions of the fault zone (Aydin, 2000; Childs *et al*., 2009).

Fault cores in brittle rocks can comprise a combination of fault gouge, cataclasites, breccias, mylonites, discrete slip surfaces, and relatively cohesive lenses or blocks of sediment (Sibson 1977; Caine *et al*., 1996; Faulkner *et al*., 2003; Bastesen *et al*., 2009) (Figure 1.3b, Table 1.1). In siliciclastic rocks strain is often accommodated by single or anastomosing deformation bands in both the fault core and damage zone (Aydin, 1978; Antonellini and Aydin, 1995) (Figure 1.3b; Table 1.1). If there is a sufficient proportion of clay in the protolith of siliciclastic and carbonate rocks clay can be smeared through the fault core (Yielding *et al*., 1997; Ferrill *et al*., 2004). Damage zones comprise subsidiary faults, veins, breccia, folds, shear deformation bands, and most commonly fracture networks (Sibson 1977; Caine *et al*., 1996; Figure 1.3b).

Caine *et al*. (1996) proposed a method to categorise the hydraulic behaviour of faults in brittle rocks from conduit through to barrier, based on the relative proportion of low hydraulic conductivity fault core elements to high hydraulic conductivity damage zone elements (Figure 1.3c). However, the specific fault zone architecture and structural elements are influenced by factors such as petrophysical and rheological properties of the protolith and crustal stress conditions – in particular burial depth (Wilson *et al*., 2003; Balsamo *et al*., 2008), therefore, fault zones cutting poorly lithified sediment that are usually deformed at <1 km in the crust exhibit considerable structural and architectural differences to brittle rock (e.g. Heynekamp *et al*., 1999; Rawling *et al*., 2001; Caine and Minor, 2009) (Figure 1.3b).

Previous studies of faults zones in poorly lithified sediment have reported fault cores comprising a continuous clay smear, slip surfaces, or a cluster of deformation bands (Heynekamp *et al*., 1999; Rawling *et al*., 2001; Bense *et al*., 2003; Rawling and Goodwin, 2003; Minor and Hudson, 2006; Rawling and Goodwin, 2006; Caine and Minor, 2009; Balsamo and Storti, 2010) (Figure 1.3b, Table 1.1). In contrast to brittle

rocks, shear deformation bands commonly replace fracture networks as the basic structural element in damage zones (Heynekamp *et al*., 1999; Rawling *et al*., 2001; Bense *et al*., 2003; Rawling and Goodwin, 2003; Minor and Hudson, 2006; Rawling and Goodwin, 2006; Wilson *et al*., 2003) (Figure 1.3b, Table 1.1). At shallow burial depths in extensional settings (<1.5 km) disaggregation bands, or even dilation bands, can form in damage zones (Du Bernard *et al*., 2002; Bense *et al*., 2003; Minor and Hudson, 2006; Balsamo *et al*., 2008) (Table 1.1).

Importantly, in poorly lithified sediment a third architectural element, the mixed zone, separates the fault core and damage zone (Mozley and Goodwin, 1995; Heynekamp *et al*., 1999; Rawling and Goodwin, 2006) (Figure 1.3b). Its name refers to the mixed structural nature of these zones (Rawling and Goodwin, 2006), and is distinct from the structural element of a zone of mixed sediment in which sediments are mixed at the grain-scale (Table 1.1). Beds are commonly rotated consistent with fault dip at the mixed zone boundary, and can form smears in the mixed zone, in which initial sedimentary bed characteristics are progressively modified with increasing fault displacement. Bed definition can eventually be lost entirely where fault displacement exceeds bed thickness, resulting in a largely homogenised zone of mixed sediment (Table 1.1) (Mozley and Goodwin, 1995; Heynekamp *et al*., 1999; Rawling and Goodwin, 2006). Lenses or blocks of relatively undeformed sediment can also be found in mixed zones (Rawling and Goodwin, 2006; Caine and Minor, 2009). Localised shear zones or deformation band shear zones can sometimes separate the mixed zone from the undeformed sediment (Rawling and Goodwin, 2006; Caine and Minor, 2009). More recent studies by Balsamo and Storti (2011; 2010) have recognised a wider range of fault zone structure in poorly lithified sediment, in which some architectural or structural elements, such as deformation bands and mixed zones, may be absent.

The processes by which sediment is deformed in fault zones cutting poorly lithified sediment control the fault zone structure, but also influence grain-size distributions, porosity and grain shape-preferred orientation of clasts, and thus sediment hydraulic conductivity and anisotropy (e.g. Rawling and Goodwin, 2003; Bense and Person, 2006; Exner and Tschegg, 2012). The dominant deformation mechanism in fault zones cutting poorly lithified sediment is particulate flow (Rawling and Goodwin,

2003; Bense *et al*., 2003; Balsamo *et al*., 2008; Caine and Minor, 2009). This can occur because grains in poorly lithified sediment are able to slide or roll individually along their boundaries (Borradaile, 1981) (Table 1.1). Grain-scale mixing and clast rotation are widespread products of particulate flow in fault zones cutting poorly lithified sediment (Mozley and Goodwin, 1995; Goodwin and Tikoff, 2002; Rawling and Goodwin, 2006). Particulate flow can be accompanied by varying degrees of cataclasis (grain fracturing). Particulate flow without cataclasis is known as independent particulate flow. In controlled particulate flow, the rate of grain sliding is controlled by the deformation (i.e. cataclasis) of grains (Borradaile, 1981); this is the most common type of particulate flow accommodating shear strain in poorly lithified sediment (Rawling and Goodwin, 2003; Rawling and Goodwin, 2006; Balsamo *et al.,* 2008). Nevertheless, cataclasis itself may the dominant deformation mechanism in some fault zones (Balsamo and Storti, 2010; 2011).

The degree of cataclasis occurring during fault zone deformation is dependent upon lithology, confining pressures and deviatoric stresses (e.g. Heynekamp *et al.,* 1999; Wilson *et al.,* 2006; Balsamo *et al.,* 2008) (Figures 1.3a; Table 1.1). Fulljames *et al*. (1997) present a model showing the increase in proportion of cataclasis with deformation depth and sediment porosity, in which significant amounts of cataclasis only occurs at depths >1.5 km. Thus the hydraulic impact of grain-size reduction would increase with depth. However, evidence of cataclasis has been found in fault zones cutting poorly lithified sediments at very shallow burial depths (e.g. Cashman and Cashman, 2000; Cashman et al., 2007; Balsamo and Storti, 2011), leading to suggest that it can be associated with co-seismic rupture. In these sediments the Fulljames *et al.,* (1997) model would under-predict hydraulic impacts of fault zone deformation. Other possible controls on the degree of cataclasis includes grain size (Balsamo and Storti, 2011), mineralogy (Rawling and Goodwin, 2003; Wilson *et al*., 2003; Exner and Tschegg, 2012), porosity (Fulljames *et al*., 1997; Balsamo *et al*., 2010), degree of lithification (Rawling and Goodwin, 2006; Balsamo *et al*., 2008) or grain contact area (Wilson *et al*., 2003; Minor and Hudson, 2006).

Other mechansims of deformation can also occur in fault zones cutting poorly lithified sediment, such as phylosilicate smearing, forming phylosilicate bands (Fossen *et al.,* 2007) and clay smears (Rawling *et al.,* 2001; Bense and Van Balen, 2004; Minor and Hudson, 2006) in faults cutting sediment with a high proportion

clay grade particles. Induration of sediment from diagenetic processes can facilitate the localisation of shear along planes (Heynekamp *et al*., 1999; Balsamo and Storti, 2010).

Outcrop studies infer a barrier behaviour of faults cutting poorly lithified sediment due to the frequent occurrence of clay fault cores and shear deformation bands, both of which reduce sediment grain-size, sorting and porosity, and therefore hydraulic conductivity in the fault zone (Rawling *et al*., 2001; Caine and Minor, 2009; Balsamo and Storti, 2010). The hydrocarbon industry use empirical equations such as the Clay Smear Potential (CSP) (Bouvier *et al*., 1989), shale smear factor (SSF) (Lindsay *et al*., 1993) and shale gouge ratio (SGR) (Yielding *et al*., 1997). These algorithms predict the occurrence of low permeability clay smears over a fault plane based on variables such as fault displacement, protolith composition and likely juxtaposition. The resultant estimates of fault hydraulic conductivity can be combined with estimates of fault zone thickness either explicitly (Bense and Person, 2006; Tveranger *et al*., 2007), or implicitly as transmissibility multipliers between grid cells for fault zones in reservoirs, to predict the seal capacity of a fault zone (Walsh *et al*., 1998; Manzocchi *et al*., 1999; Sperrevik *et al*., 2002; Childs *et al*., 2009; Manzocchi *et al*., 2010).

Bense and Van Balen (2004) found that the SGR could be applied to shallow fault zones cutting sand and clay in the Lower Rhine Embayment. However, these algorithms do not account for the possibility of along-fault fluid flow that is necessary for assessing the conduit behaviour of a fault zone. A modified algorithm developed by Bense and Person (2006) that can account for along-fault flow resulting from fault zone anisotropy due to clay and sand smears and grain rotation, was able to demonstrate conduit-barrier behaviour in numerical models of faults cutting poorly lithified sediment. Nevertheless, the role of deformation band damage zones and mixed zones was not accounted for. A more recent development that has the potential to represent all these features in fault zone hydraulic models is the Fault Facies approach, in which fault zone structural elements are categorised as facies. These can be empirically linked by field observations to protolith petrophysical properties and fault zone displacement and strain distributions. Fault Facies are then

stochastically generated from these input parameters and used to populate fault zone volumes (Fredman, 2007; Tveranger *et al*., 2007; Braathen *et al*., 2009).

The hydraulic impact of a fault zone is proportional to the volume of rock deformed, and therefore its thickness and length (fault-perpendicular and parallel extent of the fault zone respectively) (Figure 1.3a). These attributes have been found to be positively correlated with fault displacement across a wide range of lithologies and tectonic settings, over seven orders of magnitude (Childs *et al.*, 1996a; Childs *et al.*, 2009; Torabi and Berg, 2011). Therefore fault size is potentially a major influence on the impact of faults on fluid flow (Walsh *et al*., 1998; Sigda *et al*., 1999; Bense and Person, 2006; Balsamo *et al*., 2010; Childs *et al*., 2009; Manzocchi *et al*., 2010), and as such it commonly believed that only large scale faults have significant impacts on fluid flow at reservoir scales (Walsh *et al*., 1998; Manzocchi *et al*., 2010). However, since even shear deformation bands, with millimetres to centimetres of displacement (Table 1.1), can reduce permeability locally by 3 to 4 orders of magnitude (Antonellini and Aydin, 1994), the cumulative impacts of many deformation bands (Sternlof *et al*., 2006), or small faults, may be significant.

Fault interactions, controlled by fault size, density, and the orientation of faults in a population, can influence the potential for aquifer compartmentalisation and connectivity of preferential fluid-flow pathways (Gibson *et al*., 1998; Mohamed and Worden, 2005; Needham, 2006; Childs *et al*., 2009; Torabi and Berg, 2011). However, knowledge of fault population characteristics in a region is often incomplete due to the limited scales of investigation techniques. For example, small faults are difficult to identify in the field, and therefore may not be mapped (Sigda *et al*., 1999; Wilson *et al*., 2003; Grauch *et al*., 2004), borehole studies sample a very limited extent of a region, and the resolution of seismic surveys is generally too poor to identify faults with displacement <~30 m (Long and Imber, 2010; Torabi and Berg, 2011). To compensate, numbers of faults of certain sizes in an array can be predicted using characteristic fault size population distributions for the particular geological setting (Needham *et al*., 1996; Torabi and Berg, 2011). This can be particularly important when using seismic data, in order to attribute resolvable bed displacement to the correct number of faults and throw magnitudes and avoid over-

simplification of juxtaposition effects (Childs *et al*., 1997; Knipe, 1997; Finch *et al*., 2004; Huang and Johnson, 2010; Long and Imber, 2010; Manzocchi *et al*., 2010).

Fault zone hydraulic impacts are often transient due to a variety of secondary fault zone processes. Over time, mineral-saturated fluids can precipitate cements in pores and/ or fractures, and form significant barriers to fluid-flow (Knipe, 1997; Micarelli *et al*., 2006b; Eichhubl *et al*., 2009). In active fault zones, subsequent episodic fault rupture can increase the hydraulic conductivity of faults previously sealed with cement (Woodcock *et al*., 2007). In soluble rocks such as carbonates, the flow of mineral under-saturated fluids through fault fractures can cause dissolution, leading to potentially significant increases in fault zone hydraulic conductivity (Roberts and Stewart, 1994; Micarelli *et al*., 2006b; Kim and Sanderson, 2009).

The specific hydraulic impact of a fault will also depend on additional factors including the properties (buoyancy and viscosity) of the fluid under consideration (e.g. Hiscock, 2005) and the hydrogeological boundary conditions (Haneberg, 1995; Gudmundsson, 2000). The hydraulic behaviour of fault zones may reverse depending on aquifer saturation, for example, Sigda *et al*. (2003) found that fault zones with reduced porosity and permeability that would behave as barriers in phreatic conditions acted as preferential flow conduits in vadose conditions.

1.4 Thesis structure

This thesis has been constructed in seven chapters. Chapter 2 provides background to the subsequent chapters, and provides background to the tectonic, sedimentological and hydrogeological setting of the Gulf of Corinth rift. The geological settings specific to each of five outcrop locations, established through field mapping and combined with published literature, are also presented. Chapters 3 to 6 address Objectives 1 to 3:

1. Identify the structure and deformation processes of fault zones in poorly lithified sediment of the Gulf of Corinth rift.

Chapter 3 is an in-depth case study that identifies the structure and deformation processes of faults in an outcropping fault array exposed to the north of the Loutraki town, at the eastern boundary of the Gulf of Corinth (Figure 1.2). Micro to macro-

scale fault zone structure and deformation mechanisms of minor (1 to 10 m throw) faults cutting heterogeneous syn-rift sediment were deduced through observations from hand samples, thin sections and grain-size distributions and measurements taken in the field. A model of fault zone evolution is proposed for faults cutting consistently poorly lithified sediment and those cutting sediment of contrasting competency. This Chapter is based on a paper that was published in the *Journal of Structural Geology* (Loveless *et al.*, 2011). Additional data has been added, including data on fault zone structure for Faults 3 and 4, and the text has also been modified in places.

Chapter 4 constrains the models of fault zone structure and evolution proposed in Chapter 3 using data from across all five outcrops. This enabled investigation of the structure of fault zones with throws ranging from 0.01 m to 80 m, and in a wider range of lithologies. A third fault zone type was identified in which fine and coarse-grained sediment are juxtaposed across the fault zone. Fault size population distributions and array characteristics are also considered in this chapter.

2. Ascertain the changes to the hydraulic conductivity of poorly lithified sediment in fault zones.

Chapter 5 investigates the impact of fault zones on sediment hydraulic conductivity. Porosity was estimated from fault zone thin section samples using image analysis, and hydraulic conductivity estimated using empirical equations. The hydraulic impact of fault zone heterogeneity identified in Chapters 3 and 4 was also investigated using a combination of thin section image analysis and grain-size distributions with empirical equations to estimate hydraulic conductivity. Hydraulic anisotropy is also estimated based on flow path tortuosity. The impact of fault throw on sediment porosity and hydraulic conductivity was assessed.

3. Establish the ways in which fault zones in poorly lithified sediment influence fluid flow.

In Chapter 6 numerical fluid-flow models of fault zones are presented. These models are developed using fault zone structure and evolution identified from Chapters 3 and 4, combined with estimates of hydraulic conductivity from Chapter 5. Characteristic fault zone hydrogeological structures are represented for three model sets:

homogeneous gravels (1m and 5m throw), sediment of contrasting competency (1 m throw) and faults juxtaposing fine and coarse-grained sediment (5m throw). Fault zone structures, hydraulic conductivity, thickness and anisotropy are varied in each model set within the ranges determined in the previous chapters. The most common hydraulic impacts for each model set, and the most hydraulically significant fault zone parameters are identified for each model set. Evidence of fluid-flow from outcrop is also presented in order to verify the numerical fluid-flow model outputs.

Chapter 7 provides a summary of Chapters 3 to 6 in terms of the objectives, and subsequently addresses the thesis hypothesis. The wider context of the findings is then discussed, with the limitations of this research. Recommendations for further work are made and a concluding statement presented.

2. Geological and hydrogeological setting of the Gulf of Corinth rift

This chapter describes the Gulf of Corinth rift, the setting for this research. It sets the scene for the subsequent chapters and provides additional information on the research locations, including sediment characteristics and tectonic settings, which may contribute to an understanding of fault zone hydrogeological structure and impacts. The geological structure and evolution of the Gulf of Corinth rift is first summarised, with a description of the key syn-rift lithological facies. This description focuses the southern rift flank and the Lechaion gulf – the areas in which the five outcrop sites are located. Current understanding of the hydrogeology of the southern flank and eastern margin of the Lechaion Gulf is described in this context. Lastly, the five outcropping fault array locations chosen for investigation are described in greater detail.

2.1 The Gulf of Corinth rift

The Gulf of Corinth rift is a rapidly extending (about 5-15 mm yr^{-1}) half-graben ~100 km long by 30 km wide, trending ESE-WNW, in Central Greece (e.g. Bell *et al*., 2009)(Figure 1.2). The 800 m deep Gulf is connected to two sub-basins at the eastern boundary – the Alkyonides and Lechaion Gulfs, and the Ionian Sea to the west, beyond the shallow Rion sill. Crustal-scale normal-faults, with throws up to 1500 m, accommodate the north-south orientated rift extension, trending parallel or slightly oblique to the basin axis (Ford *et al*., 2012). Uplift of the fault footwalls produce the characteristic fault-controlled topography of the southern rift flank (Figures 1.2 and 2.1a) not found on the northern rift flank (Ori, 1989). Throughout the majority of the southern rift flank, Mesozoic basement rock is overlain by voluminous poorly lithified syn-rift deposits (e.g. Rohais *et al*., 2007; Leeder *et al*., 2012) cut by small to medium scale intra-crustal faults that are the focus of this research.

2.1.1 The Gulf of Corinth rift evolution

The Gulf of Corinth rift is a forearc basin resulting from slab roll-back of the African tectonic plate that subducts beneath the Anatolian tectonic plate at the Hellenic collision zone, approximately 200 km to the south of the Gulf of Corinth rift (inset in Figure 1.2) (e.g. Jovilet, 2001; Leeder *et al*., 2003). The westward propagation of the

Northern Anatolian fault (Armijo *et al*., 1996; 1999; Pik *et al*., 2009), and/ or gravitational collapse of regionally over-thickened lithosphere from the Miocene Hellenide Orogeny (Le Pichon and Angelier, 1979) may also contribute rift structure and evolution. Nappes emplaced during the Miocene Hellenide Orogeny provide the highly deformed alpine Mesozoic carbonate, radiolarite and clay pre-rift basement rocks of the present day Gulf of Corinth rift (Doutsos *et al*., 1992; Doan and Cornet, 2007). Rift extension rates are believed to have increased from east to west over time as the rift is "unzipped" from anti-clockwise rotation of a rigid Peloponnesus tectonic block about a vertical axis pole (Goldsworthy *et al*., 2002; Mattei *et al*., 2004; Leeder *et al*., 2012). Today, extension rates increase westwards from 5 mm yr^{-1} at the eastern edge of the gulf to 10-16 mm yr^{-1} in the western gulf (Clarke *et al*., 1998; Avallone *et al*., 2004).

Distributed deformation formed multiple half-grabens with shallow continental and lacustrine depositional environments across the initial, early Pliocene (~5 Ma) rift (Ori, 1989; Rohais *et al*., 2007; Leeder *et al*., 2008; Ford *et al*., 2012; Leeder *et al*., 2012), of which the Lechaion Gulf is believed to be a part (Leeder *et al*., 2005) (Figure 1.2). The Exochi and Valimi Formations, characterised by alluvial and fluvial facies, comprise the earliest Lower Group syn-rift sediment (Rohais *et al*., 2007) (Figure 2.1b). The upper Lower Group deposits of the Aiges Formation comprises silt and marl interbedded with fine to coarse-grained sand, representing distal fan delta and debris flow depositional systems, which either correspond to the distal Valimi Formation or pro-delta deposits of Middle Group Gilbert-type deltas (Rohais *et al*., 2007) (Figure 2.1b).

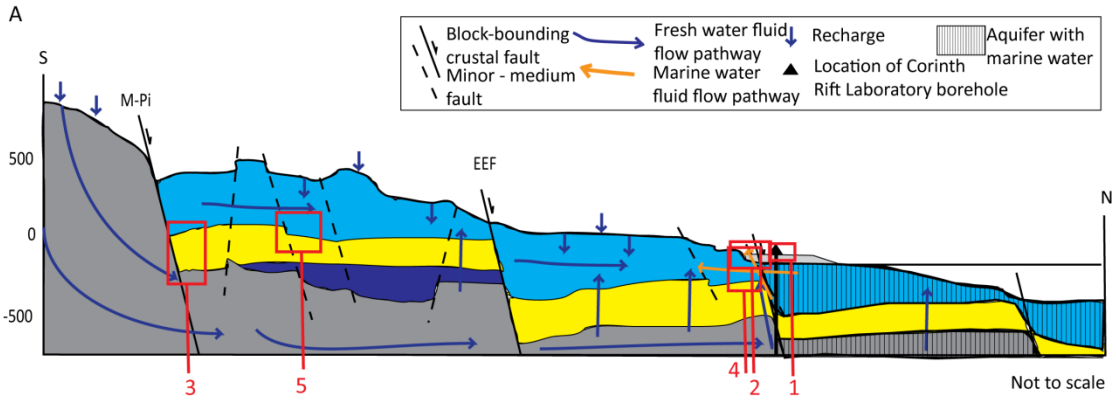

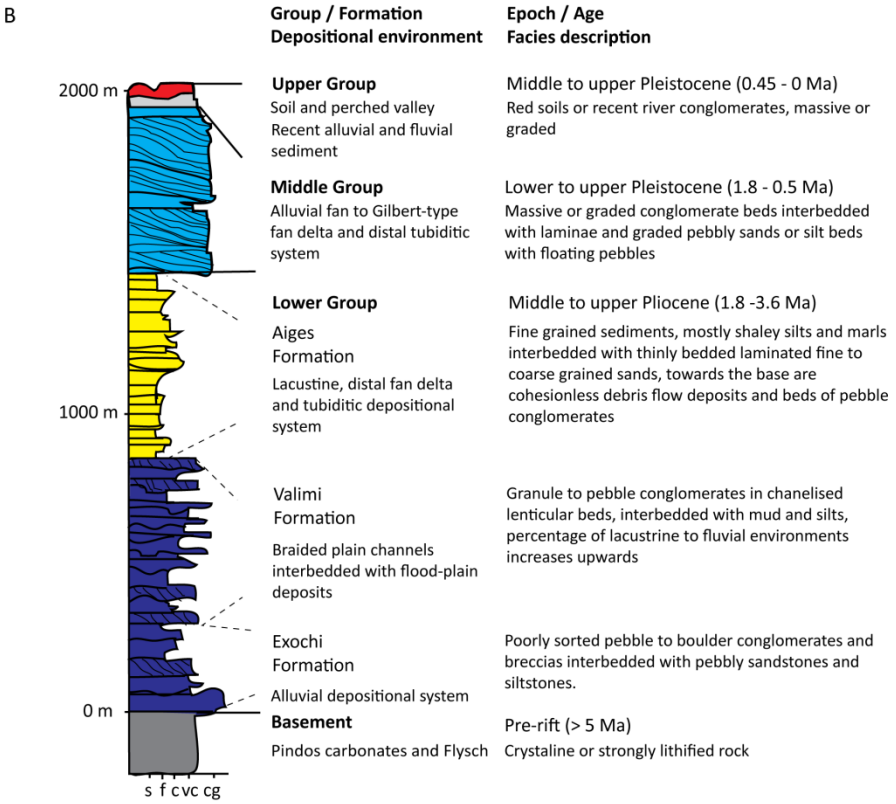

Figure 2.1 Geology and hydrogeology of the central-west southern flank of the Gulf of Corinth rift. A) Conceptual cross section interpreted from Rohais *et al.* (2007; 2008) and Ford *et al.* (2012), with major aquifers (blue and grey units) and hypothesised fluid-flow pathways, after Giurgea *et al.* (2004). Lithology corresponds to (B). Red squares indicate possible, but not actual, locations of Outcrops 1 to 5 (Figure 2.2). B) Summarised log of syn-rift sediment, after Rohais *et al.* (2007). Unit thickness, characteristics and ages vary spatially.

Between 3.2 – 3.0 Ma (Leeder *et al.*, 2012) rift strain became focused on a few block-bounding normal faults. Subsidence of the hangingwalls of these block-bounding normal faults subsequently outpaced rates of sediment deposition, resulting in a single, deep (300-600 m), lake. Deposition of Middle Group Giant Gilbert-type fan delta fluvial and alluvial topset and foreset sediment ensued at the Gulf margin. This fed sub-lacustrine fans with debris flow and hemipelagic sediment of the Aiges Formation (Ori, 1989; Doutsos *et al*., 1992; Doan and Cornet, 2007; Rohais *et al*., 2007; Leeder *et al*., 2012) (Figure 2.1b). Rift strain was initially focused along the most southerly rift faults, and migrated northwards in two main stages; first in the early Pleistocene (0.8 to 1.8 Ma), then to its current offshore and shoreline-proximal location at least 0.5 Ma (Keraudren and Sorel, 1987; Ford *et al*., 2012; Leeder *et al*., 2012). Bell *et al.*, (2009) estimate 60 - 80% of rift strain is now accommodated offshore.

Concurrent uplift of the southern rift flank, with rates of up to 1.5 mm a^{-1} (Stewart and Vita-Finzi, 1996), is believed result from shallow slab subduction of the African plate under the Peloponnesus Mountains (e.g. Leeder *et al*., 2003) coupled with co-seismic footwall uplift (Vita-Finzi, 1993). This uplift has resulted in syn-rift sediment at elevations >1000 m (e.g. Ori, 1989; Vita-Finzi, 1993; Ford *et al*., 2012). Giant Gilbert-type delta deposits thus decrease in age and elevation from the Peloponnesus Mountains towards the Corinth Gulf (Ori, 1989). A flight of coastal terraces are also cut into uplifted sediment along the southern rift flank, attributed to a combination of Pleistocene sea level change and uplift (Armijo *et al*., 1996).

Subsequent north-south fluvial incision by rivers flowing perpendicular to the structural grain of the rift, across the southern rift flank, reveal numerous fault arrays cutting syn-rift sediment. Outcrops in which these arrays are exposed provide an ideal opportunity to investigate the hydrogeological structure of faults cutting poorly lithified syn-rift sediment. Faults cutting the poorly lithified Gilbert-type delta and Aiges Formation sediment are the focus of investigation at Outcrops 2 to 5 (Figures 1.2 and 2.1). The Exochi and Valimi Formations are also exposed in certain areas but tend to have a greater degree of lithification, therefore have not been considered in this work. Outcrop 1 is located in the exhumed margin of the Lechaion Gulf, east of the Gulf of Corinth rift itself. The isostatic uplift rate of this basin (0.2 mm a^{-1}) is

much lower than the southern flank of the Gulf of Corinth rift, and has a maximum sediment elevation of 400 m. It is considered to no longer be part of the active rift (Turner *et al*., 2010). Sediment exposed in this area originates from a smaller-scale delta system with predominantly beach and alluvial facies, which overlie fine-grained Pliocene basin fill.

2.1.2 Hydrogeology of the Gulf of Corinth rift

As part of the recent Corinth Rift Laboratory (CRL) project, a 1 km deep borehole was drilled through the Aigion fault zone in the west of the southern rift flank (Figure 1.2). This, and associated projects, has considerably improved conceptual models of the hydrogeology of the southern flank of the Corinth rift. It has allowed hydrogeological characterisation of the major aquifers and confining units, fluid-flow pathways, and the impact of major faults (Figure 2.1) (e.g. Cornet *et al*., 2004; Giurgea *et al*., 2004).

The southern flank of the Corinth rift comprises three major aquifers (Figure 2.1a). Basement limestone of the Pindos nappe provides a continuous and largely confined lower aquifer across the region that has long been a regionally significant source of fresh water (Crouch, 1996; Micarelli *et al*., 2006b). High pressures and flow rates (50 m^3 h^{-1} over three days) (Giurgea *et al*., 2004) measured in this aquifer indicate a hydraulic conductivity upwards of 1.1 x 10^{-5} m s^{-1} (Cornet *et al*., 2004; Giurgea *et al*., 2004; Doan and Cornet, 2007), probably due to karstification of the carbonate rocks (e.g. Roberts and Stewart, 1994). Gilbert-type delta conglomerates provide an upper, unconfined aquifer, with a hydraulic conductivity of 1 x 10^{-2} m s^{-1} to 1 x 10^{-3} m s^{-1} (Giurgea *et al*., 2004) across most of the southern rift flank (Figures 2.1 and 2.2). Holocene coastal and inland alluvial sediments form the third, unconfined aquifer, and are the primary source of water north of the Peloponnese Mountains (Voudouris *et al*., 2005). The dominantly fine-grained Aiges Formation of the Lower Group (Figure 2.1) is a major aquitard unit between the upper conglomerate and lower carbonate aquifers (Cornet *et al*., 2004; Micarelli *et al*., 2006b), though Giurgea *et al*. (2004) suggest that leakage upwards through this unit could be forced by artesian pressures in the lower aquifer, thereby providing a hydraulic connection between these two aquifers.

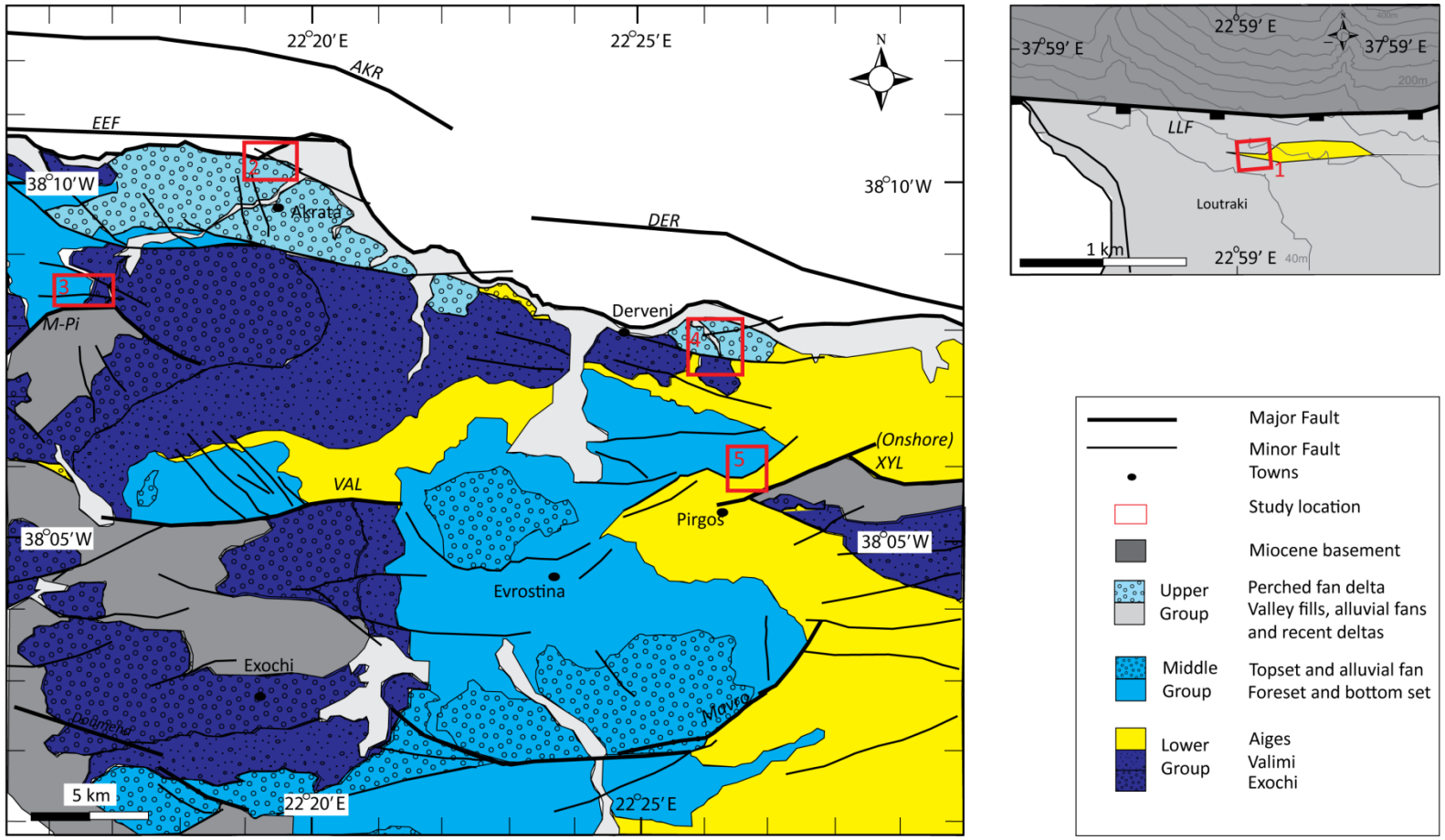

Figure 2.2 Geological setting of outcrop locations in the southern flank of the Gulf of Corinth rift basin (large map) and the Corinth Isthmus/ Gerania range (small map), after IGME (1972; 1989; 1993), Rohais *et al*. (2007) and Bell *et al*. (2009). Faults; Akrata (AKR); East Eliki Fault (EEF); Mamoussia-Pirgaki (M-Pi); Dervei (DER); Valimi (VAL); Xylokastro (XYL).

The geochemical composition of groundwater in the southern rift flank is dominantly Ca-HCO_3 (Total Dissolved Solids <0.7 g l^{-1}), neutral to slightly alkaline and has a positive Eh (redox potential), thus should be oxidising (Pizzino *et al*., 2004). Calcite cement and iron oxide precipitates often found in sediment pores reflect these geochemical characteristics and can be used to delineate fluid-flow pathways. Based on geochemical and isotope data, Pizzino *et al*. (2004) suggest a dominantly meteoric origin of the groundwater. Recharge to the limestone aquifer occurs high in the Peloponnese Mountains to the south of the Gulf of Corinth, by direct rainfall, during the November to March wet season (Pizzino *et al*., 2004; Voudouris *et al*., 2005). The Giant Gilbert-type delta gravel conglomerate aquifer is predominantly recharged by river flow (Voudouris *et al*., 2005). Groundwater of marine origin has been found in coastal conglomerates (Cornet *et al*., 2004). Pizzino *et al*. (2004) hypothesise two topographically controlled circulation pathways; a quick, shallow circulation with local recharge in conglomerate and upper carbonate aquifers, and a longer, deeper circulation (flow path 5 to 10 km) in alkaline artesian aquifers (Pizzino *et al*., 2004; Giurgea *et al*., 2004; Micarelli *et al*., 2006b).

Unusually for such a rapidly rifting zone, no evidence has been found for hydrothermal activity across the southern flank of the Gulf of Corinth rift (Pizzino *et al*., 2004; Doan and Cornet, 2007; Pik *et al*., 2009). This anomaly has been attributed to masking of the expected thermal gradient by the strong topographic flow (Cornet *et al*., 2004; Pik *et al*., 2009), or extensive re-plumbing of the hydrogeological system caused by propagation of the Northern Anatolian Fault at ~5 Ma (Pik *et al*., 2009). However, groundwater geochemistry around several fault zones indicates flow of deeper waters (Pizzino *et al*., 2004; Pik *et al*., 2009).

Warm springs do exist in the Loutraki area, though geochemical data indicate that this is part of a waning, low enthalpy, geothermal system (Dotsika *et al*., 2010). Stamatis and Voudouris (2003) identify two aquifers across this region; an unconfined aquifer corresponding to delta conglomerates and recent alluvial sediment (up to 15 m thick), and sand beds of the Pliocene succession inter-bedded with, and confined by, marl. These have a total maximum thickness of 1000 m. Topographic flow is less significant across the more subdued topography of the Corinth Isthmus, east of the Lechaion Gulf (Figure 1.2).

Evidence from the CRL reveals paradoxical hydrogeological behaviour of major basement faults. Regional aquifer connections allowing topographic flow from the Peloponnese Mountains to the coast are necessary to sustain the high water pressures experienced in the coastal aquifer (Figure 2.1a). However, the significant differences in measured pore pressures across the Aigion fault zone, and the separation of groundwater of marine origin in the hangingwall, from fresh groundwater in the footwall, indicates that these faults behave as major barriers (Cornet *et al.*, 2004). This interpretation is supported by the presence of low permeability clay smearing and cementation along and adjacent to the fault zone (Cornet *et al.*, 2004; Giurgea *et al.*, 2004; Micarelli *et al.*, 2006b; Doan and Cornet, 2007). Hydraulic connections could result from spatial variations in fault zone properties, potentially enhanced by the high pressures in the lower aquifer (Giurgea *et al.*, 2004), or by fluid-flow through relay zones at fault tips (Micarelli *et al.*, 2006b). Evidence indicative of the hydraulic behaviour of fault zones in the syn-rift sediment is limited, though geochemical evidence for mingled marine and meteoric groundwater in gravel conglomerates suggests fault zones do not prevent fluid-flow across them (Giurgea *et al.*, 2004) (Figure 2.1a).

Voudouris *et al.* (2005) report a significant decrease in groundwater levels and saline intrusion since the 1980s due to over-abstraction of groundwater; demonstrating the sensitivity of groundwater resources in this arid climate. Nitrate contamination into aquifers from agricultural sources is also an issue across the region. In particular, there are concerns over the role of faults and their potential to behave as preferential fluid-flow pathways to contaminants (Stamatis and Voudouris, 2003; Giurgea *et al.*, 2004; Voudouris *et al.*, 2005).

2.2 Geological settings of outcrops

The specific geologic evolution of the Gulf of Corinth rift provides an excellent opportunity to investigate the hydrogeological structure of fault zones in poorly lithified sediment in outcrop. Five outcrop locations were chosen for this research, each characterised by a high frequency, or array, of normal-faults. All five outcrops are proximal to crustal-scale faults (Figure 2.2), suggesting a probable tectonic origin. An initial case-study was carried out at Outcrop 1, north of Loutraki town, at the eastern margin of the Lechaion Gulf (Figure 1.2) because it offered a particularly

well exposed and accessible three-dimensional fault array in a cutting for a new, and at the time, unopened road. The remaining four outcrop locations (2 to 5) are exposed in the voluminous syn-rift sediment of the central-southern rift flank (Figures 1.2 and 2.2).

Local geological settings were established for each outcrop location to identify their geological and hydrogeological context, including factors such as crustal stress conditions, lithology and fault array characteristics. These are summarised in the following section. Fault data are presented in Chapters 3 to 5 and Appendices 1 and 3.

2.2.1 Outcrop mapping methods

Through reconnaissance exercises across the southern and eastern flanks of the Gulf of Corinth rift the five best exposed and accessible fault arrays cutting poorly lithified sediment were identified for detailed outcrop studies of fault zone hydrogeology. Exposure conditions varied across the outcrops; for example, the Voutsimos and Pirgos outcrops (3 and 5) were partially concealed by marl washed down from overlying beds. The local geological setting was established for each outcrop from a combination of field mapping and published data.

The extent of mapped outcrop areas was delineated by fault density diminishing to background levels (i.e. 1/ 100 m^2) or by the limit of the outcrop exposure. Mapped areas ranged from 0.01 to 4 km^2. Hellenic Military 1:10 000 topographic maps were used as outcrop base-maps. Crustal-scale through to medium sized (>50 m displacement) faults, and stratigraphy were correlated with 1:50 000 IGME (1972; 1989; 1993) geological maps and published literature, and in particular the stratigraphic maps of Rohais *et al*. (2007; 2008). Stratigraphy and tectonic structures were recorded, including fault and bed strike and dip, fault throw, fault zone structure and mixed zone thickness (Appendix 1). Photographs were taken of key features. Fault size was identified using fault throw rather than displacement because the exact sense of shear could rarely be elucidated from fault zones cutting poorly lithified sediment. Lithology was classified based on the Wentworth grain-size scale and mineralogy from hand samples and thin sections collected from outcrops. The

occurrence of fluid-flow indicators such as cement, precipitate and springs occurring at the outcrops were also documented.

Geological maps were constructed for each outcrop location, using European 1979 grid system co-ordinates (included with outcrop descriptions). The cross sections accompanying the geological maps were constructed using the map data for Outcrops 2 to 5, and whole-section scaled photographs for Outcrop 1. Stratigraphy is presented following classifications proposed by Rohais *et al*. (2007), described in section 2.2.1 (Figure 2.1). Photographs of key fault array sections are presented for each outcrop location.

2.2.2 Outcrop 1 – Loutraki

The 0.01 km^2 Loutraki study area is the focus of the case study in Chapter 3. The area is located immediately north of Loutraki town, to the NE of the Lechaion Gulf (Figures 1.2 and 2.2). A minor normal-fault array is exposed in a road cutting on the outskirts of Loutraki. Three near-parallel sections, two either side of the road, the third tens of meters to the south (Figure 2.3), provide a quasi-3D view of the fault system.

The minor-fault array is in the hangingwall to the crustal-scale E-W trending Lower Loutraki normal fault, approximately 150 m to the south of the main fault scarp (Figure 2.2). The Lower Loutraki fault separates the relatively flat Loutraki plain on the hangingwall and the topographic high of the Gerania Range on the footwall to the north. Based upon local topography it is likely that the minimum throw across the Lower Loutraki fault is greater than 600 m. A highly irregular and eroded Lower Loutraki fault scarp (Leeder *et al*., 2005) and limited displacement of Holocene fan breccia and colluvium (Turner *et al*., 2010), suggest a lack of Holocene activity along the Lower Loutraki fault.

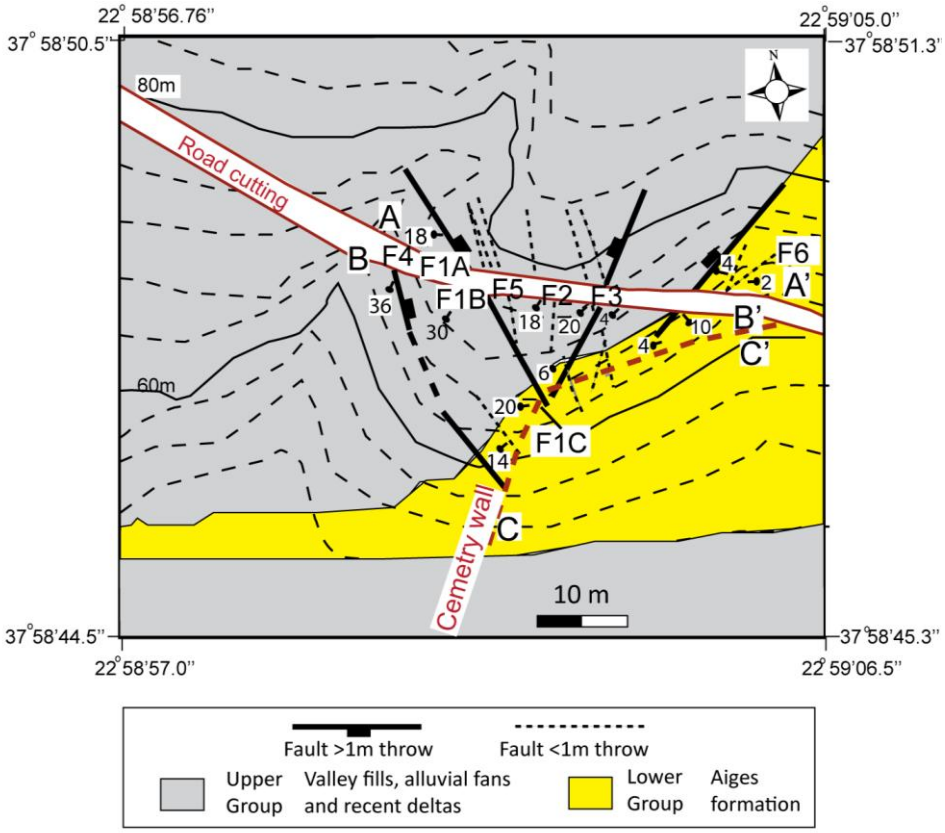

Figure 2.3 Geological map of the Loutraki outcrop (Outcrop 1) and mapped graben structure of the exposed fault array. Faults F1 to F5 are discussed in Chapters 3 and 5. AA', BB' and CC' indicate locations of cross sections in Figure 2.4.

In the Loutraki outcrop, Pliocene to early Pleistocene shallow basin sand and marl is unconformably overlain by a sequence of Pleistocene deltaic sediment typical of uplifted basin margin sediment along the coastline of the Lechaion Gulf (e.g. Collier, 1990; Dia *et al*., 1997; Turner *et al*., 2010). Marl is either cohesive fine-grained (silt-clay) carbonate or less cohesive silty-carbonate inter-bedded with sand. This sequence is cut by small-scale (throw <1 m) conjugate faults, not discussed in this study. The overlying Pleistocene sediment is part of a small-scale deltaic system, and comprises alternating beds of coarse sand, bladed beach pebbles, alluvial gravel and cobbles and very poorly sorted talus. Bed thickness ranges from 0.1 m to 5 m, with considerable lateral variability. Hand specimens from this section show sediment to be approximately 60% limestone, 20% chert, 15% quartz and 5% serpentinite fragments, probably sourced from the Gerania range.

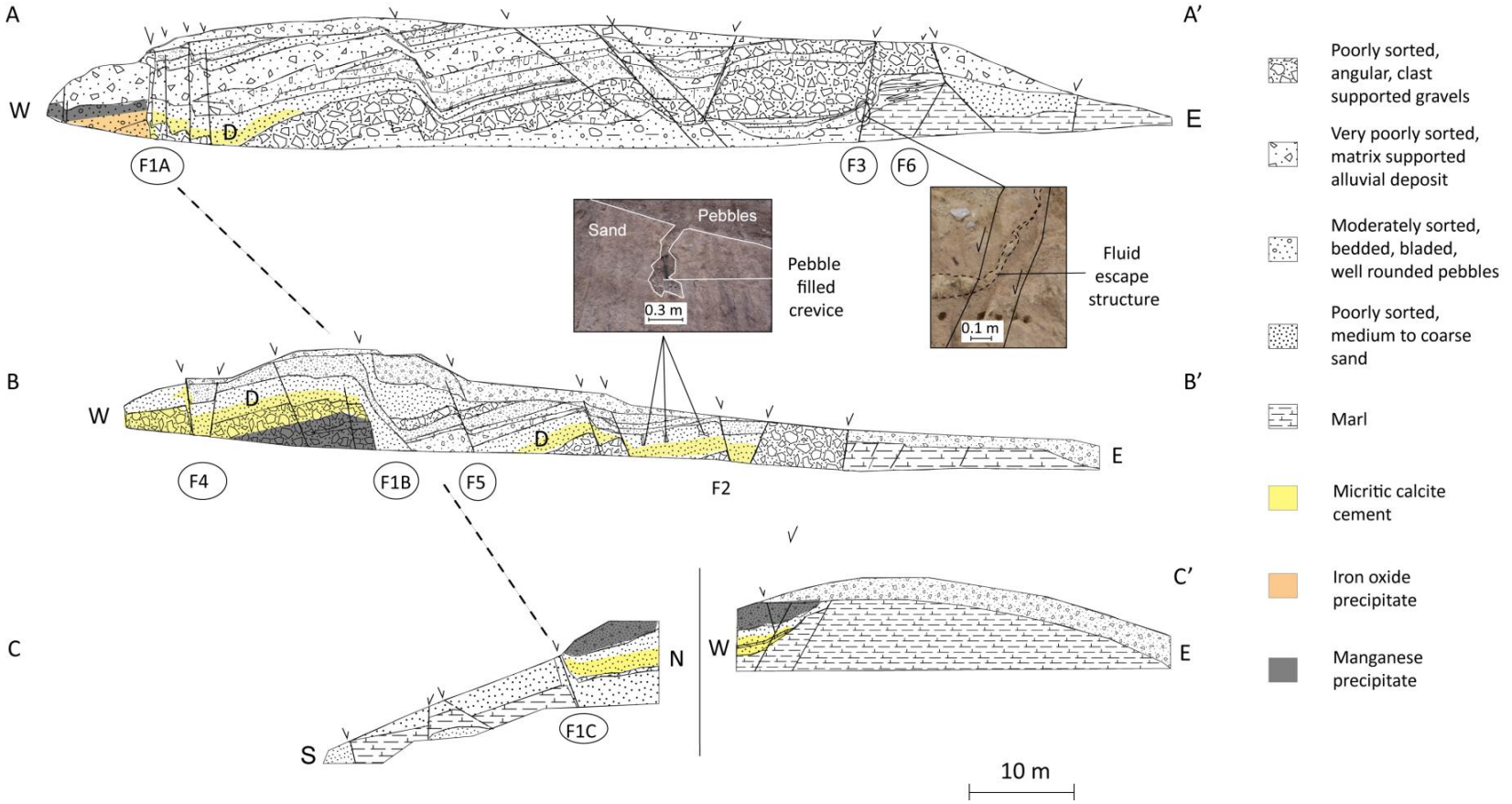

Figure 2.4 Cross sections of the Loutraki fault array, sections AA' and BB' (reflected) are along the Loutraki road cutting, and CC' is exposed in the cemetery wall (Figure 2.3). Faults 1 and 3-5 (F1 and 3 to 5) are described in Chapter 3. The lower half of coarse sand Bed D is cemented with micritic calcite and can be traced through most of sections AA' and BB'. Colours correspond to discernible cement and precipitate in the section. Photographs show possible fluid escape structures in the fault zone of Fault 3, and footwall of Fault 2.

The normal-fault array forms an asymmetric graben bounded by Faults 1 and 3, which probably formed in response to activity on the Lower Loutraki fault (Figure 2.2). Faults 1 and 3 have throws ~7 m, and the remaining faults record between 1 and 4 m throw. Fault 1 is exposed in all three sections, AA', BB' and CC'. On the east side of the graben faults strike approximately NE and dip to the NW, and faults in the west side of the graben strike approximately NW, and dip approximately NE; in planform these faults should converge towards the south of the outcrop (Figure 2.3). Slickenlines on localised shear surfaces plunge obliquely on normally separated fault surfaces, indicating a SE motion on the NE dipping fault, and a SW motion on the NW dipping fault.

The Pleistocene marine and beach sediments are at an elevation of 80 m above present day sea level such that with the estimated uplift rate of 0.22 mm yr^{-1} (Turner *et al*., 2010) the maximum burial of these sediments is likely to be equivalent to the maximum thickness of the succession, 50 m, and are therefore largely unlithified. However, some beds are slightly lithified due to localised cementation by iron oxide or micritic calcite (Figure 2.4). An irregularly shaped smear of fine sand in the mixed zone of Fault 3, and crevices filled with pebbles from the overlying bed in the hangingwall sand of Fault 2 (Figure 2.4), can be interpreted as fluid escape structures indicative of liquefaction, probably as a result of seismicity. This suggests that sediments were water-saturated at the time of deformation, which is further corroborated by the presence of extensive bed-parallel calcite cementation (Figure 2.4), a feature of sediment in the intertidal zone (Rey *et al*., 2004). Fault zone characteristics are detailed in Chapter 3.

2.2.3 Outcrop 2 – Akrata

The 0.7 km^2 Akrata outcrop is exposed along the edge of a perched fan delta (Rohais *et al*., 2007) forming a cliff 200 m above sea-level and the present day Akrata delta (Figure 2.2). The fault array cuts gravel and coarse sand conglomerate exposed along the road that traverses the cliff front. The thickness of the perched delta sediment is not known, but it probably overlies Middle Group Gilbert-type delta deposits (Figure 2.2). The main focus of this outcrop was a small quarry on the SW margin of the perched delta that reveals a series of minor (<5 m throw) and a larger (>7 m throw) faults (Figures 2.5 and 2.6).

The Akrata outcrop is in the footwall of an along-strike splay of the East Eliki Fault, which splits from the primary fault as it trends offshore, just west of the Akrata delta. The splay fault trends SE along the perched delta front, east of the Akrata outcrop (e.g. Bell *et al*., 2009). The steep cliff face of the perched delta, and apparently large faults striking roughly parallel to its trend, could be the vertical expressions of this splay fault (Figures 2.2 and 2.5). The structure of these faults suggests a possible relay zone stepping back into the footwall to the west. Estimated uplift along the East Eliki Fault footwall is 1.25 mm a^{-1} over the last 200-300 ka (De Martini *et al*., 2004). Coastal terraces cut into the perched delta at 110-120 m and 100 m, immediately west of the Akrata outcrop (Figure 2.5a) therefore probably correspond to Marine Isotope Stages 5e (125 ka) and 5a/c (70-90 ka).

Medium-grained red sand, classified as a red mantle (IGME, 1993), and could be a Holocene soil, is apparently down-faulted from the top of the delta across a number of faults exposed along the road to the east. Therefore it is possible that these faults were active relatively recently. Similar to the Loutraki outcrop, the sediment burial depth is likely to be the maximum depth of the succession, probably no more than 50 m (Figure 2.5). Sediment exposed in the outcrop is not cemented, but iron oxide precipitate coats clasts in coarse-grained beds. This precipitate is strongly focused close to fault zones, suggesting that the sediment has been saturated at some point after fault formation (Figure 2.6).

Perched delta sediment exposed in the Akrata outcrop comprises poorly sorted, pebble to gravel clast-supported conglomerate foresets that dip to the north (Figure 2.6). Delta topsets are exposed towards the top of the road section, in the quarry (Figure 2.5). These comprise clast-supported, poorly sorted, pebble to gravel fluvial conglomerates with a coarse sand matrix, and occasional well-sorted clast supported gravel channel deposits. Above and below these beds is a unit (exposed in the hangingwall and lower half of the exposed footwall of Fault 3) of coarse-grained sand to fine-grained gravel conglomerate, interspersed with laterally discontinuous, relatively thin (<0.25 m), silt beds (Figure 2.6). Clasts are dominantly sub-spherical and sub-rounded, and comprise approximately 70% limestone, and 15% chert and quartz, probably sourced from the Peloponnese Mountains to the south.

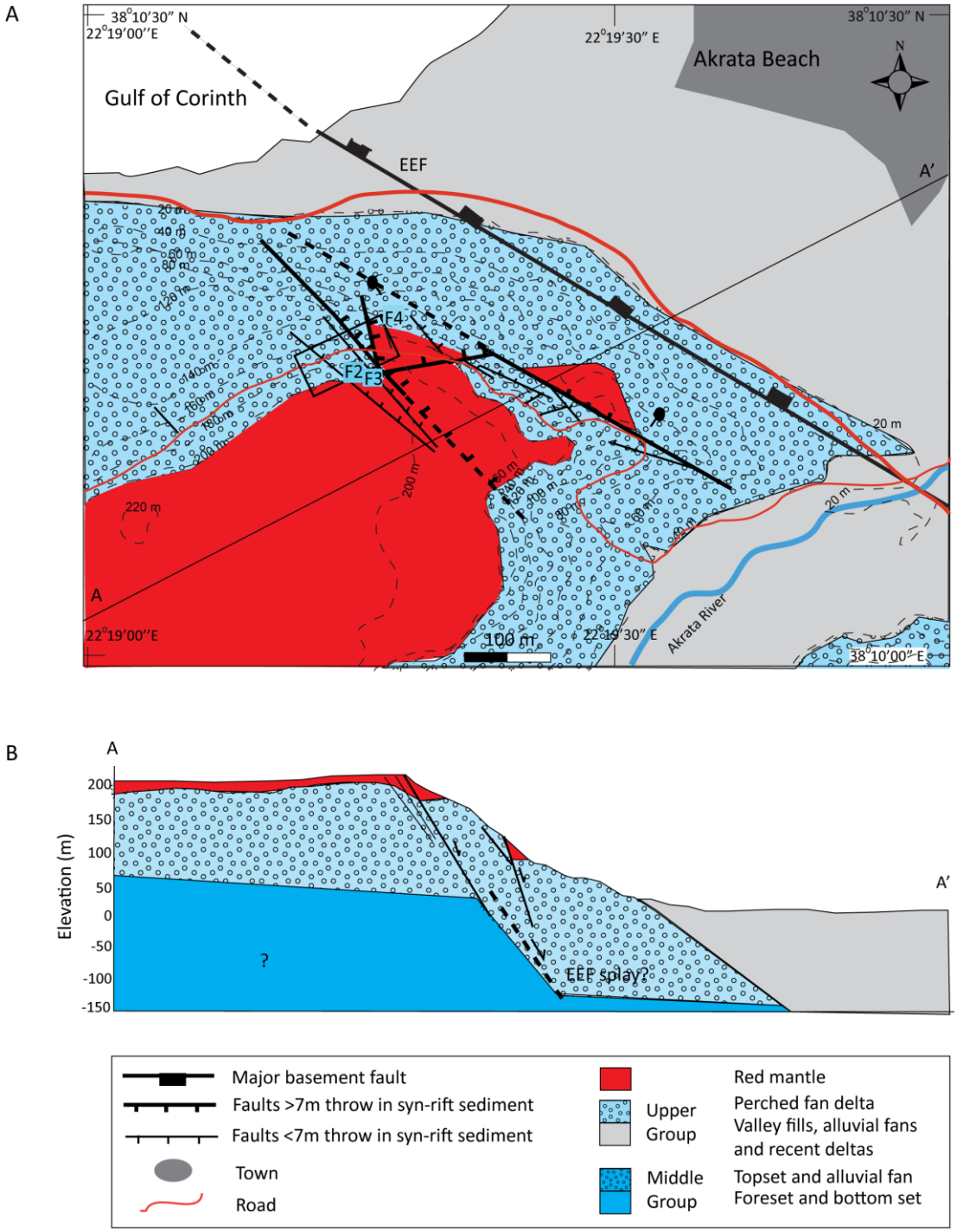

Figure 2.5 Geology of the Akrata outcrop (Outcrop 2) in perched delta sediment. A) Geological map with major splay fault from the East Eliki Fault. Section AA' in (B). Fault array exposed in the quarry shown by black box. Faults 2 to 4 (F2 to 4) are discussed in Chapters 4 and 5. B) Interpreted cross section AA'.

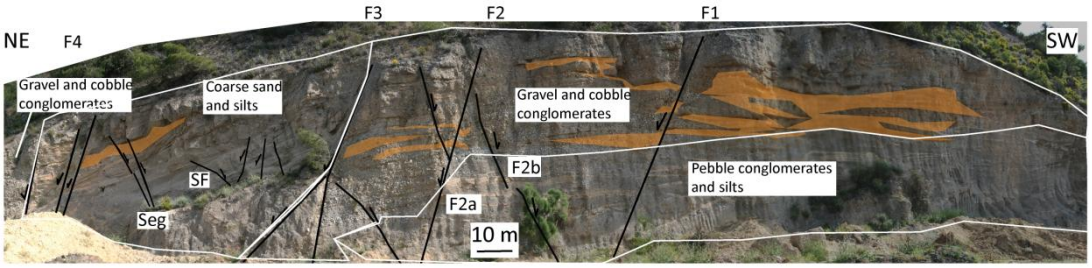

Figure 2.6 Photograph of the Akrata outcrop (Outcrop 2) quarry exposing the fault array cutting delta topset sediment. Fault throws increase SW to NE from 0.5 m (F1) to >7 m (F4). F2 to 4 discussed in Chapters 4 and 5. Orange colouring highlights the distribution of iron oxide precipitate across the exposure (Chapter 6). Seg is Segmented Fault and SF is small fault (Appendix 1).

The four largest faults exposed in the Akrata outcrop quarry (F1 to F4) have apparent strikes NW-SE (Figure 2.5a), and dip to the NE. Fault throw increases from faults in the SW to NE, from 0.5 m (F1) to >7 m (F4) (Figure 2.6). F2 and F3 also have subsidiary antithetic faults in their damage zones and a number of small faults (<0.2 m throw) cut the coarse-grained sand in the section between F3 and F4, in which sand beds can be seen dipping steeply to the north (Figure 2.6).

2.2.4 Outcrop 3 – Voutsimos

The 0.9 km^2 Voutsimos outcrop is exposed along two roads that traverse the steeply incised valleys between the villages of Voutsimos and Kalamias, 10 km south of the Akrata outcrop. In this outcrop, sediment is exposed from throughout the syn-rift succession (Figure 2.7). The cliff face to the south of the road provides vertically extensive exposures of fault zones with throws up to 23 m. Faults investigated cut either the Aiges Formation or foreset to topset deposits of the Middle Group Gilbert-type deltas.

Syn-rift sediment of the Voutsimos outcrop lies in the immediate hangingwall of the locally E-W trending crustal-scale Mamoussia-Pirgaki fault (Figures 2.2, 2.7 and 2.8). This fault, which has accommodated up to 1000 m vertical displacement (Malatre *et al*., 2004), is exposed at the southern edge of Voutsimos village. It tips out ~1 km to the east of this exposure, close to a N-S orientated gorge incised 30 m into basement rocks (Figure 2.2). Activity along this fault pre-dates the marine terraces cut into uplifted delta sediment to the south (Malatre *et al.*, 2004).

Relatively well lithified fluvial and alluvial conglomerate of the Exochi and Valimi Formations directly overly basement rocks west of the gorge (level with the viewpoint of the photograph in Figure 2.8). Overlying these is a ~100 m thick succession of massive, thick-bedded (>5 m), medium-graded sand of the Aiges Formation. Localised lignite beds exposed in this sediment indicate deposition in an endoheric depression typical of early rift distributed deformation (Rohais *et al*., 2007). The Aiges Formation is overlain by another 100 m thick succession of foreset and bottomset Middle Group Gilbert-type delta deposits of roughly planar marl and fine-grade sand beds (0.1 m to 1 m thick) inter-bedded with coarse sand to cobble debris flow deposits that are laterally variable in thickness and extent. Middle Group Giant Gilbert-type delta topset and alluvial fan deposits comprising loosely bedded, coarse gravel conglomerate, caps the bottomset deposits 2 m from the top of the northern-most edge of the cliff, and are subsequently down-faulted to the south (Figures 2.7 and 2.8). Sediment is comprised roughly 70 % limestone, 18 % quartz, 10 % chert and 2 % serpentinite fragments.

The two largest faults, Big Faults 1 and 2 (17 and 23 m throw, respectively), cut syn-rift sediment, and trend approximately E-W; parallel but antithetic to the Mamoussia-Pirgaki fault, forming a local half-graben (Figure 2.7b). Across these fault zones fine-grained Gilbert-type delta foreset and bottomset sediment is juxtaposed against coarse-grained topset and alluvial conglomerate (Figures 2.7 and 2.8). Two springs that produce large quantities of water, and feed abundant vegetation, originate at these fault zones. A number of other faults are exposed in the footwalls and hangingwalls of Big Faults 1 and 2. Faults BD 2 and 3 (~5 m throw) cut sand and silt beds of the Aiges Formation, lower in the succession (Figure 2.7).

Sediment exposed in the Voutsimos outcrop is older than sediment exposed closer to the coast (Ori, 1989), and it is possible that the succession was previously thicker. Nevertheless, lithification of sediment remains minimal, particularly higher in the succession, with the exception of localised cementation by micritic calcite cement around fault zones.

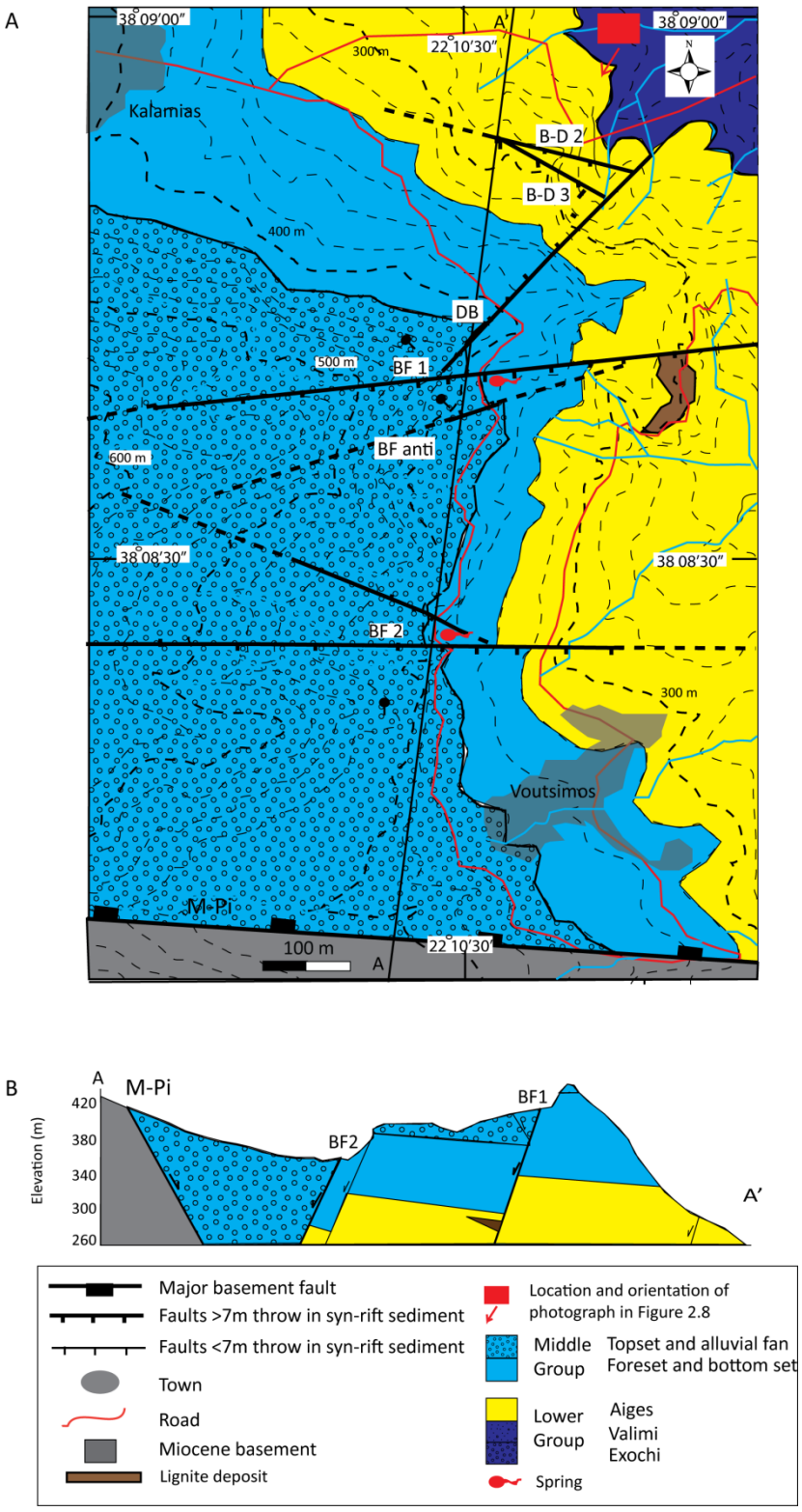

Figure 2.7 Geology of the Voutsimos outcrop (Outcrop 3) in hangingwall of the Mamoussia-Pirgaki fault. A) Geological map with Big Fault 1 and 2 (BF1 and 2) juxtaposing fine and coarse-grained sediment. DB (Disaggregation Band Fault) and BF Anti (BF1 Antithetic) are discussed in Chapters 4 to 6. AA' shows line of cross section in (B). B) Interpreted cross section AA'.

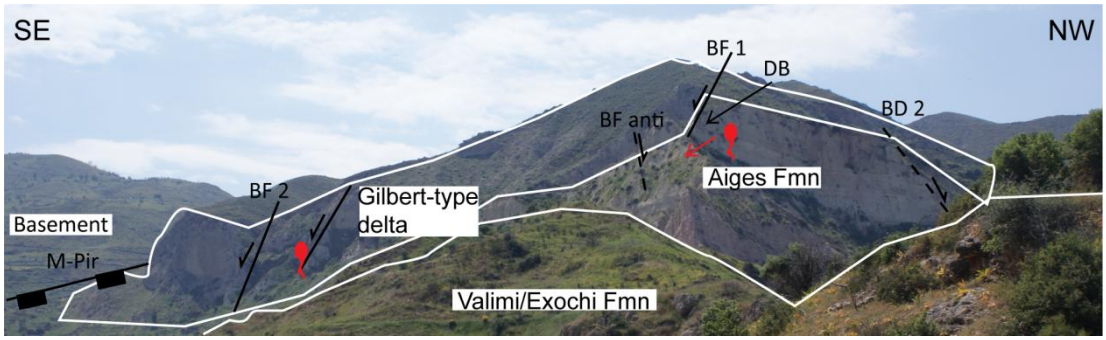

Figure 2.8 Overview photograph of the Voutsimos outcrop (Outcrop 3). Big Faults 1 and 2 (BF 1 and 2) and location of springs (red dots with tail). DB (Disaggregation Band Fault), BF Anti (BF1 Antithetic) and DB are also shown. Photograph shows approximately 1 km across the front cliff face.

2.2.5 Outcrop 4 – Mentourgianika

The 4 km^2 Mentourgianika outcrop is exposed along three roads immediately south of Mentourgianika village, 10 km east of the Akrata outcrop (Figure 2.2). Perched delta sediment is exposed along roads traversing the east and west sides of the Mentourgianika valley and one orientated N-S along the valley floor (Figure 2.9). Fine-grained sediment of the Aiges formation (Rohais *et al*., 2007) is exposed in the south of the valley. A high density fault array extends through most of the outcrop area, with exposed faults with <0.2 m to 80 m throw.

The Mentourgianika outcrop lies between the crustal-scale onshore Xylokastro and offshore Derveni faults (Figure 2.2). Six of the faults cutting syn-rift sediments have throws from 20 to 80 m (Faults A to F in Figure 2.9). Faults B, C and E correspond to the West-big Fault, Gravel-marl Fault and Terrace Fault respectively (Appendix 1). This area might be a transfer zone between the Xylokastro and Derveni faults, or related to the oblique transfer segment between the Valimi and Derveni fault (e.g. Rohais et al., 2007). Pleistocene marine terraces cut into the perched delta sediment have been uplifted to 80 m and 200 m on the east side of the valley, and 200 m on the west side of the valley (Figure 2.9). The 80 m terrace on the east side of the valley might result from displacement of the hangingwall of Fault E (Terrace Fault), the near-linear scarp of which is exposed at the back of this terrace (Figure 2.9).

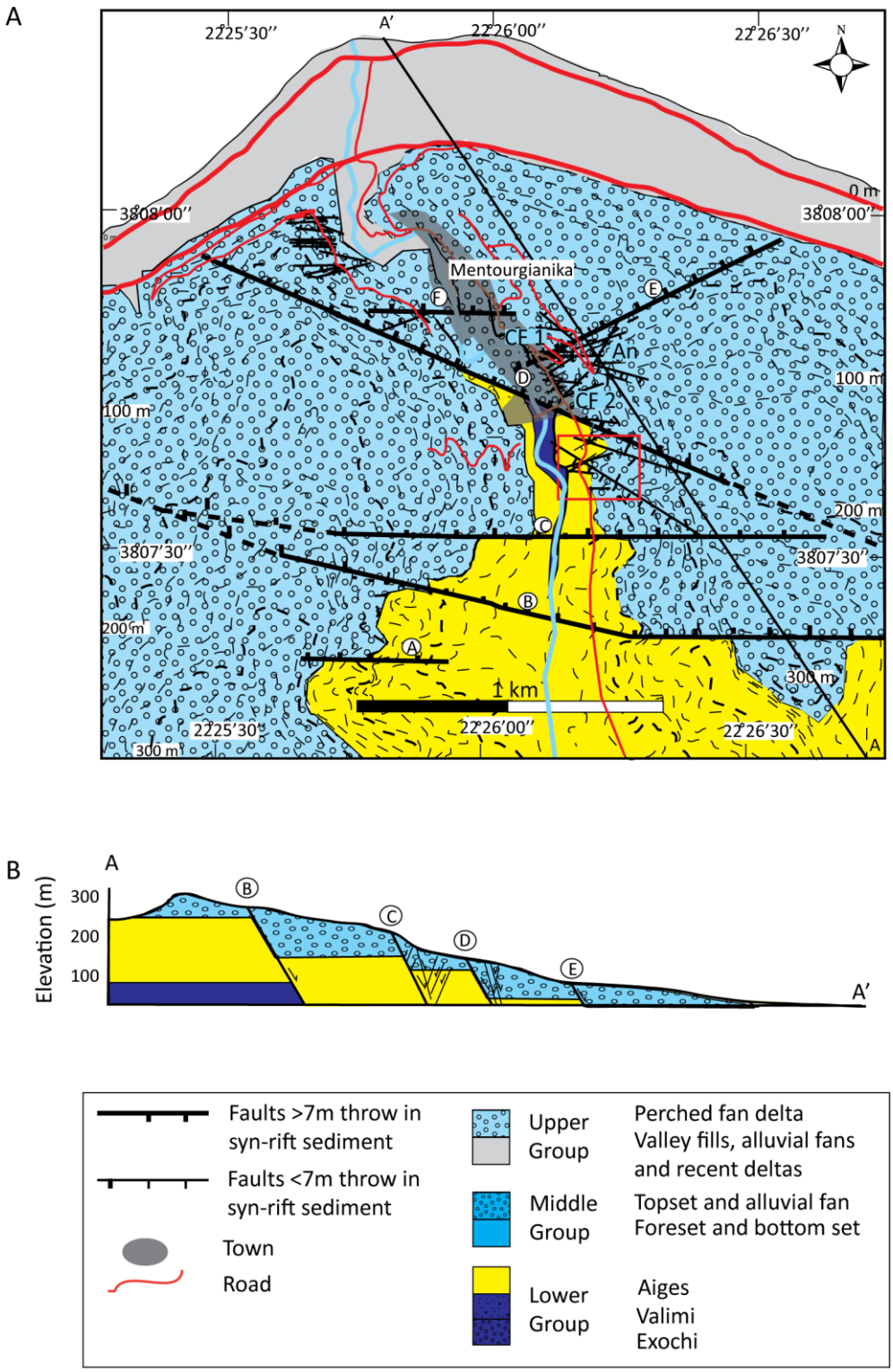

Figure 2.9 Geology of the Mentourgianika outcrop (Outcrop 4). A) Geological map of the outcrop. Lettered faults have throws > 20 m. Fault D, Gravel-marl Fault, and Fault E, Terrace Fault, are discussed in Chapters 4 and 5. AA' shows line of the cross section in (B). Red box shows location of the outcrop section in Figure 2.10. B) Cross section AA' in (A).

Perched delta sediment of the Mentourgianika outcrop comprises crudely bedded, poorly sorted, clast-supported pebble to gravel foreset conglomerate. The extremely poorly lithified nature of this sediment is demonstrated by the actively eroding cliff faces, creating hollows and caves (Figure 2.10). Perched delta sediment comprises roughly 50% limestone, 40% Quartz and 10% chert fragments. These perched delta conglomerates overlie, and are juxtaposed against, the thickly bedded marl, silt and sand of the Aiges Formation, across fault zones A to D (Figure 2.9).

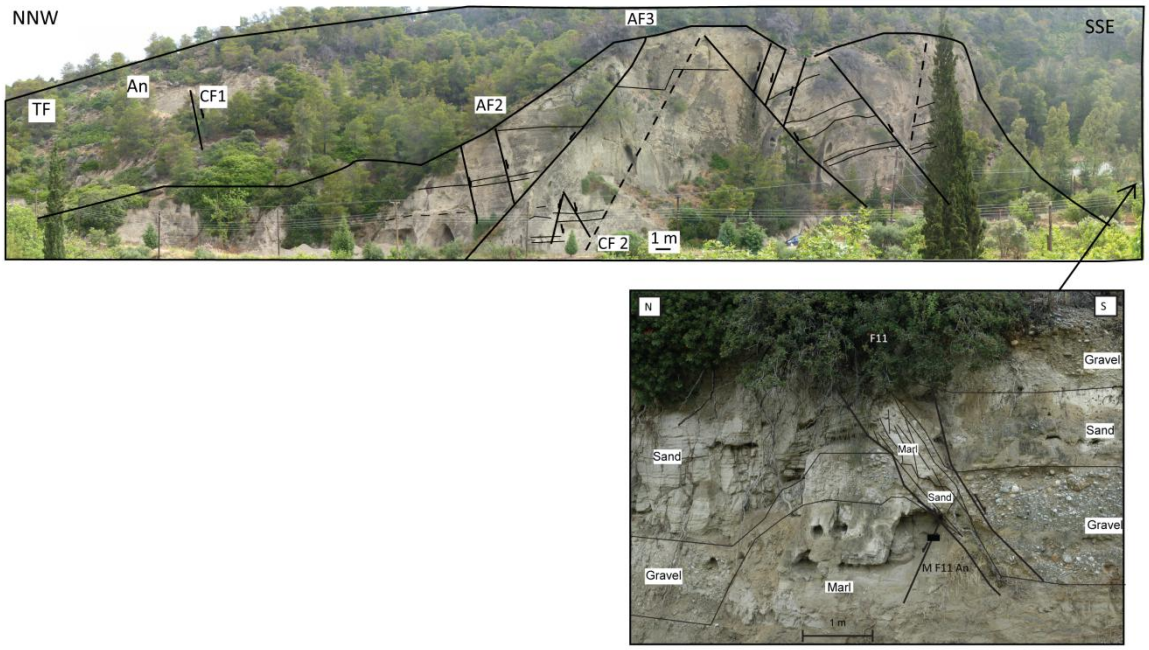

Figure 2.10 Photograph showing faults cutting perched delta sediment at the Mentourgianika outcrop. TF indicates (location of) Terrace Fault (Fault E in Figure 2.9). An, CF 1 and CF 2 are discussed in Chapters 4 to 6. M F11 An is discussed in Chapter 5.

The majority of faults exposed in the Mentourgianika outcrop have 1 to 10 m throw, and cut perched delta conglomerate (Figure 2.10). Exposed faults are particularly clustered in the hangingwall of Fault D, on the west side of the valley, and between Faults C and D on the east side of the valley (Figure 2.9). Burial depth of the perched delta sediment is probably minimal, and equivalent to the maximum depth of succession (200 m). Cementation with micritic calcite cement causes fault zones to protrude from the outcrop face since the remainder of the outcrop is largely free of cement (Figure 2.10).

2.2.6 Outcrop 5 – Pirgos

Exposed in the 1.5 km^2 Pirgos outcrop are two sets of faults, separated by a shallow E-W orientated valley. Both sets of faults are exposed along the road between Derveni and Pirgos, 5 km south of the Mentourgianika outcrop. North of the valley faults with <2 m throw cut sediment of the Aiges Formation, to the south, larger faults cut foreset gravel conglomerate of the Middle Group (Figures 2.11 and 2.12).

The Pirgos outcrop is in the hangingwall to the crustal-scale onshore Xylokastro fault, the western tip of which is exposed across the valley to the SE. Several intermediate-sized faults have been mapped in syn-rift sediment across the region (e.g. Ori, 1989; Rohais *et al*., 2007; IGME, 1989;1993), though the exact locations of these are ambiguous. However, a steep scarp, 250 m in height, trends NE-SW between the two exposures and to the SE, is probably a NW dipping fault (Figure 2.11a).

Faults exposed to the north of the shallow valley, at 360 m elevation, cut planar beds of marl and silt (0.1 to 1 m thick) of the Aiges Formation, that are inter-bedded with sand and gravel-grade debris flow deposits of laterally variable thickness and extent, and dip NE (e.g. Rohais *et al*., 2007) (Figure 2.11). These faults are relatively small-scale (throw <2 m), and relatively discrete (Figure 2.12a). A number show evidence of syn-depositional formation, and therefore were probably fluid-saturated at the time of deformation.

Faults exposed to the south of the shallow valley, at 300 to 540 m elevation, cut apparently massive, poorly sorted, coarse sand and gravel foresets of the Middle Group Giant Gilbert-type delta (e.g. Rohais *et al*., 2007). This unit is juxtaposed against bedded, moderately-sorted, coarse sand and gravel topsets of the Middle Group across the fault zone of Fault G1 (>40 m throw) (Figure 2.12b). No further faults are exposed in the topset gravels west of Fault G1. The prevailing exposure-parallel strike orientations of faults in the gravels prevented analysis of their fault zone structure, with the exception of Fault G1. Nevertheless, fault throw appeared to be >7 m.

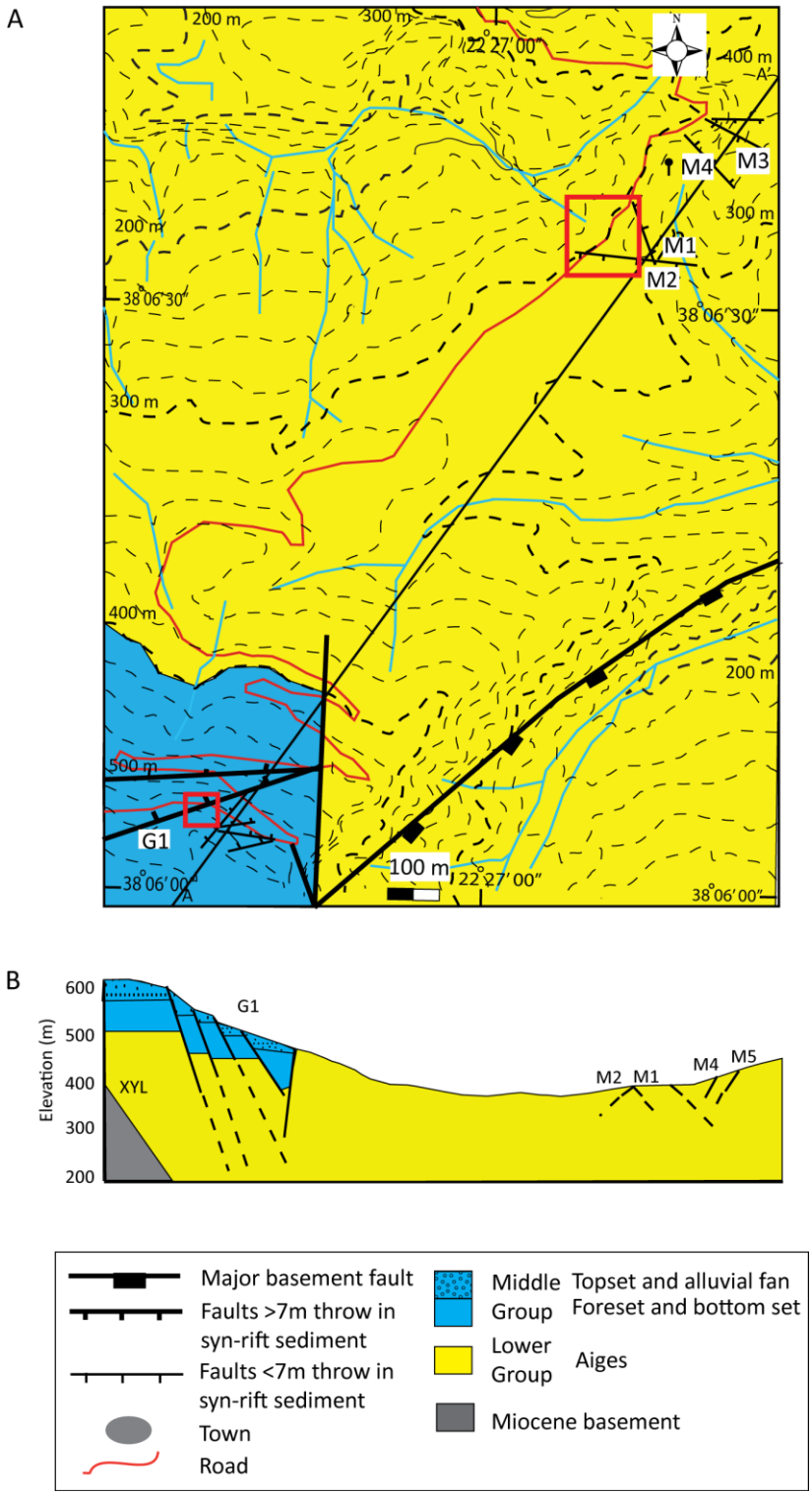

Figure 2.11 Geology of the Pirgos outcrop (Outcrop 5), with both sets of exposed faults. A) Geological map of the outcrop. G1 and M4 are discussed in Chapters 4 and 5. AA' shows line of cross section in (B). Red boxes show locations of photographs in Figure 2.12. B) Interpreted cross section AA'.

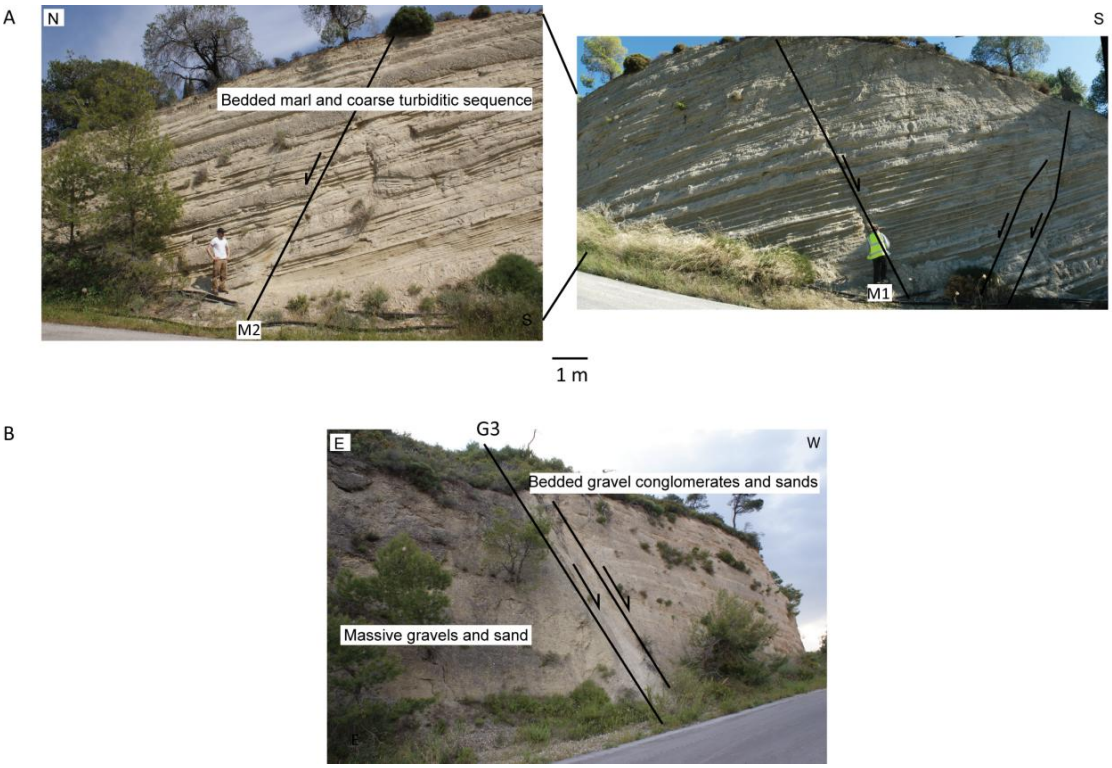

Figure 2.12 Photographs of faults exposed in the north (A) and south (B) of the Pirgos outcrop (Figure 2.11).

Apparent fault orientations are similar for faults exposed in both outcrops, between E-W and NW-SE, dipping north or south. Sediment of the Aiges Formation appears somewhat better consolidated than the very poorly lithified sediment of the Gilbert-type delta deposits to the south. However, the syn-depositional growth of these sediments indicates that they were shallowly buried at the time of formation. Cementation is only found in fault zones – in the form of micritic calcite cement in fault zones of the conglomerates, and precipitates of red iron oxides in small disaggregation band zones adjacent to faults in the fine grained sediment.

2.3 Summary

The specific tectonic evolution history of the Corinth rift basin provides an excellent opportunity to study fault zone hydrogeological structure in poorly lithified sediment, due to the high frequency of exposed faults cutting uplifted sediment. In addition, the value of groundwater in aquifers in poorly lithified sediment makes the question of fault hydraulic behaviour a particularly pertinent question for this region. The five outcrops at which investigations of fault zone hydrogeological structure have been conducted provide access to faults cutting a range of lithologies and with a wide

range of fault throws, thus enabling collection of a substantial amount of fault zone data.

3. Fault zone structure and evolution – Loutraki case study

3.1 Introduction

The primary focus of the case study at the Loutraki outcrop is the influence of lithology and stratigraphy on fault zone structure and evolution. The outcrop provides a good opportunity to assess these factors because the high sediment heterogeneity occurs in a small area (Figure 2.3), providing a natural control on the influencing factors of burial depth and deviatoric stress. Details of the fault array, sediment cut by it, and tectonic evolution of the outcrop have been described in section 2.2.2.

Fault zone macro and micro-structure described in this chapter have been used to elucidate a characteristic fault zone structure and evolution from this well-exposed minor (<10 m) normal fault array that might be applied across the Gulf of Corinth rift. Investigations into fault zone structure were carried out for four faults considered representative of the faults exposed in the Loutraki field area; Fault 1A, B and C, and Faults 3, 4, and 5 (Figures 2.3 and 2.4).

Fault zone microstructures, including; fragmented grains, grain shape, grain fabric, and grain-scale spatial distribution of different source beds, were identified from hand samples and thin sections of sediment from four of the fault zones. Grain-size was sampled across three fault zones and adjacent undeformed footwall and hangingwall beds. Fault zone deformation mechanisms are inferred from the microstructures identified in hand samples and thin sections following previous studies (Bense *et al.,* 2003; Rawling and Goodwin, 2003; Rawling and Goodwin, 2006; Balsamo *et al.,* 2008), as well as differences in grain-size distributions between fault zone and protosediment samples (e.g. Balsamo and Storti, 2010; 2011). Grain orientations were compared for fault zone and protosediment because grain rotation can be indicative of particulate flow in fault zones (Mozley and Goodwin, 1995; Goodwin and Tikoff, 2002).

Two models of fault zone evolution emerged based on fault zone macro and micro-structure and inferred deformation mechanisms, and aided by trends of fault throw and thickness at the outcrop; 1, for faults cutting only poorly lithified sediment, and 2, for faults cutting sediment of contrasting competency.

3.2 Fault zone structure data collection

3.2.1 Fault zone structure characterisation

The fault zone architecture; fault core, mixed zone and damage zone (Figure 1.3b), was ascertained for each mapped fault. Mixed zones are identified as the regions of mixed nature within fault zones that are structurally analagous to those reported by Rawling and Goodwin (2006). Because these zones accommodate most of the fault displacement they could also be termed fault cores. However, the absence of architectural elements commonly found in fault cores, such as clay smears and deformation band clusters, would be misleading for the purpose of fault zone hydrogeology. Due to the ambiguities in classifying fault zone architecture, a greater emphasis is placed on identifying fault zone structure and structural elements.

Mixed zones were easily identifiable across the exposures as having accommodated most fault strain. Structural elements are identified following definitions in Table 1.1. The thickness of the mixed zone was taken to be the fault zone thickness. Minimum and maximum mixed zone thickness was measured from a combination of direct field measurements and from scaled photographs. The average mixed zone thickness for each studied fault was determined from the mean of ten equally spaced locations along the dip of the fault. A damage zone was identified where any damage zone structural elements (Figure 1.3b) could be attributed to a particular fault (e.g. Childs *et al.*, 2009). Damage zone structural elements did not necessarily cut all beds. Unless damage zones are identified it is assumed that the footwall and hangingwall protosediment are undeformed.

3.2.2 Measurement of clast orientation

Two-dimensional clast orientation was first visually identified, as illustrated by the manually defined clast outlines of elongate clasts in Figure 3.2a. Subsequently three-dimensional pebble plunge, plunge orientation, and pebble dimensions, were measured in the field at 0.1 m intervals along horizontal transects across the footwall and mixed zone of the same fault. Before pebble orientation analysis, results were filtered to remove spherical clasts, identified if both the intermediate axis length: long-axis length, and short axis length: intermediate axis length >0.68 (cf. Perry and

Taylor, 2007). The orientation data were plotted on equal area stereonets using the GEOrient mapping software (Holcombe, 2010). Long-axis trend direction was also plotted against distance across the fault zone, to examine the spatial pattern of clast orientation.

3.2.3 Hand sample collection and thin section preparation

Impregnation of sediment with a low viscosity resin was required before collection of poorly indurated mixed zone hand samples. Blue dye was thoroughly mixed with approximately 25 ml of low viscosity epoxy resin and resin hardener in the field. The mix was poured into a divot excavated into the fault trace, and allowed to permeate. The hardened block of resin-impregnated sediment was removed from the outcrop after 24 hours. Later, samples were fully impregnated in the laboratory using the same type of resin, and sliced, usually perpendicular to the fault strike. Thin sections were prepared from regions of specific interest, such as proximal to mixed zone/ protosediment boundaries, or randomly selected from mixed zone and protosediment samples, and analysed using a petrographic microscope.

A point count of two-dimensional grain shape was conducted for thin sections of the mixed zone and footwall protosediment of Fault 5. A grid with equally spaced horizontal and vertical transects was placed over the thin section images, and mineralogy, shape, roundness and grain edge characteristics were recorded at the intersections. More than thirty grains were examined in both the mixed zone and protosediment.

3.2.4 Production of grain-size distributions

The grain-size of samples from mixed zones and hangingwall and footwall sediment was analysed. 50 to 250 g of sediment were collected from the field. Clasts greater than 20 mm in diameter were measured in the field using vernier callipers. The remainder of the sample was dry sieved in the laboratory to 1.4 mm, and fractions weighed to an accuracy of 0.1 g. Fractions <1.4 mm were suspended in 50 ml of water and analysed by a Malvern 2000 Laser Particle Scanner. A small amount of Calgon was added to the solution to break up cohesive grains. The mean of three analyses was used in the final results. Field, sieve and Malvern 2000 data were combined to produce a complete grain-size distribution for each sample.

3.3 Analysis of fault zone structure

3.3.1 Fault 1A

Road section AA' (Figures 2.3 and 2.4) exposes Fault 1 (throw ~7 m) cutting a heterogeneous sequence of coarse sediment (Figure 3.1a). Sediments are very poorly lithified with the exception of sand Bed C in the footwall, which is cemented by iron-oxide, and sand Bed D in the hangingwall, which is partially cemented with micritic calcite. Beds cut by the fault are entrained and smeared within a mixed zone. These beds are rotated at the mixed zone boundary and dip 50^{o} to 60^{o} in the mixed zone, becoming increasingly attenuated and less identifiable with distance from the source bed. Bed A, for example, is attached to the source bed in the footwall and hangingwall but appears to be mixed with surrounding beds through most of the mixed zone (Figure 3.1a). Bed C is bound by a localised shear zone at the mixed zone boundary. The mixed zone/ protosediment contact dip is ~60E along the exposed fault dip. In the hangingwall three synthetic faults, each with up to 1 m throw, cut the beds. Throw on these faults decreases upwards, and they tip out towards the top of the exposure.

Figure 3.1 Photographs and corresponding schematic diagrams of Fault 1 (Figures 2.3 and 2.4). Schematics show the mixed zone (between the thick black lines), damage zones and structural elements. Only one bed is shaded in each schematic for clarity. "Figs." 3.2, 3.3 and 3.4 indicate locations referred to in subsequent figures. Labelled beds are referred to in the text. A) Fault 1A, stippling shows a zone of mixed sediment. T1 to T3 show location of grain orientation transects (Figure 3.2). B) Fault 1B (reflected view) with continuous sediment smears in the mixed zone. C) Fault 1C, the mixed zone is dominated by an undeformed marl block. Dashed box in the photograph shows the location of Figure 3.4.

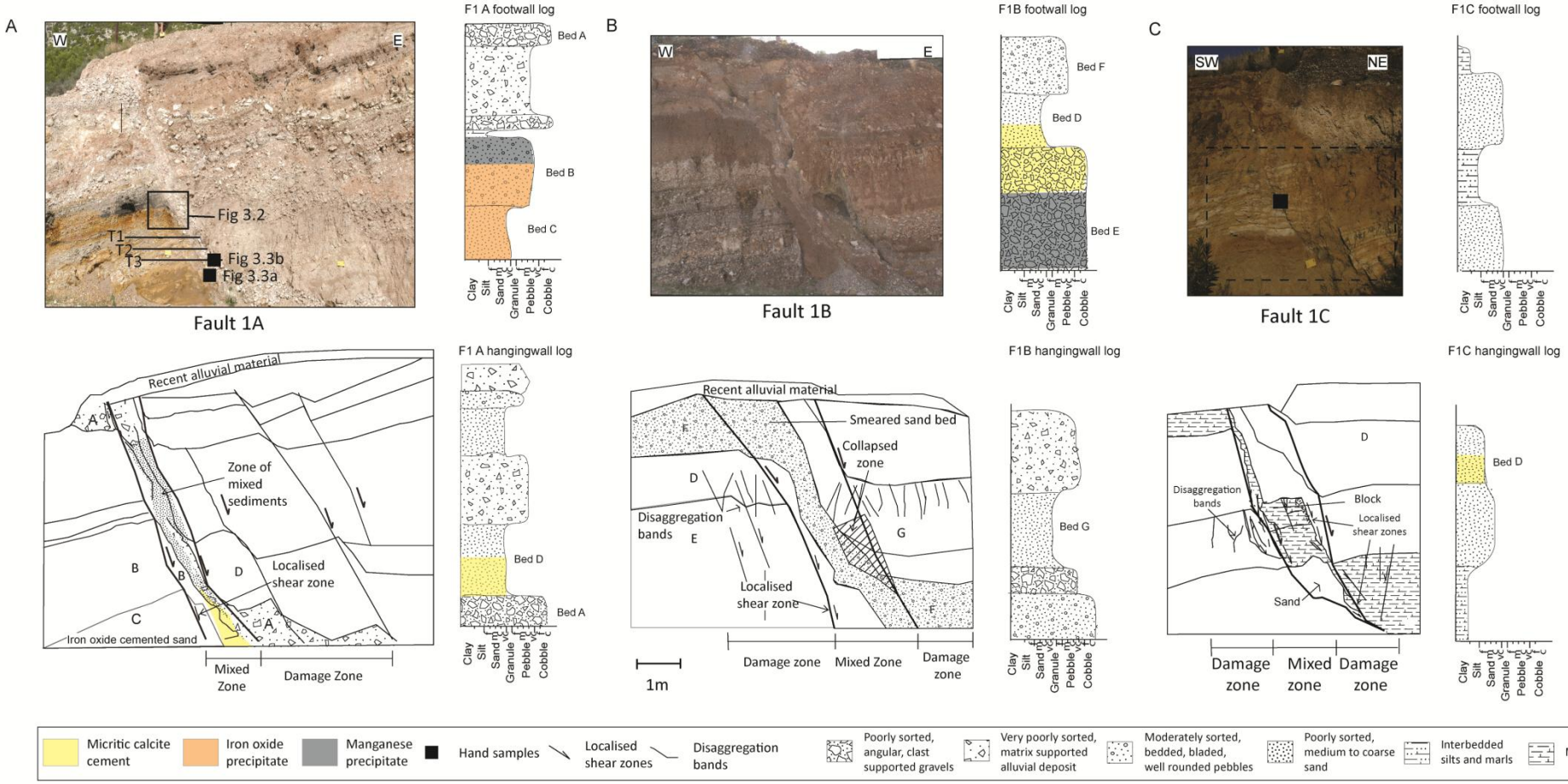
A
W
E
Fig 3.2
T1
T2
T3
Fig 3.3b
Fig 3.3a
Fault 1A
F1 A footwall log
Bed A
Bed B
Bed C
Clay
Silt
Sand
Granule
Pebble
Cobble
B
W
E
Fault 1B
F1B footwall log
Bed F
Bed D
Bed E
C
SW
NE
Fault 1C
F1C footwall log
Recent alluvial material
Zone of mixed sediments
Localised shear zone
Iron oxide cemented sand
Mixed Zone
Damage Zone
F1 A hangingwall log
Bed D
Bed A
Smeared sand bed
Collapsed zone
Disaggregation bands
Damage zone
Mixed Zone
1m
F1B hangingwall log
Bed G
Block
Sand
F1C hangingwall log
Micritic calcite cement
Iron oxide precipitate
Manganese precipitate
Hand samples
Localised shear zones
Disaggregation bands
Poorly sorted, angular, clast supported gravels
Very poorly sorted, matrix supported alluvial deposit
Moderately sorted, bedded, bladed, well rounded pebbles
Poorly sorted, medium to coarse sand
Interbedded silts and marls
Marl

Figure 3.2b shows long axis plunge magnitude and orientation of bladed pebbles in the footwall and mixed zone. Pebble long-axes in the undisturbed Bed B have a mean plunge of 36^{o} SSW (spherical variance 0.29), slightly shallower, but in a similar orientation, to the dip of the sedimentary bedding (average 65^{o} to the WSW). Pebble long-axes in the mixed zone have a mean plunge of 37^{o} ESE (spherical variance 0.37), again, slightly shallower than, but in the same direction as the fault (60E/ 144N). Figure 3.2c shows a plot of measured pebble long-axes oreintations, from 1 m into the footwall through to the mixed zone/ hangingwall boundary across Bed B. Clasts plunge to the SW in the footwall furthest from the mixed zone, with orientations altering towards NW closer to the mixed zone boundary. The plunge orientation then appears to change abruptly at the mixed zone boundary from NW to SE. This is followed by a subsequent increase in variation in plunge orientation towards the centre of the mixed zone.

Five hand samples were taken from across the Fault 1A mixed zone. Figure 3.3 shows examples of the footwall/ mixed zone boundary (a) and the centre of the mixed zone (b). Both samples contain larger clasts (>5 mm) that tend to be aligned consistent with the fault dip. Smaller clasts (<5 mm) and small regions of matrix can exhibit a fabric not aligned with fault dip. Fabric aligned with fault dip appears to be better developed in the sample from the mixed zone boundary (Figure 3.2a) than from the centre of the mixed zone (Figure 3.2b).

Thin sections show a greater proportion of intra-clast space is occupied by a fine-grained matrix (Figure 3.3e) and micritic calcite cement (Figure 3.3c) in the hand sample taken from the centre of the mixed zone than the hand sample from the mixed zone/ footwall boundary. The hand sample in Figure 3.3a shows a fine matrix adjacent to the footwall Bed C/ mixed zone contact. Thin sections and hand samples from the mixed zone show evidence for grains having fractured by a combination of spalling and flaking (Figures 3.3d and f), and surface crushing (Figure 3.3a).

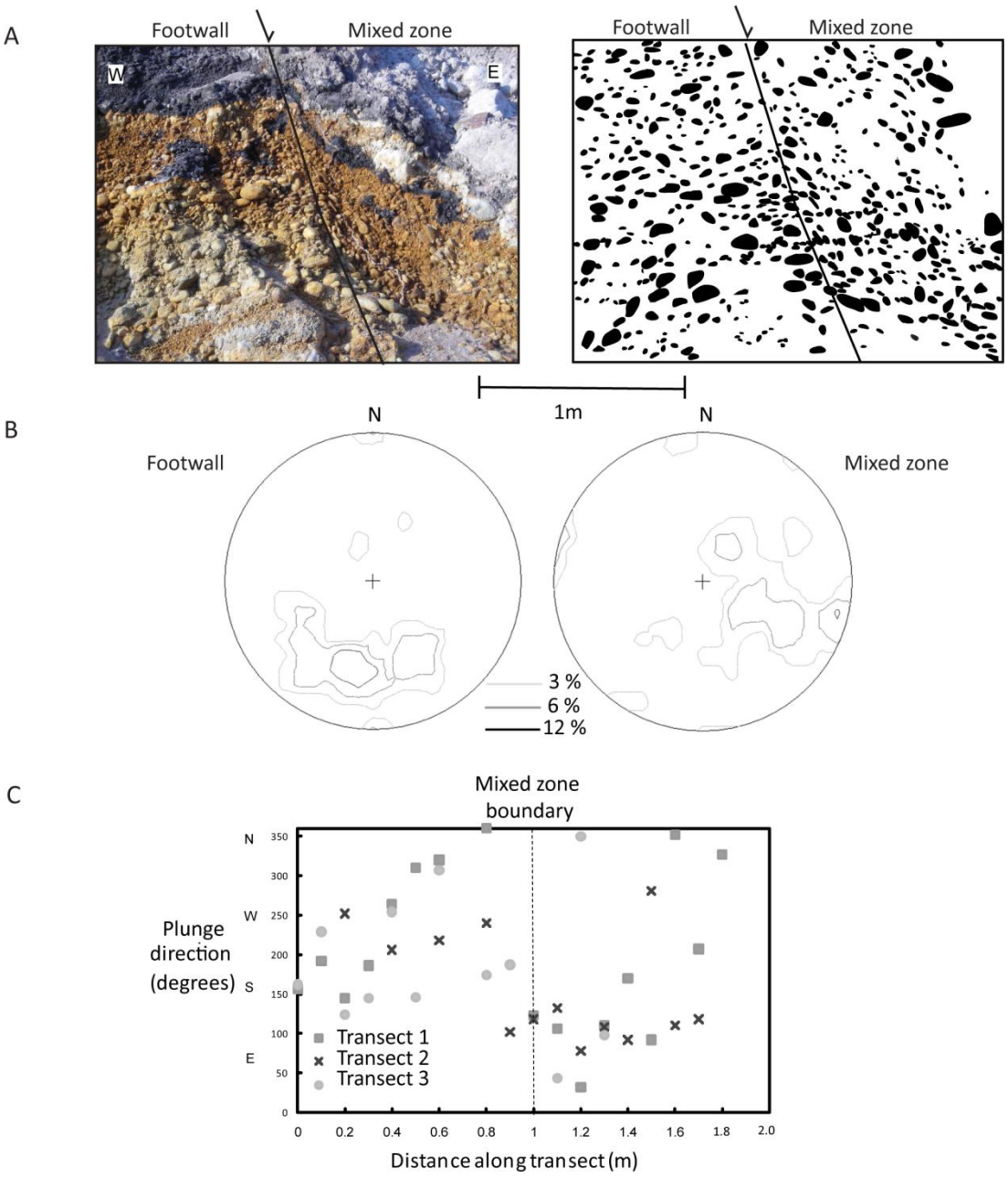

Figure 3.2 Clast orientations of bladed pebble Bed B across Fault 1A (Figure 3.1a). A) Photograph of Bed B at the mixed zone/ footwall boundary and 2D orientations of elongate clasts picked out visually demonstrate differences in clast orientation between the footwall and mixed zone. B) Equal area stereoplots of percentiles of 3D pebble orientations from the footwall and mixed zone. Footwall N= 22, mixed zone N= 20. C) Plunge directions of bladed pebble long-axes from horizontal transects (Figure 3.1a) crossing from the footwall into the mixed zone (each data point indicates one clast).

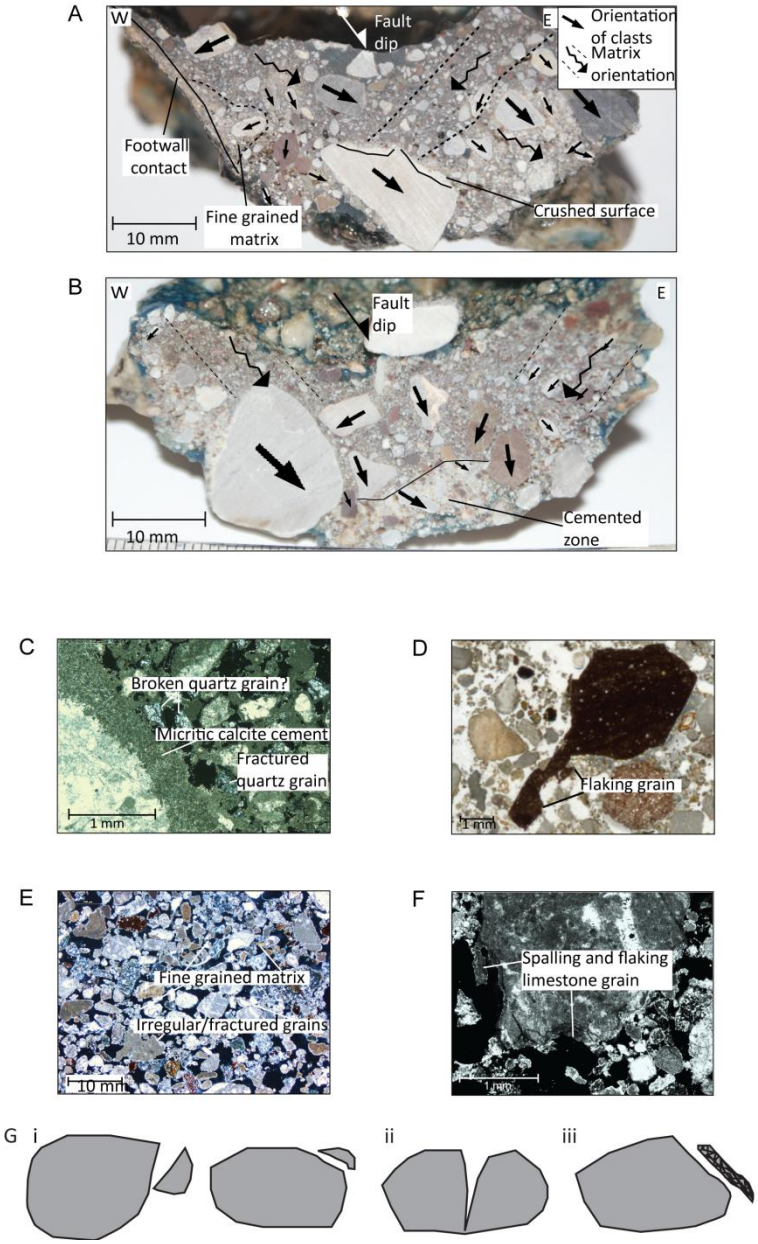

Figure 3.3 Hand samples and thin sections from the mixed zone of Fault 1A. A) Hand sample from the footwall Bed C/ mixed zone contact (Figure 3.1a) with fabric shown by large clasts (arrows). B) Hand sample from the centre of the mixed zone (Figure 3.1a) showing a more tightly packed matrix and poorly developed clast fabric, and a micritic calcite cement coating grains towards the base of the hand sample. C) Photomicrograph of a thin section showing micritic calcite cement coating clasts, from the mixed zone in (B). D) Scanned thin section showing flaking from a chert grain, from the mixed zone in (A). E) Photomicrograph of thin section showing fine-grained matrix and irregular and fractured grains from the mixed zone in (B). F) Flaking and spalling limestone grain from the mixed zone in (B). G) Illustration showing types of grain fracture: i) Flaking and spalling. ii) Intra-granular fracture. iii) Surface crushing.

3.3.2 Fault 1B

Fault 1B is exposed across the road from Fault 1A, and similarly cuts poorly lithified, coarse clastic sediments (Figure 3.1b). The calcite cemented gravel Bed (E) in the footwall at the base of the exposure is separated from the mixed zone by a localised shear zone. Other beds cut by the fault are entrained and smeared within a single mixed zone. In contrast to beds entrained within the fault zone of Fault 1A, the coarse sand Bed D and pebble Bed F (footwall) retain definition within the mixed zone throughout the exposure, despite a fault throw approximately four times greater than the thickness of the undeformed bed. The localised shear zone at the footwall/ mixed zone boundary of the cemented gravel Bed E dips 68^{o} NE compared to an average dip in poorly lithified beds of 55^{o} NE. In the footwall damage zone the cemented gravel Bed E has sustained a number of brittle fractures and is cut by a small subsidiary fault synthetic to the dip of the main fault (throw ~0.2 m). There are possibly disaggregation bands in sand Beds D and G. In Bed G these are associated with region of collapsed sediment at the mixed zone/ hangingwall contact (Figure 3.1b).

3.3.3 Fault 1C

Fault 1C is exposed down dip and along strike from Faults 1A and B (Figures 2.3 and 2.4). Section C exposes poorly lithified sand, slightly cohesive bedded marl and silts, and fine-grained marl that was noticeably more cohesive than other beds during sample collection, with greater than 45% grains 0.03 mm (Figure 3.4d). Deformation across Fault 1C is again focused within a mixed zone (Figure 3.1c). Poorly lithified sand is entrained and smeared within the mixed zone in a similar fashion to that observed in Fault 1A and B, however a block of the cohesive marl bed (shaded bed in Figures 3.1c and 3.4a) forms a major component of the Fault 1C mixed zone. This block appears undeformed internally except for a few fractures, and is bound by near-vertical localised shear zones. A smear connects this block to the source bed in the hangingwall and footwall (Figure 3.1c). There are a number of similar smaller blocks towards the base of the exposure (Figure 3.1c). The mixed zone boundaries in silt and marl are invariably more discrete than in poorly lithified sand. Contacts in the cohesive marl are generally localised shear zones (Figures 3.1c and 3.4b and c), occasionally with slickenlines. Silt and marl beds exhibit conjugate disaggregation

bands forming a minor damage zone in these beds, and a small antithetic fault originates in the marl bed at the base of the footwall exposure (Figure 3.1c). Locally the marl has steeper contact dips, 60^{o} (sdev ± 9^{o}), than sand bed contacts, 47^{o} (sdev ± 6^{o}) (Figure 3.1c).

Grain-size data from across Fault 1C demonstrate distinguishing characteristics for each sediment type. These are similar for the protosediment and mixed zone. Sand beds are mostly bimodal with relatively broad primary peaks at ~1 mm, and a smaller secondary peak at 0.03 mm (Figures 3.4d iii to viii). Silty-marl in the footwall is also bimodal, with a primary peak at 0.03 mm, and a positively skewed secondary peak at 1.5 mm (Figures 3.4d i). The cohesive marl in the hangingwall and mixed zone has a primary peak at 0.03 mm and a smaller secondary peak at 0.2 mm (Figure 3.4d ii and ix).

In the mixed zone sand there are a number of samples in which grain-size distribution profiles differ from those typical for the beds – these are identified by stars in Figures 3.4a and d. The grain-size distributions of sand samples T1 7 (Figure 3.4d v), T2 H (Figure 3.4d vi) and T5 V (Figure 3.4d viii) all show a greater peak height at 0.03 mm, and a smaller, broader peak at 1 mm. Sand samples T5 Q (Figure 3.4d viii) and T3 g (Figure 3.4d vii) have a greater peak at 1 mm than the typical grain-size distributions. Samples T2 F and T2 G (Figure 3.4d vi) have primary peaks at 15 mm. In the mixed zone marl, sample T3 e and j (Figure 3.4d ix) have a smaller primary peak at 0.03 mm and a third peak at 0.7 mm.

A hand specimen was taken from sand smeared between a localised shear zone in marl at the footwall/ mixed zone boundary and another that bounds the mixed zone marl block (Figure 3.4b). It contains a gradational footwall marl/ sand contact, with the proportion of marl in the mixed zone steadily decreasing away from the contact, up to 20 mm into the sand smear (Figure 3.4b and c). In contrast, the surface separating the cohesive marl block/ sand is more discrete, with no evidence of marl mixing into the sand from this contact (Figure 3.4b). This latter contact is representative of localised shear zones in the more cohesive marls indicated in Figure 3.1c. The hand specimen does not show modifications of the marl itself.

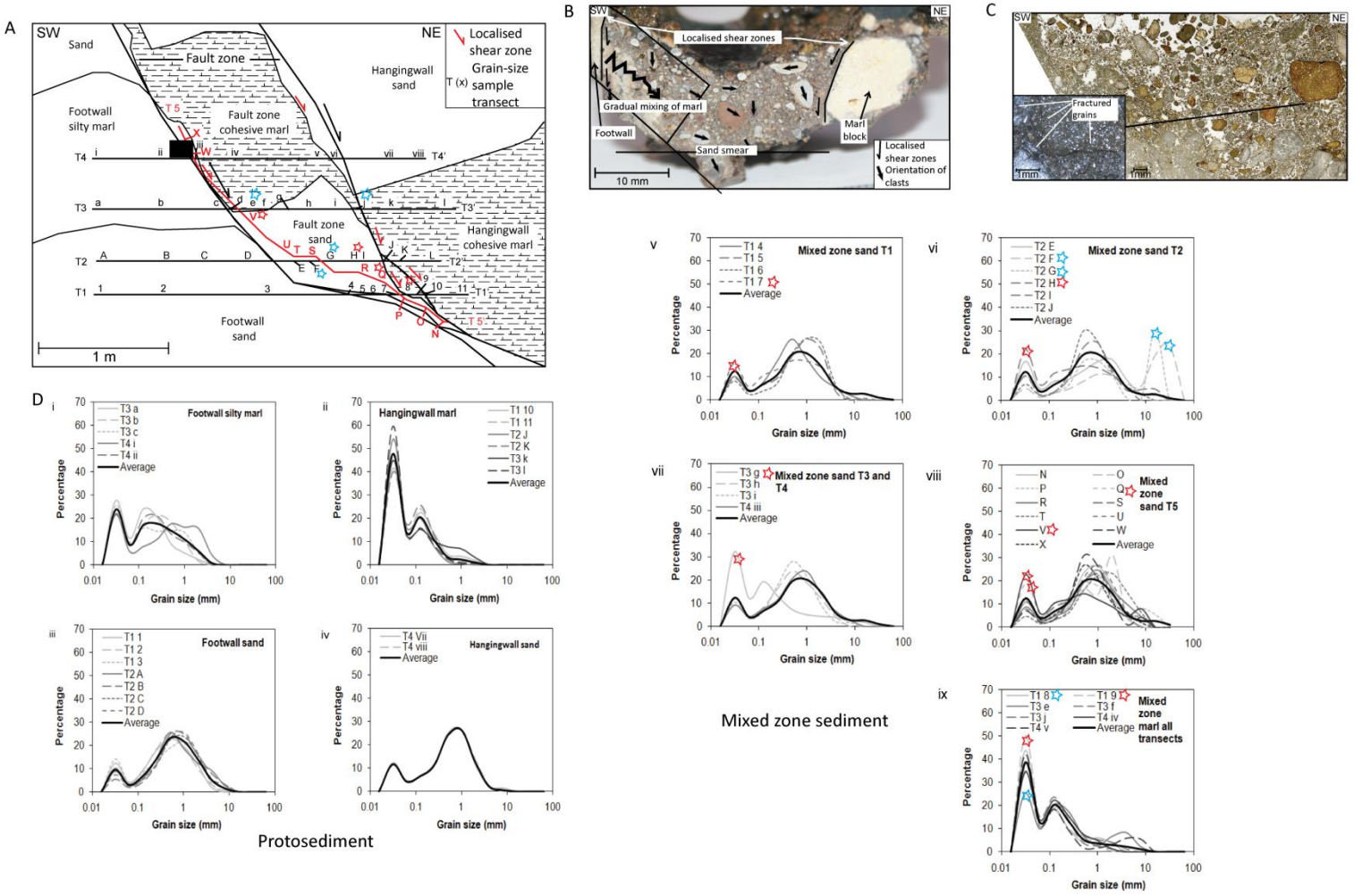
A
SW
NE
Sand
Fault zone
Hangingwall sand
Localised shear zone
Grain-size sample transect
Footwall silty marl
Fault zone cohesive marl
Fault zone sand
Hangingwall cohesive marl
Footwall sand
1 m
B
Localised shear zones
Gradual mixing of marl
Footwall
Marl block
Sand smear
10 mm
Localised shear zones
Orientation of clasts
C
Fractured grains
1mm
D
Footwall silty marl
Hangingwall marl
Footwall sand
Hangingwall sand
Percentage
Grain size (mm)
Protosediment
Mixed zone sand T1
Mixed zone sand T2
Mixed zone sand T3 and T4
Mixed zone sand T5
Mixed zone sediment
Mixed zone marl all transects
Average

Figure 3.4 Fault 1C (Figure 3.1c). A) Schematic diagram of the fault with grain-size sample transects (T1-5). The same marl bed is shaded in Figure 3.1c. Box shows location of hand sample in (B). Stars correspond to samples with grain-size distributions that differ from those typical of the sediment type in (D). B) Hand sample (black box in a) from the sand smear between the footwall marl and marl block. Marl from the footwall is seen mixing into the sand smear whereas the marl from the mixed zone block has a discrete localised shear zone. Larger clasts in the sand smear are predominantly orientated in the direction of fault dip (arrows). C) Scanned thin section from hand sample in (B) showing gradational incorporation of marl and irregularly shaped sand grains. Inset shows fractured chert and quartz grains from this thin section. D) Grain-size distributions of individual beds, for protosediment and mixed zone sediment. Average grain-size distributions for each sediment is shown by the black line. Stars indicate grain-size distributions that are noticeably finer (red) or coarser (blue) than average. i to iv) Samples from the protosediment. v to ix) Samples from the mixed zone.

3.3.4 Fault 3

Fault 3 forms the eastern boundary of the Loutraki graben (Figures 2.3 and 2.4). Bed offset towards the top of the exposed fault is 3.9 m, although the increased bed thickness in the hangingwall indicates this may be a growth-fault, thus throw below this could be greater. The unconformity between the fine-grained Pliocene and coarser Pleistocene sediment is halfway up the exposed section. The mixed zone is widest at the base of the exposure, comprising two relatively undeformed marl and sand blocks bound by near-vertical localised shear zones and separated by coarse sand smears 20 mm thick (Figure 3.5). Above these blocks, the mixed zone comprises coarse-grained sediment smears that have largely retained their sedimentary characteristics. There is an irregular smear of marl between the two marl blocks (Figures 2.4 and 3.5a). Antithetic faults (maximum fault throw 0.5 m) form a damage zone in both the footwall and hangingwall, and are cut by Fault 3. Two regions of apparent disaggregation bands antithetic to Fault 3 are found in the footwall (Figure 3.5a), but are not directly adjacent to the fault.

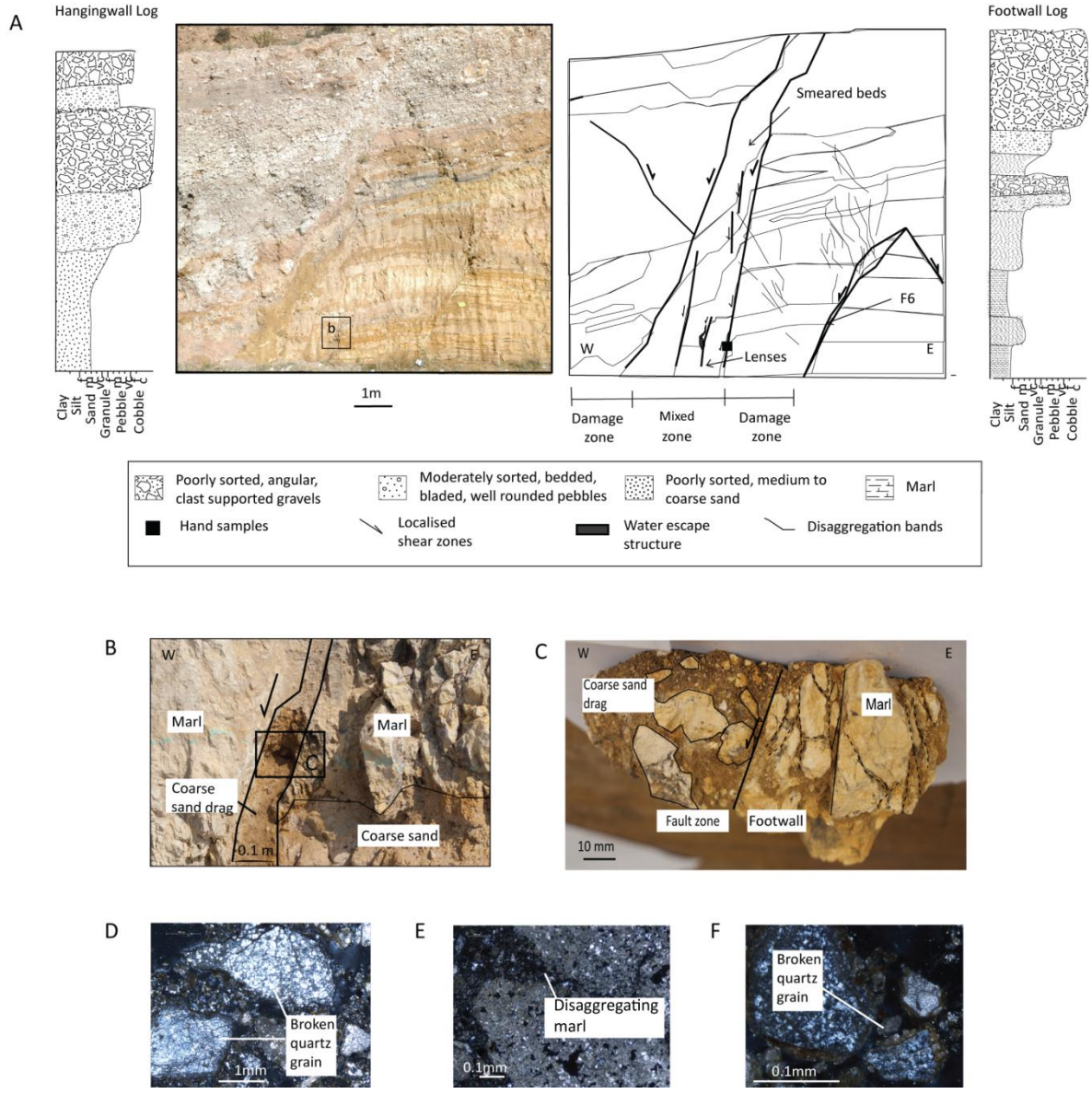

Figure 3.5 Fault 3, easterly graben fault (Figures 2.3 and 2.4). A) Photograph, schematic diagram and corresponding sediment logs of exposed hangingwall and footwall. The mixed zone is between the thick black lines. Fault 6 is synthetic to Fault 3 in the footwall. B) Photograph of hand sample location in the exposure shown by box in (A). C) Hand sample from marl/ sand smear contact at the footwall boundary in (B) and in the schematic diagram in (A). D-F) Photomicrographs of the coarse sand smear in (C). D) Broken quartz grain. E) Disaggregating marl. F) Broken quartz grain with iron oxide coating.

A hand sample from across the footwall marl/ sand smear contact shows a localised shear zone bounding the footwall marl (Figure 3.5a to c). The footwall marl is broken into blocks adjacent to this zone of localised shear. Fissures between marl blocks have apertures ~5 mm, and most are filled with coarse sand (Figure 3.5c). The boundaries of the fissures are apparently discrete but are not planar (Figures 3.5c and e). Marl comprises a matrix in the hand sample sand smear, and is also found as large clasts. Sand grains are 50% chert, 30% quartz and 20% limestone. There are a high proportion of irregularly shaped, angular clasts in this smear. Fragments of broken grains can be traced in the smear, as seen in Figures 3.5d and f. Iron oxide coats many of the grains in the sand smear (Figure 3.5f).

3.3.5 Fault 4

Fault 4 (~1 m throw) cuts a micritic calcite cemented gravel bed in the footwall, at the base of the exposure, and very poorly lithified sand and pebble beds (Figure 3.6). The mixed zone is an ill-defined, non-planar zone of sand and beach pebbles through which individual beds cannot be traced. The mixed zone is best defined at the top of the exposure by the hard veneer of calcite cement, from the surface to 0.5 m below the surface. This veneer connects to a region in the mixed zone with a high concentration of micritic calcite cement, 0.2 m thick. In places, the micritic calcite cement fingers horizontally up to 0.5 m from the mixed zone into footwall and hangingwall sediment (Figure 3.6). There is no evidence of a damage zone flanking the mixed zone.

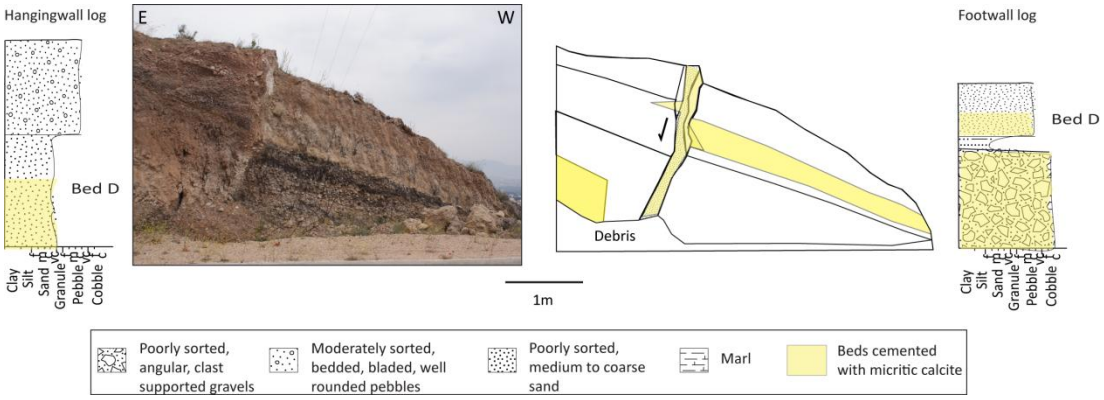

Figure 3.6 Photograph and schematic diagram of Fault 4, with hangingwall and footwall logs. The mixed zone is a poorly defined zone of sand and pebbles, distinguished primarily by the existence of a micritic calcite cement. Bed D is the same bed as Figure 3.1.

3.3.6 Fault 5

Fault 5 (throw ~0.6 m) (Figures 2.3 and 2.4) is probably the trace of one of the subsidiary faults cutting the hangingwall of Fault 1A (Figure 3.1a). This fault offsets poorly lithified bedded beach pebbles and alluvial sediments (Figure 3.7a). Beds cut by Fault 5 are entrained and smeared, with a continuous-displacement geometry, in a mixed zone. On a macro-scale there are no blocks of sediment or localised shear zones in the fault zone.

The pebble bed offset by Fault 5 comprises a number of visually distinctive beds considerably thinner (<0.25 m) than the fault throw (Figure 3.7a). In Figure 3.7 grain-size distributions for the footwall, hangingwall, and where the bed crossed the mixed zone are compared for the three sampled beds, A to C. There is a general decrease in grain-size from the footwall to the hangingwall. In the footwall and hangingwall, Beds A and C have uni-modal grain-size distributions. Small secondary peaks exist at 2-3 mm in the mixed zones samples, that are not found in the hangingwall or footwall samples (Figure 3.7b). Bed B is bi-modal in the mixed zone and hangingwall, and unimodal, but negatively skewed, in the footwall. It is not possible to infer a peak at 2-3 mm over the original sediment variability in this sample. Beds A to C are poorly sorted, with little difference between the average sorting parameters for the mixed zone (1.30), hangingwall (1.33) and footwall (1.48).

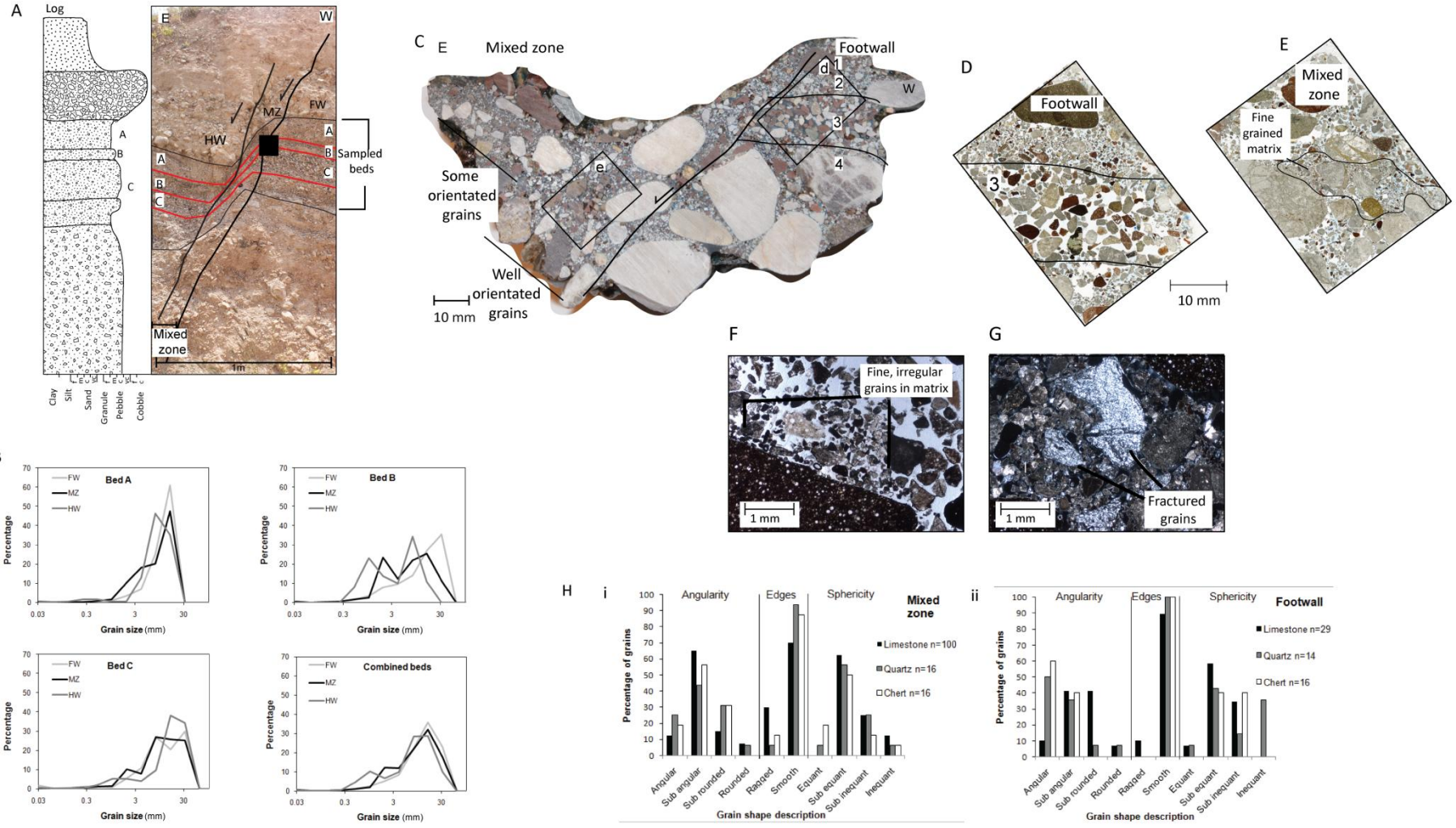
A
Log
E
W
FW
MZ
HW
A
B
C
Sampled beds
Mixed zone
1m
Clay
Silt
Sand
Granule
Pebble
Cobble
B
Bed A
Bed B
Bed C
Combined beds
FW
MZ
HW
Percentage
Grain size (mm)
C
E
Mixed zone
Footwall
W
Some orientated grains
Well orientated grains
10 mm
D
Footwall
10 mm
E
Mixed zone
Fine grained matrix
F
Fine, irregular grains in matrix
1 mm
G
Fractured grains
1 mm
H
i
Mixed zone
Angularity
Edges
Sphericity
Limestone n=100
Quartz n=16
Chert n=16
Percentage of grains
Angular
Sub angular
Sub rounded
Rounded
Ragged
Smooth
Equant
Sub equant
Sub inequant
Inequant
Grain shape description
ii
Footwall
Limestone n=29
Quartz n=14
Chert n=16

Figure 3.7 Fault 5, Loutraki outcrop, section BB' (Figures 2.3 and 2.4). A) Fault 5 with a mixed zone (thick black lines) comprising a continuous smear of the bladed gravel bed (thin black lines). Sediment log applies to both the footwall and hangingwall. Distinctive Beds A to C sampled for grain-size. Black box is the location of the resin sample in (C). B) Grain-size distributions correspond to beds in (A), footwall (FW), mixed zone (MZ), and hangingwall (HW). C) Sliced hand sample from the footwall/ mixed zone boundary showing the truncation of beds labelled 1-4. Sample shows grain rotation and mixing in the mixed zone. D and E) Scanned thin section of the footwall, with Beds 2 to 4, and mixed zone, with a fine grained matrix. F) Scanned thin section with a fine grained irregular matrix associated with a larger clast. G) Photomicrograph of broken quartz grain from the mixed zone thin section. H) Grain shapes in the mixed zone (i) and footwall (ii).

A hand specimen of the mixed zone/ footwall boundary provides a more detailed view of the well-defined Beds 1 to 4, both inside and outside the mixed zone (Figure 3.7c). The apparently well sorted, coarse sand Bed 3 can be traced throughout the footwall, and 10 mm into the mixed zone, after which definition is lost as it is mixed with surrounding beds (Figure 3.7c to e). In the mixed zone, clasts, particularly the larger ones, are often aligned with the fault dip, though this fabric is less pronounced closer to the centre of the mixed zone (Figure 3.7c).

Thin sections from the hand specimen show zones of fine matrix (<0.25 mm) (Figure 3.7e) and a zone of irregularly shaped grains proximal to a larger clast (Figure 3.7f), in addition to evidence of fragmented grains in the mixed zone thin section (Figure 3.7g). Point counts show a greater proportion of spherical grains and grains with ragged edges in the mixed zone than in the footwall for grains of all lithologies (Figure 3.7h i and ii). However, limestone grains were more angular, and chert and quartz less angular, in the mixed zone than the footwall. The proportion of limestone grains was two thirds higher in the mixed zone than in the footwall.

3.3.7 Mixed zone thickness with fault throw

Mean mixed zone thickness for faults in the Loutraki outcrop increases with fault throw ($R^2 = 0.64$) (Figure 3.8). There is a strong correlation between mixed zone thickness and fault throw for faults cutting only poorly lithified sediments ($R^2 = 0.99$), though this is based on only three data points. The correlation is weaker for

faults cutting sediment of contrasting competency (R^2 = 0.34), i.e. where beds are alternately cohesive and non-cohesive. Error bars show the high variability of mixed zone thickness along-dip of each fault, particularly for faults cutting sediment of contrasting competency. This is particularly large for Fault 1C. The inset equal-angle stereoplot in Figure 3.8 shows little difference in overall fault dip for faults cutting only poorly lithified sediment, and those cutting sediment of contrasting competency.

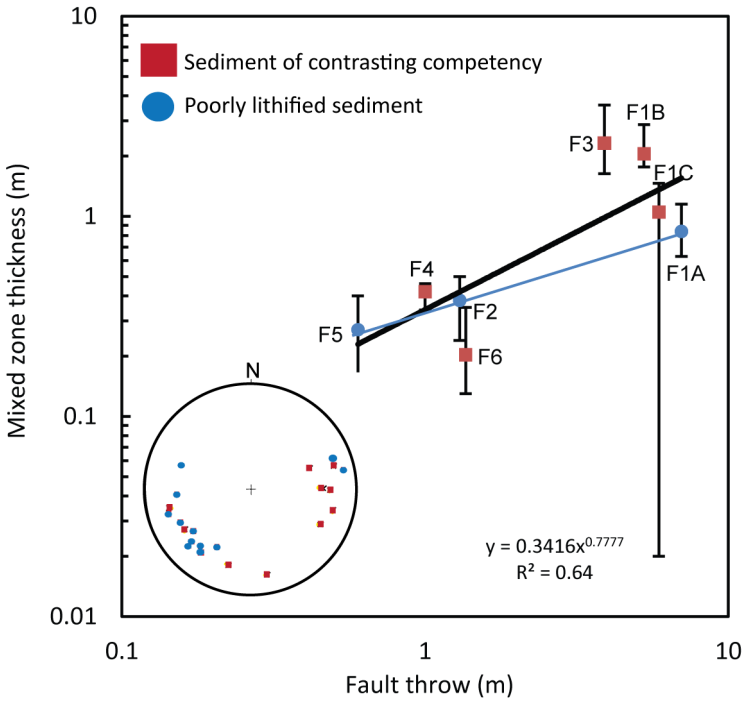

Figure 3.8 Mixed zone thickness and fault throw for six faults (F1 is exposed 3 times) in the Loutraki outcrop. Minimum and maximum mixed zone thickness along-dip of each fault indicated by error bars. The black trendline and equation relates to all the faults. The blue trendline describes poorly lithified sediment only. Equal angle stereoplot inset shows poles to planes for apparent fault dip orientations for different sediment types, including damage zone faults.

3.4. Fault zone structure and evolution

The architecture of fault zones exposed at the Loutraki outcrop predominantly comprise a mixed zone, with occassional damage zones. Fault zone structure appears to vary as a function of lithology and stratigraphy. As such, fault zone structure and evolution of faults cutting only poorly lithified sediment, and those

cutting sediment of contrasting competency (i.e. inter-bedded cohesive marls or cemented beds and poorly lithified sediment) are discussed separately.

3.4.1 Fault zones in poorly lithified sediment

3.4.1.1 Fault zone structure in poorly lithified sediment

The mixed zones of faults cutting poorly lithified, low competency sediment, exposed in the Loutraki outcrop, are comprised of beds cut by the fault that have been entrained, rotated, and subsequently smeared and attenuated along the fault trace (Figures 3.1a and 3.7a). Shear deformation of beds in the mixed zone can destroy bedding characteristics found in the undeformed sediment. A zone of mixed sediment in which sediment is mixed at the grain scale can occur where fault throw exceeds the undeformed bed thickness (e.g. Mozley and Goodwin, 1995; Heynekamp *et al.,* 1999) (Figure 3.1a and 3.7c).

Clay cores and shear deformation bands (Figure 1.3, Table 1.1), previously considered the key structural elements of fault zones in poorly lithified sediment (e.g. Rawling *et al.,* 2001; Caine and Minor, 2009), are absent from fault zones in the Loutraki outcrop. This is likely to be because faults in the Loutraki outcrop cut relatively coarse, poorly sorted sediment, thus there is a lack of clay-sized grains with which to form a clay core (e.g. Lindsay *et al.,* 1993; Yielding *et al.,* 1997; Heynekamp *et al.,* 1999; Fisher and Knipe, 2001; Minor and Hudson, 2006). Shear deformation bands have predominantly been found in well-sorted sand in the past (e.g. Fossen *et al.,* 2007).

3.4.1.2 Clast rotation in mixed zones

In the mixed zones of faults cutting poorly lithified sediment, mechanical clast rotation causes an overall grain-shape preferred orientation of bladed clasts, parallel to fault dip (Figures 3.2, 3.3a, b and 3.7c). This results from simple shear accommodation by particulate flow (Goodwin and Tikoff, 2002). Similar observations have been made in shear deformation bands in gravels (Exner and Grasemann, 2010), sands (Cashman and Cashman, 2000), silts and clays (Arch and Maltman, 1990) and ignimbrites (Wilson *et al.,* 2003), as well as in fault cores and mixed zones (Mozley and Goodwin, 1995; Rawling and Goodwin,

2006; Balsamo *et al.*, 2008). Clasts in poorly lithified sediment rotate as individual units when subjected to simple shear. Angular velocity of the rotating clast is at a minimum when its long axis is co-incidental with the direction of shear, thus despite continued rotation, the clast spends longest orientated in the direction of shear (Glen, 1957; Ildefonse *et al.*, 1992a; Piazolo *et al.*, 2002). Consequently, at any point in time, a larger proportion of clasts will be orientated in the direction of shear than in other directions, resulting in a grain-shape preferred orientation. The increase in variability of clast orientation with distance from the mixed zone margin (Figures 3.2c and 3.7c), is likely to result from a greater number of clast interactions with increased bulk strain (Ildefonse *et al.*, 1992a).

Larger clasts are more commonly aligned with fault dip direction than small grains or zones of groundmass, which may locally dip in different directions to the fault dip (Figures 3.3a and b). Heterogeneous strain patterns around large clasts have previously been reported to cause localised matrix and clast foliation (in matrix supported or closely packed sediments respectively) for a distance of up to twice the length of the clast, from the clast itself (Ildefonse *et al.*, 1992a and b).

3.4.1.3 Grain-scale mixing in mixed zones

Mixing of grains from different sedimentary beds is another characteristic of particulate flow in poorly lithified sediment (e.g. Heynekamp *et al.*, 1999; Rawling and Goodwin, 2006). Grain-scale mixing of the thin coarse sand Beds 1 to 4 in the hand sample of Fault 5 is observed in the mixed zone (Figure 3.7c), and also between silty-marl and sand sediment of Fault 1C (Figures 3.4c and d). However, there is no decrease in sediment sorting in the mixed zone of Fault 5, for Beds A to C, compared to the footwall and hangingwall (Figure 3.7b). This suggests that in Fault 5, sampled grain-size distributions are not greatly influenced by grain-scale mixing processes; in this mixed zone, natural sediment variability dominates over grain-scale mixing processes – a situation that may also hold true for other mixed zones, especially those in faults with small throws (<1m). Conversely, an increase in the fine fraction (0.03 mm) of between 5% (sample V) and 20% (sample g), is detectable in grain-size distributions for four

grain-size samples of sand from the mixed zone of Fault 1C (Figure 3.4d). These samples were all sourced from sand proximal (<50 mm away from) to contacts with marl beds, indicating that these peaks may result from marl grains mixing into the sand bed. This can be seen in the corresponding hand sample (Figures 3.4b and c). The coarser peaks in two of these sand grain-size distributions, and two marl samples (Figures 3.4d vi and ix) probably result from cemented grains that were not sufficiently disaggregated during analysis, rather than mixing of coarser beds. It is likely that grain-scale mixing is more easily detected in Fault 1C because the sediment is better sorted. The degree of grain-scale mixing might increase with fault throw (and bulk strain), as demonstrated by the presence of a zone of mixed sediment in Fault 1A compared to Fault 5 (Figures 3.1a and 3.7a).

3.4.1.4 Cataclasis in mixed zones

The negatively skewed grain-size distribution peak for three samples from the mixed zone of Fault 1C (7, V and H, Figure 3.4d), and the slight increase in the proportion of the 2 mm fraction in the mixed zone samples of Fault 5, compared to the protosediment (Beds A and C, Figure 3.7b), indicate an increase in fine-grained sediment fractions in some mixed zone samples. These increases could result from mixed zone deformation processes. Increases in finer sediment fractions in fault zones have previously been observed in fault cores (Balsamo *et al.*, 2008; Balsamo and Storti, 2011) and cataclastic deformation bands (Cashman and Cashman, 2000; Rawling and Goodwin, 2003) in poorly lithified sediment, and attributed to the process of cataclasis (e.g. Sammis *et al.*, 1987). This is supported by fractured grains shown in thin sections of mixed zone sediment (Figures 3.3e to f, 3.5c and f, 3.7f, g and h).

An overall increase of both the sphericity and angularity of grains in the mixed zone compared to protosediment was also observed by Balsamo and Storti (2011), and attributed to the chipping of grains as they roll during particulate flow. However, chert and quartz grains alone were more rounded in the mixed zone (Figure 3.7h). This could result from chipping removing initial grain irregularities. However, different fracturing mechanisms resulting from contrasting grain hardness (Rawling and Goodwin, 2003), could also cause this difference, whereby grains composed of harder minerals (in this case quartz and

chert) fracture by spalling or flaking, in contrast to softer lithic grains (limestone) (Middleton & Wilcock, 1999) that have a greater propensity to fracture intra-granularly, or crush along their surfaces (Figure 3.3g). The higher proportion of limestone fragments in the mixed zone (Figure 3.7h) could result from pervasive intra-granular fracturing of limestone grains that produces a greater number of daughter fragments than were a grain to singularly flake or spall under equivalent stress. The greater proportion of limestone grains with ragged edges in the mixed zone in comparison to quartz and chert alludes to their relative weakness. Not only do grain-shape variations in footwall and mixed zone sediment provide further evidence for cataclasis in mixed zones, but the preferential fracturing of limestone grains demonstrates the importance of mineralogy on the propensity and style of cataclasis within poorly lithified sediments (Rawling and Goodwin, 2003; Exner and Tschegg, 2012). The presence of cataclasis in these fault zones, while minor, supports previous suggestions that high confining pressures are not required for cataclasis to occur (cf. Cashman and Cashman, 2000; Rawling and Goodwin, 2003; Balsamo and Storti, 2011).

Nevertheless, evidence of cataclasis is not abundant, indicating that it is unlikely to be the dominant deformation mechanism in mixed zones. Instead, it is more likely to arise as a secondary effect of controlled particulate flow whereby continued particulate flow and deformation in the mixed zone is facilitated by the fracturing of occasional grains (Borradaile, 1981). The prevalence of cataclasis is believed to increase as strain is accumulated (Engelder, 1974; Balsamo and Storti, 2010). This is in response to progressive strain hardening whereby the tectonic imbrication and porosity decrease resulting from strain accommodation in a fault zone can increase the number of grain contacts and therefore friction between grains. This can inhibit further strain accommodation by independent particulate flow, causing grains to fracture (e.g. Exner and Grasemann, 2010). The dominance of controlled particulate flow is consistent with earlier outcrop studies of deformation mechanisms in deformation bands and fault cores cutting poorly lithified sediment (Rawling and Goodwin, 2003; Balsamo *et al.*, 2008).

3.4.1.5 Fault zone evolution in poorly lithified sediment

The overall positive correlation between fault throw and mixed zone thickness for faults exposed in the Loutraki outcrop (Figure 3.8) has been found across all lithologies (e.g. Childs *et al.*, 1996a; Shipton *et al.*, 2006; Childs *et al.*, 2009). The apparent strong correlation for faults cutting poorly lithified sediment ($R^2 = 0.99$) could result from a continuous and steady contribution of footwall and hangingwall sediment into the mixed zone, possibly via particulate flow (Rawling & Goodwin, 2003; Caine & Minor, 2009). However, the strong correlation could result from the extremely limited data and/or it being plotted on a log-log graph. Figure 3.9b shows a possible model of mixed zone evolution faults cutting poorly lithified sediment, based on fault zone structure and deformation mechanisms found at the Loutraki outcrop. Deformation is initially manifested in the rotation of grains and disaggregation of sediment, which progresses to the smearing of beds and grain-scale mixing with increasing fault displacement. During which, incipient cataclasis may also occur. The mixed zone progressively widens due to the incorporation of new material also via particulate flow.

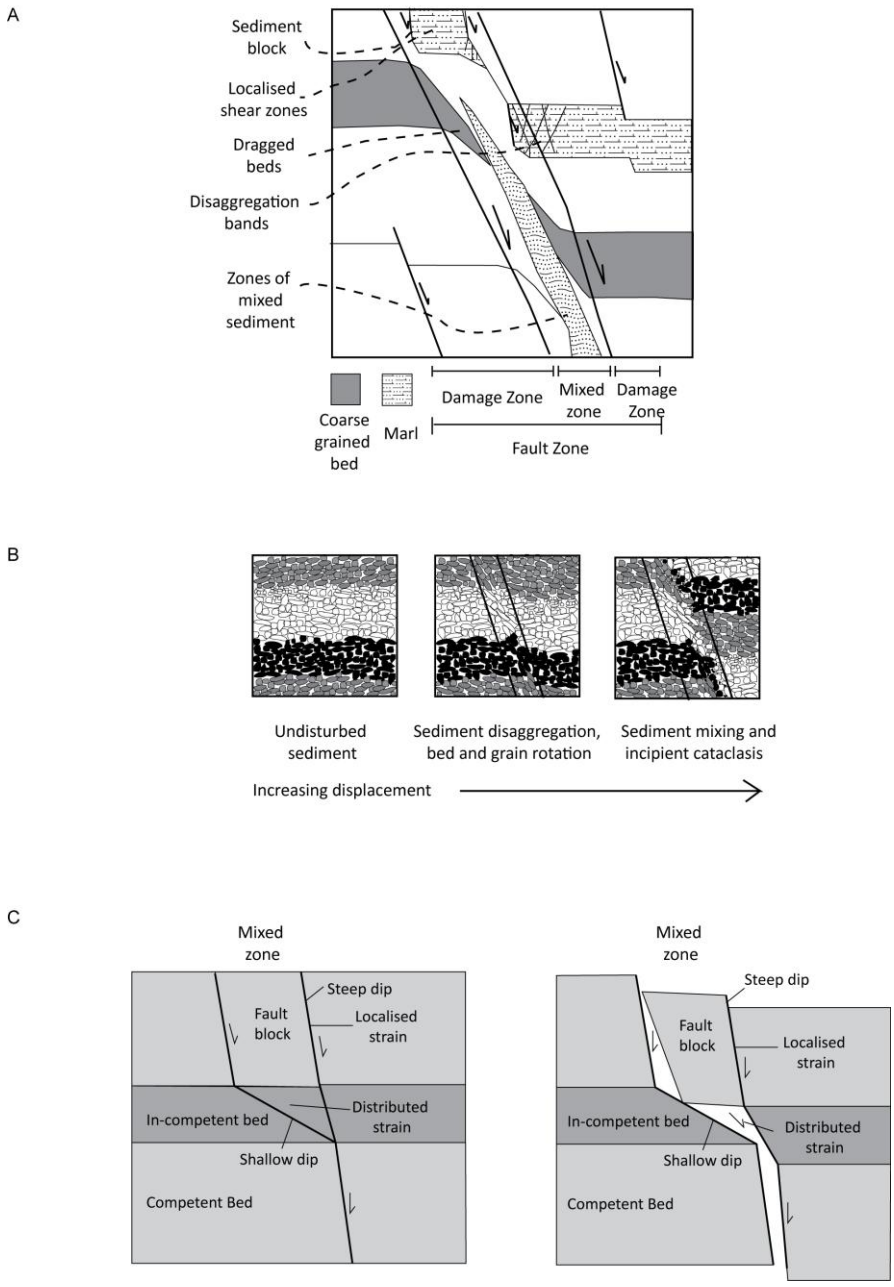

Figure 3.9 Fault zone structure and evolution in poorly lithified sediment based on the faults in the Loutraki outcrop. A) Model of fault zone structure with a mixed zone and damage zone, but no clay core. Fault zone structure is likely to vary along the dip and/ or strike (e.g. Childs *et al.*, 1997). B) Evolution of a mixed zone by particulate flow with a corresponding increase in mixed zone thickness with fault throw. C) Formation of a cohesive block of undeformed sediment in the mixed zone of a fault cutting sediment of contrasting competency, due to differing dip angles and strain localisation in competent beds.

3.4.2 Fault zones in sediment of contrasting competency

3.4.2.1 Fault zone structure in sediment of contrasting competency

Mixed zones of faults cutting sediment of contrasting competency are generally more complex than those cutting consistently poorly lithified sediment at the Loutraki outcrop. The key difference in the fault zone structure is the existence of localised shear zones. These occur in marl or cemented coarser sediment that are mechanically stronger than un-cemented sands and gravels due to the presence of silt and clay (Middleton and Wilcock, 1999) or cement (Arch and Maltman, 1990) (Figures 3.1b and c). Mixed zone/ protosediment contacts are 10^{o} to 20^{o} steeper where strain is localised than where strain is distributed across the mixed zone (Figures 3.1b and c), although the overall dip of faults does not differ from faults in poorly lithified sediment (inset in Figure 3.8). The localised shear zones often bound blocks or lenses of cohesive sediment in the mixed zone, which have largely intact bed characteristics, as described in earlier outcrop studies (Heynekamp *et al.,* 1999; Rawling and Goodwin, 2006; Minor and Hudson, 2006; Kristensen *et al.,* 2008; Wilson *et al.,* 2009). In poorly lithified beds, deformation remains distributed across the mixed zone (Figures 3.1c and 3.5a).

3.4.2.2 Fault zone evolution in sediment of contrasting competency

The significant variability in fault zone thickness along-dip of Fault 1C, and the weaker correlation between fault throw and mixed zone thickness in faults cutting beds of contrasting competency, compared to those in poorly lithified sediment (R^2 = 0.34) (Figure 3.8), suggest that a mechanism other than particulate flow may govern evolution of these mixed zones. Mixed zone thickness may increase intermittently with fault throw, associated with the formation of blocks and lenses. Blocks and lenses can form as a result of fault-tip bifurcation (Watterson *et al.,* 1998; Rawling and Goodwin, 2006; Childs *et al.,* 2009). A fault trace can be deflected and bifurcate in bed sequences in which there are contrasts in competency (Antonellini and Aydin, 1995; Childs *et al.,* 1996b; Rawling and Goodwin, 2006; Bastesen *et al.,* 2009; Childs *et al.,* 2009), or bed friction angles resulting from grain shape (Egholm *et al.,* 2008). This creates asperities at the mixed zone/ protosediment boundary that are intermittently removed and incorporated as blocks of sediment in the mixed zone, with subsequent fault

deformation (Rawling and Goodwin, 2006; Lindanger *et al.*, 2007). This process might be occurring at the footwall/ mixed zone boundary of Fault 3, as disaggregation bands are progressively enlarged and filled with coarser sediment, until they detach fully and are included within the mixed zone (Figure 3.5c). Fault-tip bifurcation can also occur along strike (Childs *et al.*, 1996b). Figure 3.9c shows the evolution of a block of sediment in a mixed zone based on Fault 1C, due to alternating strain localisation and distribution in beds with contrasting competencies.

Localised shear zones may influence fault zone structure without forming lenses or blocks in the mixed zone. The mixed zone of Fault 1B is dominated by smeared beds, similar to Fault 1A, yet these are less internally deformed (Figures 3.1a and b). Two possible hypotheses are proposed to explain this. The first is that localisation of deformation along the shear zone at the cemented footwall/ mixed zone boundary decreases grain disaggregation and bed mixing throughout the mixed zone, such as in the mixed zone of Fault 1A. The second is that because Fault 1B is wider than Fault 1A (2 m and 0.8 m, respectively) the intensity of grain-scale deformation at a particular point in the mixed zone may be decreased as strain is distributed over a wider area. These processes may, however, be linked. The wider mixed zone of Fault 1B could result from a step-back of the footwall/ mixed zone boundary (e.g. Childs *et al.*,1996a) into the footwall, above the cemented Bed E, due to the change in the strain distribution and contact dip. Where a fault segment steps into the footwall, slip along near-vertical, localised shear zones causes an increase in pressure in the shallow dipping, weaker beds that connect the steeply dipping fault segments. This pressure forces sediment into a region of lower pressure - the fault zone. This process may contribute to the supply of sand to the mixed zone at the back-step of Fault 1B (e.g. Egholm *et al.*, 2008).

3.4.3 Damage zones in the Loutraki outcrop

Damage zones are typically poorly developed in fault zones exposed in the Loutraki outcrop, with a maximum fault parallel thickness of 2 m. However it is possible that some damage zones, particularly those comprised of disaggregation bands were not identified due to the erodibility of the sediment.

The most common features of fault damage zones are subsidiary faults. These cut all lithologies and have throws at least an order of magnitude less than the primary fault (Figures 3.1a and 3.5a). Fault throw decreases up-dip along the three synthetic subsidiary faults in the damage zone of Fault 1A. Assuming that these faults are kinematically related to Fault 1A, this could indicate that deformation initially occurred simultaneously on all four faults, but was subsequently focused on the most westerly, Fault 1A (Figure 3.1a). Throw does not decrease up-dip along the antithetic faults in the damage zones of Fault 1C and 3, yet throw is significantly less than the primary fault, suggesting that these formed after the main fault, possibly as a passive response to sediment deformation (e.g. Figures 3.1c and 3.5).

Disaggregation bands (Figures 3.1b, c and 3.5a) similar to those reported previously (e.g. Du Bernard *et al.*, 2002; Bense *et al.*, 2003; Balsamo *et al.*, 2008) are also found in sand and marl beds. In Fault 1B a collapsed region of sediment is associated with disaggregation bands at the maximum curvature of smeared beds –the mixed zone/ hangingwall boundary (Figure 3.1b and 3.5a). This may indicate a decrease in sediment strength due to the existence of disaggregation bands at low confining pressures.

3.5 Summary

Mixed zones are the principal architectural element of fault zones in poorly lithified sediment in the Loutraki outcrop. Variations in the structural characteristics of these mixed zones result from lithology, stratigraphy and fault throw. Damage zones are not always present, but comprise disaggregation bands and subsidiary faults. Two models of fault zone evolution are proposed for faults in the Loutraki outcrop that might be applicable throughout the Gulf of Corinth basin.

Strain is distributed across the mixed zone in fault zones cutting poorly lithified sediment, within rotated and smeared beds. Microstructural observations indicate that mixed zone deformation occurs via particulate flow, resulting in considerable grain rotation, grain-scale mixing of smeared beds, and steadily thickening fault zones. The presence of fragmented grains, and grain shape and grain-size

distribution changes suggests that cataclasis facilitates particulate flow, and is therefore controlled particulate flow. Increasing fault throw can result in zones of mixed sediment in the mixed zone, with possible decreases in grain-size and sorting.

In marl and locally cemented sediment deformation is focused along localised shear zones, with locally steeper bed dips. Fault tip-bifurcation occurs as a consequence of vertically contrasting bed competencies. Asperities are created by fault tip bifurcation along the mixed zone boundary. Removal of these asperities results in incorporation of internally undeformed cohesive lenses and blocks of sediment within the mixed zone, and sporadic increases in mixed zone thickness.

4. Constraints on fault zone structure and evolution

4.1 Introduction

This chapter investigates the fault zone structure and size attributes of 43 faults exposed in the five outcrop study locations (Chapter 2). The validity of fault zone structure and evolution models proposed for normal-faults cutting syn-rift sediment, described in Chapter 3 (Figure 3.9), is assessed for this extended dataset. The dataset includes faults cutting different lithology, and throws ranging four orders of magnitude – from 0.01 to 80 m. Local stress conditions at the remaining four outcrops may also differ slightly to the Loutraki outcrop (e.g. Chapter 2). Additional fault zone structure and evolution characteristics are elucidated from fault zones exposed in these outcrops. In particular, lenses and zones of localised shear in the form of slip-surface cataclasites are further characterised to aid their parametisation in numerical fluid-flow models (Chapter 6). Details of a third category of fault zone found cutting the syn-rift sediment are also presented. Finally, fault array characteristics, including fault density and the fault size population distribution are evaluated.

Fault zone structure is typically investigated using small to medium sized faults (<10 m throw) and extrapolated to large faults (>20-30 m throw) because they are more easily observed (Tueckmantel *et al.,* 2010) and generally exhibit fewer complexities (Faulkner *et al.,* 2003). However, the models of fault zone evolution proposed in Chapter 3 suggest some differences in fault zone structure and deformation mechanisms with fault throw (Figure 3.9). If fault zone evolution is self-similar, for example block and lens formation, or even linear, including the gradual evolution of zones of mixed sediment and increase in cataclasis, then extrapolation of fault zone structure and evolution across scales is reasonable. However, if fault zone evolution is neither self-similar or linear, straight-forward extrapolation is impractical. Balsamo and Storti (2010) found that the greatest changes to sediment characteristics in fault zones cutting high-porosity, poorly lithified sand, occur at throws <20 m. Therefore extrapolation of fault zone evolution processes for faults with throws >20 m could over-estimate alterations to fault zone properties. In this case fault size could be described as a hierarchy whereby faults above and below a certain size are considered to belong to

different groups (Torabi and Berg, 2011). In this chapter, the effects of fault size on fault zone structure and evolution is identified, and the legitimacy of extrapolating between different fault sizes considered.

The relationship between mean mixed zone thickness and fault throw, shown for faults exposed in the Loutraki outcrop (Figure 3.8), is explored for faults exposed in all five outcrops. Average mixed zone thickness is imperative for estimating fault zone transmissivity, however Lunn *et al.* (2008) suggest that it is at least as important to quantify minimum fault (mixed) zone thickness, because this parameter can control fault leak potential. The Loutraki faults showed considerable variability in mixed zone thickness along-dip, therefore minimum and maximum mixed zone thickness relationships with fault throw are also examined for this dataset.

Fault size distributions of fault populations – in which fault throw, thickness or length of each fault is plotted against the cumulative size occurrence, are commonly described by a single power-law relationship, indicating a fractal fault-size distribution (e.g. Scholz and Cowie, 1990; Walsh *et al.,* 1991; Needham *et al.,* 1996). Fractal fault size populations reveal the abundance of small faults in comparison to large faults in a fault population; the specific distribution is indicated by the power-law exponent (Cowie *et al.,* 1996; Nicol *et al.,* 1996). Fault array characteristics may vary depending on lithology and stress regimes (Needham *et al.,* 1996; Torabi and Berg, 2011). Fractal fault-size distributions have also been used to suggest self-similar deformation throughout fault zone evolution, thus justifying extrapolation of fault zone structure and evolution from small to large faults. Torabi and Berg (2011) argue, however, that many fault size population distributions are better described by separate power-law trends for faults of different sizes, indicating bi- or multi-fractal populations that represent fault size hierarchies.

Combined with spatial distribution and fault orientation data, population distributions can be used to infer fault zone connectivity, aquifer (or reservoir) compartmentalisation and sediment juxtapositions across fault zones (e.g. Walsh *et al.,* 1991; Needham *et al.,* 1996; Yielding *et al.,* 1996; Walsh *et al.,* 1998). Fault size population distributions were constructed for faults in this dataset

primarily to identify whether fault zone evolution processes are self-similar or hierarchical. Findings from the fault size population distributions are considered with fault density and average fault throw at the five outcrops to gain an appreciation of strain distribution across fault arrays in syn-rift sediment of the Corinth rift basin.

4.2 Fault data collection and analysis methods

Many data collection and analysis methods used in this chapter are detailed in Chapter 3.2. All additional methods are described in this section and the data collected for each fault is outlined (Appendix 1).

4.2.1 Data collection and analysis of fault zone structure

Fault zone structure and size attributes of 43 well exposed faults in the five outcrop locations were recorded in the field (Appendix 1). Fault zone data collection methods are described in Chapter 3.2.1. Fault throws >10 m were estimated by mapping stratigraphic units instead of field measurements or scaled photographs.

Lithology cut by each fault was recorded. In Chapter 3, key differences in fault zone structure were identified for faults cutting only poorly lithified sediment and faults cutting sediment of contrasting competency. In the Voutsimos and Mentourgianika outcrops a third category of fault zone structure was identified across which fine and coarse-grained sediment is juxtaposed. Fault zone structure and size attributes were analysed separately for these three fault categories and comprised data for 24, 16 and 3 faults respectively (Appendix 1).

The presence or absence of the main structural elements identified in Chapter 3 was recorded for each fault. These were: zones of mixed sediment, localised shear zones, disaggregation bands, fine-grained smears, lenses, and damage zones. In recording this data, care was taken to adhere to definitions outlined in Chapters 1 to 3. In each of the three fault categories data was sub-divided according to fault throw and the percentage of faults in each sub-category exhibiting each of the identified structural elements was calculated and displayed on a bar chart.

Fault size attributes, including fault throw and mixed zone thickness, were recorded. The minimum, maximum and arithmetic mean of mixed zone thickness was assessed for each fault using the method outlined in Chapter 3.2.1. Faults with ambiguous throw estimates were removed from this dataset leaving a total of 32 faults. Fault throw and mixed zone thickness were plotted on log-log scatter graphs and power-law trends fitted. Logarithmic scales were always used for plotting fault size attributes because of the range in magnitudes. However, trends emerging from logarithmic scales should be viewed with caution because they may have been enhanced or obscured (cf. Nicol *et al.,* 1996). The range of sampled fault throw and mixed zone thickness in this dataset exceeds the order of magnitude considered essential for the robust analysis of fault scale relationships (Gillespie *et al.,* 1993).

The number of lenses across mixed zones, and their geometry, was assessed from field diagrams and scaled-photographs for fault zones cutting sediment of contrasting competency. The number of lenses across the mixed zone was recorded for each fault at ten equally spaced locations along fault-dip. Two-dimensional lens geometry was characterised by the c: a (along-dip length: fault perpendicular thickness) aspect ratio (cf. Lindanger *et al.,* 2007). The mean number of lenses across the mixed zone, the proportion of the mixed zone comprising lenses, and the mean c: a aspect ratio were compared with fault throw, mixed zone thickness, mean thickness of beds cut by the fault, mean thickness of competent beds cut by the fault, and fault throw: mean bed thickness ratio. Log-normal trends were fitted to these data. Average lens attributes for all faults were also calculated.

Slip-surface cataclasite, a specific type of localised shear zone was identified in the mixed zones of a number of faults cutting poorly lithified sediment (described in section 4.3.1). The number of exposed slip-surface cataclasites across mixed zones was counted from field diagrams and photographs. Graphs were plotted to assess the relationship between number of slip-surface cataclasites across a mixed zone and fault throw. Localised shear zones not along the surface of cataclasites were not included in this analysis because they form through different mechanisms.

4.2.2 Data collection and analysis of fault zone micro-structure

Microstructural data was collected from mixed zones of faults cutting poorly lithified sediment. Orientation measurements were made for bladed clasts from transects across (Fault 3, Akrata, 7 m throw) and along (Fault An, Mentourgianika, 1.5 m throw) mixed zones and adjacent protosediment (method described in Chapter 3.2.2). Clast orientations are compared with fault orientations.

The percentage of broken clasts in the mixed zone and protosediment of three faults with throws of 1, 7 and 80 m, cutting gravel conglomerate were identified. A paper frame 0.1 m^2 was attached to the outcrop surface at two randomly selected locations in the mixed zone and protosediment of each fault. Each clast found in the centre of the frame >10 mm in diameter was removed from the outcrop and assessed for fresh surfaces associated with angular edges that might indicate in-situ grain breakage. The percentage of grains with these characteristics was compared for the mixed zone and adjacent sediment. The statistical significance of any differences in percentages was evaluated using the Chi Squared test of variance.

Fault zone microstructure was also analysed for fifteen hand specimens and thin sections from mixed zones and protosediment primarily obtained for porosity analysis in Chapter 5. The fault zone microstructures of hand specimens of two slip surfaces, a fine-grained smear and a disaggregation band are discussed in section 4.3.

4.2.3 Analysis of fault population characteristics

Fault-size population distributions were constructed for fault throw and mixed zone thickness for each outcrop, for faults that had good estimates of fault throw and mixed zone thickness, by plotting the logarithm of the fault size attribute with its cumulative frequency. For outcrops with sufficient data (> 5 faults), a single power-law trend was initially fitted to these data, followed by two separate power-law trends after identification of differences in the trend gradients for smaller and larger faults.

Fault density was calculated for each outcrop from the most continuous, well exposed horizontal mapped section. The number of mapped faults in this section was divided by the horizontal distance to obtain fault density (number of faults m^{-1}) . Fault density was plotted with the mean throw of faults exposed in the outcrop. These are presented with the poles to planes of the faults in each outcrop, plotted on equal-angle stereonets.

4.3 Fault zone structure

Similar to fault zones exposed in the Loutraki outcrop (Chapter 3), the fault zone architecture exposed in all five outcrops comprises a mixed zone and damage zones. Mixed zone structure differs between the three lithological categories and is presented separately for each in this section. The fault structure dataset is included in Appendix 1.

4.3.1 Fault zones in poorly lithified sediment

Poorly lithified sediment exposed in the four outcrop locations in the southern flank of the Corinth rift basin is most commonly gravel conglomerate inter-bedded with coarse sand beds of the Giant Gilbert-type deltas (Figure 2.2). Faults with throws <10 m that cut this sediment have relatively tabular mixed zones. Most of these mixed zones comprise a zone of mixed sediment (79%) that appears internally homogeneous (Figure 4.1). The remaining mixed zones comprise only smeared beds. Fault An, in the Mentourgianika outcrop (throw 1.5 m) (Figure 4.1b), is an example of a fault zone with only a central mixed zone and damage zones. All three faults with >10 m throw comprise zones of mixed sediment, for example Fault G1 at the Pirgos outcrop with >40 m throw (Figure 4.1c).

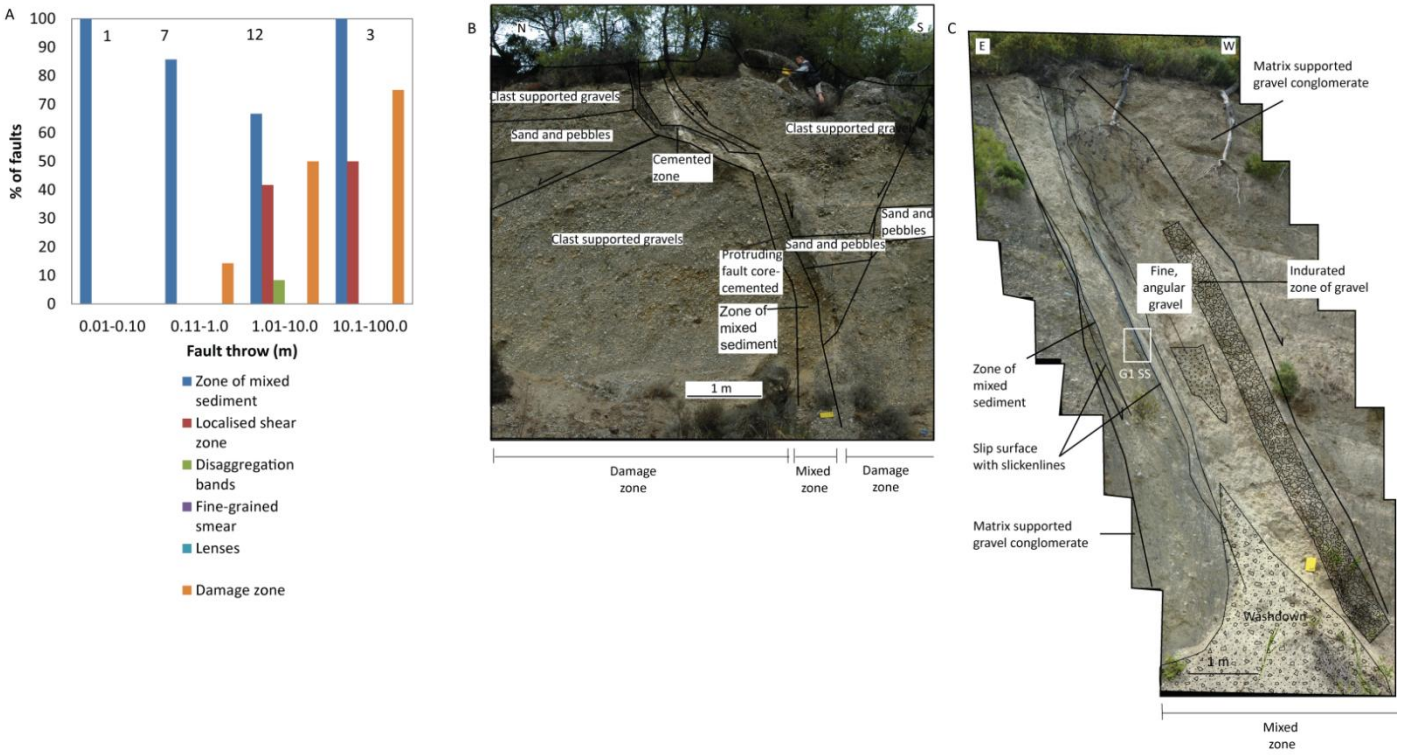

Figure 4.1 Fault zone structure in poorly lithified sediment. A) Percentage of structural elements with fault throw and total number of faults in the category. B) Fault An, Mentourgianika, cutting poorly lithified gravel conglomerate with a zone of mixed sediment and damage zone (Figure 2.10). Fault dip shallows towards the top and micritic calcite is found in the mixed zone, from the surface to halfway down the exposure. C) Fault G1, Pirgos (south section) cutting poorly lithified gravel conglomerate (Figure 2.12). Mixed zone comprises two zones of mixed sediment and two indurated slip-surface cataclasites. Location of G1 SS hand sample from slip-surface cataclasites shown by white box.

Mean plunge and plunge orientations of bladed clasts differ in mixed zones to protosediment (Figure 4.2). Mean clast plunge in the hangingwall protosediment of Fault An, Mentourgianika, is 53^{o} WSW (spherical variance 0.27) (Figure 4.2a). The mean clast plunge for the footwall protosediment, 86^{o} SE (spherical variance 0.57), is not reliable because the data are not uni-modal. The clasts actually plunge shallowly (<45^{o}) in a range of directions. Mean plunge of clasts in the mixed zone of this fault is 68^{o} SW; closer to the apparent fault orientation N 083/86 S, and with a greater degree of clustering (spherical variance 0.1).

Clast plunge and plunge orientations are clustered in both the hangingwall and footwall protosediment cut by Fault 3, Akrata (Figure 4.2b); mean clast plunge and plunge orientation is 80^{o} W and 72^{o} SW (spherical variance 0.15 and 0.24) respectively. Clasts in the mixed zone have a comparable degree of clustering (spherical variance 0.23) but mean plunge and plunge orientation, 83^{o} ENE, is in the direction of apparent fault orientation, N 136/72 NE.

A greater proportion of clasts appeared to be broken in-situ in the mixed zones of Fault 3, Akrata, and the Terrace Fault, Mentourgianika, 44 and 57% respectively, than the protosediment, 5 and 22% respectively (significant to 99%) (Figures 4.3a and b). Conversely, the proportion of broken clasts in the mixed zone of Cement Fault 2, Mentourgianika (41%), was smaller than the protosediment (52%), though this was not statistically significant (Figure 4.3c).

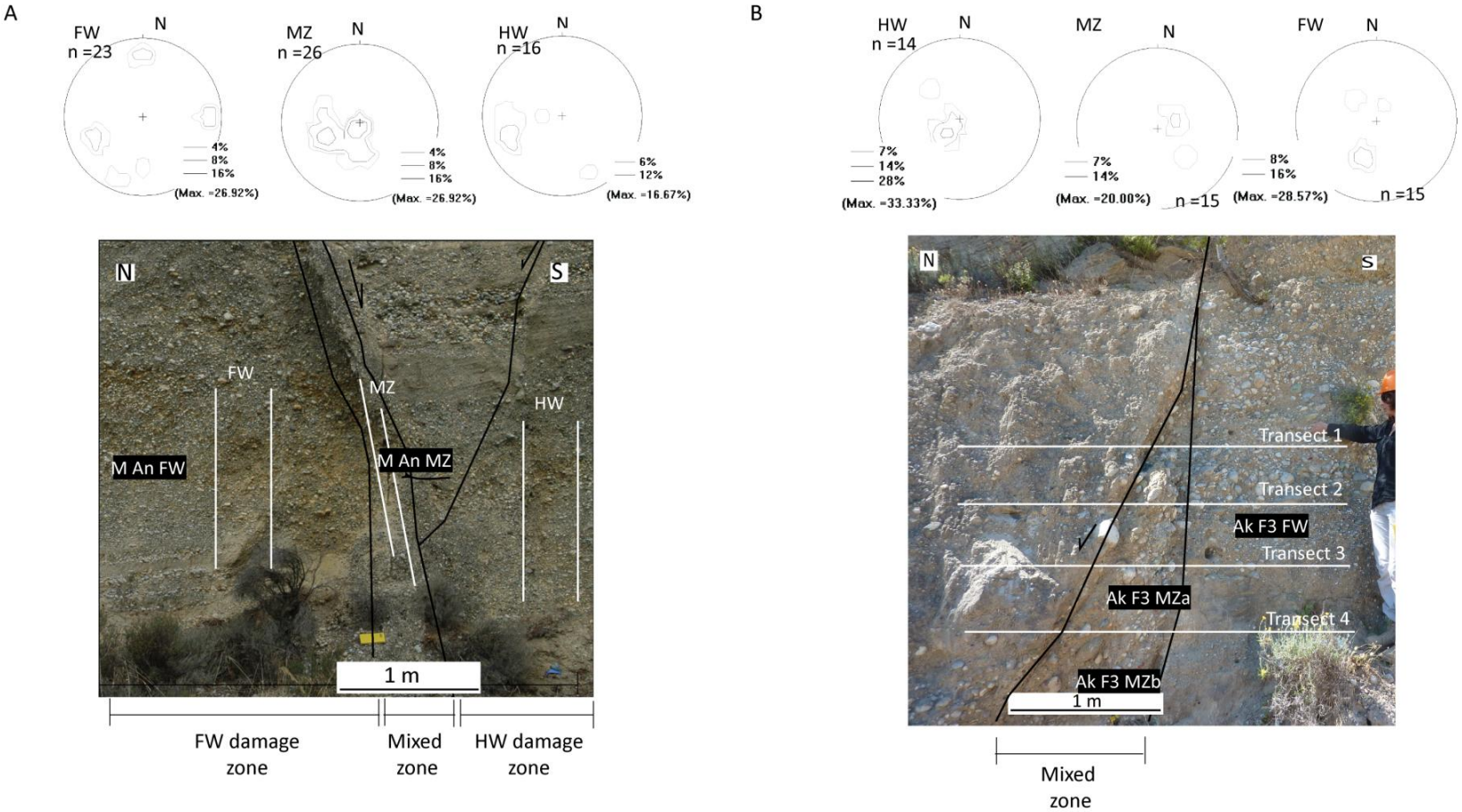

Figure 4.2 Bladed clast orientation percentiles in mixed zones and protosediment with the number of clasts included in the analysis (n). Sample transect locations shown in photographs. FW, HW and MZ indicate footwall, hangingwall and mixed zone samples respectively. Black boxes show locations of hand specimens collected from these faults. A) Fault An, Mentourgianika (Figure 4.1). B) Fault 3, Akrata, throw 7m (Figure 2.6).

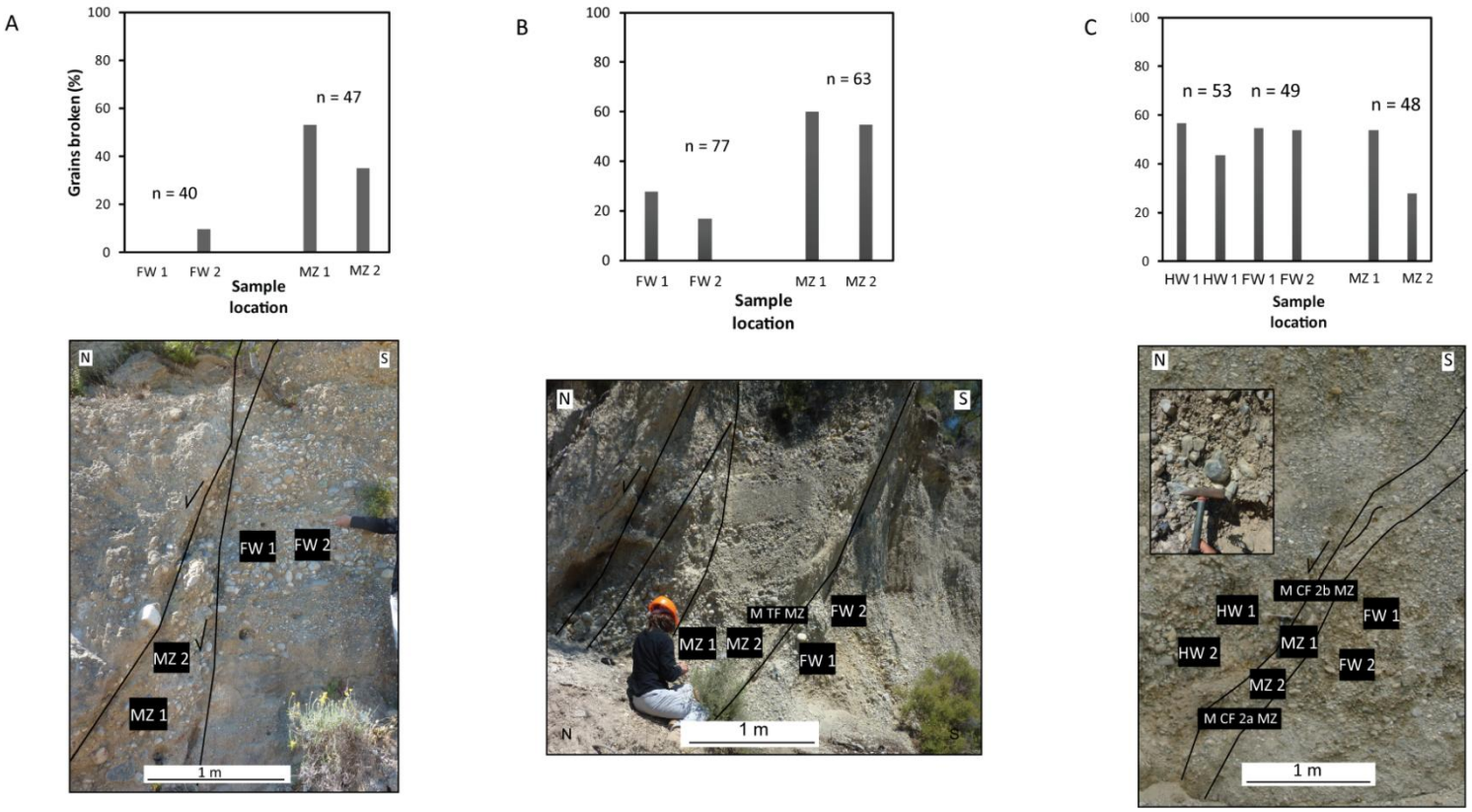

Figure 4.3 Percentage of broken grains in mixed zones and protosediment. FW, HW and MZ indicate footwall, hangingwall and mixed zone respectively, with the number (n) of clasts sampled in each quadrant, quadrant locations shown by black boxes. A) Fault 3, Akrata, 7 m throw (Figure 4.2a). B) Terrace Fault, Mentourgianika, ~80 m throw (Figure 2.10), with location of hand specimen (M T MZ). C) Cement Fault 2, Mentourgianika, 1 m throw (Figure 2.10). Inset photograph shows example of a broken clast in the mixed zone, with location of hand specimens (M CF 2a and b MZ).

In addition to zones of mixed sediment, approximately 40% of faults with 1 to 10 m throw, and 50% of faults with 10 to 100 m throw have localised shear zones (Figure 4.1a). These either dissect or bound zones of mixed sediment, and are largely continuous throughout fault exposures, such as in Fault G1, Pirgos (Figure 4.1c). In contrast to the localised shear zones in cemented or fine-grained, cohesive sediment (Chapter 3), these localised shear zones are found along the surface of strongly indurated 0.02 m to 0.2 m thick cataclasite (Figure 4.4a). The exposed cataclasite surfaces often show slickenlines, indicating that these are slip surfaces (Figure 4.4a). The slip-surface cataclasite sample from Fault G1, Pirgos, shows a number of relict limestone clasts surrounded by a fine-grained matrix of irregularly shaped grains, many of which are intra-granularly fragmented (Figures 4.4a ii to iv). Porosity of the cataclasite appears very low, and there does not appear to be grain shape-preferred alignment, though most grains are sub-equant (Figure 4.4a). Slip-surface cataclasites were not found in mixed zones of faults with throws <1.5 m (Figure 4.1a), and there is an apparent increase in the number of exposed slip-surface cataclasites in mixed zones with an increase in fault throw (Figure 4.4b).

Damage zones were attributed to 41% of all faults cutting poorly lithified sediment, but the percentage increases from 15% for faults with 0.01 to 1 m throw, to 75% for faults with 10 to 100 m throw (Figure 4.1a). Damage zones are dominantly comprised of antithetic or synthetic subsidiary faults (Figure 4.1b) although disaggregation bands were found in fine-grained sediment adjacent to Fault 1B, Loutraki (Figure 3.1b). Fine-grained smears and lenses were not identified in these fault zones.

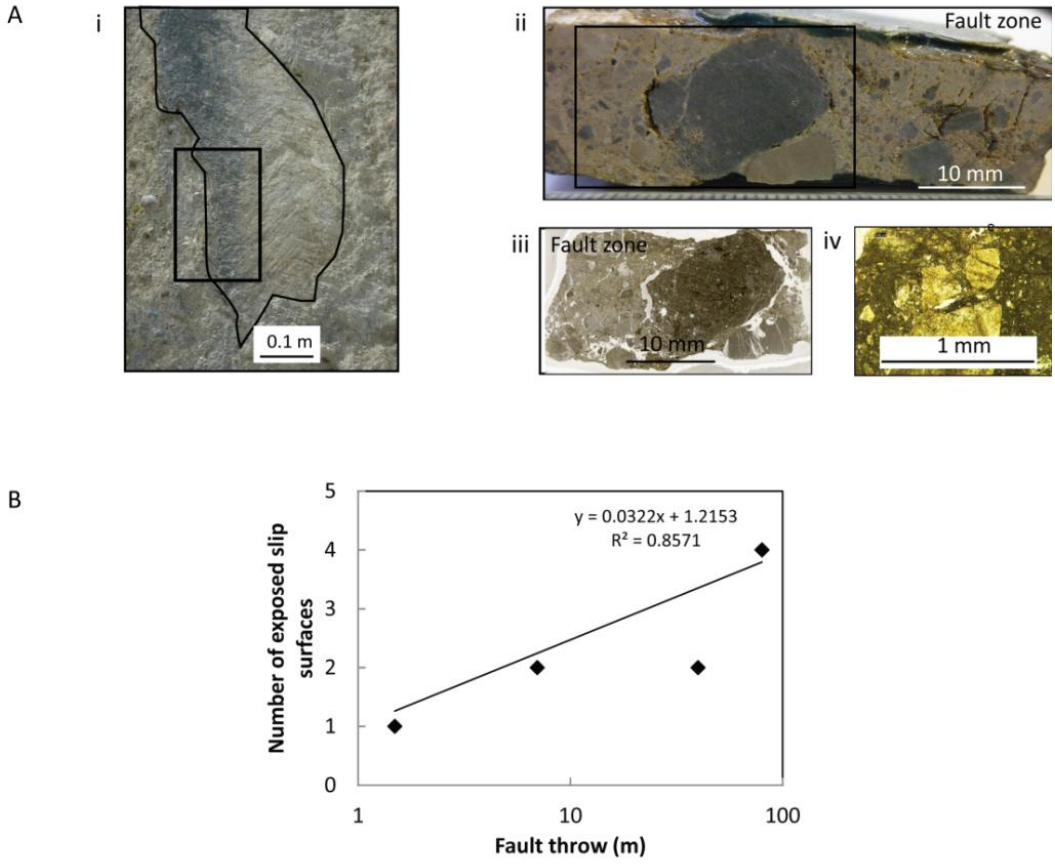

Figure 4.4 Slip-surfaces cataclasite in poorly lithified sediment. A) Example of slip-surface cataclasite from Fault G1, Pirgos (Figure 4.1c). i) Slip-surface with slickenlines, in the field. ii) Hand specimen P G1 SS sliced perpendicular to the fault strike, from location shown by black box in (i). Relict clasts are supported by a matrix of irregular and fragmented grains. iii) Scanned thin section showing relict clast in (ii). iv) Photomicrograph taken under plane-polarised light of an intra-granularly fragmented grain from the cataclasite matrix in (ii). B) Number of slip-surface cataclasites exposed in mixed zones with fault throw.

4.3.2 Fault zones in sediment of contrasting competency

Sediment of contrasting competency exposed in the five outcrops is dominantly silt and marl inter-bedded with sand and gravel beds of the Aiges Formation (Figure 2.2). Competency contrasts are also found in outcrops exposing Giant Gilbert-type delta topset sediment where gravel and coarse sand conglomerate is inter-bedded with silt (Figure 2.6). The maximum throw of faults in exposed in the outcrops for this category is an order of magnitude less than in poorly lithified sediment.

The majority (88%) of mixed zones in faults cutting sediment of contrasting competency comprise lenses of largely undeformed sediment (Figure 4.5a). There is no overall trend in lens occurrence with fault throw. Lenses often include less competent (generally coarse-grained beds) between competent (generally fine-grained) beds (Figures 4.5b and c). The number of lenses across mixed zones ranges between 0 and 3 at any one point along fault dip. Multiple lenses across the mixed zone are generally en-echelon, whereby they are connected but offset in the direction of fault shear (Figures 4.5b and c).

Lens attributes are poorly correlated with fault size attributes and bed thickness (Figure 4.6). The strongest relationship is the positive correlation between the mean number of lenses across the mixed zone and mean mixed zone thickness (R^2 = 0.32) (Figure 4.6b). The average number of lenses across the mixed zone and proportion of the mixed zone comprising lenses slightly increase with fault throw (R^2 = 0.24 and 0.20 respectively) (Figures 4.6a and c). The proportion of the mixed zone comprising lenses is slightly positively correlated with mean bed thickness (R^2 = 0.19) (Figure 4.6d). The c: a lens aspect ratio is slightly positively correlated with both fault throw and mean competent bed thickness (R^2 = 0.15 and 0.23 respectively) (Figures 4.6e and f). The mean lens c: a aspect ratio was 2.9: 1 (along-dip length: fault perpendicular thickness). The maximum measured lens aspect ratio was 8.5: 1 and the minimum was 0.43: 1. At any one point across the mixed zone thickness there was an average of one lens comprising roughly 65% of the mixed zone.

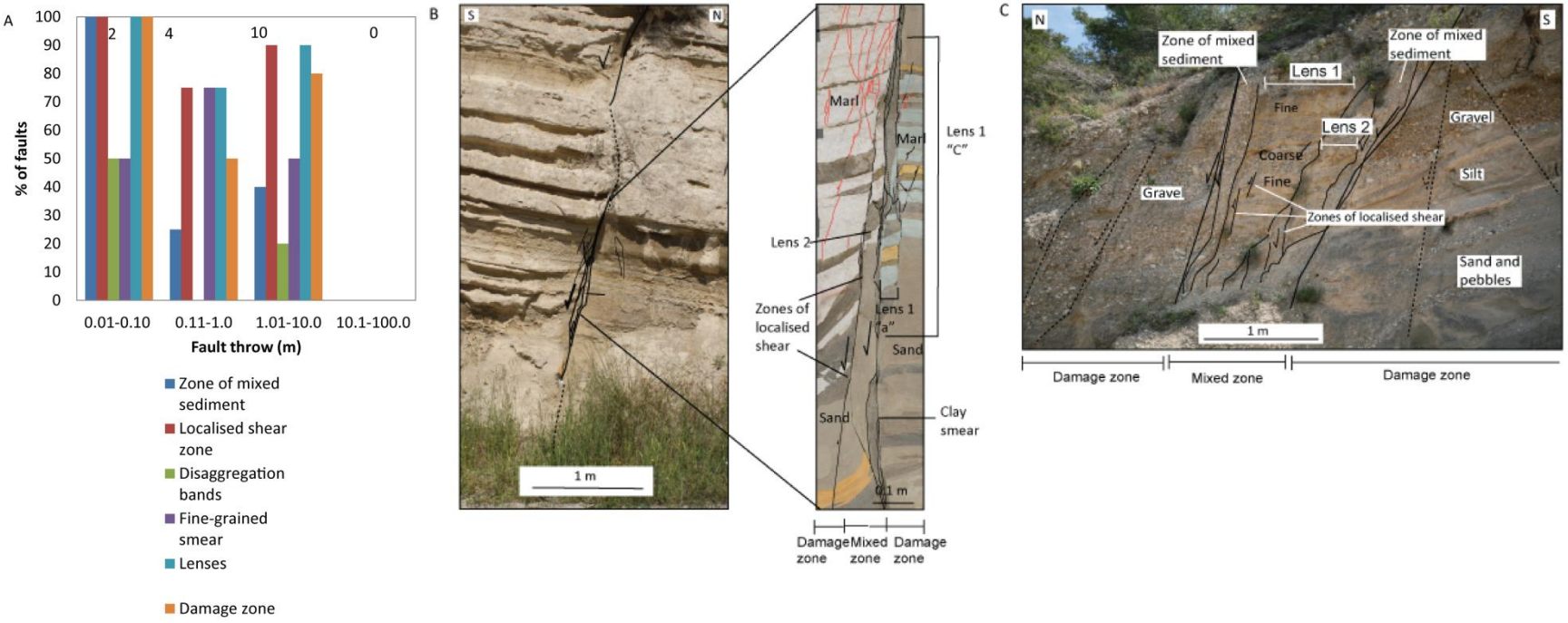

Figure 4.5 Fault zone structure in sediment of contrasting competency. A) Percentage of structural elements with fault throw and total number of faults in the category. B) Fault M3, Pirgos, throw 1.2 m (Figure 2.11), cutting marl inter-bedded with medium to coarse-grained sand. Mixed zone comprises two lenses bound by localised shear zones and a thin clay smear. Lens aspect ratio parameters "c" and "a" shown for lens 1. Disaggregation bands stained with iron oxide precipitate comprise the hangingwall damage zone. In the close-up to the right colours are enhanced for clarity. C) Fault 4, Akrata, throw >7 m (Figure 2.6), cutting coarse gravel conglomerates with thin beds (~0.1 m) of silt in the footwall, and gravel conglomerate in the hangingwall. Mixed zone is dominated by lenses of cohesive silt and gravel conglomerate bound by localised shear zones. The mixed zone itself is bound by zones of mixed sediment.

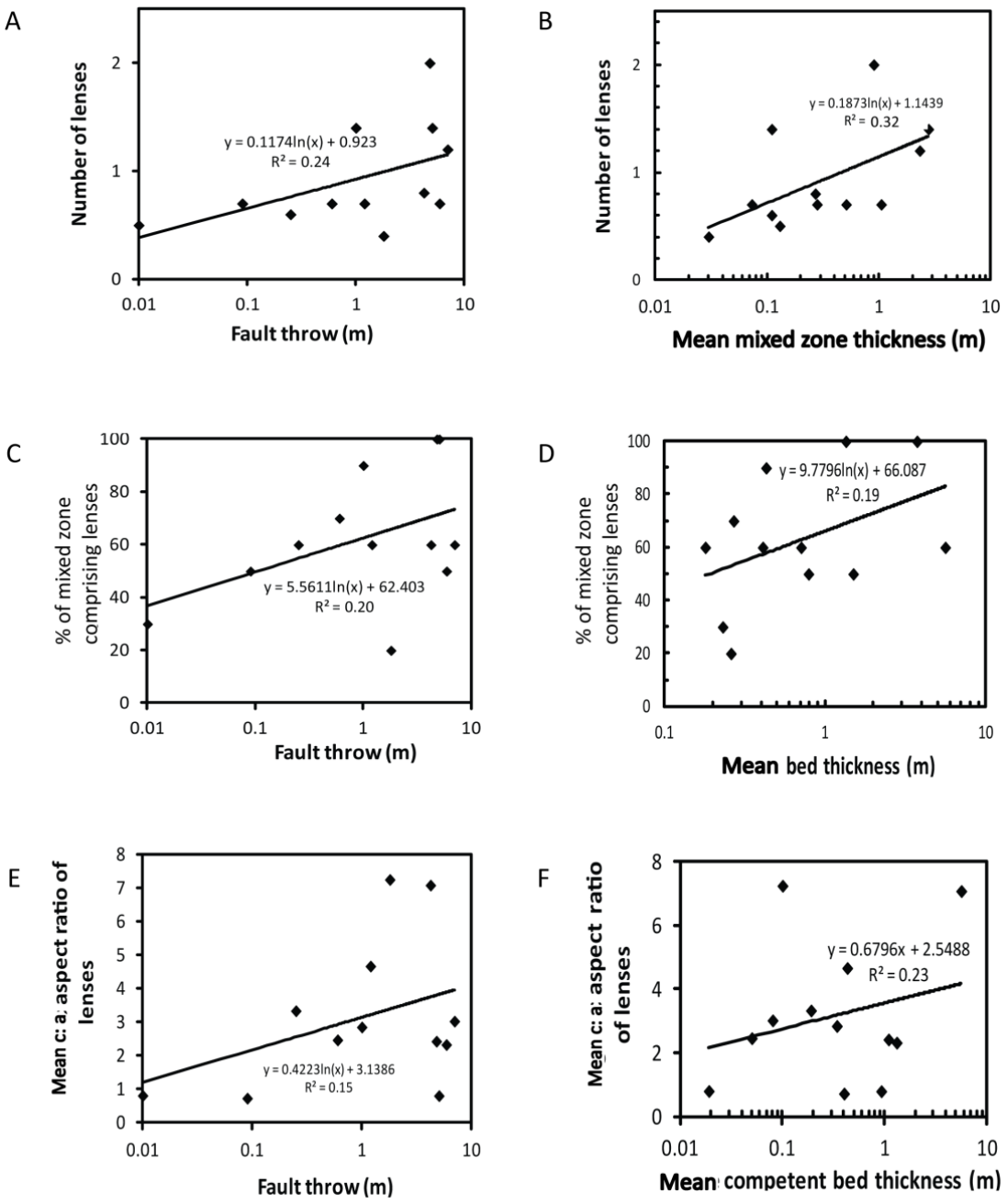

Figure 4.6 Lens attributes with fault and bed size attributes in sediment of contrasting competency. A) Number of lenses across the mixed zone and fault throw. B) Number of lenses across the mixed zone and mean mixed zone thickness. C) Percentage of mixed zones comprising lenses and fault throw. D) Percentage of mixed zones comprising lenses and mean bed thickness. E) Mean lens aspect ratio (c: a) with fault throw. E) Mean lens aspect ratio (c: a) with mean competent bed thickness.

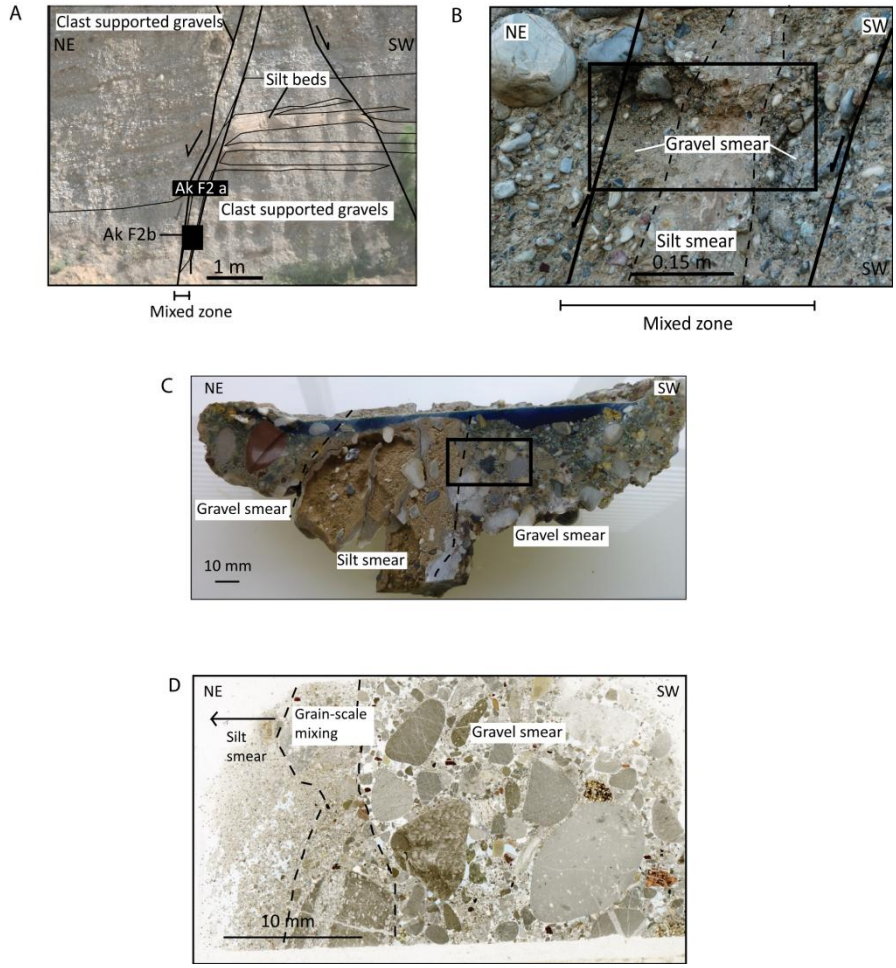

Figure 4.7 Fine-grained silt-smear in the mixed zone of Fault 2, Akrata (Figure 2.6). A) Fault 2 exposed in outcrop with location of hand sample Ak F2a (and Ak F2b). B) Silt-smear in the mixed zone of Fault 2, black box shows location of Ak F2a. C) Hand specimen of silt-smear and gravel smears sliced perpendicular to fault strike (box in B). D) Scanned thin section showing the thin zone of mixed sediment contact between silt and gravel smear (box in C).

Fine-grained smears were found in 56% of mixed zones of faults cutting sediment of contrasting competency. There was no correlation in the occurrence of fine-grained smears with fault throw (Figure 4.5a). Fine-grained smears encompass both clay (Figure 4.5b) and silt smears (Figure 4.7). Clay smears generally form a thin surface veneer of clay grains along localised shear zones, such as between the lenses of Fault M3, Pirgos (Figure 4.5b). These were only found in mixed zones of faults cutting fine-grained marls. Silt smears are similar to the rotated and attenuated beds in mixed zones, described in Chapter 3. However, silt-smears generally form more continuous smears along the fault-dip than coarser-grained

smears, for example Fault 2, Akrata (Figure 4.7). At macro and micro-scales the silt smear in Fault 2, Akrata, appears to be minimally mixed at the grain-scale with the adjacent gravel smear (Figure 4.7).

Localised shear zones were found in 88% of mixed zones cutting sediment of contrasting competency, there does not appear to be a correlation with fault throw (Figure 4.5a). These localised shear zones were primarily found in fine-grained sand and marl, and often bound sediment lenses (Figures 4.5b and c). Slip-surface cataclasites were not found in fault zones cutting sediment of contrasting competency.

Only 44% of mixed zones in faults cutting sediment of contrasting competency have zones of mixed sediment, and on average these comprise <35% of the mixed zone area (Figure 4.5). Zones of mixed sediment can flank lenses in the mixed zone (Figure 4.5c) though are rarely found in combination with localised shear zones or fine-grained smears. Apart from the two faults with throws 0.01 to 0.1 m, there is a slight increase in the percentage of faults with zones of mixed sediment with fault throw, from 25 to 55% (Figure 4.5a).

Damage zones were found in 75% of fault zones cutting sediment of contrasting competency, though there is again no apparent trend in damage zone occurrence with fault throw (Figure 4.5a). Subsidiary faults are the most common structural element in the damage zone. Disaggregation bands are present in the damage zones of faults cutting fine-grained sediment, such as the Disaggregation Band Fault, Voutsimos, with 0.09 m throw (Figure 4.8). The porosity of the sampled disaggregation band is greater than the protosediment, and it could therefore be a dilation band (Figure 4.8d). However, the Disaggregation Band Fault itself is probably a subsidiary fault in the damage zone of the Big Fault, Voutsimos (Figure 2.8). In M3, Pirgos, iron-oxide staining also highlights possible disaggregation bands (Figure 4.5b).

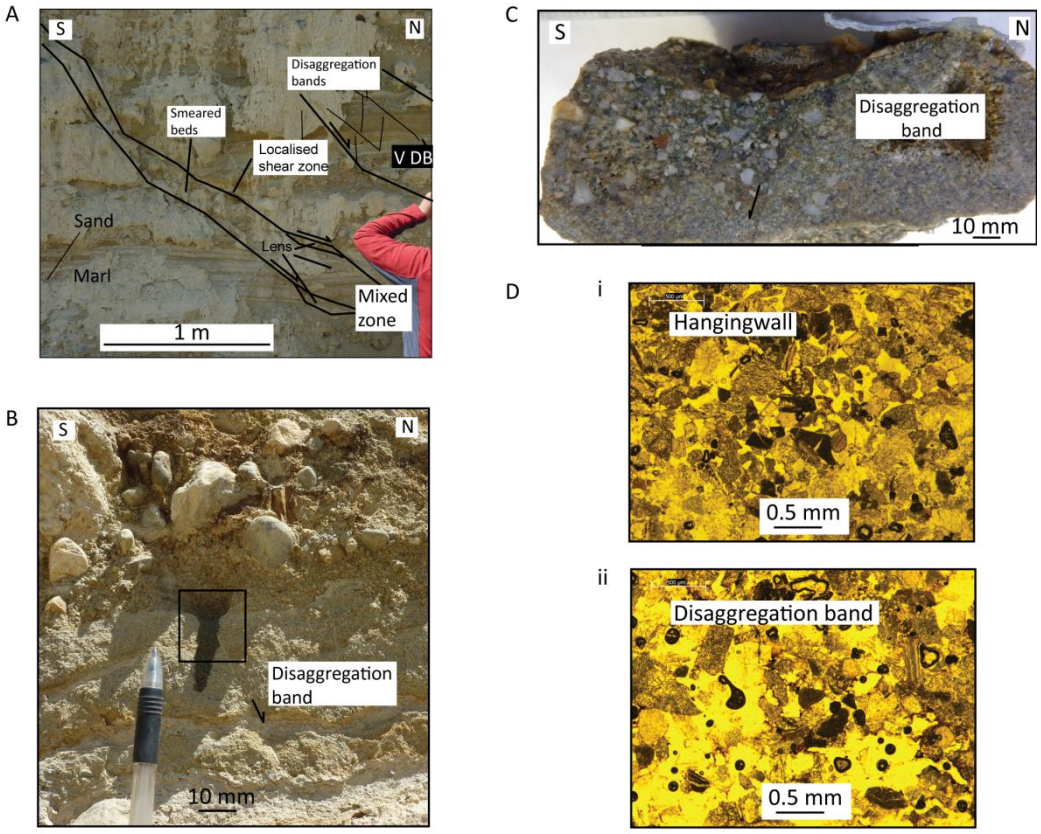

Figure 4.8 Disaggregation band in the damage zone of the Disaggregation Band Fault, Voutsimos, cutting sediment of contrasting competency (Figure 2.8). A) Disaggregation Band Fault with disaggregation bands in the damage zone and location of hand sample V DB. B) View of the disaggregation band in hand sample V DB in outcrop, in fine-grained sand. C) Hand sample V DB sliced perpendicular to the disaggregation band, showing the disaggregation band offset (arrow). D) Photomicrographs under plane-polarised light, showing differences in porosity between the hangingwall protosediment (i) and the disaggregation band (ii).

4.3.3 Faults zones juxtaposing fine and coarse-grained sediment

Faults in the third fault zone category, across which fine and coarse-grained sediments are juxtaposed, are found at the Voutsimos and Mentourgianika outcrops (Figure 2.2), proximal to the transition from the fine-grained silt and marl (sometimes inter-bedded with coarse sand and gravel debris flow deposits) of the Aiges Formation or Giant Gilbert-type delta bottomset and foreset deposits, to coarse-grained Giant Gilbert-type delta gravel conglomerate. The stratigraphic circumstances in the Gulf of Corinth rift results in the footwall comprising fine-

grained sediment and the hangingwall coarser-grained sediment. All three of these faults had throws >17 m (Figure 4.9; Appendix 1).

The structure of fault zones across which fine and coarse-grained sediment is juxtaposed differs somewhat from faults in poorly lithified and sediment of contrasting competency (Figure 4.9). Most notably, in these fault zones, coarse-grained hangingwall and fine-grained footwall sediment is separated by a discrete contact, such as a localised shear zone or fine-grained smear (Figures 4.9b and c). In the Gravel-marl Fault, Mentourgianika, relatively thick (~0.1 m) slip-surface cataclasite provides a discrete boundary between the hangingwall gravel conglomerate and footwall marl (Figure 4.9c). The microstructure of this cataclasite differs to the slip-surface cataclasite from G1, Pirgos (Figure 4.4), as it comprises well-sorted angular grains of coarse-sand grade, supported by a fine-grained matrix. A high proportion of grains are visibly fragmented (Figure 4.9c ii to iv).

The structure of the mixed zone differs either side of these discrete boundaries (Figures 4.9b and c). Fine-grained sediment in mixed zones adjacent to the footwall is cut by many localised shear zones, sometimes forming lenses. In this zone beds can also be rotated in the direction of fault dip (Figure 4.9c). Deformation in coarse-grained sediment adjacent to the hangingwall is distributed through rotated and smeared beds. Towards the centre of the mixed zone these can form zones of mixed sediment (Figures 4.9). With the exception of disaggregation bands, all mixed zone structural elements were found in at least two of the three faults juxtaposing fine and coarse-grained sediment (Figure 4.9a). Damage zones comprised a high density of synthetic and antithetic subsidiary faults (Figure 4.9b). Disaggregation bands, possibly including the sample in Figure 4.8, were also found cutting fine-grained footwall sediment throughout the damage zone of Big Fault 1, Voutsimos (Figure 4.9b).

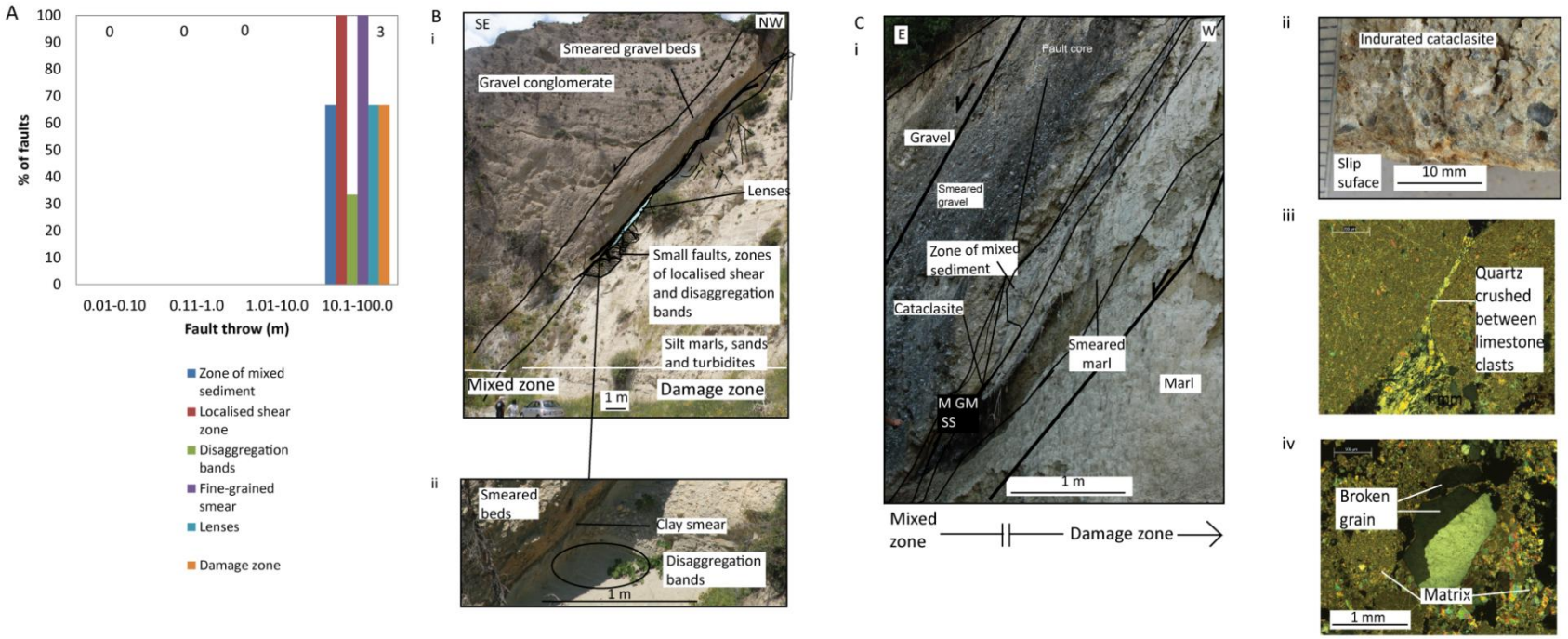

Figure 4.9 Fault zone structure of faults juxtaposing fine and coarse-grained sediment. A) Percentage of structural elements with fault throw and total number of faults in the category. B) Big Fault, Voutsimos, fault throw 23 m (Figure 2.8). i) Fault exposure with separate hangingwall and footwall sides of the mixed zone. Subsidiary faults and disaggregation bands in the damage zones. ii) Discrete contact between fine and coarse-grained sediment in the mixed zone. C) i) Gravel-marl Fault, Mentourgianika, throw 40 m (Figure 2.9) with separate hangingwall and footwall sides of the mixed zone and location of hand sample M GM SS. ii) Indurated slip-surface cataclasite sample (M GM SS, in i), perpendicular to the fault strike. iii) Photomicrograph under cross-polarised light from hand specimen M GM SS with a quartz grain crushed between two limestone clasts. iv) Fragmented quartz grain and fine-grained matrix in the cataclasite.

4.3.4 Mixed zone thickness and fault throw

Faults in the five exposed outcrops have throws ranging four orders of magnitude and mean mixed zone thickness ranging three orders of magnitude (0.1 to 80 m and 0.03 m to 2.6 m) (Figure 4.10). Mean, maximum and minimum mixed zone thicknesses are positively correlated with fault throw. The correlation coefficient for faults cutting poorly lithified sediment is relatively high (R^2 = 0.46 to 0.61), but very low for faults cutting sediment of contrasting competency (R^2 = 0.12 to 0.18) (Figures 4.10a to c). For faults cutting sediment of contrasting competency there is a slightly stronger correlation coefficient (R^2 = 0.35) between mixed zone thickness and fault throw: mean bed thickness, than fault throw alone (Figure 4.10d). The two faults in which fine and coarse-grained sediment are juxtaposed across the fault zone plot either side of the line describing the trend for faults in poorly lithified sediment (Figures 4.10a to c).

The mean and maximum mixed zone thickness for faults cutting poorly lithified sediment and sediment of contrasting competency were similar at <0.3 m throw (Figure 4.10a and b). However, the minimum mixed zone thickness at these throws is thinner for faults cutting sediment of contrasting competency than for faults cutting poorly lithified sediment (Figure 4.10c). The gradients of the trendlines for mean and minimum mixed zone thickness with fault throw are steeper for faults cutting poorly lithified sediment than sediment of contrasting competency. The fault throw/ mixed zone thickness trend gradient is steeper for minimum than maximum values (Figures 4.10b and c). The mixed zone thickness/ throw relationship is most strongly correlated for throws between 1 and 10 m (Figures 4.10a to c). Mixed zone thickness range along-dip of each fault varies between 0.01 and 2 m, and increases with fault throw for faults cutting poorly lithified and sediment of contrasting competency (Figure 4.10e).

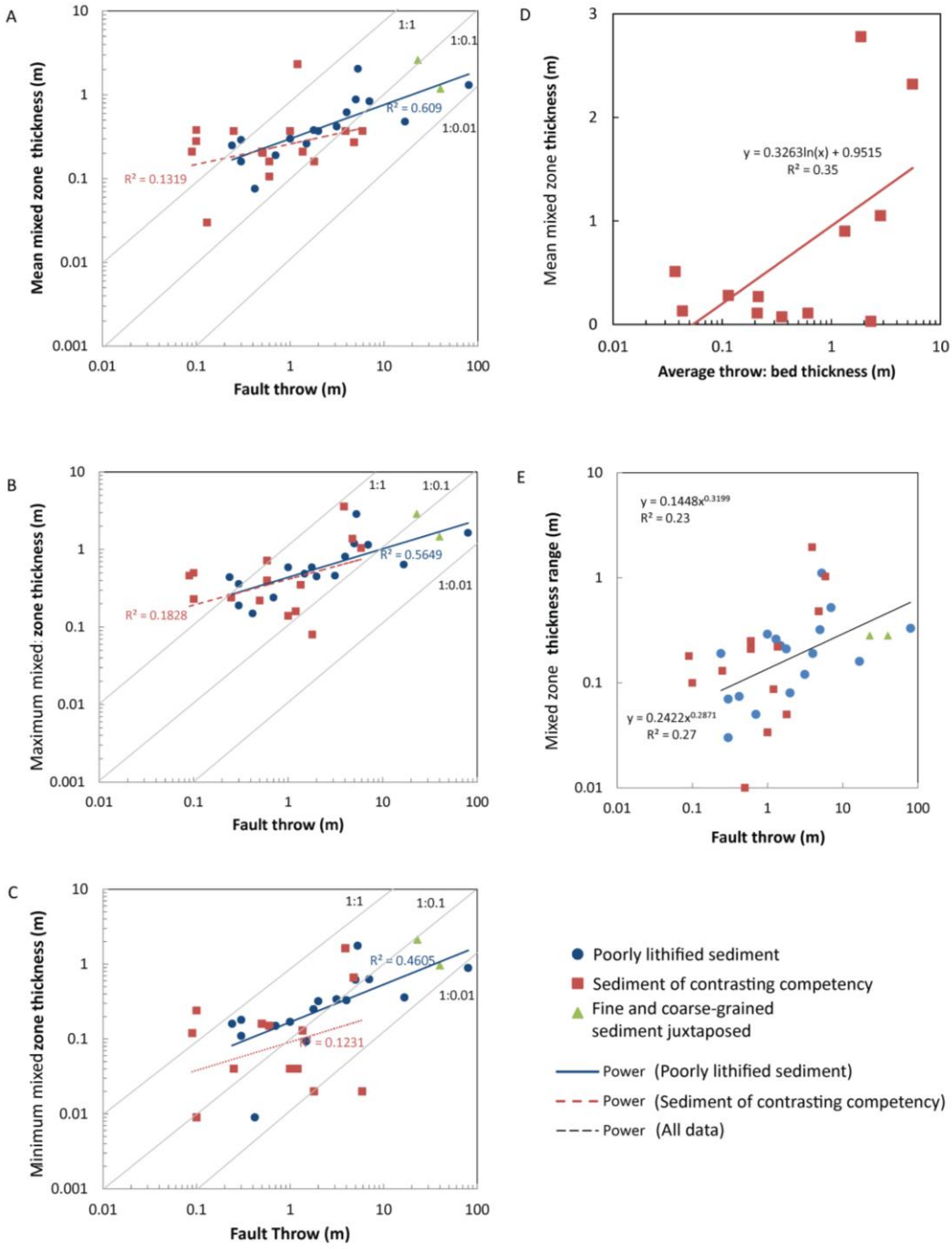

Figure 4.10 Mixed zone thickness and range with fault throw for 32 faults. A) Fault throw and mean mixed zone thickness. B) Fault throw and maximum mixed zone thickness. C) Fault throw and minimum mixed zone thickness. D) Mean mixed zone thickness and throw: bed thickness for faults cutting sediment of contrasting competency. E) Mixed zone thickness range along-dip, with fault throw.

4.4 Fault population attributes

Trends fitted to the fault throw cumulative distributions for faults exposed in the Loutraki and Mentourgianika outcrops have power-law exponents of -0.49 and -0.62 respectively, correlation coefficients are 0.68 and 0.92 (Figure 4.11a). The remaining outcrops do not have sufficient data to identify such trends. Faults with small and large throws plot below the trendline. At ~4 m (Loutraki) and 1.5 m (Mentourgianika) throw there are discontinuities in the fault throw population distribution. Above and below these points two trendlines with different gradients were fitted to the data, with power-law exponents of -0.2 (smaller throws) and -0.59 to -2.2 (larger throws). The mean correlation for these separate trend lines (R^2 for Loutraki is 0.94, Mentourgianika is 0.98) is greater than the single trendline describing each dataset. There is a similar trend in the mixed zone thickness cumulative distribution, with power-law exponents between -1.03 and -1.11 (R^2 between 0.86 and 0.92). Faults with small and large mixed zone thicknesses plot below this trendline. Bi-fractal distributions were fitted to these trends at ~0.2 m and 0.8 m thickness, with power-law exponents of between -0.56 and -0.64 (thin faults) and -1.12 and -2.88 (thick faults). This strengthens the overall correlation for Akrata and Mentourgourianika (R^2 = 0.97 and 0.90), but weakens it for Loutraki (R^2 = 0.90).

Fault density in the five outcrops ranges from 0.002 m^{-1} (Pirgos) to 0.7 m^{-1} (Mentourgianika). There is a positive correlation between mean fault throw and fault density for the five outcrop locations (R^2 = 0.89) (Figure 4.11c). Equal-angle stereoplots of fault orientations for each outcrop show that faults exposed in each section tend to have similar strike orientations, but dip in a conjugate arrangement (Figure 4.11c), though maps in Chapter 2 show that there is generally an asymmetrical sense of throw.

Figure 4.11 Fault population characteristics for all five outcrops. A) Fault throw population distribution with logarithm of cumulative frequency for each outctop. B) Mean mixed zone thickness population distribution with logarithm of cumulative frequency for faults in each outcrop. C) Fault density (number of faults m^{-1}) with average fault throw at each outcrop locality and equal-angle stereoplots with poles to planes of mapped faults. The Pirgos outcrop has two stereonets, for the faults in the south (right) and north (left) of the outcrop.

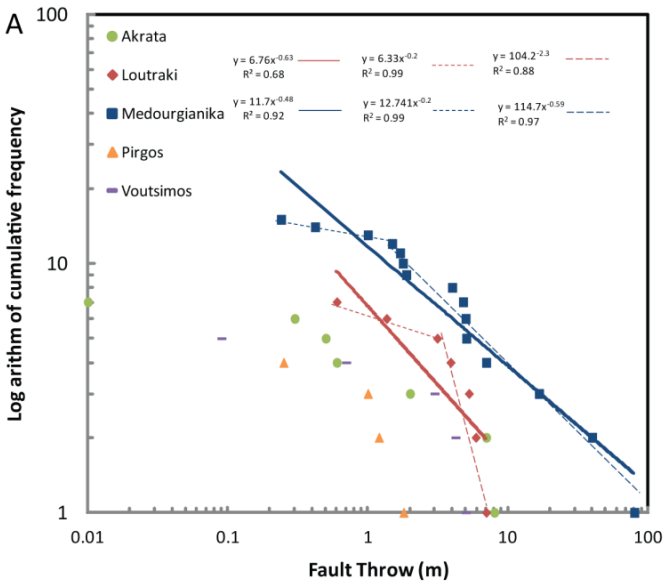
A
Akrata
Loutraki
Medourgianika
Pirgos
Voutsimos
y = 6.76x^-0.63 R² = 0.68
y = 6.33x^-0.2 R² = 0.99
y = 104.2^-2.3 R² = 0.88
y = 11.7x^-0.48 R² = 0.92
y = 12.741x^-0.2 R² = 0.99
y = 114.7x^-0.59 R² = 0.97
Log arithm of cumulative frequency
Fault Throw (m)
100
10
1
0.01
0.1
1
10
100

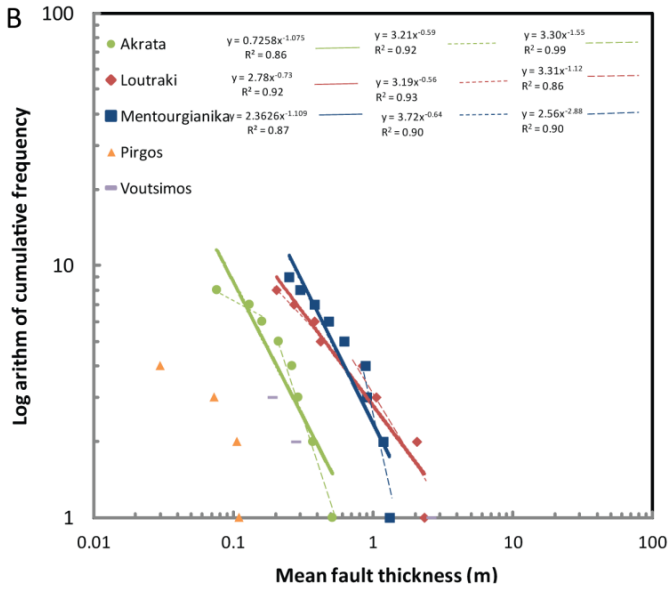
B
Akrata
Loutraki
Mentourgianika
Pirgos
Voutsimos
y = 0.7258x^-1.075 R² = 0.86
y = 3.21x^-0.59 R² = 0.92
y = 3.30x^-1.55 R² = 0.99
y = 2.78x^-0.73 R² = 0.92
y = 3.19x^-0.56 R² = 0.93
y = 3.31x^-1.12 R² = 0.86
y = 2.3626x^-1.109 R² = 0.87
y = 3.72x^-0.64 R² = 0.90
y = 2.56x^-2.88 R² = 0.90
Log arithm of cumulative frequency
Mean fault thickness (m)
100
10
1
0.01
0.1
1
10
100

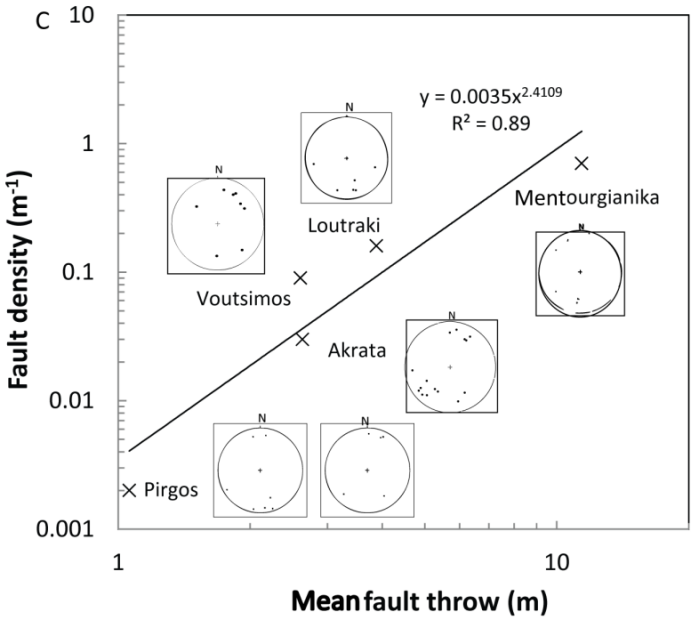
C
y = 0.0035x^2.4109
R² = 0.89
Mentourgianika
Loutraki
Voutsimos
Akrata
Pirgos
N
Fault density (m⁻¹)
Mean fault throw (m)
10
1
0.1
0.01
0.001
1
10

4.5 Fault zone structure and evolution

Fault zone structure and evolution are now discussed for the three fault categories – poorly lithified sediment, sediment of contrasting competency and faults across which fine and coarse-grained sediments are juxtaposed – in light of the findings from across all five outcrops. The models of fault zone structure and evolution proposed in Chapter 3 (Figure 3.9) are evaluated.

4.5.1 Fault zone structure and evolution in poorly lithified sediment

Fault zone structure, in particular the widespread occurrence of zones of mixed sediment, in fault zones cutting poorly lithified sediment, is similar to the structure of fault zones exposed in the Loutraki outcrop, described in Chapter 3. Whilst all three faults with 10 to 100 m throw have zones of mixed sediment, they are also prevalent in fault zones with smaller throws. Based on the model presented in Figure 3.9 an increase in the proportion of fault zones with zones of mixed sediment might be expected with an increase in fault throw, due to the greater likelihood of fault throw exceeding bed thickness, thus allowing substantial grain-scale mixing (Chapter 3; Mozley and Goodwin, 1995; Heynekamp *et al.,* 1999). This demonstrates the importance of individual bed thickness and possibly other processes, in addition to fault throw, for developing zones of mixed sediment.

Mean plunge and plunge orientation of bladed clasts in the mixed zones differ from those in the protosediment, and are either more closely aligned with fault dip direction, or have a lower spherical variance (Figure 4.2). Similar to the Loutraki outcrop, this grain-shape preferred clast alignment with fault dip indicates clast rotation in mixed zones (Figure 3.2). This, in addition to the grain-scale mixing required to form zones of mixed sediment, suggests that particulate flow functions as the dominant deformation mechanism throughout a range of faults with different throws and lithology (Figure 3.9b).

This idea is supported by the correlation between mixed zone thickness and fault throw (Figures 4.10a to c). The scatter in this relationship could result from sampling error, sampling bias and outcrop limitations, or for mechanical reasons such as overlapping and linking faults, specific tectonic settings and stress regimes or lithology (Marrett and Allmendinger, 1991; Walsh *et al.,* 1998; Heynekamp *et al.,*

1999; Minor and Hudson, 2006; Torabi and Berg, 2011). The slightly greater minimum mixed zone thickness in faults cutting poorly lithified sediment with <1 m throw, than those cutting sediment of contrasting competency (Figure 4.10a to c), might reflect the coarse grain-size of these faults cutting poorly lithified sediment and the wider distribution of strain (Needham *et al.,* 1996; Heynekamp *et al.,* 1999; Minor and Hudson, 2006).

The significant increase in the apparent proportion of clasts broken in situ in the mixed zones of Fault 3 (Akrata), and the Terrace Fault (Mentourgianika), than their corresponding protosediment suggests that cataclasis has contributed to strain accommodation in these mixed zones (Figure 4.3). The coarse grain-size of this gravel possibly contributes to the prevalence of cataclasis due to residual intra-clast weaknesses and greater stress concentrations at clast-clast contacts (Balsamo and Storti, 2010). It is likely that cataclasis is not detected in the broken-grain counts of Cement Fault 2 (Mentourgianika) because it has a small throw compared to the other two faults (1 m compared with 7 and 80 m). This supports the fault zone evolution model presented in Figure 3.9b, that cataclasis increases with fault throw and mixed zone evolution.

Importantly, localised shear zones in the form of slip-surface cataclasites (e.g. Tueckmantel *et al.,* 2010), comprised of a high proportion of angular and fragmented grains, were found in some faults with >1.5 m throw (Figure 4.1a and c). These are similar to those described in poorly lithified sands (Balsamo *et al.,* 2008; Balsamo and Storti, 2010), and in high porosity sandstone (Antonellini and Aydin 1994; 1995; Tueckmantel *et al.,* 2010). The specific grain-size characteristics of slip-surface cataclasites investigated by Tueckmantel *et al.* (2010) did not vary once formed. The absence of slip-surface cataclasites in faults with <1.5 m throw (Figure 4.1a), indurated nature, low porosity (Figure 4.4a), and grain-size characteristics established at the time of formation (Tueckmantel *et al.,* 2010), implies that these represent the maximum possible strain hardening from shear accommodation in mixed zone sediment. Slickenlines along the surfaces indicate subsequent strain localisation (slip) along this surface i.e. strain softening (e.g. Fowles and Burley, 1994; Walsh *et al.,* 1998; Rawling and Goodwin, 2006).

While only based on data from four faults, the apparent increase in the number of slip-surface cataclasites with fault throw (Figure 4.4b) reflects findings of Balsamo and Storti (2010) who report multiple slip-surface cataclasites in faults with >20 m displacement. Balsamo and Storti (2010) and Tueckmantel *et al.* (2010) also find an increase in slip-surface cataclasite thickness with fault throw. This suggests that not all fault zone strain will be accommodated along a single slip-surface once it has formed, despite some strain localisation. Grain re-configuration and strain hardening probably continues to some degree in the remainder of the mixed zone, which would allow a repeat of the strain-hardening and softening processes with increased throw (Maltman, 1988). This is supported by the continued increase in mixed zone thickness after slip-surfaces have developed (Figures 4.10a to c). It is possible that slip-surface cataclasites form as a result of instantaneous stress resulting from fault rupture, since instantaneous deviatoric stress can exceed effective normal stress by more than an order of magnitude – particularly under low confining pressures (Hooke, 1995; Similox-Tohon and Sintubin, 2006). In which case, multiple slip-surfaces could indicate successive rupturing events (e.g. Maltman, 1988).

Investigation of fault zone structure in faults with a greater range of throws has revealed an additional stage of fault zone evolution, not identified from the Loutraki outcrop, of slip-surface formation from strain-hardening and subsequent strain softening (Figure 4.12). This substantial change to fault zone structure in larger faults indicates that caution should be taken when extrapolating fault zone structure from small to large faults cutting poorly lithified sediment. Nevertheless, the positive correlation between mixed zone thickness with fault throw is relatively consistent throughout fault zone evolution.

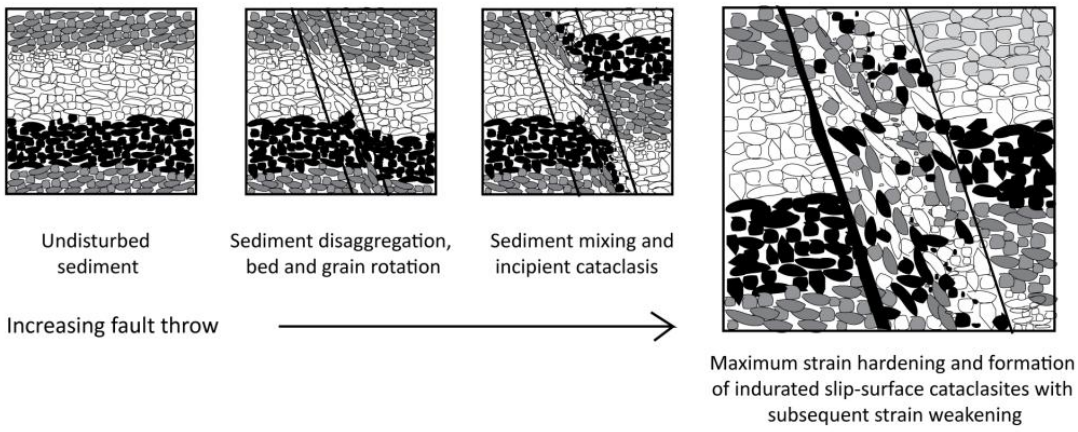

Figure 4.12 Fault zone evolution in poorly lithified sediment with the later stage of slip-surface cataclasite development in faults >1 m throw.

4.5.2 Fault zone structure and evolution in sediment of contrasting competency

As described in Chapter 3.4.2, lenses of relatively undeformed sediment bound by localised shear zones are a major component of fault zones in sediment of contrasting competency (Figure 4.5). Similarly, there is considerably more scatter about the mixed zone thickness/ fault throw trend for faults cutting sediment of contrasting competency than faults cutting poorly lithified sediment (Figures 4.10 a to c). This supports the primary mechanism for mixed zone evolution in sediment of contrasting competency by fault tip bifurcation and asperity removal, as a result of mechanical stratigraphy heterogeneity and differences in strain distribution, rather than particulate flow (Figure 3.9c).

The greatest scatter about the mixed zone thickness/ fault throw trend is found for faults with throws <1 m. The mixed zone thickness/ fault throw: mean bed thickness correlation shown in Figure 4.10d shows the influence of mechanical layer thickness on mixed zone thickness. The decrease in scatter in mean mixed zone thickness for faults with throws >1 m (Figure 4.10a), and the steeper gradient of the minimum than the maximum mixed zone thickness/ fault throw trends (Figures 4.10b and c) might result from the influence of the thickest part of the mixed zone along-dip on overall mixed zone thickness; as fault throw accumulates, more sediment moves past the thickest along-dip point of the mixed zone removing asperities from the mixed zone walls (e.g. Childs *et al.,* 1996b). Therefore small faults would have a greater probability of retaining thin (and potentially leaky) zones than large faults. This

would also be true for faults cutting poorly lithified sediment. Despite this, the absolute range in mixed zone thickness is greater for faults with greater throws, though this reflects absolute thickness, not as a proportion to fault size.

Lens attributes are very weakly correlated with a number of fault and stratigraphic variables (Figure 4.6), revealing the compexities of predicting these attributes (e.g. Kurz *et al.,* 2008). The large range of c: a lens aspect ratios reveals the wide range of lens geometries. The slight increase in lens a: c aspect ratio with mean competent bed thickness (Figure 4.6f) supports the findings by Bastesen *et al.* (2009) and Gross *et al.* (1997) that mechanical strength of sediment or rock is an important control on lens geometry. However, the lower lens aspect ratio in faults with larger throws found by Lindanger *et al.* (2007) was not found in this work (Figure 4.6e). The process of periodic lens size and shape change believed to cause this decrease in lens aspect ratio with fault zone evolution, whereby lenses progressively split into lower order lenses, cannot be said to be a dominant mechanism in the evolution of lenses in these mixed zones.

The mean lens c: a aspect ratio (2.9:1) indicates a tendency for slightly elongate lenses, though these are still more equant than those observed by Lindanger *et al.* (2007) (13:1) in faults of comparable size and lithology. Some of these differences may result from discrepancies in the definitions of lenses since in this investigation extensively deformed sediment was not classified as a lens, which excluded those that had undergone significant stretching or thinning. Nevertheless, differences could also arise from the specific lithology, mechanical stratigraphy, and interactions of extensional, normal and shear stresses.

The geometry, spatial distribution (and whether they occur in isolation, en echelon or in duplexes) and degree of lens deformation, could be an important control on fault hydraulic properties (e.g. Lindanger *et al.,* 2007). However, due to the unpredictability of lens attributes, average values will be used as an approximation in numerical fluid-flow models (Chapter 6). There are, however, problems with this approximation, for example, the average of one lens across the mixed zone at any one point along-dip implies that lenses occur in isolation, yet it was clear from outcrop that lenses more frequently occur en-echelon (Figures 4.5b and c). The creation of lenses, their geometry, and spatial relationships are necessarily

estimations and therefore represent a major uncertainty in fault zone hydrology (Lindanger *et al.*, 2007).

Fine-grained smears, sometimes comprising clay but more commonly silt, were relatively common components of faults cutting fine-grained protosediment. These smears contribute little to total mixed zone volume, yet they could have significant consequences for fault zone hydraulic properties (e.g. Gibson 1998). Clay smears form by grains aligning and sliding past one another (Wojtal, 1996; Heynekamp *et al.*, 1999), which is dependent to a large degree on the platy structure of clay grains. Whilst silt smears do not attenuate as efficiently as clay (Yielding *et al.*, 1997), the thin zone of mixed sediment at the contact between the silt and gravel smears in Fault 2, Akrata (Figure 4.7) suggests grain-scale mixing of silt-smears with surrounding sediment is retarded to some degree. Silt-smears may therefore remain relatively continuous throughout the mixed zone. The limited grain-scale mixing might result from an immiscibility of sediment of different grain sizes, and/ or cohesive fine-grained sediment. The occurrance, continuity and thickness of fine-grained smears is dependent on the grain-size composition of the protosediment cut by the fault (Yielding *et al.*, 1997; Bense *et al.*, 2003).

Zones of mixed sediment are considerably less common in faults cutting sediment of contrasting competency than those cutting poorly lithified sediment (Figure 4.5a). This could be due to the more common structural elements; lenses, localised shear zones, and fine-grained smears, behaving as physical barriers across which sediment is unable to mix at the grain-scale. In addition, as discussed in section 3.4.2.1, if strain is focussed along localised shear zones or in fine-grained smears, significant grain-scale mixing of sediment might not be required in order to accommodate strain. Nevertheless, there is an increase in the proportion of zones of mixed sediment with fault throw, suggesting that grain-scale mixing might increase as these faults evolve (Figure 4.5c).

Overall, in contrast to faults in poorly lithified sediment, there does not appear to be a significant change in fault zone structure or deformation mechanisms with fault throw and evolution in faults cutting sediment of contrasting competency. This suggests a generally self-similar evolution, thus these faults need not be considered as part of a fault size hierarchy. The influence of fault size attributes and stratigraphic

and lithological parameters on the evolution of major fault zone structural elements such as lenses and fine-grained smears supports recommendations by Manzocchi *et al.* (2007) that such fault zones are best characterised by dimensionless ratios between the fault system and sedimentological variables.

4.5.3 Fault zone structure and evolution in faults juxtaposing fine and coarse-grained sediment

Despite only three faults in this category, fault zone structure was unmistakably distinct due to the separation of fine and coarse-grained sediment in the mixed zone across a discrete boundary (Figure 4.9). The division between the two sides of the mixed zone appears to result from an immiscibility of fine and coarse-grained sediment similar to that seen at the boundary of the fine-grained smear in Fault 2, Akrata (Figure 4.7). The differing mixed zone structures either side of this boundary implies each side evolves by separate deformation mechanisms. This type of fault can be expected close to the transitions between different sediment types, as shown in Figure 4.13.

Localised shear zones and lenses in the fine-grained footwall sediment inter-bedded with coarser-grained debris flow deposits reflects deformation by fault-tip bifurcation and asperity removal comparable to mixed zone evolution in sediment of contrasting competency. However, the rotation of fine-grained beds at the mixed zone/ footwall boundary was only found in mixed zones of faults where fine-grained sediment is juxtaposed against coarse-grained sediment. Distributed deformation across the rotated and smeared beds of the coarse-grained hangingwall sediment is likely to form by (controlled) particulate flow, and results in the zones of mixed sediment, similar to faults cutting poorly lithified sediment (Figure 4.9). Slip-surface cataclasite forming the discrete boundary in the Gravel-marl fault, Mentourgianika (Figure 4.9c), indicates that strain hardening and softening can also occur in these mixed zones. The combined fault evolution processes results in many of these fault zones results exhibiting all of the fault zone structural elements (e.g. Figure 4.13).

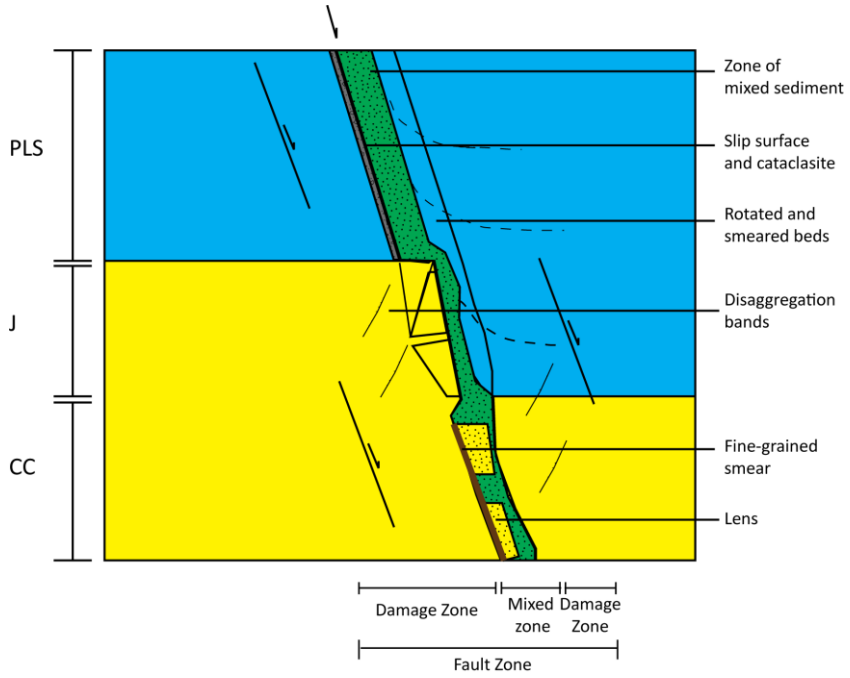

Figure 4.13 Changes to fault zone structure from faults cutting poorly lithified sediment (PLS) to faults in which fine and coarse-grained sediment is juxtaposed (J) and faults cutting sediment of contrasting competency (CC). This model is for a large fault cutting stratigraphy for the southern flank of the Gulf of Corinth rift with additional structural elements reported in this chapter included.

4.5.4 Damage zone structure

Overall, the proportion of faults with damage zones is higher in faults with greater throw (Figures 4.1a, 4.5a and 4.9a). However, this is still less than two thirds of all fault zones. Since faults were attributed damage zones even when the damage zone was not present in all beds, a mean weighted for the proportion of beds that have or do not have damage zones would demonstrate a yet smaller occurrence of damage zones. Similar to the Loutraki outcrop, subsidiary faults were the most common structural element, and disaggregation bands were found in fine-grained sediment. The apparent absence of disaggregation bands in coarse-grained sediment could be due to difficulties differentiating between small subsidiary faults and disaggregation bands from ambiguities in the scale distinctions between the two in coarse sediment (e.g. Exner and Grasemann, 2010), especially since Balsamo *et al.* (2008) suggest that disaggregation bands can be the locus of faults in extensional settings. The increase in porosity of the disaggregation band in Figure 4.8, in comparison to the protosediment, suggests it is probably a dilation band. These form under very low

confining pressures, generally in tensile quadrants of a fault damage zone (e.g. Du Bernard *et al.,* 2002; Balsamo *et al.,* 2008).

4.6 Fault population characteristics

The single power-law trend fitted to the fault throw and mean mixed zone thickness cumulative distributions would indicate a fractal dimension to fault size over the four and three orders of magnitude of sampled fault throw and mixed zone thickness (Figures 4.11a and b) (e.g. Scholz and Cowie, 1990; Needham *et al.,* 1996; Torabi and Berg, 2011). However, the faults with smaller or larger throws or mixed zone thickness plot below this trendline. This could be caused by sample bias known as censoring and truncation, whereby the smallest faults are not always identified, and the sample area may be too small to include the largest faults (e.g. Needham *et al.,* 1996; Nicol *et al.,* 1996; Wojtal, 1996; Yielding *et al.,* 1996; Torabi and Berg, 2011). In addition, in this study, faults were deliberately excluded from the dataset due to difficulties defining their throw and/ or mixed zone thickness, and these tended to be the larger faults.

Departure from the power-law trend could also indicate multi-fractal fault size population distributions (e.g. Wojtal, 1994; Torabi and Berg, 2011). Possible bi-fractal distributions are shown by trendlines with differing power-law exponents. With the exception of the mixed zone thickness for the Loutraki outcrop, these exhibit general improvements in correlation coefficients. Multi-fractal fault size population distributions such as these can imply different deformation mechanisms acting at different fault scales (Gross *et al.,* 1997). In such cases Torabi and Berg (2011) advocate regarding fault populations as hierarchical.

The formation of slip surfaces in faults cutting poorly lithified sediment with throws >1.5 m coincides with the discontinuity in the slope of the fault throw population distribution of the Mentourgianika outcrop. These faults cut only poorly lithified sediment. Speculatively, this correspondence could reflect the development of slip-surface cataclasites. Due to the potential hydraulic importance of slip-surface cataclasites and the fault zone heterogeneity they impart, fault zones cutting poorly lithified sediment with throws greater or less than 1.5 m throw should be considered as part of a hierarchy. Other distinction points (e.g. Loutraki and Akrata) could

reflect specific dimensions of mechanical stratigraphy related to lens development in this region (e.g. Wojtal, 1996; Gross *et al.*, 1997; Wilkins and Gross, 2002) despite no changes in fault zone deformation being identified with fault throw for faults cutting sediment of contrasting competency.

Torabi and Berg (2011) also find that a hierarchical distinction can be made at 1 m and 1.25 m fault throw in a range of fault populations. Distinction points differ between different fault populations, due to structural settings (Scholz and Cowie, 1990; Wojtal, 1996), processes of fault interaction and linkage (e.g. Wojtal, 1996; Gross *et al.*, 1997; Wilkins and Gross 2002), and as shown here, lithology and stratigraphy. An additional fault throw distinction point was reported at 400 m throw (Zygouri *et al.*, 2008) for faults cutting basement rocks in the Corinth rift basin.

All five outcrops were located in regions of high strain relative to other outcrops in the Gulf of Corinth syn-rift sediment, proximal to major crustal-scale faults (Figure 2.2), and therefore the comparatively high fault densities (Figure 4.11c) cannot be extrapolated across the region. Nevertheless, average fault density (<0.7 m^{-1}) is lower than the reported fault densities for many other outcrops, which can have densities of up to 3 m^{-1} (Wojtal, 1996). Under-sampling of faults, for reasons outlined above, will influence the reported fault density, but it could also reflect the mechanical properties of poorly lithified sediment compared to the sandstone and shale sequences that previous fault densities were estimated from (e.g. Nicol *et al.*, 1996).

The conjugate nature of faults exposed in the outcrops implies considerable fault connectivity, with the exception of the Pirgos outcrop that has a low fault density. Fault connectivity would be higher still if there was a greater variation in fault strikes. Apparent fault strike orientations are predominantly perpendicular to outcrop exposures, indicating an element of bias in their measurement.

The positive correlation between fault density and mean fault throw (Figure 4.11c) indicates local strain accommodation both by an increase in fault throw on certain pre-existing faults, and the nucleation of new faults (e.g. Wojtal, 1994; Nicol *et al.*, 1996). The power-law exponent of the fault density/ throw trend (2.4) falls within the range of previous fault population datasets (e.g. 4.0 to 1.0) (e.g. Nicol *et al.*, 1996). The maximum fault throw of 80 m, found in syn-rift sediment is small compared

with the crustal-scale faults of the Corinth rift basin, possibly reflecting a limit on absolute fault size in the syn-rift sediment.

4.7 Summary

Findings presented in this chapter indicate that the models of fault zone evolution and structure for faults cutting poorly lithified sediment and sediment of contrasting competency, identified in Chapter 3, can largely be applied to faults exposed in all five of the Gulf of Corinth rift outcrops. Extension of the fault dataset to incorporate a wider range of geological factors has revealed additional characteristics of fault zone structure and evolution in syn-rift sediment.

Controlled particulate flow is the dominant mixed zone deformation mechanism in faults cutting poorly lithified sediment. This produces zones of mixed sediment and a steady increase in mixed zone thickness, with fault throw. The greater percentage of broken grains in mixed zones of faults with >7 m throw than their protosediment demonstrates the increase in cataclasis with fault throw. Investigations of faults with larger throws show that when strain hardening in the mixed zone reaches its limit indurated slip-surface cataclasites develop. Slip surfaces represent subsequent strain weakening processes in the mixed zone. Slip-surface cataclasites first occur in faults with >1.5 m throw, and could be reflected in bi-fractal fault-size population distributions. Faults cutting poorly lithified sediment should thus be considered to have a fault size hierarchy.

Combinations of fault zone structural elements vary more widely in faults cutting sediment of contrasting competency than faults cutting poorly lithified sediment. Significant scatter around the fault throw/ mixed zone thickness trend for faults cutting sediment of contrasting competency reflects the importance of fault tip bifurcation, asperity removal, and lens formation in the evolution of these mixed zones. There are a wide range of possible controls on lens attributes. Mixed zones cutting sediment of contrasting competency often also comprise localised shear zones and fine-grained smears. Mechanical stratigraphy and fault throw are major controls on fault zone structure and mixed zone thickness.

A third category of fault zone has been identified across which fine and coarse-grained sediment is juxtaposed. These comprise distinct hangingwall and footwall mixed zones, separated by a discrete boundary. These fault zones are likely to comprise all fault zone structural elements. Models of fault zone evolution for poorly lithified sediment and sediment of contrasting competency can largely explain the respective hangingwall and footwall structure of the mixed zones in these faults.

5. The hydraulic properties of fault zones

5.1 Introduction

In this chapter, hydraulic properties i.e. porosity, hydraulic conductivity, and anisotropy, of fault zones exposed at the five outcrop locations in the Gulf of Corinth rift are estimated. These properties are compared with their undeformed protosediment. Porosity was calculated by thin section image analysis, and hydraulic conductivity estimated from porosity and grain-size distributions, using empirical equations. Anisotropy was estimated from the tortuosity of fluid-flow pathways through sediment. The impact of lithology and fault throw on fault zone hydraulic properties is considered.

Chapters 3 and 4 recorded differences in sediment properties between fault zones and undeformed protosediment. Deformation by controlled particulate flow can result in a decrease in grain-size, sorting and changes in grain-shape, roundness and packing (Figure 4.12). These changes can alter sediment porosity and pore connectivity, and thus impact intrinsic permeability (k).

Hydraulic conductivity (K) is a measure of the ease with which a fluid moves through a rock or sediment:

$$K = k\frac{\rho g}{\mu} \qquad \textbf{Equation 5.1}$$

Where k is the intrinsic permeability of a rock or sediment, ρ the fluid density, g acceleration due to gravity, and μ the viscosity of the fluid in question. K can be determined directly by:

a) Hydraulic pumping and injection tests in the field (e.g. Giurgea *et al.*, 2004).

b) In-situ permeability measurements of outcrop exposures using air permeameters (e.g. Sigda *et al.*, 1999; Rawling *et al.*, 2001).

c) Laboratory permeameter experiments on sample cores (e.g. Evans *et al.*, 1997; Bense *et al.*, 2003).

However, these methods could not be used in this investigation because:

a) Well-test data and equipment were not available.

b) The coarse grained sediment exposed in outcrops made exposure surfaces too rough for field based air permeametry, and the high hydraulic conductivities exceeded pump volume.

c) Sediment samples could not be obtained without in-situ resin impregnation, which would prevent subsequent permeameter experiments.

As a result, hydraulic conductivity has been estimated indirectly using empirical equations based on the physical properties of sediment (e.g. Masch and Denny, 1966; Beard and Weyl, 1973; Shepherd, 1989; Van den Berg *et al.*, 2003).

The changes to porosity and hydraulic conductivity resulting from grain-scale deformation processes are quantified here for seven fault zones comprising apparently homogeneous zones of mixed sediment (e.g. Figure 4.1), that cut either sand or gravel (Table 5.1). Porosity and grain-size was assessed by digital image analysis of thin sections, following the method outlined by Van den Berg *et al.* (2003). Hydraulic conductivity is estimated from these data using the Kozeny-Carman equation which includes a porosity parameter (Bear, 1972 in Freeze and Cherry, 1979). Since two-dimensional porosity and grain-size are not necessarily representative of these properties in three dimensions measured characteristics will be considered as apparent and used primarily as comparisons with other samples in this work (Bouabid *et al.*, 1992; Francus, 1998; Van den Berg *et al.*, 2003).

The porosity and hydraulic conductivity of zones of mixed sediment and corresponding protosediment were compared directly for four faults in which beds cut by the faults could be traced directly into the mixed zone; two in gravel (Mentourgianika Fault An and Akrata Fault 3) and two in sand (Mentourgianika Fault 11 An and Akrata Small Fault (SF)) (Table 5.1). The porosity and hydraulic conductivity of three other fault zones cutting gravel and comprising zones of mixed sediment were also calculated (Akrata Fault 1, Mentourgianika Terrace Fault and Cement Fault 2) along with two slip-surface cataclasites (Pirgos Fault G1 and Mentourgianika Gravel-Marl Fault), a fine-grained smear (Akrata Fault 2) and two disaggregation bands (Mentourgianika Fault 11 Antithetic and Voutsimos Disaggregation Band Fault) (Table 5.1). The variability in estimates of porosity and hydraulic conductivity of mixed zones due to differences in fault throw (between 0.1 and 80 m) were investigated.

Thin section ID	Structural element	Hand sample ID	Fault ID	Fault throw (m)	Lithology	Figure
Ak F1 MZ	Zone of mixed sediment	Ak F1	Fault 1	0.5	Gravel	2.6
Ak SF (FW)	Footwall	Ak SF	Small fault	0.01	Sand	2.6
Ak SF (MZ)	Zone of mixed sediment					
Ak SF (HW)	Hangingwall					
Ak F2a FZ (S)	Silt-smear	Ak F2a FZ	Fault 2	2	Gravel and silt	4.7 & 5.8
Ak F2a FZ (M)	Zone of mixed sediment					
Ak F2a FZ (P)	Gravel smear					
Ak F2b MZ	Zone of mixed sediment	Ak F2b FZ				
Ak F3a FW	Footwall	Ak F3a FW	Fault 3	7	Gravel	4.2b & 4.3 a
Ak F3b MZ	Zone of mixed sediment	Ak F3b FZ				
Ak F3c MZ	Zone of mixed sediment	Ak F3c FZ				
V DB (FW)	Footwall	V DB	Disaggregation band fault	0.09	Sand	4.8
V DB (DB)	Disaggregation band					
V DB (HW)	Hangingwall					
M F11 An (FW)	Footwall	M F11 An	F 11 Antithetic	0.1	Sand	2.10.
M F11 An (HW)	Hangingwall					
M F11 An (MZ)	Zone of mixed sediment					
M F11 An (DB)	Disaggregation band					
M F11 An (FW B)	Footwall					
M GM SS a	Slip-surface cataclasite	M GM SS a	Gravel/marl fault	40	Gravel	4.9c
M GM SS b	Slip-surface cataclasite	M GM SS b				
M TF MZ	Zone of mixed sediment	M TF FZ	Terrace Fault 1	80	Gravel	4.3b
M An FW a	Footwall	M An FW	An	1.49	Gravel	4.1b
M An FW b	Footwall					
M An MZ a	Zone of mixed sediment	M An FZ				
M An MZ b	Zone of mixed sediment					
M CF 2a MZ	Zone of mixed sediment	M CF 2 FZ a	Cement fault 2	1	Gravel	4.3c
M CF 2b MZ	Zone of mixed sediment	M CF 2 FZ b				
P G1 SS	Slip-surface cataclasite	P G1 SS	G1	40	Gravel	4.1c

Table 5.1 Details of image analysis samples, including the original fault, fault throw, and structural element with figures showing sample locations. Ak is Akrata, V is Voutsimos, M is Mentourgianika and P is Pirgos.

Chapters 3 and 4 show that in heterogeneous sediment, development of lenses and smears cause bed reconfiguration in mixed zones, producing heterogeneities and anisotropies. Mixed zone hydraulic heterogeneity is addressed in this chapter by mapping hydraulic conductivity across the fault zone and protosediment. Thin section image analysis could not be used for this due to the high density of sampling required to map hydraulic conductivity across these complex fault zones. Hydraulic conductivity was calculated using grain-size distributions and the Krumbein and Monk (1942) empirical equation. Alterations to sediment porosity due to mixed zone

processes were not explicitly accounted for in this analysis, though Van den Berg *et al.* (2003) suggest that the use of grain-size in empirical equations can account for some changes to porosity due to the dependency of sediment packing on the grain-size distribution. Fault zone heterogeneity was assessed for three faults cutting heterogeneous sediments exposed at the Loutraki outcrop (Fault 1A, Fault 1C and Fault 5 in Figures 3.1a, c and 3.7) and one with a fine-grained smear exposed at the Akrata outcrop (Fault 2 in Figure 4.7).

In mixed zones, hydraulic anisotropy, which is the difference in hydraulic conductivity with the orientation of measurement, can result from the orientation of structural elements such as slip-surface cataclasite or bed smears (Bense and Person, 2006). Preferential alignment of non-spherical clasts (Figures 3.2 and 4.2) can also cause hydraulic anisotropy by causing differences in flow-path tortuosity perpendicular and parallel to the direction of clast alignment (Arch and Maltman, 1990). Flow path tortuosity is estimated from three photographs of clasts in mixed zones and adjacent protosediment for Loutraki Fault 1A and Fault 5, and Akrata Fault 3, and used to estimate hydraulic anisotropy.

5.2 Estimating sediment hydraulic properties

5.2.1 Estimating porosity and grain-size from thin section image analysis

Sixteen hand samples were taken from hand samples and undeformed protosediment (Table 5.1). Samples were sliced perpendicular to fault strike. Thin sections were made from parts of hand samples that appeared representative of overall hand sample properties (Table 5.1). Some specific small-scale features were targeted for thin sections, including thin zones of mixed sediment cutting sand and disaggregation bands (Ak SF MZ, M 11 An and V DB), and the thin zone of mixed sediment between the fine-grained smear and gravel smear in sample Ak F2a FZ (Table 5.1).

Photomicrographs were taken of randomly selected regions of each of the 29 thin sections. Microscope magnifications of two or four were used depending on the dominant grain-size. For the coarsest gravel samples (M An FW and MZ) a high resolution scan was also made of the whole thin section (Figure 5.1). Photomicrographs were taken under both plane-polarised and cross-polarised light.

The image with the greatest colour contrast between pores and grains was used for image analysis. Photographs were imported into the image analysis freeware ImageJ (Rasband, 2011), and a scale attached. For each image the software was manually trained to identify blue (dyed resin) or white (resin without dye) pixels for photographs taken under plane-polarised light, and black pixels for photographs taken under cross-polarised light, as pore spaces. ImageJ then reclassified the whole photomicrograph image into a binary image in which black and white pixels represented grains and pores respectively (Figure 5.1). This image was compared with the original photomicrograph to identify any mis-classifications of pixels which were rectified by re-training the software identification for the whole image, or by manual adjustment in drawing software, until the binary image was of sufficient quality for analysis. The ImageJ watershed tool was used to define and separate pores and grains before analysis of the image. A detailed description of image analysis steps is presented in Appendix 2.

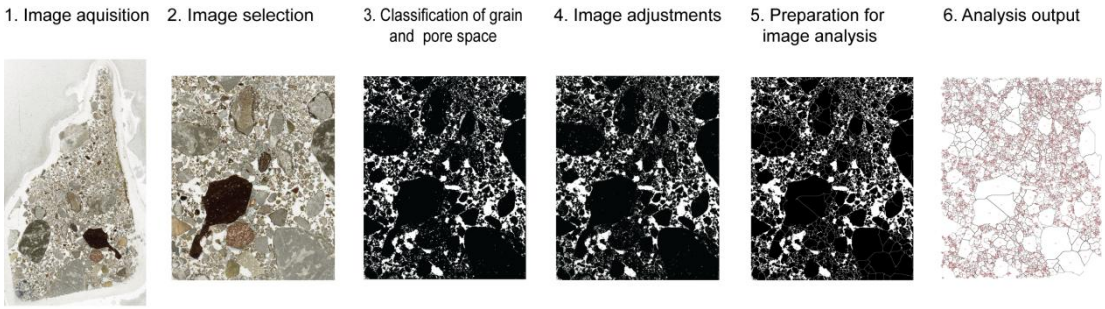

Figure 5.1 Steps of the image analysis procedure for thin sections in ImageJ. 1. Image acquired of thin section. This image is from a scanned thin section however most images were acquired through the microscope. 2. Area of image selected for analysis. 3. Pore spaces and grains classified to produce black and white binary images. 4. Smoothing and sharpening of image, and filling of holes in pore space or grains. This involved small scale changes that are barely visible at the scale of this image. 5. Grain and pore boundaries identified and separated by ImageJ. 6. Size analysis by ImageJ for individual grains and pores. Further details of these steps for the ImageJ software are included in Appendix 2.

Porosity was calculated as an "Area fraction" in ImageJ. This was converted to percentage porosity (n). ImageJ calculated grain-size distributions (number of grains per grain-size fraction) and D_{50} (median grain-size diameter in mm) based on the "Feret Diameter" – the longest distance between any two points along the selection boundary for each grain. Grain-size distributions were converted to grain-size distribution by mass, assuming all grains are spherical, using Equation 5.2:

$$Mass\ of\ class = \left(\frac{4}{3}\ \pi(0.5{D_{50}}^2\right)(\rho g)N_g \qquad \textbf{Equation 5.2}$$

Where ρ is the grain density (average of 2631 kg m^{-3} for crustal rocks), g is acceleration due to gravity (9.81 m s^{-1}), N_g is the total number of grains in the class fraction. Grain-size sorting parameters were calculated from the grain-size distributions.

5.2.2 Estimating hydraulic conductivity from empirical equations

Intrinsic permeability (k) was calculated from thin section porosity and average grain-size using the Kozeny-Carman equation:

$$k = \left[\frac{n^3}{(1-n)^2}\right]\left(\frac{d_{50}^2}{180}\right) \qquad \textbf{Equation 5.3}$$

where k is in darcies, and n is fraction porosity (e.g. Freeze and Cherry, 1979; Van den Berg *et al.*, 2003). K was then calculated from k using Equation 5.1 where ρ is the density of water (999.7 kg m^{-3}), and μ is the viscosity of water (1307 x 10^{-6} N s m^{-2}) at 10^{o} C.

It was not possible to use the Kozeny-Carman equation to calculate hydraulic conductivity for grain-size samples since porosity was not known, therefore it was necessary to use methods based on grain-size distributions alone. The applicability of equations developed by Hazen (1911) (cf. Freeze and Cherry, 1979) and Krumbein and Monk (1942), and graphical methods developed by Masch and Denny (1966) and Shepherd (1989), were assessed for these samples. The Masch and Denny (1966) graphical method could not be used because the majority of sampled grain-sizes exceed the grain-size limit on the graph. The Shepherd (1989) graphical method could not be used because sorting characteristics were estimated based on the depositional environment, thus could not account for alterations resulting from fault

zone processes. Estimates of hydraulic conductivity from Hazen's (1911) equation differed considerably to estimates using the other methods. Therefore, the Krumbein and Monk (1942) equation:

$$k = b(D_{50})^2 e^{-\alpha\sigma\emptyset} \qquad \textbf{Equation 5.4}$$

Where b and α are dimensionless constants of 760 and 1.31 respectively (Krumbein and Monk, 1942), and Ø the sorting parameter, was most appropriate for this purpose. Despite having been developed for moderately well-sorted to extremely well-sorted medium to very coarse-grained sand samples (σØ 0.04 to 0.8, and D_{50}0.42 to 1.68 mm), estimates of hydraulic conductivity for these samples, even in coarse grained, very poorly sorted gravel, reflect typical values suggested in the literature (e.g. Freeze and Cherry, 1979; Hiscock 2005).

5.2.3 Estimating hydraulic anisotropy

Two-dimensional flow path tortuosity was estimated from photographs of two outcrops and a hand sample in which the outlines of clasts were easily distinguishable. Clasts from both the mixed zone and protosediment can be seen in each photograph which reduces disparities in clast identification that may arise from using different images. The photographs were converted to binary images showing clast outlines either manually, or using ImageJ (section 5.2.1). A number of equally spaced vertical, horizontal, fault parallel and perpendicular lines were drawn across each image with length L (Figure 5.2). The tortuous path length (L_T) was measured across the image by hand, beginning at the same start point as the straight lines and traversing the image in the same orientation as each transect, but following the shortest path around clasts, rather than direct line routes (Figure 5.2). Tortuosity (T) was calculated using Equation 5.5 (Arch and Maltman, 1990).

$$T = \frac{L_T}{L} \qquad \textbf{Equation 5.5}$$

Intrinsic permeability influenced by tortuosity can be calculated using Equation 5.6 (Arch and Maltman, 1990):

$$k = C\,\frac{r^2}{T^2} \qquad \textbf{Equation 5.6}$$

where C is a constant and *r* is the mean pore radius. Assuming C and *r* do not vary in the same sediment, permeability anisotropy resulting from tortuosity was determined using Equation 5.7:

$$k_{relative} = \frac{1}{T^2} \qquad \textbf{Equation 5.7}$$

Permeability anisotropy resulting from tortuosity was derived for the vertical/ horizontal, and fault parallel/ fault perpendicular orientations. This was plotted as permeability ellipses over the original images.

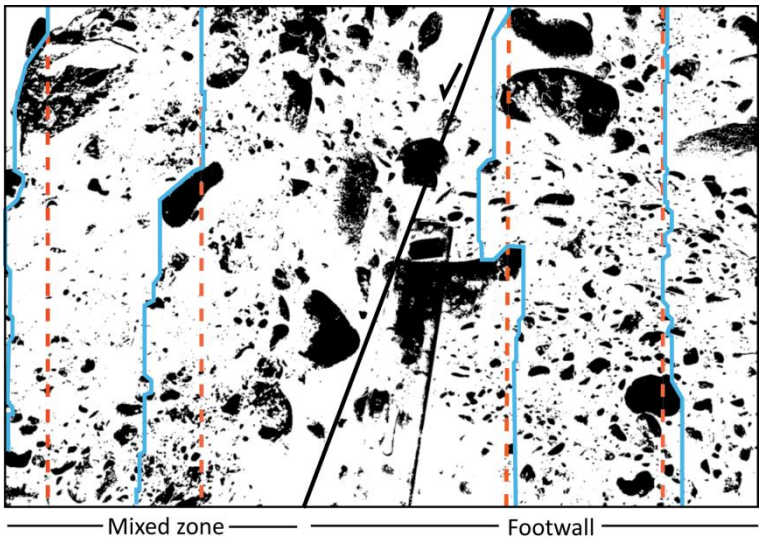

Figure 5.2 Example of flow path tortuosity measurements in the vertical orientation. Red grids indicate direct pathways (length L), and blue lines show potential fluid-flow pathways resulting from flowpath tortuosity (length L_T). Measurements were also made in fault parallel and fault perpendicular orientations.

5.3 Porosity and hydraulic conductivity of sediment samples

5.3.1 Porosity and hydraulic conductivity from image analysis

Porosity and hydraulic conductivity calculated from image analysis are included in Appendix 3, and shown in Figure 5.3. The mean porosity for all protosediment samples was 21% (standard deviation +/- 5%) and mean hydraulic conductivity was 5.04 x 10^{-3} m s^{-1}. The mean porosity for all samples from fault zones was 12% (standard deviation +/- 10%) and mean hydraulic conductivity was 3.75 x 10^{-3} m s^{-1}. The mean range of estimated porosity for each sample is 6.1%. The greatest porosity

range measured for single samples (18 to 19.4%) were found in three of the coarsest gravel samples (Mentourgianika An FWa and b and An MZb). The smallest mean porosity range (0.3%) was found in the sample from Mentourgianika Cement Fault 2 MZ b (Figure 5.3). The greatest range in estimated hydraulic conductivity was found in the gravel sample Mn An MZ b (1.80×10^{-1} m s^{-1}) and the smallest range was found in gravel sample P G1 SS (1.57×10^{-7} m s^{-1}). Overall, the greatest estimated hydraulic conductivity range for zones of mixed sediment and their protosediment was from gravel samples (Figure 5.3, Table 5.3).

5.3.1.1 Zones of mixed sediment

The estimated porosity and hydraulic conductivity of samples from zones of mixed sediment were generally lower than that of the protosediment (Figure 5.3; Tables 5.2 and 5.3). The mean porosity of samples from zones of mixed sediment in fault zones cutting coarse-grade sand was 9.6% lower, and from zones of mixed sediment cutting fine to medium-grade gravel was 8.5% lower, compared with the mean porosity for protosediment sand and gravel samples respectively (Table 5.2). Mean porosity of samples from zones of mixed sediment compared directly to their protosediment is an average of 9% lower in sand, and 3% lower in gravel. However, the mean porosity of mixed zone gravel samples Ak F1 MZ and M An MZa is slightly higher than that of the protosediment mean (Figure 5.3). The extremely low mean porosity of the sample M CF 2b (0.75%) probably results from cement within it. The range for estimated porosity for zone of mixed sediment samples is 3.5% for sand and 23.65% for gravel, compared with 16.7% and 7.4% for the protosediment (Table 5.2).

Type of sediment	Mean porosity (%)	Standard deviation of porosity (%)	Porosity range (%)	No. of samples
Sand protosediment	22.6	5.6	10.4 to 27.1	7
Zone of mixed sediment (sand)	13.0	2.5	11.2 to 14.7	2
Disaggregation band (sand)	32.7	13.9	22.9 to 42.5	2
Gravel protosediment	19.9	4.0	15.3 to 22.7	3
Zone of mixed sediment (gravel)	11.4	7.9	0.75 to 24.4	9
Slip-surface cataclasites (gravel)	3.7	3.2	1.3 to 7.3	3
Smear (gravel)	20.0	N/A	N/A	1
Zone of mixed sediment (gravel/silt)	5.8	N/A	N/A	1
Fine-grained smear (silt)	8.1	N/A	N/A	1

Table 5.2 Mean, standard deviation and range of estimated sample porosity for each type of sediment, identified from thin section image analysis. N/A indicates where values could not be obtained.

Type of sediment	Mean hydraulic conductivity ($m\ s^{-1}$)	Standard deviation of hydraulic conductivity (+/- $m\ s^{-1}$)	Hydraulic conductivity range ($m\ s^{-1}$)	No. of samples
Sand protosediment	3.0×10^{-3}	2.0×10^{-3}	3.2×10^{-4} to 6.0×10^{-3}	7
Zone of mixed sediment (sand)	5.5×10^{-4}	5.7×10^{-4}	1.5×10^{-4} to 9.5×10^{-4}	2
Disaggregation band (sand)	1.2×10^{-2}	1.0×10^{-2}	4.6×10^{-3} to 1.9×10^{-2}	2
Gravel protosediment	9.9×10^{-3}	7.2×10^{-3}	1.2×10^{-2} to 1.8×10^{-3}	3
Zone of mixed sediment (gravel)	9.3×10^{-3}	2.0×10^{-2}	1.6×10^{-7} to 6.0×10^{-2}	9
Slip-surface cataclasites (gravel)	1.5×10^{-5}	2.5×10^{-5}	9.4×10^{-8} to 4.4×10^{-5}	3
Smear (gravel)	3.1×10^{-4}	N/A	N/A	1
Zone of mixed sediment (gravel/silt)	1.6×10^{-5}	N/A	N/A	1
Fine-grained smear (silt)	1.4×10^{-5}	N/A	N/A	1

Table 5.3 Mean, standard deviation and range of sample hydraulic conductivity identified from thin section image analysis and the Kozeny-Carman equation, for each type of sediment. N/A indicates where values could not be obtained.

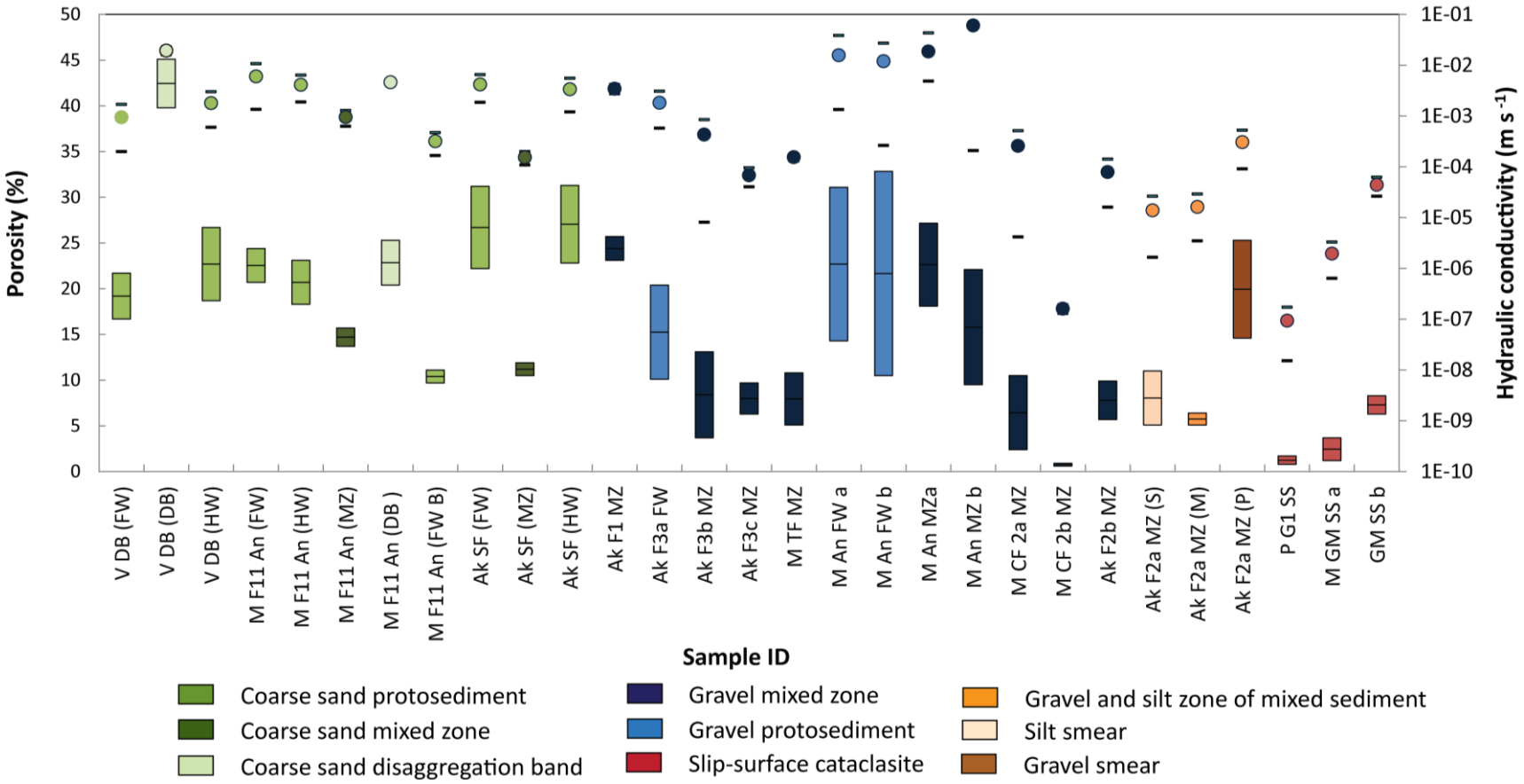

Figure 5.3 Mean and range of porosity (left axis) and hydraulic conductivity (right axis) of samples measured from thin section image analysis. Mean porosity is shown in the centre of the rectangles and the porosity range by the rectangles. Hydraulic conductivity is shown by the markers, and the range by black bars. Sample ID corresponds to Table 5.1.

The mean hydraulic conductivity of samples from zones of mixed sediment cutting sand is nearly an order of magnitude lower than the sand protosediment. The mean hydraulic conductivity of samples from zones of mixed sediment cutting gravel is half an order of magnitude lower than the protosediment mean (Figure 5.3; Table 5.3). Mean estimated hydraulic conductivity of zones of mixed sediments in sand is one to two orders of magnitude lower than the direct protosediment. In gravel samples, the mean estimated hydraulic conductivity ranges from one order of magnitude higher to two orders of magnitude lower than the direct protosediment. The zone of mixed sediment samples with higher estimated hydraulic conductivity are again from Mentourgianika Fault An (M An MZa and b) (Figure 5.3; Appendix 3). The estimated hydraulic conductivity for zones of mixed sediment in sand is the same order of magnitude for both samples and ranges five orders of magnitude for gravel samples. Estimated hydraulic conductivity ranges by an order of magnitude for both sand and gravel protosediment samples (Table 5.3).

5.3.1.2 Slip-surface cataclasite

Mean porosity and estimated hydraulic conductivity of slip-surface cataclasites are lower than the other fault zone structural elements (Tables 5.2 and 5.3). Mean porosity of slip-surface cataclasites, 3.7%, is 19% lower than the mean porosity of gravel protosediment, and nearly 10% lower than the mean porosity of samples from zones of mixed sediment in gravel (Table 5.2). Mean estimated hydraulic conductivity of the slip-surface cataclasite is nearly three orders of magnitude lower than the mean for the gravel protosediment and zones of mixed sediment. The total porosity range is 6% (Table 5.2), equating to a range in hydraulic conductivity of three orders of magnitude; from 9.4×10^{-8} m s^{-1} to 4.4×10^{-5} m s^{-1} (Table 5.3).

5.3.1.3 Disaggregation bands in sand

Mean porosity of the disaggregation bands in sand was 10.1% higher than the mean porosity of sand protosediment (Table 5.2). Mean estimated hydraulic conductivity is an order of magnitude higher in disaggregation bands than the mean for sand protosediment (Table 5.3). However, there was a considerable difference in mean porosity between the two sampled disaggregation bands; 42.5% for V DB (DB) and

22.9% for M F11 An (DB), which was only 0.3% higher than mean of the sand protosediment (Figure 5.3; Table 5.2).

5.3.1.4 Sediment smears

Estimated porosity of the gravel smear sample Ak F2a MZ (P), flanking the silt smear in Fault 2, Akrata (Figure 4.7), is similar (20%) to adjacent gravel protosediment porosity (Figure 5.3; Table 5.2). Estimated porosity of the silt-smear sample Ak F2a MZ (S) is 12% lower than this, 8.1%. Estimated porosity of the sample Ak F2a MZ (M), from the thin zone of mixed sediment between the silt and gravel smears (Figure 4.7) is lower than either the gravel or silt-smear (5.8%) (Figure 5.3, Table 5.2). However, estimated hydraulic conductivity for the silt smear sample is slightly lower than the zone of mixed sediment sample (1.4×10^{-5} m s^{-1} and 1.6×10^{-5} m s^{-1} respectively), owing to the larger mean grain-size sampled in the latter.

5.3.1.5 Trends in porosity and hydraulic conductivity with fault throw

In Figure 5.4 estimated porosity and hydraulic conductivity of samples from zones of mixed sediment and slip-surface cataclasites are plotted against the throw of the fault from which the sample was sourced. Samples M CF 2 b and Ak F2a are not included in this analysis because the porosity of the former is strongly influenced by cement and because the latter sample originates from a mixed zone dominated by a silt-smear rather than a zone of mixed sediment (Figure 4.7).

Inverse logarithmic and power-law trends have been fitted to porosity and hydraulic conductivity data respectively (Figure 5.4). The steepest gradient in sample porosity and hydraulic conductivity decrease with fault throw occurs in faults with <2 m throw. The gradient for the decrease in porosity and hydraulic conductivity parameters with fault throw is smaller at greater fault throws, apparently ceasing when fault throw exceeds 5 m (Figure 5.4). Despite relatively poor correlations between porosity and hydraulic conductivity and fault throw, the trends in Figure 5.4a would suggest an apparent 18% decrease in porosity with each order of magnitude increase in fault throw ($R^2 = 0.33$), equating to an absolute decrease in porosity of 3-4% with each order of magnitude increase in fault throw (Figure 5.4a). Calculated hydraulic conductivity decreases by an order of magnitude with 1.5 orders of magnitude increase in fault throw ($R^2 = 0.22$) (Figure 5.4b). When only

zones of mixed sediment cutting gravel are considered, porosity decreases by ~8%, and hydraulic conductivity decreases by an order of magnitude, with each order of magnitude increase in fault throw. The correlations between fault throw and porosity and hydraulic conductivity improve slightly for only samples of zones of mixed sediment cutting gravel, to $R^2 = 0.54$ and 0.34 respectively.

There is a possible initial increase in porosity and hydraulic conductivity in faults with throw <~1 m, before the porosity decreases with fault throw (Figure 5.4). However, no trend was identified at throws <1 m because the zone of mixed sediment samples were from sand only, which complicates comparisons to gravel fault zones due to differences in accuracy of porosity and hydraulic conductivity estimates and the possible influence of grain-size distributions on porosity. The large range of estimated porosity and hydraulic conductivity for the two gravel samples with increased porosity and hydraulic conductivity suggests these estimates are not reliable alone.

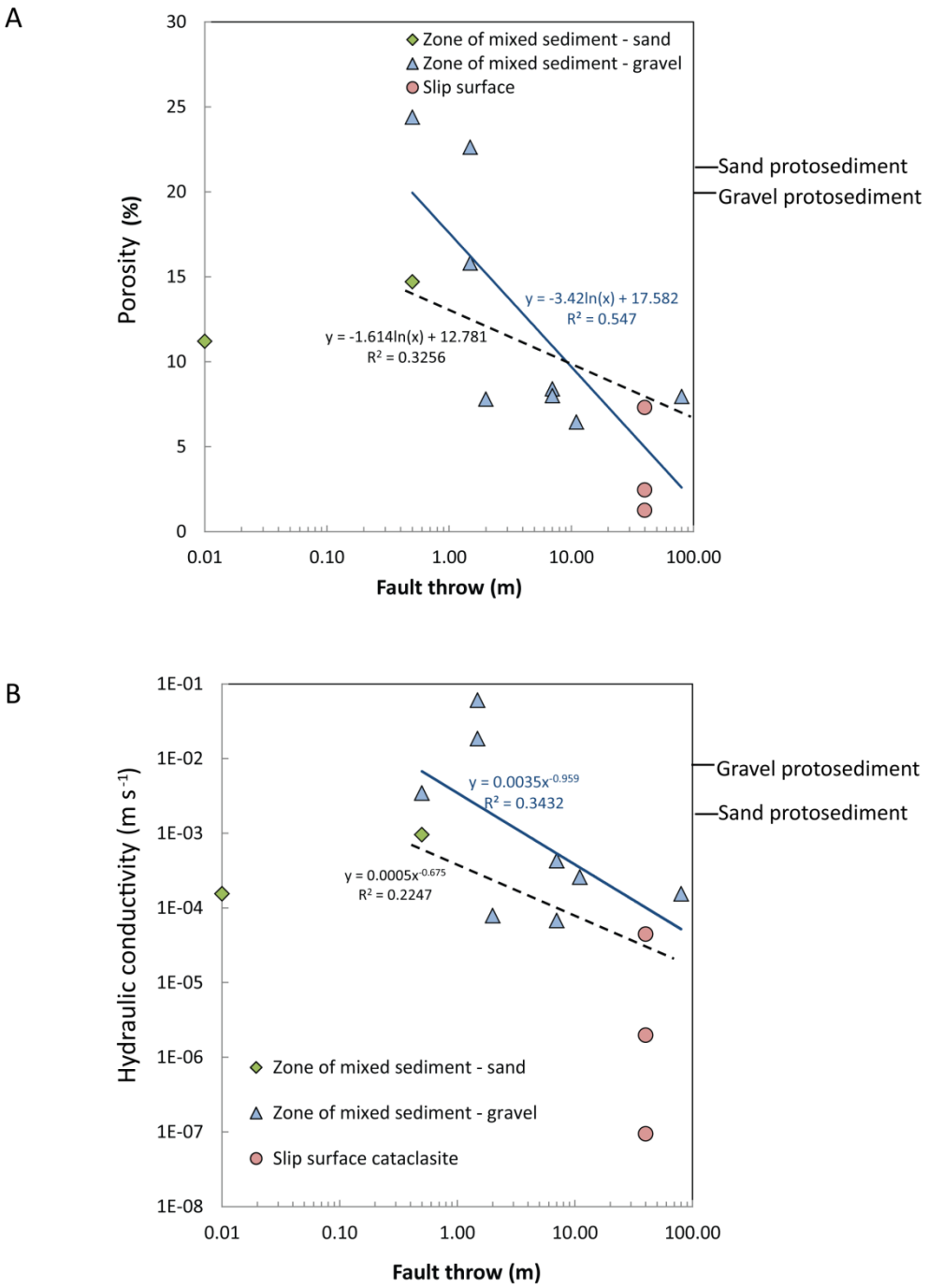

Figure 5.4 Porosity and hydraulic conductivity of samples from zones of mixed sediment and slip-surface cataclasites estimated from thin section image analysis, with fault throw. Mean protosediment porosity and hydraulic conductivity for sand and gravel indicated along the right hand axis. A) Estimated sample porosity with fault throw and logarithmic trends fitted to log-normal data. B) Estimated hydraulic conductivity with fault throw and power-law trends fitted to log-log data. Broken black trendline applies to all samples from faults with >1 m throw, blue trendline applies only to gravel zones of mixed sediment samples with >1 m throw.

5.3.2 Spatial patterns of hydraulic conductivity across fault zones

5.3.2.1 Fault 1A, Loutraki

Fault 1 exposed in the Loutraki outcrop, section AA' (Figure 2.3), cuts a variety of poorly lithified beds. The mixed zone is characterised by smeared beds and a zone of mixed sediment (Figures 3.1a and 5.5). Estimated hydraulic conductivity from grain-size distributions varies greatly from the footwall to hangingwall and across the mixed zone (Figure 5.5). There is a considerable difference in estimated hydraulic conductivity between the footwall sand ($1x\ 10^{-4}$ m s^{-1}) and the hangingwall gravel (10 m s^{-1}) along transect 1, but estimated hydraulic conductivity increases relatively steadily from the footwall to the hangingwall across the mixed zone (Figure 5.5b). Differences in estimated hydraulic conductivity are not as great between the footwall and hangingwall along transect 2, but there is a considerable difference in hydraulic conductivity between adjacent smears of different beds in the mixed zone (Figure 5.5). Maximum estimated hydraulic conductivity range in individual hangingwall and footwall beds is one order of magnitude, across the mixed zone sediment smears and zone of mixed sediment it is three orders of magnitude.

Mean estimated vertical hydraulic conductivity for the footwall and hangingwall differs by nearly four orders of magnitude between transects 1 and 2, but only one order of magnitude in the mixed zone (Figure 5.5b). Mean estimated mixed zone hydraulic conductivity is higher than mean hangingwall and footwall hydraulic conductivity for both transects (Figure 5.5b). The maximum estimated hydraulic conductivity in the mixed zones of both transects exceeds the maximum found in the hangingwall and footwall by at least an order of magnitude (Figure 5.5b). The lowest estimated hydraulic conductivity is found in pebble sample 7 (transect 2), at the footwall/ mixed zone boundary (Figure 5.5).

Estimated hydraulic conductivity range is greatest for the pebble and gravel beds (Table 5.4). With the exception of the bladed pebble bed, the mean hydraulic conductivity of each sampled bed is slightly higher in the mixed zone than in the protosediment (Table 5.4). Estimated mean hydraulic conductivity of the bladed pebble bed is two orders of magnitude lower in the mixed zone than the footwall. The estimated mean hydraulic conductivity of the zone of mixed sediment is within

an order of magnitude of the mean hydraulic conductivity of all the beds contributing to the fault zone at this point.

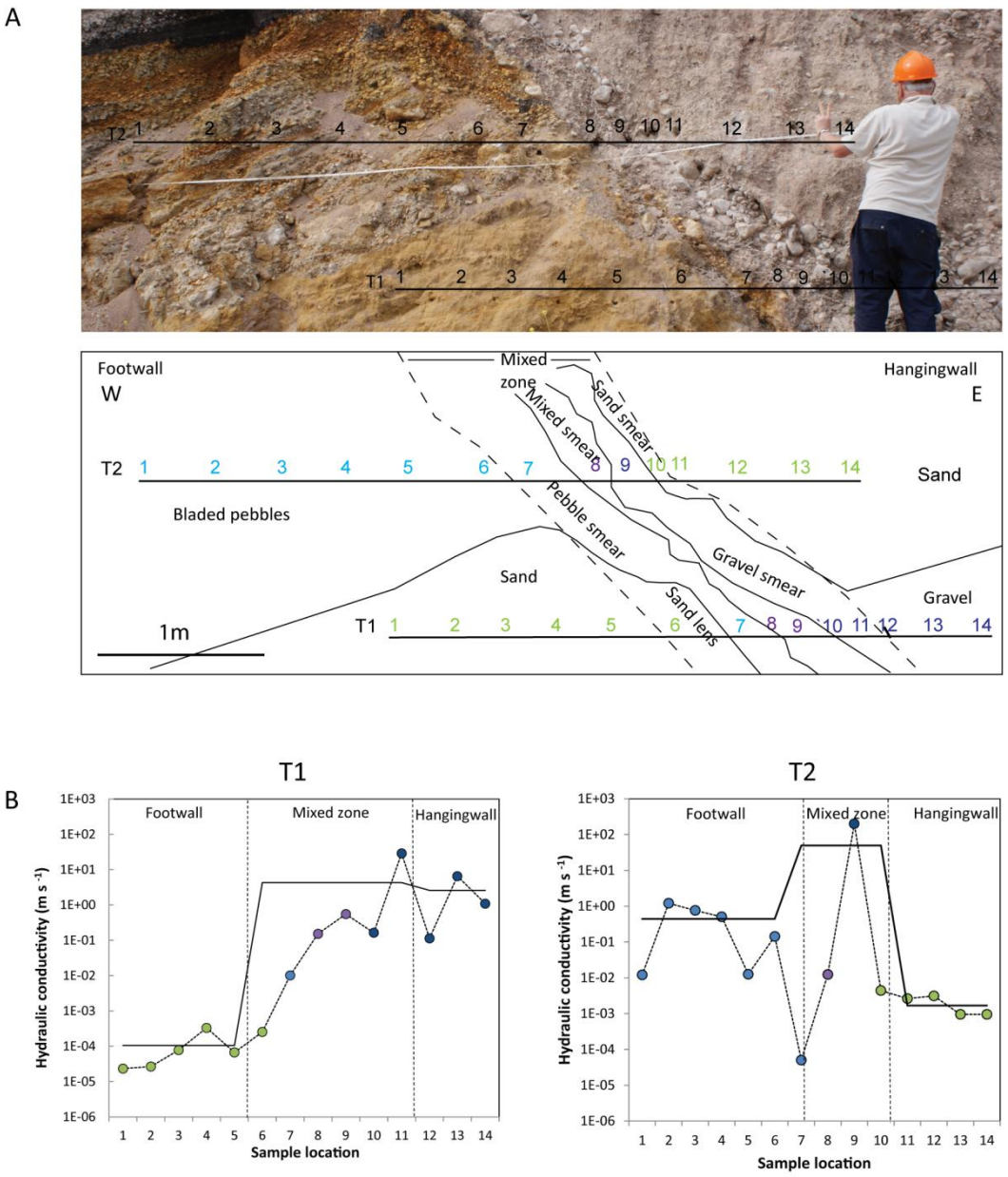

Figure 5.5 Hydraulic conductivity estimated from grain-size distribution samples for Fault 1A Loutraki (Figure 3.1a). A) Photograph and schematic of Fault 1A showing the sediment sample locations along transects 1 and 2 (T1 and T2), mixed zone structural elements, and beds cut by the fault. B) Hydraulic conductivity across T1 and T2. Marker colours correspond to sample locations in the schematic in (A). Solid black line is the average hydraulic conductivity for the footwall, mixed zone or hangingwall. Vertical dashed lines indicate boundaries to the mixed zone.

Sediment type	Mean hydraulic conductivity ($m\ s^{-1}$)	Hydraulic conductivity standard deviation ($+/-\ m\ s^{-1}$)	Hydraulic conductivity range ($m\ s^{-1}$)
Footwall sand (T1)	1.05×10^{-4}	1.28×10^{-4}	3×10^{-4} to 2×10^{-5}
Mixed zone sand (T1)	2.54×10^{-4}	N/A	N/A
Hangingwall sand (T2)	1.63×10^{-3}	1.46×10^{-3}	1 to 1×10^{-3}
Mixed zone sand (T2)	4.42×10^{-3}	N/A	N/A
Footwall pebbles (T2)	4.41×10^{-1}	4.81×10^{-1}	1 to 1×10^{-2}
Mixed zone pebbles (T1 and T2)	5.09×10^{-3}	7.13×10^{-3}	1×10^{-2} to 5×10^{-5}
Hangingwall gravels (T1)	2.58	3.46	7 to 1×10^{-1}
Mixed zone gravels (T1 and T2)	$5.71 \times 10^{+1}$	$9.58 \times 10^{+1}$	$3 \times 10^{+1}$ to 2×10^{-2}
Zone of mixed sediment (T1 and 2)	2.38×10^{-1}	2.79×10^{-1}	$5 \times 10^{+1}$ to 1×10^{-2}

Table 5.4 Mean estimated hydraulic conductivity for sediment from across Fault 1A, Loutraki (Figure 5.5), with standard deviation and range.

5.3.2.2 Fault 1C, Loutraki

The exposure of Loutraki Fault 1 in the section CC' (Figure 2.3), cuts alternating coarse sand and marl beds. The mixed zone is dominated by a largely undeformed block of marl, surrounded by smeared sand beds (Figures 3.1c and 5.6). The maximum variation in estimated hydraulic conductivity within a particular protosediment bed is two orders of magnitude (Table 5.5). Maximum variability in estimated hydraulic conductivity is more than two orders of magnitude across the mixed zone (Figure 5.6).

Estimated mean hydraulic conductivity between the footwall and hangingwall of Fault 1C differs by a maximum of two orders of magnitude, along transect 2 (Figure 5.6). Along the other transects the maximum difference in mean estimated hydraulic conductivity between the footwall and hangingwall is one order of magnitude. Mean estimated hydraulic conductivity of the mixed zone is higher than the mean for the footwall or hangingwall in transects 1 and 3, lower in transect 2, and lower (hangingwall) and higher (footwall) in transect 4 (Figure 5.6). However, the maximum difference is only half an order of magnitude.

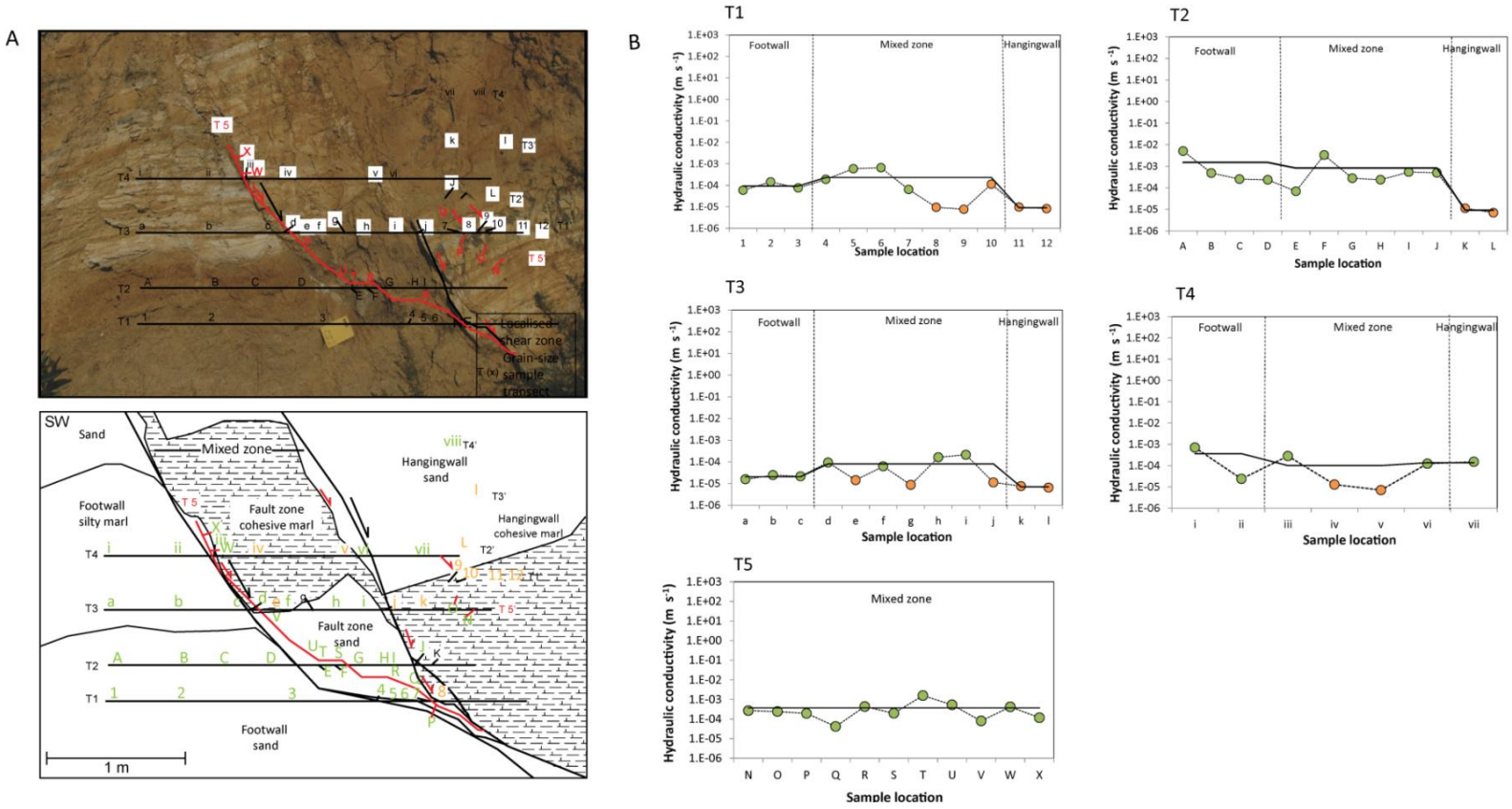

Figure 5.6 Hydraulic conductivity estimated from grain-size distributions and the Krumbein-Monk equation across Fault 1C Loutraki (Figure 3.1c). A) Photograph and schematic diagram for Fault 1C with grain-size sample locations along transects 1 to 5 (T1 to T5). B) Estimated hydraulic conductivity along T1 to T5 (A). Marker colours correspond to the beds in the schematic in (A). Solid black line is the mean hydraulic conductivity for the footwall, mixed zone or hangingwall. Dashed lines show the mixed zone boundaries.

Hydraulic conductivity of marl in the mixed zone is slightly lower than marl protosediment, but there is little difference between protosediment and mixed zone sand (Table 5.5). Estimated hydraulic conductivity range is slightly greater for samples from the mixed zone sediment (four orders of magnitude for sand and one order of magnitude for marl), than the protosediment (three orders of magnitude for sand and half an order of magnitude for marl) (Figure 5.6).

Sediment type	**Mean hydraulic conductivity ($m\ s^{-1}$)**	**Hydraulic conductivity standard deviation (+/- $m\ s^{-1}$)**	**Hydraulic conductivity range ($m\ s^{-1}$)**
Protosediment sand	5.36×10^{-4}	1.12×10^{-3}	5.89×10^{-5} to 5.08×10^{-2}
Mixed zone sand	4.57×10^{-4}	7.88×10^{-4}	8.74×10^{-6} to 3.31×10^{-2}
Protosediment marl	7.61×10^{-5}	2.07×10^{-4}	7.69×10^{-6} to 6.21×10^{-5}
Mixed zone marl	1.79×10^{-5}	1.97×10^{-5}	7.05×10^{-6} to 2.46×10^{-5}

Table 5.5 Mean estimated hydraulic conductivity for sediment from across Fault 1C, Loutraki (Figure 5.6), with standard deviation and range.

5.3.2.3 Fault 5, Loutraki

The focus of the exposure of Fault 5, in Loutraki section BB' (Figure 2.3) was the poorly lithified pebble bed (Figures 3.7 and 5.7). Mean estimated hydraulic conductivity of the footwall, hangingwall and mixed zone transects was between 0.1 and 1 $m\ s^{-1}$ (Figure 5.7, Table 5.6). The decrease in estimated hydraulic conductivity from the footwall to the hangingwall is associated with a decrease in grain-size (see Figures 3.9 and 5.7). Vertical differences in estimated hydraulic conductivity are greater along the footwall and hangingwall transects (up to an order and a half magnitude), than along the mixed zone transect (less than half an order of magnitude) (Figure 5.7).

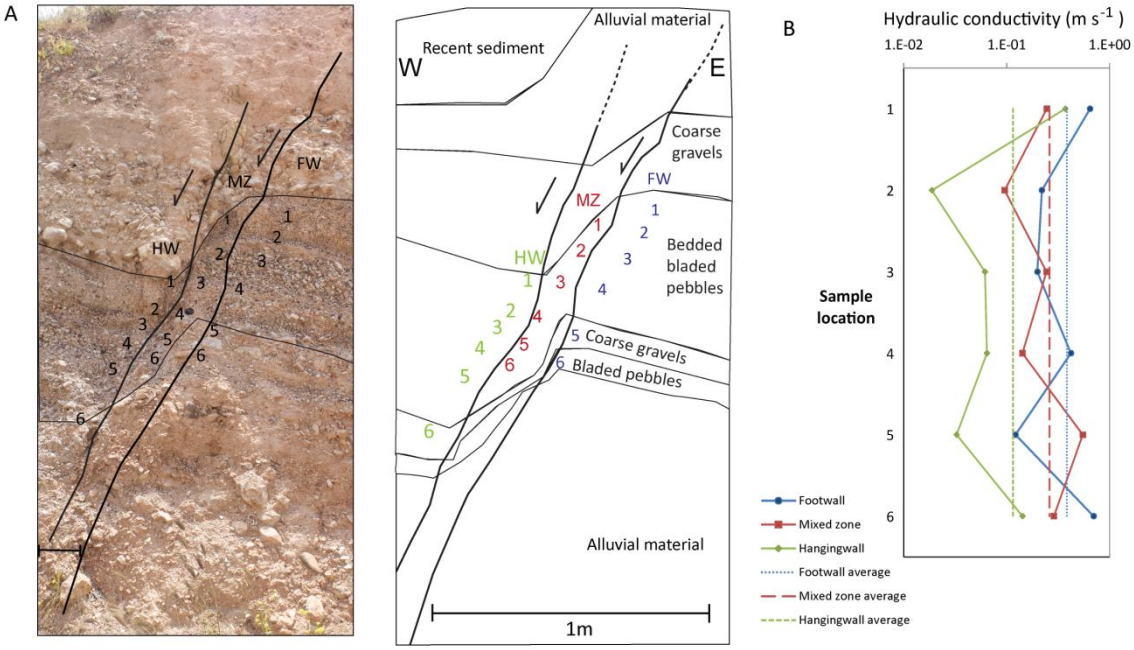

Figure 5.7 Hydraulic conductivity estimated from grain-size distribution samples and the Krumbein-Monk equation for Fault 5 Loutraki (Figure 3.7). A) Photograph and schematic diagram of Fault 5 showing the sample locations along the hangingwall, mixed zone and footwall transects. B) Estimated hydraulic conductivity for each sample, and the mean hydraulic conductivity for the hangingwall, footwall and mixed zone.

Sediment type	**Mean hydraulic conductivity ($m\ s^{-1}$)**	**Hydraulic conductivity standard deviation (+/- $m\ s^{-1}$)**	**Hydraulic conductivity range ($m\ s^{-1}$)**
Footwall	0.38	0.24	0.12 to 0.7
Mixed zone	0.26	0.16	0.9 to 0.54
Hangingwall	0.12	0.13	0.019 to 0.37

Table 5.6 Mean estimated hydraulic conductivity for sediment from across Fault 1C, Loutraki (Figure 5.7), with standard deviation and range.

5.3.2.4 Fault 2, Akrata

Fault 2, exposed in the Akrata outcrop, cuts predominantly poorly lithified gravels, but these are inter-bedded with thin (0.1 to 0.2 m thick) silt beds towards the base of the exposure (Figure 4.7 and 5.8). In the lower half of the exposure, the mixed zone comprises smears of gravels and a smear of silt in the centre of the mixed zone (Figure 4.7). The mean estimated hydraulic conductivity of the silt-smear in the mixed zone from grain-size distributions, 1.61 x 10^{-5} m s^{-1} (Table 5.7), is similar to the estimate for the same smear from thin section image analysis, 1.4 x 10^{-5} m s^{-1} (Ak F2a MZ (S)) (Figure 5.3). The estimated hydraulic conductivity from the zone of mixed sediment is two orders of magnitude greater than the estimate based on thin section image analysis (8 x 10^{-3} m s^{-1} compared with 1.6 x 10^{-5} m s^{-1}). Mean estimated hydraulic conductivity for the gravel protosediment using grain-size distributions is also an order of magnitude higher than the mean estimated from thin sections (1.13 x 10^{-2} m s^{-1} compared with 9.9 x 10^{-3} m s^{-1}) (Figure 5.3; Table 5.7). Hydraulic conductivity varies by nearly three orders of magnitude across the fault zone of Akrata Fault 2 based on grain-size distributions and the Krumbein and Monk (1942) equation (Figure 5.8). Variations in estimated hydraulic conductivity are greater for the gravel samples than the fine-grained smear (Figure 5.8b).

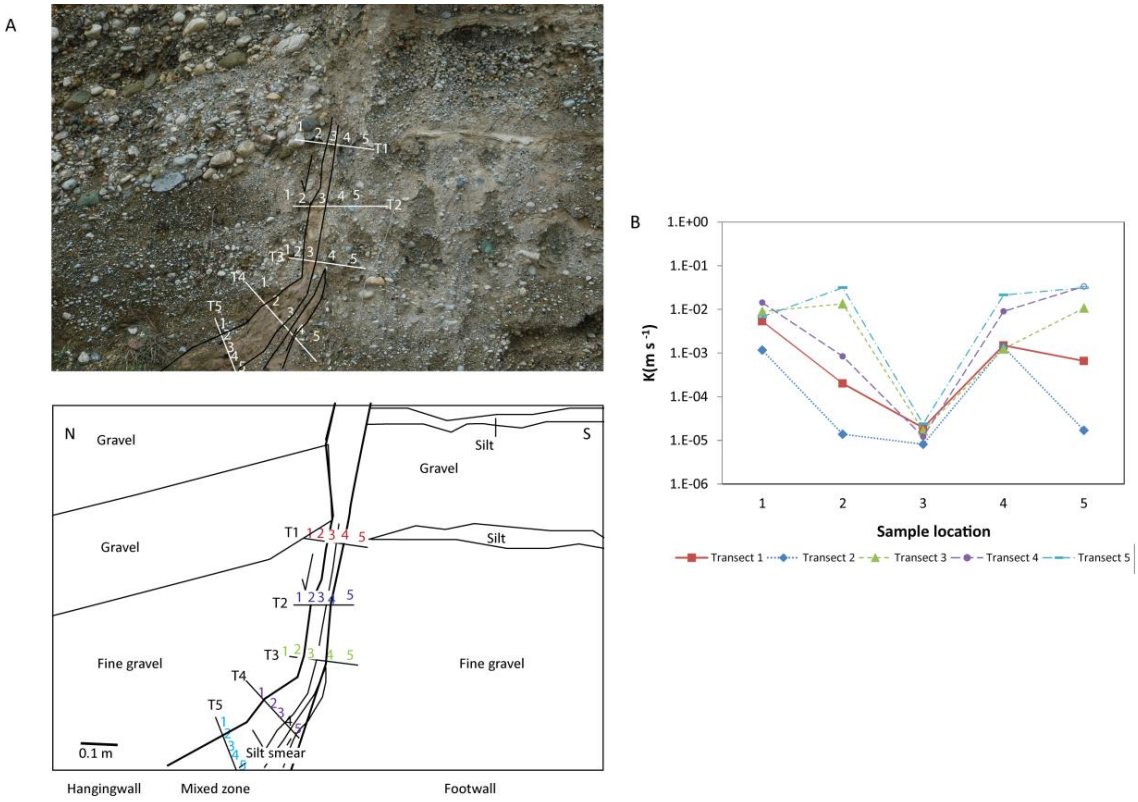

Figure 5.8 Hydraulic conductivity estimated from grain-size distribution samples and the Krumbein-Monk equation for Fault 2, Akrata (Figure 4.7). A) Photograph and schematic diagram of Fault 2 showing the sample locations along the five transects. B) Estimated hydraulic conductivity for each grain-size sample, colours correspond to transects in the schematic.

Sediment type	**Mean hydraulic conductivity ($m\ s^{-1}$)**	**Hydraulic conductivity standard deviation ($m\ s^{-1}$)**	**Hydraulic conductivity range ($m\ s^{-1}$)**
Gravel protosediment	1.13×10^{-2}	1.21×10^{-2}	1.69×10^{-5} to 3.35×10^{-2}
Fine-grained smear (silt)	1.61×10^{-5}	6.14×10^{-6}	8.11×10^{-6} to 2.39×10^{-5}
Zone of mixed silt and gravel	$8. \times 10^{-3}$	1.09×10^{-2}	3.38×10^{-5} to 3.14×10^{-2}

Table 5.7 Mean estimated hydraulic conductivity (K) for sediment from different regions across Fault 2, Akrata (Figure 5.8), with standard deviation and range.

5.3.3 Hydraulic anisotropy from flow path tortuosity

Permeability ellipses illustrate two-dimensional permeability anisotropy estimated from tortuosity measurements from mixed zone and protosediment (footwall) images (Figure 5.9). Anisotropy from these estimates appears to be small. Horizontal permeability exceeds vertical permeability in the footwall sediment of Loutraki Fault 1A and 5 (Figures 5.9b and c). Vertical permeability exceeds horizontal permeability in the mixed zone sediment of Fault 2, Akrata, and Fault 5, Loutraki (Figures 5.9a and c). Permeability from tortuosity measurements in the footwall of Fault 2, Akrata and the mixed zone of Fault 1A, Loutraki looks to be largely isotropic (Figures 5.8a and b, Table 5.8).

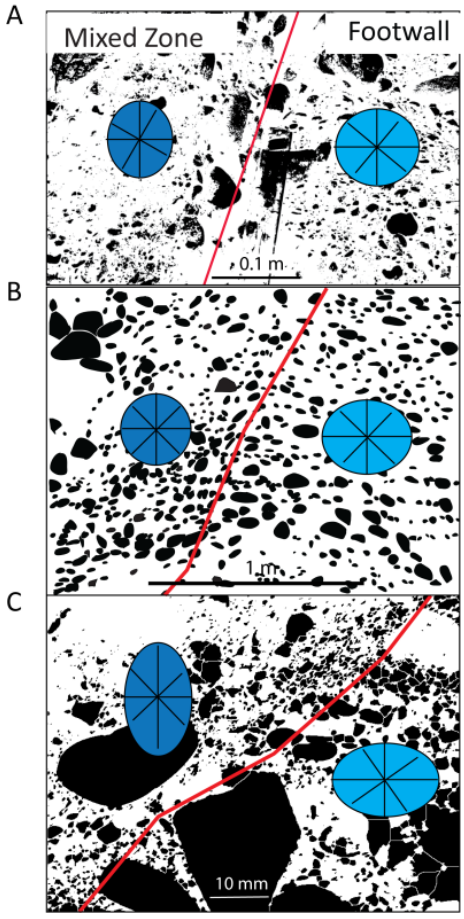

Figure 5.9 Hydraulic anisotropy from flow path tortuosity estimated from images across mixed zones and footwall sediment of three faults. Ellipses indicate orientation and relative magnitude of anisotropy. A) Fault 3, Akrata, photograph from the outcrop (Figure 4.2b). B) Visually picked clasts, Loutraki Fault 1A, photograph from the outcrop (Figure 3.2a). C) Loutraki Fault 5, photograph from a hand sample (Figure 3.7c).

		Mixed zone				Footwall			
Fault	Parameter	Y	X	Par	Perp	Y	X	Par	Perp
Akrata fault 3	T	1.08	1.03	1.07	1.03	1.13	1.06	1.13	1.06
	k	**Y:X**	**1.10**	**Par: perp**	**0.93**	**Y:X**	**1.14**	**Par: perp**	**0.88**
Loutraki Fault 1	T	1.12	1.09	1.09	1.08	1.15	1.06	1.10	1.05
	k	**Y:X**	**1.06**	**Par: perp**	**0.98**	**Y:X**	**1.18**	**Par: perp**	**0.91**
Loutraki Fault 5 Hand sample	T	1.32	1.07	1.09	1.17	1.33	1.12	1.08	1.11
	k	**Y:X**	**1.52**	**Par: perp**	**1.15**	**Y:X**	**1.41**	**Par: perp**	**1.06**

Table 5.8 Tortuosity measurements and permeability (k) ratios resulting from tortuosity in the vertical: horizontal (y: x) and fault parallel: perpendicular (Par: perp) orientations for the footwall and mixed zones.

5.4 Hydraulic properties of fault zones

The similarity of protosediment porosity and hydraulic conductivity estimated for these samples with values quoted in the literature (e.g. Freeze and Cherry, 1979; Brassington, 1998; Hiscock, 2005) demonstrate the capability of image analysis, the Kozeny-Carman and Kumbein-Monk equations, to estimate relative porosity and hydraulic conductivity. Estimated variability probably results from a combination of high sediment variability and errors associated with the methods and calculations. The two orders of magnitude differences in estimated hydraulic conductivity for samples from Fault 2 from thin section image analysis and grain-size samples is probably due to the absence of porosity in estimates for grain-size samples. This is possibly a considerable source of error.

The mean range of porosity estimates (6%) for all samples from image analysis is fairly good; however a greater number of estimates for each sample would have improved the accuracy of the final estimate. The greatest error associated with this thin section image analysis is estimating porosity from coarse gravel (Figure 5.3), because pore size is large compared to the sample window size. This results in inadequate sampling of porosity variability, and incomplete sampling of pores at the edge of the image. The differences in porosity estimates for the scanned thin section compared with petromicrographs demonstrates this problem (Appendix 3). The error associated with correct classification of grains and pore spaces, highlighted as being

considerable by Bense *et al.* (2003) was minimised by cross-checking binary images with original images, although this does introduce an element of subjectivity into the process.

For both methods an assumption is made that pore-size and grain-size do not alter in three dimensions and that pore-space characteristics (shape and size) are uniform throughout the sediment (Bourabid *et al.*, 1992; Van den Berg *et al.*, 2003). This is unlikely to be the case in fault zones where a greater decrease in porosity is expected perpendicular to the shear zone (Dewhurst *et al.*, 1996; Wilson *et al.*, 2003). Calculating hydraulic properties perpendicular to the fault strike should minimise this variation between the samples, however these characteristics should be considered apparent values.

5.4.1 Hydraulic properties of zones of mixed sediment

Estimated porosity for zones of mixed sediment is lower than the protosediment due to fault zone deformation processes. As outlined in Chapters 3 and 4 the decrease in porosity results from a decrease in grain-size, sorting, change in grain shape and tighter grain packing, caused by the dominant deformation mechanism – controlled particulate flow. The mean decrease in absolute porosity for zones of mixed sediment is 9% however the range of 11.5% is considerable.

Hydraulic conductivity is strongly associated with sediment porosity (Figure 5.3 and 5.4). Whilst the mean estimated hydraulic conductivity for zones of mixed sediment is an order of magnitude lower than the protosediment, values range from an order of magnitude higher, to four orders of magnitude lower. The changes to sediment hydraulic conductivity in zones of mixed sediment estimated here are similar to air permeameter measurements of fault zones cutting poorly lithified sediment (e.g. Sigda *et al.*, 1999; Balsamo and Storti, 2010; Balsamo *et al.*, 2010). According to Gibson (1998), fault zones with an order of magnitude alteration in hydraulic conductivity will have hydraulic impacts; therefore the hydraulic consequence of these fault zones could be considerable, even at sub-seismic scales (e.g. Balsamo *et al.*, 2010). Although not investigated here, Sigda *et al.* (1999), and Balsamo *et al.* (2010) found a reduction in pore size resulting from fault zone processes, which would also impact fault zone intrinsic permeability.

The high variability in estimated porosity and hydraulic conductivity for zones of mixed sediment could be related to fault throw (Figure 5.4). Porosity and hydraulic conductivity decrease with fault throw, such that a fault mixed zone with 10 m throw may have porosity 11% lower and hydraulic conductivity two orders of magnitude lower, than a fault with 1 m throw. Unpublished findings by Fisher and Knipe, described in Tueckmantel *et al*. (2010), suggest that the fault zones of sub-seismic and seismic-scale faults do not exhibit differences in grain-size or permeability. Results presented here do not counter this observation, but suggest a caveat as to the scale of a sub-seismic fault, since faults with throws <5 m do seem to exhibit differences in porosity and hydraulic conductivity. Nevertheless, this initial trend is based on very limited data (Figure 5.4).

The inverse logarithmic and power-law trends describing porosity and hydraulic conductivity variation with fault throw (Figure 5.4) imply a reduction in the rate of porosity and hydraulic conductivity decrease with an increase in fault throw, though because the correlation is weak and data points limited this could be an erroneous trend. Nevertheless, the improvement in correlation when only data from gravels are included suggests that some of the variability could result from differences in lithology (Figure 5.4). Similar trends were reported in high and low porosity sand by Balsamo and Storti (2010) and Balsamo *et al.* (2010), and demonstrated for experimentally deformed quartz gouge (at normal stresses equivalent to 1 km crustal depth) by Zhang and Tullis (1998). However, Balsamo *et al.* (2010) found the most significant decrease in permeability occurs during the first 10 m of fault displacement, whereas these results show the most significant porosity and hydraulic conductivity reduction to occur before 2 m throw, slowing considerably in faults with throws >5 m (Figure 5.4).

The two samples from zones of mixed sediment gravels in which estimated porosity is higher than the protosediment (Figures 5.3 and 5.4a) come from faults with throws <1.5 m. This could indicate an initial increase in porosity with small magnitudes of fault throw, as postulated by Balsamo *et al.* (2010). However, since the porosity is a maximum of 1.8% higher than the protosediment, the difference lies well within the margin of uncertainty for porosity estimates from thin section image analysis for

gravels (Table 5.2), therefore this increase cannot be attributed to fault zone processes.

The decreasing porosity for zones of mixed sediment with an increase in fault throw supports the model of mixed zone evolution in poorly lithified sediment proposed in Chapters 3 and 4 (Figure 4.12). Particulate flow initially causes grain rotation, grain-scale mixing, and some cataclasis, resulting in a rapid porosity decrease to ~2 m fault throw. The reduction in rate of porosity decrease after ~2 m throw corresponds to impedance of particulate flow from strain hardening. Further strain accommodation requires significant cataclasis, resulting in the development of very low porosity slip-surface cataclasites. The possible increase in mixed zone porosity at small fault throws (<1.5 m) might suggest that faults may initiate by grain disaggregation from dominant tensile stresses in extensional settings (e.g. Du Bernard *et al.,* 2002; Aydin *et al.,* 2006; Balsamo *et al.,* 2008; 2010).

Protosediment grain-size, porosity and mineralogy are believed to influence the magnitude of sediment porosity and hydraulic conductivity decrease in fault zones (Antonellini and Aydin, 1994; Balsamo and Storti, 2010; Balsamo *et al.,* 2010). However a direct comparison of porosity decrease in the zones of mixed sediment in gravel and sand was not possible here due to differences in fault throw. Tueckmantel *et al.* (2010) propose that stress conditions are a primary control on fault zone permeability reductions, however, a wide range of porosity values presented here for zones of mixed sediment deformed under similar stress conditions (see Chapter 2) suggests this is would be secondary to fault throw and possibly other factors.

Notably, the lowest porosity, and second lowest hydraulic conductivity of all the thin section samples was found in the cemented zone of mixed sediment sample M CF 2a (Figure 5.3). This suggests that the impact of cementation on fault zone hydraulic conductivity could be greater than any primary fault zone structure.

5.4.2 Fault zone heterogeneity

Estimates of hydraulic conductivity from grain-size distributions show that there is often considerable variability in the hydraulic conductivity of protosediment beds (Figures 5.5 to 5.8). However only in Fault 5 was sediment variability within beds

greater than variability within the mixed zone (Figure 5.7). There are also often considerable contrasts in hydraulic conductivity between the footwall and hangingwall (Figures 5.5 and 5.6), demonstrating the importance of sediment juxtapositions, as suggested by Haneberg (1995). Vertical protosediment heterogeneity generally results in mixed zone heterogeneity from the juxtaposition of different sediment in the mixed zone (Figures 5.5 to 5.8).

5.4.2.1 Sediment smears

Mixed zones cutting vertically heterogeneous sediment can comprise juxtaposed smears of highly contrasting hydraulic conductivity (Figures 5.5 and 5.9). The changes to bedding orientation and distribution transforms anisotropy resulting from this from horizontal in protosediment to sub-vertical in mixed zones (e.g. Zhang and Tullis, 1998; Eichhubl and Boles, 2000; Bense and Person, 2006).

The porosity and hydraulic conductivity of the silt smear in the mixed zone of Akrata Fault 2 (Figures 5.3 and 5.8; Tables 5.2 and 5.3) are comparable to undeformed silts (cf. Freeze and Cherry, 1979), yet even without perceptible grain-scale deformation this smear causes a contrast in hydraulic conductivity across the mixed zone of up to three orders of magnitude. Fine-grained smears such as this could have a similar hydraulic impact to clay smears described by empirical equations for faults in hydrocarbon reservoirs (e.g. Yielding *et al.*, 1997; Sperrevik *et al.*, 2002; Manzocchi *et al.*, 2010) depending on the grain-size distribution of adjacent sediment. The hydraulic conductivity of some smears, such as the gravel smears in the mixed zone of Fault 1A, Loutraki, the sand smear of Fault 1C and the mixed zone of Fault 2, Akrata (Figures 5.5, 5.6 and 5.8), can be higher than adjacent protosediment beds, thus could focus fluid-flow along the fault zone.

Mixing of sediment smears can produce zones of mixed sediment that have a more homogeneous hydraulic conductivity than the protosediment (Figures 5.5 and 5.7). Rawling *et al.* (2001) suggest the hydraulic conductivity of these zones can equal the average of its constituent sediments (Table 5.4). However, the porosity of the thin (10 mm) zone of mixed sediment between the gravel and silt smears in Fault 2, Akrata (Figures 5.3 and 5.8), is 2.3% lower than the silt smear. The estimated hydraulic conductivity of this zone remains slightly higher because the gravel

incorporated into the silt increases the average grain-size (Equations 5.3 and 5.4). Bense *et al.* (2003) suggest that pebbles mixed into the smear in this way may cause preferential fluid-flow pathways, although in this particular sample the proportion of pebbles within the mixed zone is small compared to the thickness of the silt smear, thus connectivity of potential pore spaces or fractures created by inclusion of the pebbles is limited. With increased throw and grain-scale mixing (Figure 4.12) it could be envisaged that this process would cause hydraulically significant discontinuities in the smear.

The significant heterogeneities introduced into fault zones when smears of contrasting hydraulic conductivity are juxtaposed, or beds mix, in the mixed zone supports suggestions from Balsamo and Storti (2011), that hydraulic impact from these processes might exceed that of cataclasis. However, in some cases, such as Fault 5, Loutraki, the hydraulic impact of mixed zones may be less significant than natural sedimentary heterogeneity (Figure 5.7).

5.4.2.2 Lenses and blocks

Similar to smears, lenses and blocks have a considerable impact on the hydraulic conductivity across mixed zones due to the juxtaposition of sediment of contrasting hydraulic conductivity (Figure 5.6). However, lenses and blocks are also likely to cause vertical heterogeneity in the mixed zone. Whilst lenses or blocks of lower hydraulic conductivity sediment could hinder flow across or along the mixed zone, coarser-grained smears surrounding them, such as in Fault 1C, Loutraki (Figure 5.6), could provide a flow path around the lens. Sigda *et al.* (1999) found no perceptible differences in lens hydraulic conductivity compared to the protosediment from which they derive. While the block in Fault 1C, Loutraki is not directly comparable with the sampled protosediment, mean hydraulic conductivity values were also similar (Table 5.5), indicating that the hydraulic conductivity of sediment in lenses or blocks is not vastly altered in mixed zones.

5.4.2.3 Slip-surface cataclasite

The hydraulic conductivity of slip-surface cataclasites was the lowest of the sampled fault zone elements (Figure 5.3) due to the significant reduction in porosity with cataclasis (Chapters 3 and 4). The average porosity reduction of the cataclasite

(absolute porosity 19% lower than mean gravel protosediment and 10% lower than mean zone of mixed sediment gravel) (Figure 5.3 and Table 5.2), is comparable to the porosity reductions of slip-surface cataclasites in high porosity sandstones (14 to 18.2%) reported by Tueckmantel *et al.* (2010). The decrease in hydraulic conductivity was also similar to the range reported by Antonellini and Aydin (1994; 1995) and Tueckmantel *et al.* (2010); from four to seven orders of magnitude lower than the protosediment (Figure 5.3, Table 5.3).

These similarities might suggest that the hydraulic properties of slip-surface cataclasites are relatively constant across a range of fault types and sizes. The very low porosity and hydraulic conductivity of the slip-surface cataclasites supports the suggestion by Tueckmantel *et al.* (2010) that slip surfaces may form the most continuous fluid flow barriers in fault zones without a clay smear. However, slip-surface cataclasites can often be associated with fractures (e.g. Antonellini and Aydin 1994;1995; Shipton and Cowie, 2001), which can increase fault zone permeability by up to four orders of magnitude relative to the host rock (Jourde *et al.*, 2002). The geometry of the slip-surface cataclasites will also introduce mixed zone heterogeneity and anisotropy. Therefore it will be imperative to represent these in models of faults cutting poorly lithified sediment.

5.4.2.4 Disaggregation bands

The considerable difference in porosity and hydraulic conductivity between the two disaggregation bands in sand samples (22% and 44%) (Figure 5.3) supports the speculation in Chapter 4 that the disaggregation band from Disaggregation Band Fault, Voutsimos, is a dilation band (e.g. Du Bernard *et al.*, 2002). A network of such dilation bands in fault damage zones, as was found in damage zones of faults cutting fine-grained sediment in M3 Pirgos and the Disaggregation Band Fault, Voutsimos (Figures 4.5b and 4.8), could facilitate fluid-flow in sediment adjacent to fault zones (e.g. Bense *et al.*, 2003; Balsamo *et al.*, 2008; 2010).

5.4.3 Fault zone anisotropy

Fault zone anisotropy can be caused by mixed zone heterogeneities, such as sediment smears or slip-surface cataclasites, as discussed in section 5.4.2. It can also be caused by differences in flow path tortuosity from grain fabric. Hydraulic anisotropy

resulting from flow path tortuosity is greatest in the horizontal direction in the footwall protosediment and vertical in the mixed zones (Figure 5.9). The magnitude of anisotropy is similar in fault zones and protosediment, despite the suggestion by Maltman (1988) that intrinsic hydraulic anisotropy in fault zones resulting from grain rotation and alignment (in clays) will exceed that resulting from poorly aligned host sediment.

These calculations of relative hydraulic anisotropy only provide a qualitative estimate of its existence and orientation. The measured tortuosity, between 1.03 and 1.33 (Table 5.8), is towards the lower end of tortuosity, 1 to 3.5, modelled numerically for shear zones in clays by Arch and Maltman (1990). The three orders of magnitude permeability anisotropy from flow path tortuosity cited in some works (e.g. Arch and Maltman, 1990; Bense *et al.*, 2003; Van den Berg *et al.*, 2003) is therefore greater than found here, which may be closer to the one and a half orders of magnitude derived from clay shear deformation experiments (Zhang and Cox, 2000) and field permeability measurements of fault zones (Sigda *et al.*, 1999).

However, tortuosity is probably underestimated because only larger clasts were identified and accounted for in the photographs (Figure 5.2). The omission of sediment matrix might have an important impact on estimates of anisotropy, as Murray and Dowdeswell (1992) found that the matrix can have a greater impact on flow path tortuosity than clasts. In addition, differences in alterations to pore radii in the fault parallel and perpendicular directions will also impact the hydraulic anisotropy, as permeability decrease has been found to be lower parallel to the shear zone (Dewhurst *et al.*, 1996; Wilson *et al.*, 2003).

5.5 Summary

The porosity and hydraulic conductivity of zones of mixed sediment are generally lower than their protosediment. Some variability in porosity and hydraulic conductivity values can be attributed to fault throw, as porosity and hydraulic conductivity decrease with increasing fault throw. Numerical fluid-flow models should account for the differences in hydraulic properties with fault size. However, the greatest decrease in both porosity and hydraulic conductivity occurs during the first 2 m of fault throw, such that even small faults will have significant impacts on

fault zone hydraulic properties. These findings support the models of mixed zone evolution by controlled particulate flow and strain hardening proposed in Chapters 3 and 4. Differences in flow path tortuosity resulting from preferential grain alignment in mixed zones can cause a rotation of hydraulic anisotropy from horizontal in protosediment, to vertical in the mixed zone, though values estimated here may be slightly low.

Hydraulic heterogeneity can result from sediment juxtaposition across fault zones, and in mixed zones due to smears or lenses and blocks. Juxtaposition effects in and across fault zones are greatest where protosediment beds are highly variable, and may dominate over grain-scale deformation processes in the mixed zone. Structural heterogeneities resulting from very low hydraulic conductivity fine-grained smears along the mixed zone, and low-permeability slip-surface cataclasites could create effective barriers to fluid flow, in addition to anisotropy. Heterogeneities should be explicitly represented in numerical fluid-flow models.

6. Numerical fluid-flow models representing fault zones in poorly lithified sediment

6.1 Introduction

This chapter brings together the results from the preceding chapters to investigate the possible hydraulic impacts of faults cutting poorly lithified rift sediment of the Gulf of Corinth rift. Fault zone hydrogeological structure presented in Chapters 3 to 5 have shown that fault zones cutting syn-rift sediment of the Gulf of Corinth rift are often heterogeneous; with variable mixed zone thickness, structural elements and hydraulic conductivity. A range of hydraulic impacts may be anticipated from these fault zones – the specifics of which can be identified through numerical models of these fault zones (e.g. Yang *et al.,* 2004; Bense and Person, 2006). The hydraulic impacts of a range of fault zones representing those found within poorly lithified sediment, sediment of contrasting competency, and faults that juxtapose fine and coarse-grained sediment within the Gulf of Corinth rift, described in Chapters 3 to 5, are investigated in this chapter using numerical fluid-flow models.

Deterministic numerical modelling approaches can explicitly represent fault zone structural and flow path complexities, in addition to assessing along-fault fluid-flow (Jourde *et al.,* 2002; Lunn *et al.,* 2008), critical for hydrogeological investigations. However, this approach requires detailed mapping of fault zone structural elements of individual faults, generally at outcrop, along with identification of their hydraulic properties, so that they can be explicitly represented in the numerical fluid-flow model. The hydraulic behaviour of fault zones determined by this method is highly dependent on the specific fault or faults being investigated, and is therefore not feasible for investigating the hydraulic behaviour of a range of subsurface faults (Foxford *et al.,* 1998; Jourde *et al.,* 2002; Lunn *et al.,* 2008).

Stochastic approaches can produce statistically sound representations of heterogeneous fault zones, and, by the very nature of this approach, also represent uncertainties (Walsh *et al.,* 1998; James *et al.,* 2004; Fredman, 2007; Lunn *et al.,* 2008; Braathen *et al.,* 2009). Nevertheless, for stochastic methods to be meaningful, a large quantity of data is required to establish robust empirical relationships between

independent (e.g. fault throw and lithology) and dependent (e.g. mixed zone thickness, structure and hydraulic conductivity) fault properties.

Numerical models developed and presented here have drawn on aspects of both deterministic and stochastic approaches. Fault zones were depicted as two-dimensional hydrogeological units, representing the mixed zone, in which structural elements and juxtapositions are explicitly represented in finite-element numerical models. Fault zone structure was conceptualised using the relationships with lithology and fault throw ascertained in Chapter 4, and assigned corresponding hydraulic properties identified in Chapter 5. Simplification of mixed zone properties enabled simulation of a substantial number of model realisations for faults of different sizes cutting the most common lithologies found in the Gulf of Corinth rift, and with a range of realistic input parameters. This suite of fluid-flow models allowed quantification of the range and most likely fault hydraulic behaviours. In addition, the sensitivity of fault hydraulic behaviour to different mixed zone parameters has been analysed.

Evidence for fluid-flow around fault zones at the five outcrop locations is summarised and discussed in terms of its implications for fault zone hydraulic behaviour in the Gulf of Corinth rift sediment in order to assess model results in a real-world context. Evidence for fluid-flow includes present day evidence, in the form of springs (e.g. Heffner and Fairley, 2006; Anderson and Fairley, 2008; Dockrill and Shipton, 2010) or vegetation (Catchings *et al.,* 2009). Evidence of previous fluid-flow that can persist in outcrop, in the form of cements and mineral precipitates (e.g. Foxford *et al.,* 1998; Heynekamp *et al.,* 1999; Eichhubl and Boles, 2000; Sigda and Wilson, 2003; Dockrill and Shipton, 2010) is also considered, since considerable fluid-flow is generally required in order to deposit such concentrations of minerals (Travé *et al.*, 2009).

The development of numerical fluid-flow models, including a description of model software and governing equations, and model conceptualisation and specification of input parameters, are now described. This is followed by details of the approach used for fluid-flow indicator analysis from the model output. The suite of model results for faults cutting poorly lithified sediment, sediment of contrasting competency and juxtaposed fine and coarse-grained sediment are then combined and presented. Fault

zone hydraulic behaviours have been interpreted in terms of their potential to behave as conduits, barriers or a combination of both. The primary causes for these behaviours are discussed. Methods for analysing evidence of fluid-flow around fault zones at outcrop are presented and analysed, and the implications of these findings discussed in terms of fault zone hydraulic behaviour.

6.2 Fluid-flow analysis of fault zones

6.2.1 Developing numerical fluid-flow models

Numerical fluid-flow models were designed to represent the topographically driven, saturated hydraulic flow conditions of the southern flank of the Gulf of Corinth rift (Figure 2.1 and 6.1) (e.g. Giurgea *et al*., 2004; Micarelli *et al.,* 2006b). Two-dimensional steady-state fluid-flow was solved for hydraulic head, using FlexPDE 5 (PDE Solutions, 2009), a "scripted finite element model builder and numerical solver for Partial Differential Equations". Finite element models are preferable to finite-grid methods in which the properties of small-scale features are rasterised and averaged across grid squares (e.g. Bredehoeft *et al.,* 1992; Jourde *et al.,* 2002). Variable mesh spacing within the numerical models enabled efficient flow simulations because smaller-scale structures could be depicted in higher resolution than large-scale homogeneous domains.

Saturated fluid-flow in the numerical fluid-flow models was described by Darcy's law (Equation 6.1):

$$Q = -KA\,\frac{\partial h}{\partial l} \qquad \textbf{Equation 6.1}$$

where Q is the total discharge (m^3), K is the hydraulic conductivity ($m\ s^{-1}$), A is the cross sectional area of flow (m^2), and ∂h the change in head over the change in distance, ∂l (i.e. the hydraulic gradient). The hydraulic head at any point in the domain is solved using the 2D Laplace equation for steady-state saturated flow, which describes conservation of mass (no net fluid-flow) in the domain area (assuming constant fluid density) (Equation 6.2), where x and y are orientations:

$$\frac{\partial^2 h}{\partial x^2} + \frac{\partial^2 h}{\partial y^2} = 0 \qquad \textbf{Equation 6.2}$$

Flow vectors and streamtraces indicative of fluid-flow pathways are calculated from the specific discharge (q) (discharge per unit area) in the x and y directions from the hydraulic head, using Equation 6.3:

$$q_x = -K_x \left(\frac{\partial h}{\partial x}\right)$$

$$q_y = -K_y \left(\frac{\partial h}{\partial y}\right) \qquad \textbf{Equation 6.3}$$

Confined flow conditions from south to north (CS) were used for the majority of flow models by imposing a head gradient from left to right across the domain. This was done by prescribing 10 m head along the left domain boundary and 0 m along the right domain boundary, and no-flow boundaries along the top and bottom of the domain (Table 6.1). The impact of varying hydraulic boundary conditions on fault hydraulic behaviour was investigated using a number of representative fault zone models. The topographic flow direction was first reversed, such that it represented confined flow from the north to the south (CN), secondly, topographic flow direction was kept constant (south to north) but shallow, unconfined flow conditions (US) were simulated in which upwelling was allowed to occur in the downstream region of the domain (Figure 6.1; Table 6.1).

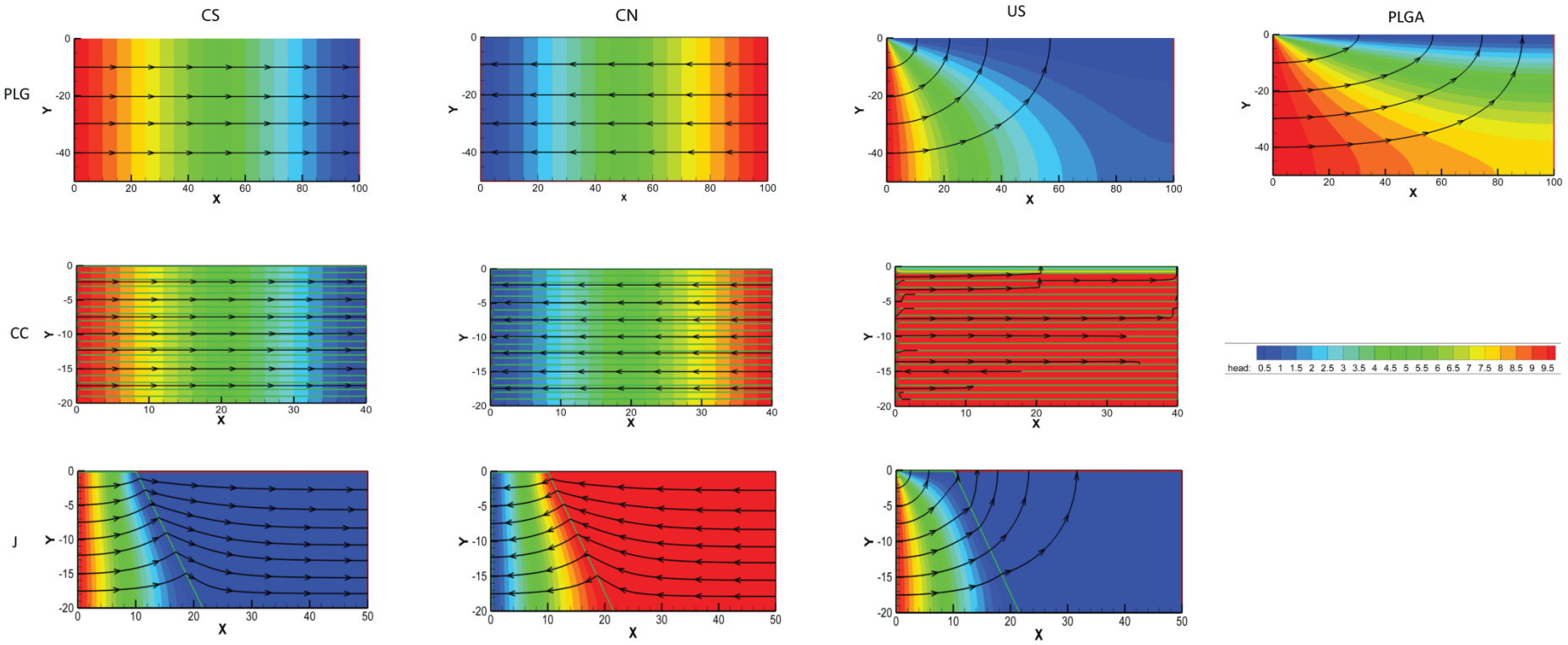

Figure 6.1 Model domains for different model sets in: poorly lithified gravels (PLG), sediment of contrasting competency (CC) and juxtaposed fine and coarse-grained sediment (J), under boundary conditions representing confined flow from south to north (CS), confined flow from north to south (CN), and unconfined flow from south to north (US). Domain flow conditions were only altered by anisotropy for the PLGA (anisotropic poorly lithified gravel) domain shown. Values of head contours (colours) shown in legend. Black lines with arrows show streamtraces indicating flow direction. Model domains are not shown to scale and vary between model sets. Model domain parameters are detailed in Table 6.1. Head, X and Y units are metres.

Parameter	PLG	CC	J
Y-axis distance	100 m	40 m	50 m
X-axis distance	50 m	20 m	20 m
Fault dip	60^{o} N	60^{o} N	60^{o} N
Hydraulic boundary conditions, CS	10 m head prescribed to the left Y-axis boundary; 0 m head prescribed to the right Y-axis boundary; X-axes no flow boundaries.		
Hydraulic boundary conditions, CN	10 m head prescribed to the right Y-axis boundary; 0 m head prescribed to the left Y-axis boundary; X-axes no flow boundaries		
Hydraulic boundary conditions, US	10 m head prescribed to the left Y-axis boundary; 0 m head prescribed to the top X-axis boundary; right Y-axis and bottom X-axis prescribed no flow boundaries.		
Lithology	Homogeneous gravel.	Alternating silt and gravel beds, both 1 m thick.	Footwall homogeneous silt, hangingwall homogeneous gravel.
Hydraulic conductivity	9.87×10^{-3} m s $^{-1}$	1×10^{-3} m s $^{-1}$ (gravel) 1×10^{-8} m s $^{-1}$ (silt)	1×10^{-8} m s $^{-1}$ (silt) 1×10^{-3} m s $^{-1}$ (gravel)
Protolith anisotropy	$Ky = 0.1Kx$	$Ky = 0.1Kx$	$Ky = 0.1Kx$

Table 6.1 Model domain parameters for different model sets, shown in Figure 6.1. PLG is poorly lithified gravels, CC is sediment of contrasting competency and J is juxtaposed fine and coarse-grained sediment. Boundary conditions refer to confined flow from the south (CS), confined boundary conditions from the north (CN) and shallow, unconfined flow from the south (US). *K* is hydraulic conductivity. X and Y are the horizontal and vertical directions.

Models were divided into three sets based on the different lithologies in which the different fault zone structures were found; poorly lithified sediment, sediment of contrasting competency and fault zones juxtaposing fine and coarse-grained sediment (Chapters 3 and 4). Model parameters were chosen to represent the most common lithology for each set found within the Gulf of Corinth rift; poorly lithified gravels (PLG); alternating beds of silt and gravels (CC) and juxtaposed silt (footwall) and gravels (hangingwall) (J) (Figure 6.1, Table 6.1). Hydraulic properties of sediment or beds within the domains were assumed to be homogeneous. Domain parameters were kept the same throughout the model runs, though both isotropic and anisotropic conditions were investigated. Domain hydraulic conductivity and anisotropy values (Table 6.1) were ascertained from a combination of the image analysis results of protosediment samples in Chapter 5 and ranges specified within the literature (cf.

Freeze and Cherry, 1979; Arch and Maltman, 1990; Brassington, 1998; Dewhurst *et al.*, 1999; Giurgea *et al.*, 2004; Hiscock, 2005; Micarelli *et al.*, 2006b; Zappa *et al.*, 2006). Differences in model domain dimensions between the sets (Figure 6.1, Table 6.1) were necessary due to computational difficulties simulating some small-scale fault heterogeneities within larger domains.

A fault zone dip of 60^{o} N was assigned to all models, such that in the majority of models groundwater would flow from the footwall to hangingwall, representing the most common condition in the Gulf of Corinth rift, where the majority of faults dip towards the centre of the rift (Figures 2.1 and 2.2). The fault zone comprised only a mixed zone, and extended the depth of the model domain and fault (mixed) zone thickness was kept constant along-dip. Key fault parameters and attributes – mixed zone thickness, structural elements, and hydraulic conductivity – were varied according to the ranges found in outcrop, and specific to the fault throw and lithology as found in Chapters 4 and 5 (Tables 6.2 and 6.3). Mixed zone parameters used for each model run were varied between each model run. These are detailed in Appendices 4 to 6. Mixed zone anisotropy was primarily determined from estimates presented in the literature (e.g. Person *et al.*, 2000; Bense and Person, 2006; Anderson and Bakker, 2008). Anisotropy used in the models was slightly greater than estimated in Chapter 5 based on grain orientation data, because it also accounts for additional anisotropy due to rotated and smeared beds that could not be explicitly represented in the modelled mixed zones (e.g. Jourde *et al.*, 2002; Bense and Person, 2006; Magri *et al.*, 2010). Damage zones were omitted from the models in order to simplify fault zone hydraulic behaviour analysis.

Mixed zone thickness	**PLG Sm**	**PLG Lg**	**CC**		**J**
	1 m	**5 m**	**1 m**	**5 m**	**20 m**
Minimum (m)	0.2	0.8	0.08	n/a	n/a
Average (m)	0.3	1	0.2	n/a	1
Maximum (m)	0.4	1.5	0.4	0.7	n/a

Table 6.2 Minimum, average and maximum mixed zone thickness values for each model set. PLG Sm refers to models of small faults in poorly lithified gravels, and PLG Lg refers to large faults in poorly lithified gravels. CC is sediment of contrasting competency and J is models in which fine and coarse-grained sediment are juxtaposed across the fault zone.

Structural element	Description of characteristics	Hydraulic conductivity
Smear	Gravel smear along the fault zone with grain-scale characteristics unchanged from the protosediment. Where included in models anisotropy is *Ky*=100**Kx*.	Average 9.87×10^{-3} m s^{-1}
Zone of mixed sediment	Continuous zone of mixed sediment along the fault zone except where overlain by other structural elements. Where included in models anisotropy is *Ky*=100**Kx*.	PLG and J, minimum 1.63×10^{-5} m s^{-1} PLG Lg and J, average 2.92×10^{-4} m s^{-1} PLG Sm, average 1×10^{-3} m s^{-1} PLG Sm and J, maximum 8.5×10^{-2} m s^{-1} CC 1.65×10^{-5} m s^{-1}
Slip-surface cataclasite	Two planar slip-surface cataclasites 20 mm thick, in large faults only. 1. From the top of the domain at the footwall-mixed zone contact to 2/3 down the fault dip 2. From 1/3 down the fault dip at the hangingwall-mixed zone contact to the lower domain boundary.	PLG Lg and J, minimum 9.83×10^{-8} m s^{-1} PLG Lg and J, average 6×10^{-7} m s^{-1} PLG and J, maximum 6×10^{-5} m s^{-1}
Lenses	Elongate lenses of undeformed silt between the footwall and hangingwall silt beds. Lenses of coarse sediment are included between fine lenses in some models. The number of lenses varies from multiple across the fault zone, to lenses every other silt bed. Lenses in minimum, average and maximum thickness mixed zones are 0.04, 0.18 and 0.2 m thick respectively. Thin lenses are 0.05 m thick for the average thickness mixed zone.	CC, fine sediment 1×10^{-8} m s^{-1} CC, coarse sediment 1×10^{-3} m s^{-1}
Fine-grained smear	Continuous smear of fine-grained sediment along the mixed zone dip, usually 9 mm thick. Thickness varied to 50 mm and 1 mm, and with small (50 mm) or large (3 m) discontinuities.	CC, 1×10^{-8} m s^{-1} (+/- 1 OM)

Table 6.3 Description of modelled fault zone structural elements and the models set they are included in, with parameter values. X and Y refer to orientations of anisotropy. OM is order of magnitude.

Models in poorly lithified gravels (PLG) were sub-divided into two sets with small (PLG Sm) and large (PLG Lg) faults, reflecting the differences in mixed zone thickness, structural elements and hydraulic conductivity with fault throw (Chapters 4 and 5) (Table 6.2). Runs were completed for 28 models of faults with small throws (<1 m). These comprised gravel smears (PLG Sm 1) or zones of mixed sediment

(PLG Sm 2). Runs were completed for 45 models of faults with large throws (>5 m). These comprised zones of mixed sediment with (PLG Lg 2) or without (PLG Lg 1) slip-surface cataclasites (Figure 6.2). Most slip-surface cataclasites were discontinuous, with a step-over region between them (Table 6.3).

Fault throw was not varied in models with sediment of contrasting competency (CC) (Table 6.2), because bed thickness relative to fault throw is likely to be a greater control on fault zone structure (Chapter 4). Combinations of fault zone structural elements varied more widely in the 82 CC model runs than the PLG models. Fault zone elements included a varying number of fine sediment lenses, with or without associated coarse sediment lenses, and fine-grained smears with variable continuity. The remainder of the fault zone volume was assigned properties of a zone of mixed sediment or unmixed gravels (Figure 6.2, Table 6.3).

Fault size was also not varied in the 23 model runs of fault zones juxtaposing fine and coarse-grained sediment (J), because the three faults of this type had throws >17 m (Chapter 4) (Table 6.2). The specific combinations of fault zone structural elements were varied in these models. The impact of changing structural element parameter values was assumed to be the same as the previous model sets and therefore generally only the average parameter values were modelled (Figure 6.2, Table 6.3).

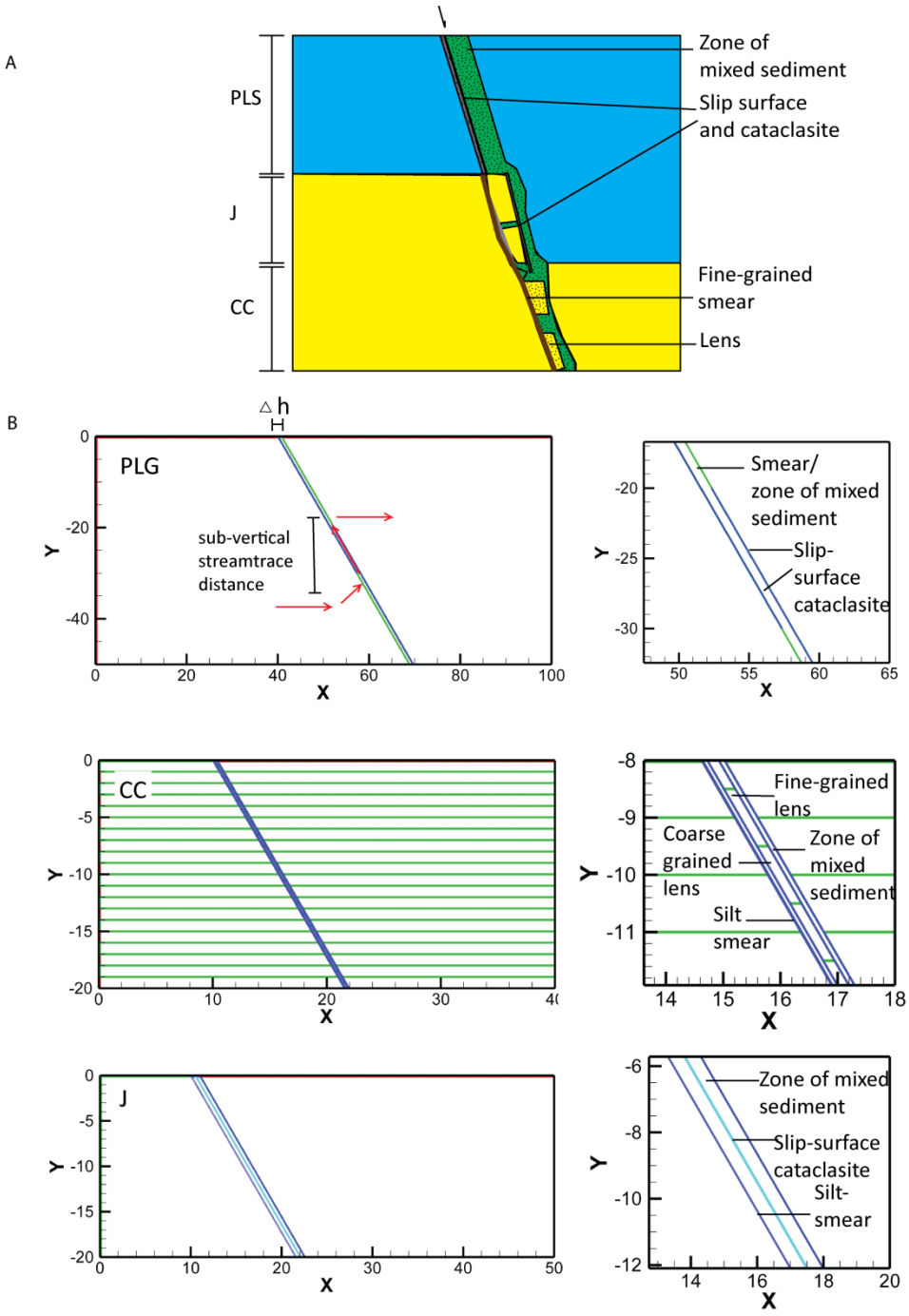

Figure 6.2 A. Simplified conceptual model of fault zones based on Figure 4.13. B) Fault zone setups in numerical models (left) and close-ups of fault zones (right). Fault zone details are in Table 6.3. In PLG models, slip-surface cataclasites were not always included, and properties of the mixed zone varied between a zone of mixed sediment or sediment smears; CC models had various combinations of lenses, a zone of mixed sediment and silt-smear; J models had various combinations of a zone of mixed sediment, slip surface cataclasite and silt smear. Δ *h* shows the location the head-drop was measured across the fault zone, along the top of the domain, and red arrows show examples of streamtraces with the maximum sub-vertical streamtrace distance measurement (Table 6.4).

6.2.2 Model result analysis

The range of possible and most likely fault zone hydraulic behaviours, in terms of their capacity to behave as conduits and/ or barriers to fluid-flow, were analysed for each model set using a range of model output parameters. Sensitivity of the fault-zone hydraulic behaviours to model input parameters was also assessed, in addition to particular fluid-flow pathways.

The capacity of a fault zone to behave as a barrier to fluid-flow was inferred from the magnitude of the stepped decrease in hydraulic head (head-drop), measured across the top of the model domain (Figure 6.2) as shown on output graphs (e.g. Bense and Person, 2006). The conduit behaviour of a fault zone was inferred from the maximum sub-vertical fluid-flow distance, along, or adjacent to, the mixed zone, as indicated by the maximum sub-vertical stream-trace distance (Figure 6.2). Sub-vertical fluid-flow, rather than along-fault fluid-flow, was used to describe the conduit-behaviour of the fault zones, so that sub-vertical fluid-flow caused by the mixed zone, but not occurring along the mixed zone itself, could be included. Whether sub-vertical fluid-flow is along-fault or adjacent to the fault (i.e. deflected) was specified in the results. Characteristic head contour, flow vector and streamtrace patterns, provided by FlexPDE and Tecplot 360 offer further information as to the behaviour of faults. In particular, these were used to infer fluid-flow pathways. Patterns for each model set were summarised as "types" and qualitatively analysed (Table 6.4; Appendices 4 to 6).

Output parameter	Description
Head-drop	The maximum difference in head across the top of the fault zone (Figure 6.2).
Head contour type	The pattern of head contours showing the distribution of head values across the domain (Appendices 4.4 and 5.2).
Flow vector type	The pattern of flow vectors showing the velocity and direction of the fluid-flow at each point across the domain. (Appendices 4.5, 5.3 and 6.2).
Streamtrace type	The pattern of streamtraces showing the pathways in which fluid will flow across the domain. (Appendices 4.6, 5.4 and 6.3)
Sub-vertical streamtrace distance	The maximum distance of the sub-vertical component of the streamtrace along or deflected adjacent to the mixed zone (Figure 6.2).

Table 6.4 Description of model output parameters used in analysis of mixed zone hydraulic behaviour.

The conduit, barrier and conduit-barrier behaviours of modelled fault zones were ascertained by plotting the maximum sub-vertical streamtrace distance against the head-drop across the fault. Models that caused only sub-vertical fluid-flow were considered conduits, those that caused only a head-drop were considered barriers, and those that caused both sub-vertical fluid-flow and a head-drop were considered conduit-barriers. Fault zones that caused neither sub-vertical fluid-flow nor a head-drop were considered to have no impact on fluid-flow. The most probable fault zone hydraulic behaviour was revealed either by clustering of models on these plots, indicating similar hydraulic behaviour (sets CC and J), or by directly assessing the hydraulic impact of models in which the mixed zone had average input parameters (set PLG). The most significant fault hydraulic impacts were deduced from the maximum head-drop or streamtrace distance produced from the model set. Groups of model behaviours were assessed for common input parameters.

6.2.3 Analysis of outcrop evidence of fluid-flow

Each outcrop was assessed for evidence of fluid-flow. Evidence of present day fluid-flow included springs and vegetation. The distribution of these, and precipitates and cements were mapped at each outcrop. Only cements that had an association with fault zones were analysed as this indicated that they post-date fault formation. The composition of cements and precipitates was identified through thin section analysis using a petrographic microscope. At the Mentourgianika outcrop the proportion of the well-exposed fault zones that were cemented was visually identified. Inferences were made about the patterns of fluid-flow at the outcrops and the significance of fault zone hydraulic behaviour, and compared with models results.

6.3 Numerical fluid-flow model results

Fault zone hydraulic behaviour from model outputs are summarised in this section. Model outputs are presented in terms of their relative hydraulic impacts because hydraulic conditions were enforced and fault zone and model domains idealised therefore specific sub-vertical streamtrace distance and head-drop values are unlikely to be exactly replicated in reality. A complete record of input parameters and output model data can be found in Appendices 4 to 6.

6.3.1 Faults in poorly lithified gravels (PLG)

Faults in PLG models produced a large range of head-drop and sub-vertical streamtrace distances (Figure 6.3), head contour, flow vector, and streamtrace patterns (Appendix 4). Hydraulic behaviour of these fault zones is predominantly conduit-barrier, though a number of models exhibit exclusive conduit or barrier behaviour (Figure 6.3). In addition, a number of fault models show minimal hydraulic impacts.

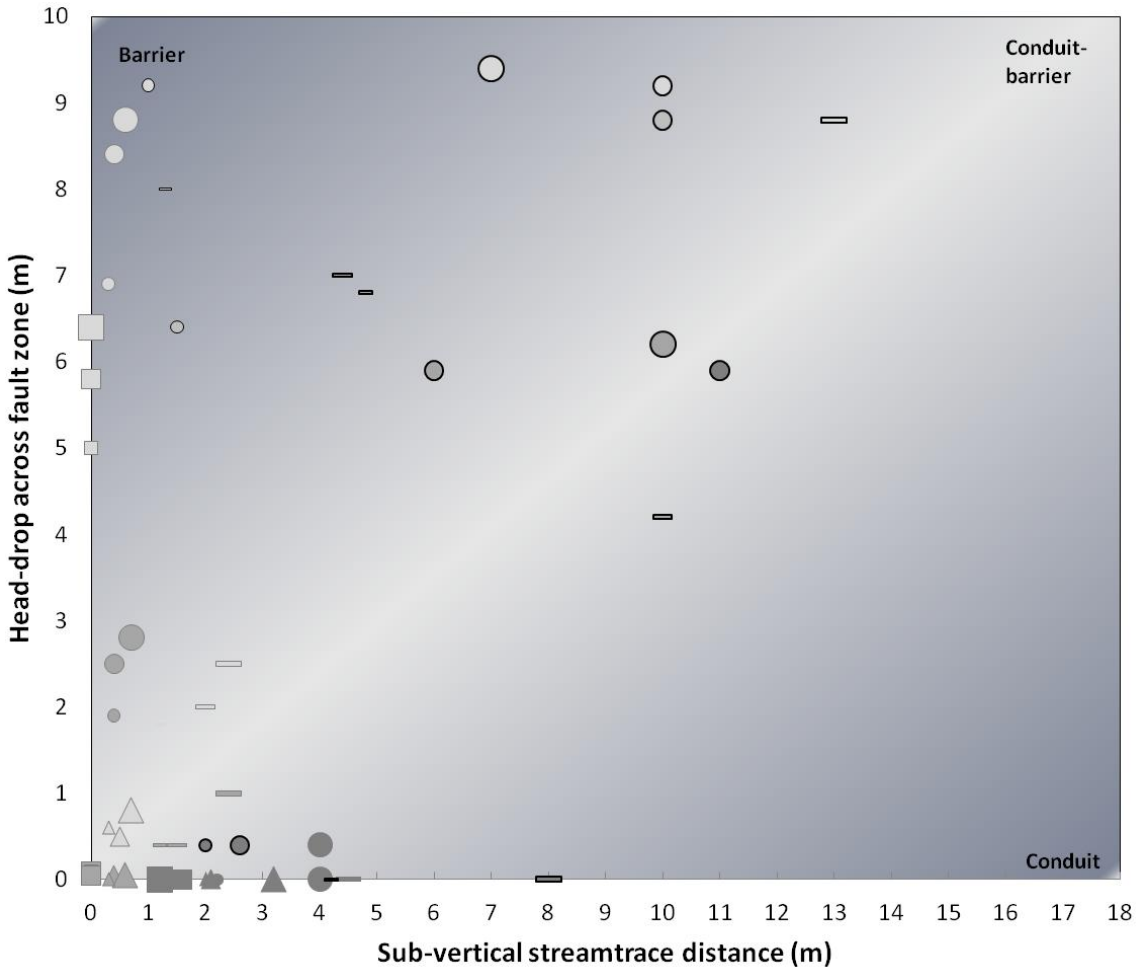

Figure 6.3 Modelled head-drop across the fault zone with maximum sub-vertical streamtrace distance, for all PLG models. Squares and triangles represent isotropic and anisotropic PLG Sm 2 models respectively (PLG Sm models have no hydraulic impact) (Appendix 4.1). Circles and lines represent isotropic and anisotropic PLG Lg models respectively. Outlined markers indicate the presence of slip-surface cataclasites. Light, medium and dark grey are the minimum, average and maximum zone of mixed sediment hydraulic conductivity; small, medium and large shapes represent the minimum, average and maximum mixed zone thickness specific to the model set (Table 6.2). Shading refers to the overall hydraulic behaviour of faults as identified in the graph corners.

6.3.1.1 Small faults in poorly lithified gravel (PLG Sm 1 and 2)

The majority of small faults modelled in poorly lithified gravels have no (PLG Sm 1), or limited (PLG Sm 2) hydraulic impact (Figure 6.3, Appendix 4.1). All sub-vertical fluid-flow in these models is along-fault. The PLG Sm 2 model with mixed zone input parameters of average values (i.e. mixed zone thickness and zone of mixed sediment hydraulic conductivity) experienced a small head-drop but no sub-vertical flow under isotropic conditions, and a minimal head-drop and slightly greater along-fault flow under anisotropic conditions (Figure 6.4). The maximum head-drop across the fault zone was caused by the fault with maximum mixed zone thickness and minimum zone of mixed sediment hydraulic conductivity in an isotropic model, and was significantly greater than the faults with average parameters (Figure 6.4). In this, and other isotropic models in which the zone of mixed sediment hydraulic conductivity was less than the protosediment, there was no associated sub-vertical flow (Figure 6.3). Likewise, models in which mixed zones had a zone of mixed sediment with maximum hydraulic conductivity produced the longest sub-vertical fluid-flows (the longest of which occurred in an anisotropic model with maximum mixed zone thickness), but did not cause a head-drop across the fault zone (Figures 6.3 and 6.4).

Of all the input parameters of the PLG Sm model sub-set, the zone of mixed sediment hydraulic conductivity and anisotropy were found to have the greatest effect on the fault zone hydraulic behaviour. Relative hydraulic conductivity of the zone of mixed sediment to the protosediment influenced whether faults primarily exhibited a head-drop across the fault zone or along-fault sub-vertical fluid-flow (hydraulic conductivity of the zone of mixed sediment < or > hydraulic conductivity of the protosediment, respectively). Furthermore, there was an order of magnitude difference in head-drop across the fault zone between faults with the minimum or average zone of mixed sediment hydraulic conductivity (a difference itself of two orders of magnitude) (Figure 6.3).

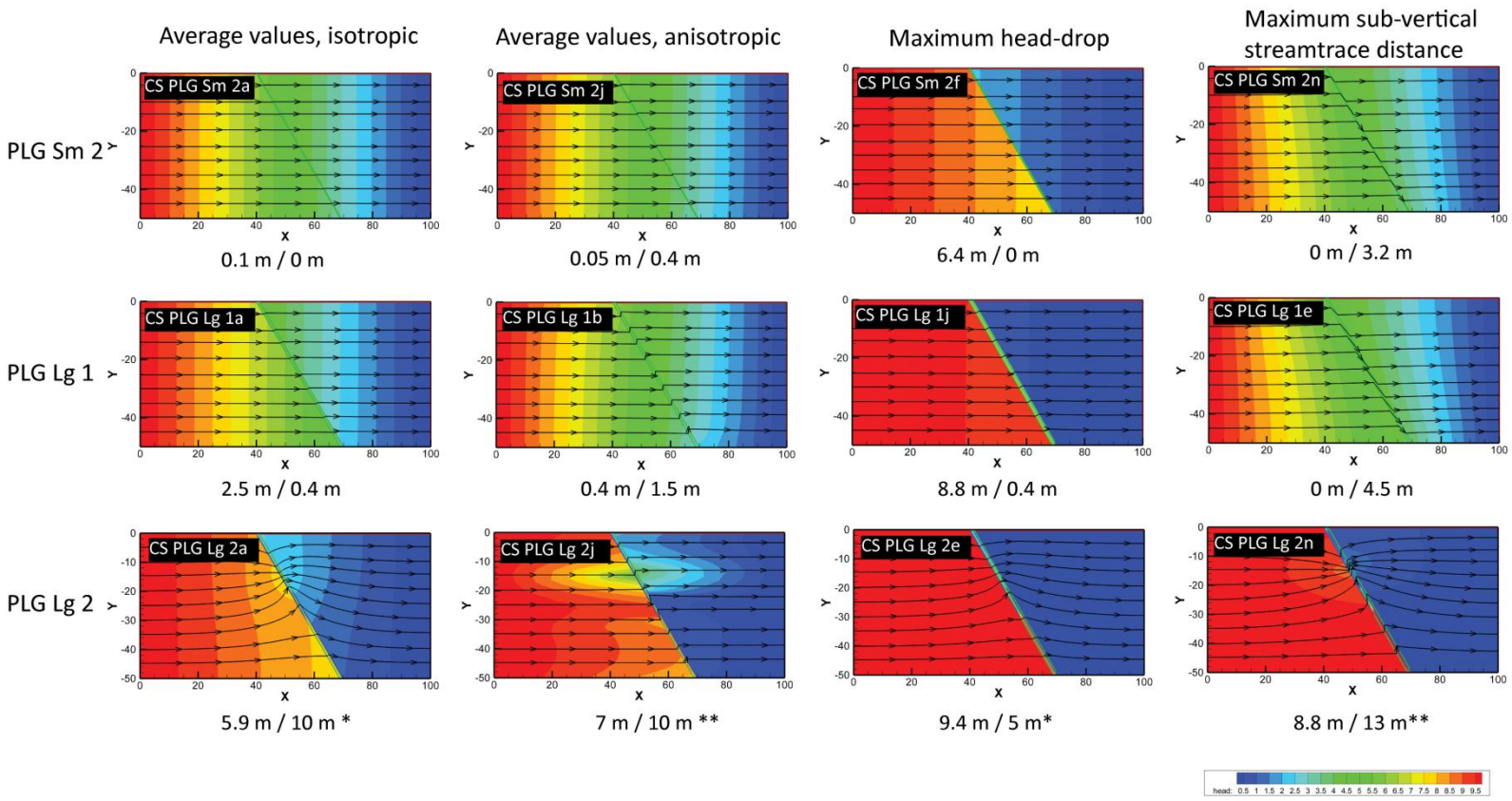

Figure 6.4 Model outputs with head contours and streamtrace patterns for average mixed zone parameter values for both isotropic and anisotropic conditions for PLG Sm 2, PLG Lg 1 and 2 models. Head-drop and maximum sub-vertical streamtrace distance included under the domain images (respectively) for each model. PLG Sm 1 models not included because the fault zones did not impact fluid-flow. * indicates deflected flow, ** indicates deflected and along-fault. Model codes in top left corners (Appendix 4.1 to 4.3). Head, X and Y units are metres.

Including anisotropy in models increased sub-vertical fluid-flow distance, and caused a simultaneous decrease in head-drop across the fault zone, of up to an order of magnitude. Anisotropy also caused the refraction of head contours towards or away from the fault dip (hydraulic conductivity of the zone of mixed sediment > and < hydraulic conductivity of the protosediment, respectively) (Figure 6.4). Mixed zone thickness did not influence the type of fault hydraulic behaviour but magnified the impacts, with a difference in minimum and maximum mixed zone thickness of 0.2 m increasing the magnitude of head-drop and sub-vertical fluid-flow distance across the fault zone by seven and six times respectively.

Altering the model hydraulic boundary conditions to north-south confined flow (CN) and in particular, shallow, unconfined south-north flow (US), resulted in changes to the head contour, vector and streamtrace patterns. Models with US boundary conditions caused fluid-flow to be focused along the mixed zone, particularly towards the top of the fault zone. For CN boundary conditions the behaviours were reversed (Appendix 4.1). The specific interactions of fault zones and fluid did not differ.

6.3.1.2 Large faults in poorly lithified gravel (PLG Lg 1 and 2)

Faults in the PLG Lg model sub-set predominantly behaved as conduit-barriers. The magnitude of conduit and barrier behaviour of fault zones in PLG Lg models was greater than for the PLG Sm models (Figures 6.3 and 6.4; Appendix 4.2 and 4.3).

Similar to PLG Sm 2 models, in PLG Lg 1 models the maximum head-drop across the fault zone was found in an isotropic model with minimum zone of mixed sediment hydraulic conductivity and maximum mixed zone thickness. The minimum sub-vertical fluid-flow again occurred in isotropic models of fault zones with minimum zone of mixed sediment hydraulic conductivity and mixed zone thickness. The maximum sub-vertical streamtrace distance (along-fault) occurred along faults with the zone of mixed sediment maximum hydraulic conductivity, under anisotropic conditions (Figure 6.4). These fault zones did not cause a head-drop across the fault zone.

Again, similar to the PLG Sm 2 models, relative hydraulic conductivity of the zone of mixed sediment and protosediment influenced whether faults in the PLG Lg models behaved predominantly as conduits or barriers. The order of magnitude variation in minimum or average zone of mixed sediment hydraulic conductivity resulted in a maximum head-drop difference of nearly three times. There was a greater difference in conduit and barrier effects between the thickest and thinnest mixed zones of the PLG Lg than PLG Sm models, corresponding to a maximum difference in mixed zone thickness of 0.7 m (PLG Lg) compared with 0.2 m (PLG Sm). Anisotropic models again resulted in smaller head-drops but an increase in sub-vertical streamtrace distance, in addition to refracted head-contours.

Including slip-surface cataclasites in PLG Lg models had the most profound impact on the hydraulic behaviour across the PLG models – increasing both barrier and conduit behaviours (Figure 6.3; Appendices 4.2 and 4.3). The maximum head-drop of PLG Lg 2 models occurred in an isotropic model with a maximum thickness mixed zone and minimum hydraulic conductivity fault zone elements. However, this was only marginally greater than the maximum head-drop in PLG Lg 1 models.

The maximum along-fault sub-vertical fluid-flow was significantly greater in PLG Lg 2 models, with the maximum distance found in anisotropic models and faults with maximum hydraulic conductivity. In isotropic PLG Lg 2 models, the majority of sub-vertical fluid-flow did not occur along the mixed zone, but directly adjacent to the mixed zone (Figure 6.4). The greatest sub-vertical streamtrace distance in PLG Lg 2 models resulted from this flow, and was nearly three times the maximum along-fault streamtrace distance from PLG LG 1 models (Figure 6.4). The irregular head contour, flow vector and streamtrace patterns in PLG Lg 2 models revealed that flow pathways were deflected by slip-surface cataclasites, as fluid was focused along the boundary of the cataclasites, and through the step-over between the over-lapping regions of the slip-surface cataclasite (Figure 6.4).

The model with the continuous slip-surface cataclasite produced the same head-drop across the fault zone as the segmented slip-surface cataclasite. However, the

maximum sub-vertical streamtrace distance was 5 m shorter. This resulted from cross fault fluid-flow being focused through the centre of the mixed zone. Streamtraces and vectors were still focused along the boundary of the slip-surface cataclasites (Appendix 4). The minimum sub-vertical streamtrace distance in the PLG Lg 2 models occurred in the isotropic mixed zone with minimum hydraulic conductivity fault zone elements and mixed zone thickness.

Hydraulic conductivity also had an impact on fault zone hydraulic behaviour in PLG Lg 2 models. The difference in mixed zone thickness increased the magnitude of sub-vertical fluid-flow to a much greater degree than the head-drop. Furthermore, thicker faults in isotropic models were more likely to cause deflected sub-vertical fluid-flow than along-fault flow. The decrease in head-drop across fault zones in anisotropic models was smaller than for faults in PLG Lg 1 models. In some anisotropic models head-drop even increased slightly. Sub-vertical streamtrace distance still increased along the fault in anisotropic models but deflection distance decreased (Appendix 4).

Similar to PLG Sm models, applying CN hydraulic boundary conditions to PLG Lg models resulted in reversal of the hydraulic patterns. US hydraulic boundary conditions again resulted in fluid-flow focused towards the top of the fault zone (Appendix 4). The interactions of the fault zone with fluid-flow did not differ.

6.3.2 Faults in sediment of contrasting competency (CC)

All the modelled faults cutting sediment of contrasting competency impacted fluid-flow (Figure 6.5). There was a smaller range of hydraulic behaviours than the models of faults in PLG models, and the majority behave as strong barriers to fluid-flow (Figure 6.5; Appendix 5).

Two fault zones, in isotropic CC models with minimum and average thickness mixed zones and minimum hydraulic conductivity silt smears, caused the maximum possible (10 m) head-drop across the fault zone (Figure 6.6). This was similar to the modal average head-drop values (clustering in top left of Figure 6.5). There was no head-drop across the fault zone with only an anisotropic zone of mixed sediment or the model with a large fault and only lenses in the mixed

zone (Appendix 5). Head contours were generally deflected to some degree by the fault zone (Appendix 5.2).

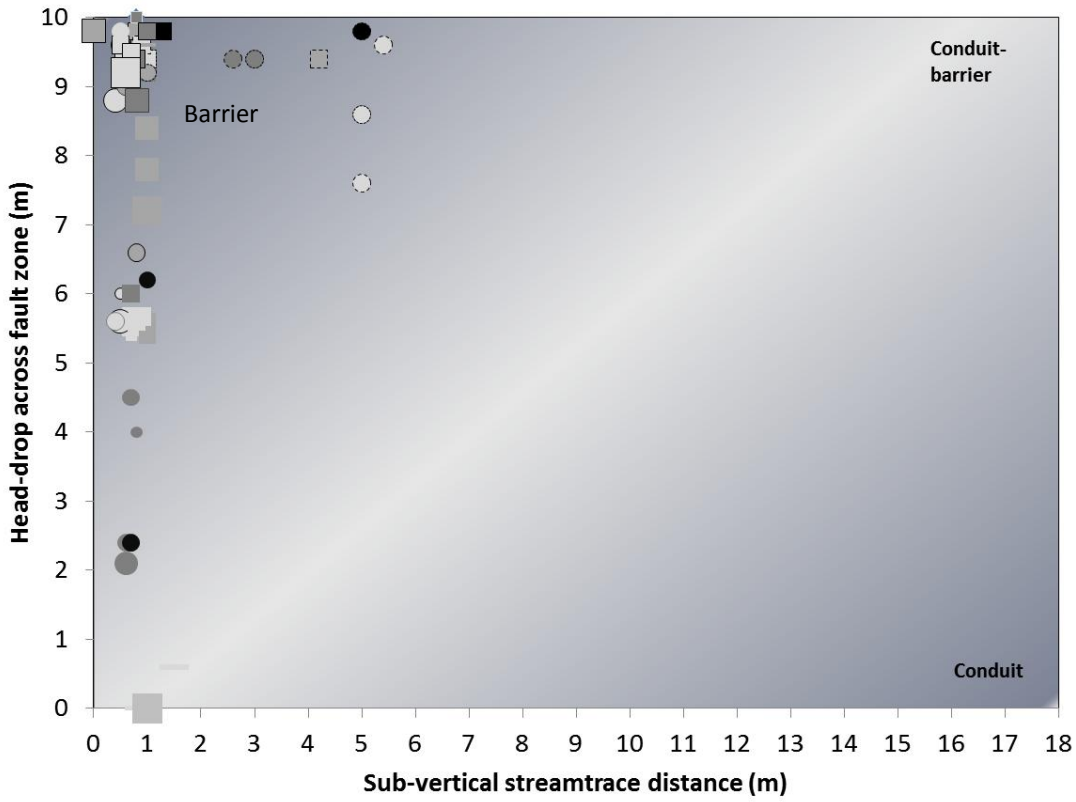

Figure 6.5 Modelled head-drop across fault zone with maximum sub-vertical streamtrace distance for CC models. Squares and circles represent mixed zones with and without zones of mixed sediment respectively, and lines with anisotropic zones of mixed sediment. Small, medium, medium-large and large symbols represent minimum, average and maximum mixed zone thickness for small faults, and maximum mixed zone thickness for faults with 5 m throw. Marker shade refers to the lens attributes– light is every other silt lens; medium-light is both gravel and silt lenses; medium-dark is only silt lenses; dark is multiple lenses and black symbols, no lenses. A black line surrounding the marker represents a 9 mm clay smear, large dashes represent large discontinuities and small dashes small discontinuities in the smear; light grey and dark grey lines indicate an order of magnitude lower and higher hydraulic conductivity respectively, and thin and thick lines smears with minimum and maximum thickness. It is not possible to show all model results in the graph due to clustering in the top left corner, but these are included Appendix 5.1. Shading refers to the hydraulic behaviour of faults as identified in the graph corners.

Strong conduit behaviour was rare. Most of the CC models had along-fault sub-vertical streamtrace distances of <1 m (Figure 6.5). The 1 m sub-vertical streamtrace distance was primarily caused by bed configuration of the CC model domain as horizontal fluid-flow from the footwall had to flow along the mixed zone before entering a bed of high hydraulic conductivity in the hangingwall that was offset by 1 m (Appendix 5.4). However, models with discontinuities in fine-grained smears had streamtrace distances up to five times the modal average.

Fine-grained smears in fault zones behaved as strong barriers (Figure 6.5). Independent of other architectural elements, a continuous fine-grained smear caused an almost complete head-drop across the fault zone. Head-drop across the fault zone was nearly doubled when the hydraulic conductivity of the fine-grained smear was decreased by two orders of magnitude or the thickness was increased from 1 mm to 50 mm (Appendix 5.1). Streamflow pathways and vectors show that fluid-flow was focused along the boundaries of the fine-grained smears (Appendices 5.3 and 5.4). Fine-grained smears generally had minimal impact on the streamtrace distance but when discontinuities were modelled in the smear flow travelled along the smear and through the discontinuity – increasing the streamtrace distance by up to five times (Figures 6.5 and 6.6). The impact of the discontinuities on head-drop across the fault zone was less consistent, however, as singular discontinuities led to an increase in the head-drop of up to 0.8 m and double discontinuities led to a slight decrease in head-drop. The specific properties of the fine-grained smear had a smaller hydraulic impact when combined with other architectural elements in the mixed zone (Appendix 5.1).

Fault zones in CC models with only a zone of mixed sediment also caused a head-drop across the fault zone, albeit almost half of that caused by the fine-grained smear. Zones of mixed sediment also increased the head-drop across the fault zone when combined with other structural elements. When zones of mixed sediment were present, flow vectors tended to be focused through the whole thickness of the mixed zone (Appendix 5.3).

Fault zones with only fine-grained lenses produced a slightly smaller head-drop across the fault zone than fault zones with only zones of mixed sediment. The head-drop decreased when lenses of coarser material were also modelled, and

when smaller lenses were modelled. It also decreased across the fault zone when multiple *and* every other fine-grained lens were modelled, but increased when the associated coarse-grained lenses were included in these models. The lenses visibly increased vector tortuosity in fault zones without a fine-grained smear, but did not influence streamtrace pathways (Appendix 5).

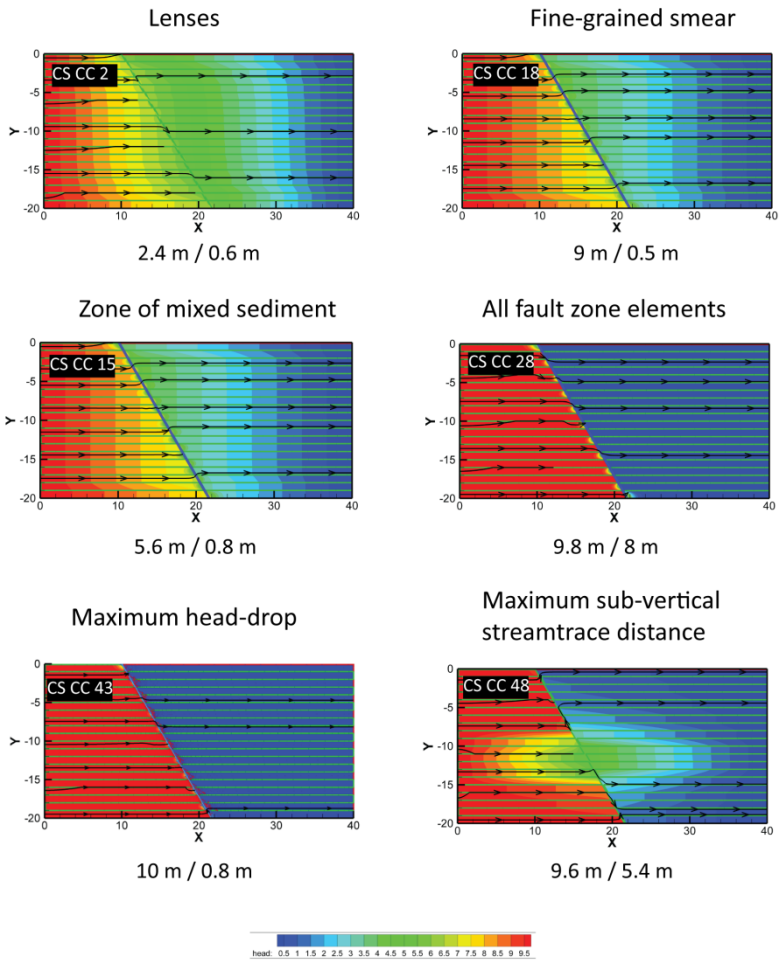

Figure 6.6 Model output with head contours and streamtraces for CC models with average values for each fault zone element individually and combined, and model outputs for the maximum head-drop and sub-vertical streamtrace distance for CC models. Head-drop and sub-vertical streamtrace distance included underneath the domain images respectively. Model code in top-left corners. Head, X and Y units are metres.

Increasing mixed zone thickness also did not have a uniform effect on the head-drop across the fault zones in CC models. Across the majority of the fault zones the head-drop decreased with increased mixed zone thickness. In some cases models in which mixed zones had the average thickness caused the smallest head-

drops across the fault zone (Appendix 5). Similarly, the effects of anisotropic models were not necessarily intuitive. The anisotropic model with only a zone of mixed sediment experienced no head-drop across the fault zone, it also decreased the head-drop across faults zones with a fine-grained smear. However, head-drop across fault zones without fine-grained smears was greater in anisotropic models. Vectors indicate that flow was preferentially focused along the anisotropic zone of mixed sediment and there was a decrease in flow path tortuosity (Appendix 5).

Altering model hydraulic boundary conditions in the CC models resulted in some changes to hydraulic impacts. NC boundary conditions again resulted in a reversal of the hydraulic impacts. Under US hydraulic boundary conditions sub-vertical streamtrace flow distance increased along the fault zone and the head-drop decreased across the fault zone. Fluid-flow was again focused towards the top of the fault zone (Appendix 5).

6.3.3 Faults juxtaposing fine and coarse-grained sediment (J)

The hydraulic characteristics of model set J varied considerably from the previous two sets of models. In all models the entire head-drop (from 10 to 0 m) occurred before the fault, irrespective of whether mixed zone features were modelled (Figure 6.1). This model setup also caused deflected sub-vertical fluid-flow. The inclusion of mixed zone elements slightly increased the streamtrace deflection distance, and also caused downwards along-fault fluid-flow in most models (Figure 6.7; Appendix 6). The isotropic model with average mixed zone thickness and all structural elements focused sub-vertical fluid-flow along the mixed zone (Figure 6.8). The same model under anisotropic conditions, however, decreased the streamtrace deflection distance and across-fault flow (Figure 6.8). Flow vectors and streamtrace patterns from this model indicate that fluid-flow in the mixed zone was irregular and apparently unstable (Appendices 6.2 and 6.3). Conversely, the maximum sub-vertical fluid-flow also occurred along the fault-zone of an anisotropic model with a zone of mixed sediment and slip-surface cataclasite, but no fine-grained smear (Figure 6.8).

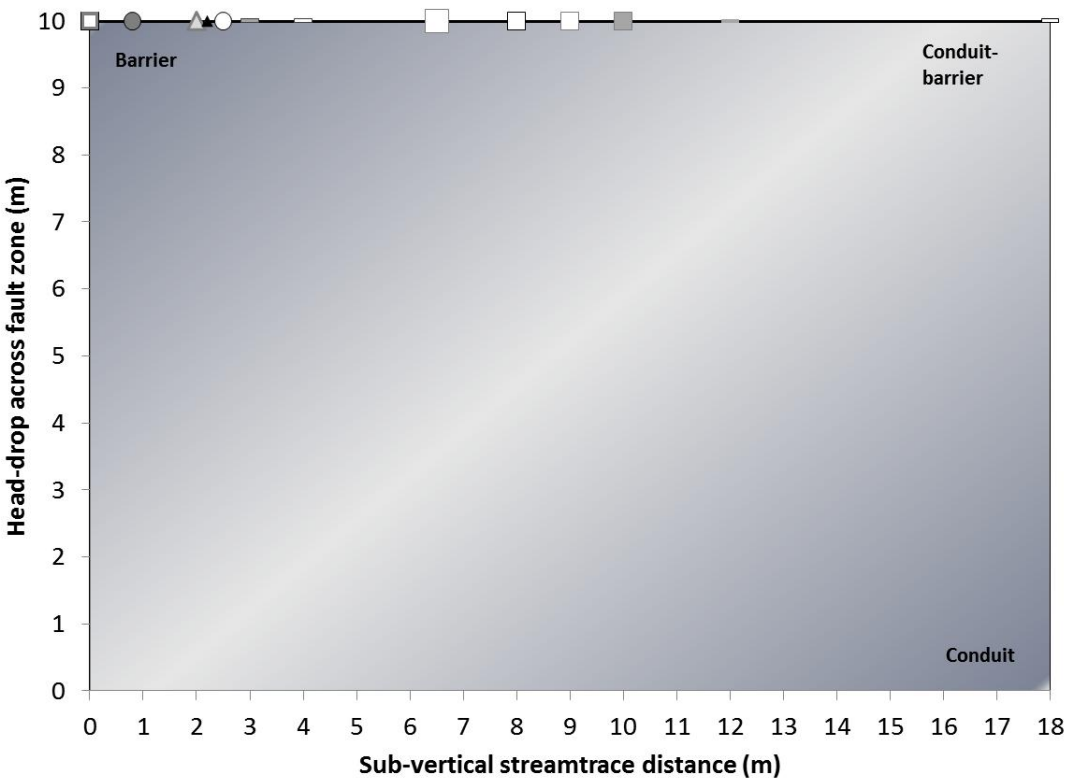

Figure 6.7 Modelled head-drop and maximum sub-vertical fluid-flow output for model set J. Square, triangular and line markers refer to mixed zones with a zone of mixed sediment, without a zone of mixed sediment and with an anisotropic zone of mixed sediment respectively. Small, medium and large markers refer to minimum, average and maximum zone of mixed sediment hydraulic conductivity. Markers that indicate fault zones with slip-surface cataclasites are grey, and without are white. Fine-grained smears are indicated by markers with a black outline and without, a grey outline. Shading refers to the hydraulic behaviour of faults as identified in the graph corners. All results are included in Appendix 6.

Zones of mixed sediment, slip-surface cataclasite and fine-grained smears caused a slight increase in the streamtrace deflection distance. Slip-surface cataclasite caused an additional component of along-fault sub-vertical fluid-flow. Along-fault fluid-flow increased considerably when a zone of mixed sediment was combined with a fine-grained smear or slip-surface cataclasite, particularly under anisotropic conditions (Figure 6.7; Appendix 6). Similar to PLG models, segmentation of the slip-surface cataclasite focused flow along the fault zone and through the discontinuity, resulting in an increased along-fault streamtrace

distance. Segmentation of the fine-grained smear did not, however, have a hydraulic impact.

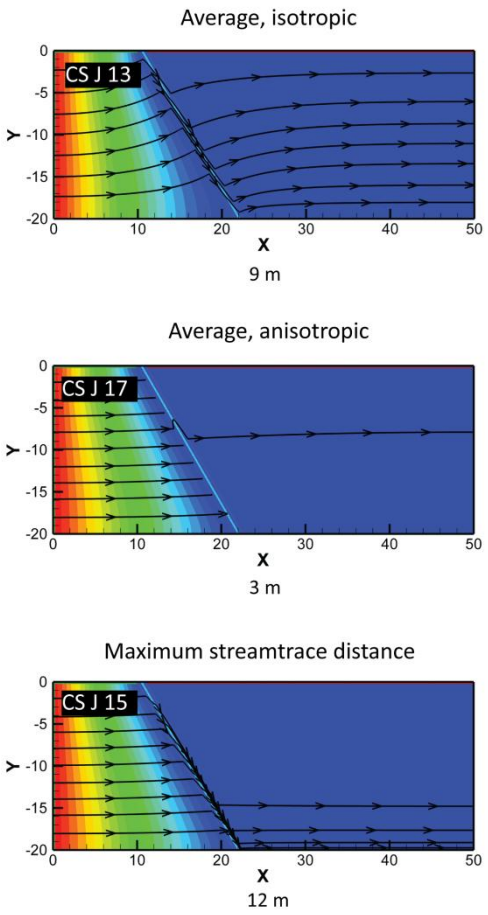

Figure 6.8 Model output for J models. Average refers to models with all mixed zone elements (zone of mixed sediment, slip surface cataclasite and fine-grained smears) and average values. Maximum sub-vertical streamtrace distance occurred in a model with a slip-surface cataclasite and zone of mixed sediment, under anisotropic conditions. Head, X and Y units are metres.

Along-fault sub-vertical fluid-flow increased in models in which zone of mixed sediment hydraulic conductivity was greater than that of the hangingwall sediment. However, there was no difference in the hydraulic impacts of models with zones of mixed sediment with minimum and average hydraulic conductivity (one order of magnitude). This was in contrast to the impacts of slip-surface cataclasites, in which those with the minimum hydraulic conductivity caused maximum along-fault fluid-flow whereas models in which slip-surface cataclasite had the maximum hydraulic conductivity (3 orders of magnitude difference in

hydraulic conductivity) produced no along-fault fluid-flow. Anisotropic models with only a zone of mixed sediment caused horizontal flow across the whole model domain (Appendix 6), thus reducing both deflected and along-fault sub-vertical flow. Fluid-flow remained horizontal in the footwall and hangingwall when additional fault zone elements were modelled in anisotropic models, but with significant along-fault fluid-flow (Figure 6.8).

Altering the hydraulic boundary conditions in model set J resulted in changes to fault zone hydraulic behaviour. CN hydraulic boundary conditions not only reversed the hydraulic impacts, but resulted in flow upwards along the mixed zone, with irregular, possibly unstable, flow characteristics shown by flow vector patterns in the isotropic and anisotropic models with slip-surface cataclasite and fine-grained smears. Streamtraces also show unstable flow patterns in the isotropic model of the fault zone with slip-surface cataclasite and a fine-grained smear. In the same model, under anisotropic conditions, streamtraces were discontinuous at the fault zone (Appendix 6). Under US hydraulic boundary conditions fluid-flow also occurred upwards along the fault zone, and streamtrace distance increased significantly (Appendix 6).

6.4 Fluid-flow evidence from outcrops

There is evidence of present and past fluid-flow associated with fault zones at all of the outcrop locations. At the Voutsimos outcrop large volumes of water are sourced from springs that emerge from along the traces of Big Faults 1 and 2 (Figures 2.7 and 2.8). Both these faults juxtapose fine and coarse-grained delta bottomset sequences in the footwall, and coarse-grained gravel conglomerates in the hangingwall (Figures 2.7 and 2.8).

A number of cements and precipitates are found at the Loutraki outcrop section – iron oxide (Figures 3.1a), manganese oxide and micritic calcite (Figures 2.4, 3.1 and 3.6). Iron oxide is associated with a sand bed in the footwall of Fault 1A, towards the base of the exposure (Figure 2.4). Micritic calcite cement is associated with a sand bed in the hangingwall of Fault 1A, and can be traced throughout sections AA', BB' and CC', and is also found within a coarse-grained conglomerate, along with a manganese oxide precipitate (Figure 2.4). These beds

are exposed towards the base of the outcrop in sections AA' and BB' and the top of the outcrop in section CC', at the road level. However, only the micritic calcite cement is visibly associated with fault zones (Figure 3.1 and 3.6). Strong micritic calcite cement coats grains, forming an indurated zone, in the centre of the zone of mixed sediment of Fault 1A (Figures 3.1, 3.3b and c). Similar micritic calcite cement is focused along Fault 4, defining the fault zone, particularly towards the top of the outcrop (Figure 3.6). The cement fingers from this fault zone up to half a metre into the sediment of the footwall and hangingwall.

Micritic calcite was also the dominant cement in the poorly sorted gravel beds of the Mentourgianika outcrop (Figures 2.9 and 2.10). Of the 34 identified fault zones in this section, 90 % exhibited significantly more calcite cement than the surrounding protosediment (Figure 6.9). Fault zones that are connected to the ground surface also exhibited a striking white veneer towards the top (Figures 4.1b and 6.9a), similar to Fault 4 at the Loutraki outcrop. Away from the ground surface the cement caused many of the fault zones to protrude from the outcrop face (Figure 6.9b). In these protruding fault zones the cement was slightly brown in colour, indicating the possible presence of clay minerals (Figures 6.9c and d).

Similarly, micritic calcite cement is found in the mixed zone of the Big Fault 1 Antithetic (0.7 m throw) exposed in the gravel conglomerate hangingwall of Big Fault 1 at the Voutsimos outcrop (Figures 2.7 and 2.8). This cement had over-printed an iron oxide from an apparently earlier phase of fluid-flow. The iron oxide precipitate could be traced through the mixed zone as a convex arch that dipped steeply away from the mixed zone in the hangingwall. It is concentrated towards the top of the coarsest-grained bed in the exposed footwall (Figure 6.10).

Iron oxide precipitate was striking in the Akrata outcrop (Figure 6.11). This precipitate was found in medium-coarse gravel conglomerate beds, but not in medium-fine gravel, sand or silt beds in the section (Figure 6.11). Traces of this precipitate were generally focussed at the fault zones, although they were not found to be focused along the mixed zones themselves (Figure 6.11).

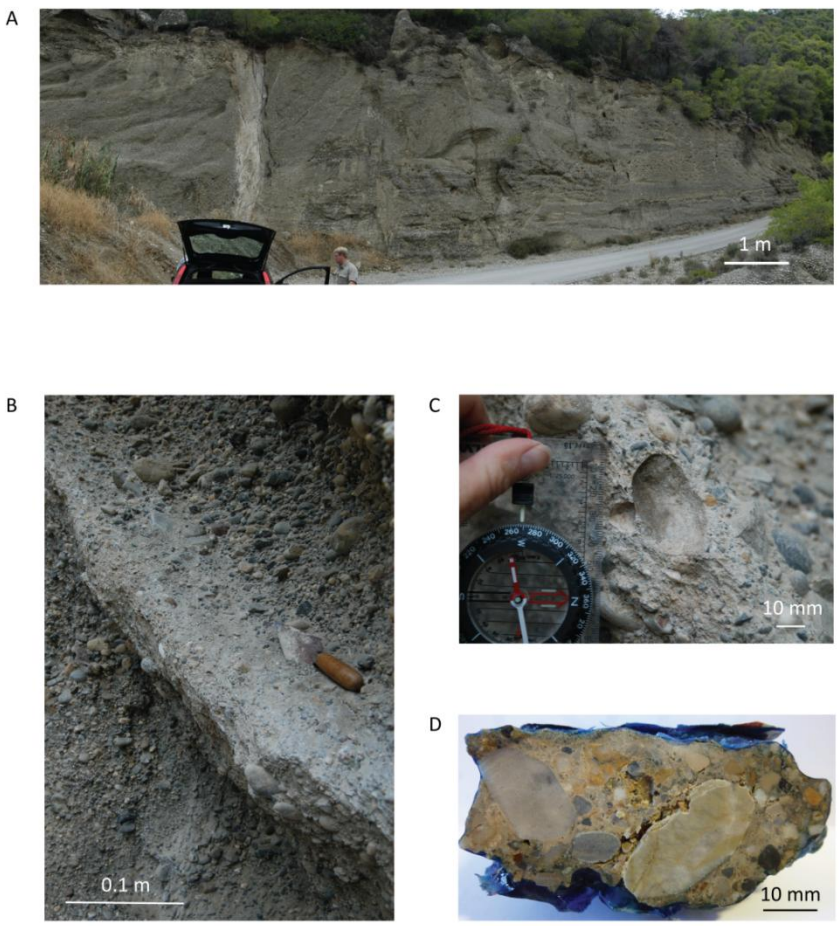

Figure 6.9 Cement as evidence of fluid-flow at fault zones cutting gravel in the Mentourgianika outcrop (Figures 2.9 and 2.10). A) Cemented Fault (1.88 m throw) with white micritic calcite cement focused at the top of the mixed zone where it connects to the ground surface (Figure 2.10). B) Protruding mixed zone from fault AF2 (Figure 2.10) cemented with micritic calcite and clays. C) Close-up of pebble cast in the same cemented fault zone as (B). D) Sliced hand sample from Cement Fault 2 (Figure 4.3) showing the cement through this fault zone.

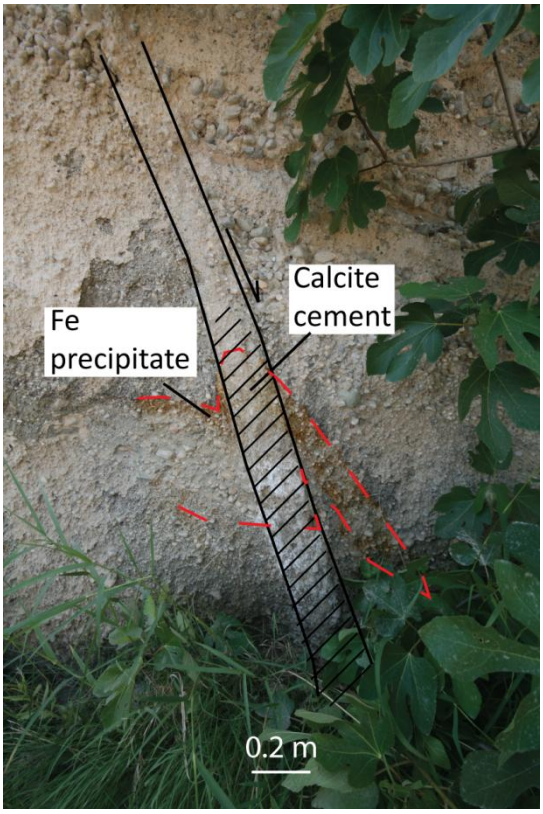

Figure 6.10 Evidence of previous fluid-flow from iron oxide and micritic calcite cement patterns associated with Big Fault 1 Antithetic Fault cutting in poorly lithified gravels in the hangingwall of Big Fault 1 (Figure 4.9b) at the Voutsimos outcrop (Figures 2.7 and 2.8).

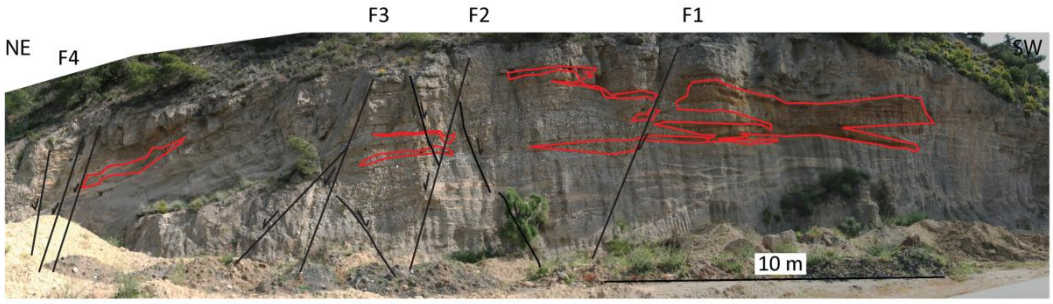

Figure 6.11 Akrata outcrop with iron oxide precipitates outlined in red, correlating to likely high hydraulic conductivity gravel and pebble beds, surrounding the fault zones (black lines) (Figure 2.6).

6.5 Implications of numerical fluid-flow model results

6.5.1 Fault zones in poorly lithified gravel (PLG)

Modelled hydraulic behaviour of faults in poorly lithified gravels covers the spectrum – barriers, conduits and conduit-barriers (Figure 6.3), although the majority of simulated faults have aspects of conduit-barrier behaviour. The magnitude of hydraulic impacts varies from minimal to substantial. The diversity of fault zone hydraulic behaviour in poorly lithified gravels can be explained by differences in specific fault zone structure.

Fault zones hindered fluid-flow, causing head-drops across them, in all models in which their hydraulic conductivity was less than that of the model domain. The magnitude of the head-drop was influenced by the mixed zone thickness (e.g. Bense and Person, 2006), zone of mixed sediment hydraulic conductivity (e.g. Bredehoeft *et al.*, 1992), and whether or not slip-surface cataclasites were present. These parameters combined control the fault zone transmissivity (e.g. Haneberg, 1995). The magnitude of head-drop across the fault zone was most sensitive to the hydraulic conductivity of the zone of mixed sediment, and the presence of slip-surface cataclasites – the fault bulk hydraulic conductivity. The significance of fault bulk hydraulic conductivity to the barrier behaviour is demonstrated by the apparently strong barrier behaviour of small faults with minimum hydraulic conductivity, regardless of mixed zone thickness (Figure 6.3). Whilst fault zones with slip-surface cataclasites produce the most significant barrier behaviours, some large faults with the minimum hydraulic conductivity also behaved as virtually comprehensive barriers (Figure 6.3). In addition it is likely that these fault zones would have also had slip-surface cataclasites, since cataclasite apparently forms in low porosity fault zones (Chapters 4 and 5). Therefore the head-drop across large fault zones is likely to be significant.

Sub-vertical fluid-flow in PLG models occurred for a number of reasons. Firstly, increasing the zone of mixed sediment hydraulic conductivity relative to the model domain caused along-fault fluid-flow, further demonstrating the importance of relative hydraulic conductivity to fault zone hydraulic behaviour (e.g. Bredehoeft *et al.*, 1992; Haneberg, 1995; Caine *et al.*, 1996; Rawling *et al.*,

2001; Barnicoat *et al.,* 2009). However, the conduit and barrier behaviours of mixed zones in which hydraulic conductivity is either higher or lower than the model domain (respectively) are necessarily mutually exclusive, and thus cannot explain the commonly hydrologically observed conduit-barrier behaviour (Bredehoeft *et al.,* 1992; Person *et al.,* 2000; Bense *et al.,* 2003; Bense and Person, 2006; Heffner and Fairley, 2006; Bense *et al.,* 2008).

Models with imposed anisotropy representing sediment smears and grain rotation in the mixed zone indicate that this can in part explain the simultaneous conduit and barrier behaviour (e.g. Person *et al.,* 2000; Bense and Van Balen, 2004; Bense and Person, 2006). However, although model anisotropy did increase sub-vertical fluid-flow distance, it also tended to decrease the magnitude of the barrier behaviour (Figure 6.3) and would therefore be less likely to cause major conduits and barrier behaviour simultaneously (e.g. Bense and Person, 2006; Heffner and Fairley, 2006).

The most likely cause of significant conduit-barrier behaviour in the faults zones of poorly lithified gravels appears to be the extrinsic anisotropy introduced to fault zones from slip-surface cataclasites. Vector patterns show that prevention of fluid-flow through low hydraulic conductivity slip-surface cataclasites (Appendix 4.5) forces fluid to flow preferentially along the slip-surfaces, and through higher hydraulic conductivity pathways between slip surface step-overs (e.g. Antonellini and Aydin, 1994; 1995) (Figure 6.4). This causes a sub-vertical deflection of streamtraces adjacent to the fault zone in the adjacent footwall and hangingwall, resulting in simultaneous conduit and barrier effects. Fluid-flow along fault zones with slip surfaces is enhanced by their segmentation, highlighting the importance of structural controls, and in particular slip-surface cataclasites, on the connectivity of fluid-flow pathways (Shipton and Cowie, 2001; Lunn *et al.,* 2008; Dockrill and Shipton, 2010; Kremer *et al.,* 2011) despite the small proportion of the fault zone that they may occupy (Walsh *et al.,* 1998). However, the constant head-drop between models with segmented and continuous slip-surface cataclasites suggests that flow path tortuosity and connectivity may have a limited influence on fault barrier behaviour, particularly the static seal capacity (e.g. Lunn *et al.,* 2008), contrary to suggestions by Antonellini and Aydin (1995) and

Faulkner *et al.* (2010). This reflects the importance of overall fault zone transmissivity on head-drop. While fault zone transmissivity may be equivalent for these specific models, it may vary depending on the slip-surface cataclasite geometry.

The capacity of slip-surfaces to cause conduit behaviour is well documented (Heffner and Fairley, 2006; De Boever *et al.*, 2011) but has previously been attributed to fractures along the slip-surface (Gudmundsson, 2000; Jourde *et al.*, 2002; Lunn *et al.*, 2008; Faulkner *et al.*, 2010). Bifurcated groundwater temperature profiles (Magri *et al.*, 2010) and fault zone mineralisation patterns adjacent to fault zones, described by a number of authors (Foxford *et al.*, 1998; Gudmundsson, 2000; Yang *et al.*, 2004; Barnicoat *et al.*, 2009), could result from significant deflected sub-vertical fluid-flow such as described here. If open fractures do occur along slip surfaces the sub-vertical fluid-flow resulting from slip-surface cataclasites may be greater still.

More generally, these model results highlight the influence of fault throw on the hydraulic impacts of faults in poorly lithified gravels. Faults with the largest throws are likely to have the greatest influence on fluid-flow since this is the primary control on mixed zone thickness, structure and hydraulic conductivity (Chapters 4 and 5). The largest faults are more likely to behave as conduit-barriers due to the presence of slip-surface cataclasites, whereas small faults may occasionally form conduits as a result of a possible initial increase in fault zone hydraulic conductivity (e.g. Balsamo *et al.*, 2010; Chapters 4 and 5).

6.5.2 Faults zones in sediment of contrasting competency (CC)

Fault zones in the CC model set produced a much smaller range of potential hydraulic behaviours than the PLG set. Faults behaved predominantly as major barriers to fluid-flow, and though a small number behaved as conduit-barriers, none behaved only as conduits (Figure 6.5). The head-drop and sub-vertical streamtrace distances are consistent across models with a range of fault zone element combinations, indicating that the specific combination has a minimal impact on the fault zone hydraulic behaviour (Figure 6.5).

Clay smears along fault zones have long been known to contribute to the barrier behaviour of faults (e.g. Rawling *et al.,* 2001; Bense and Van Balen, 2004; Caine and Minor, 2009). However, these model results show that fine-grained smears, with the slightly higher hydraulic conductivity values of silts, could also produce significant head-drops across fault zones (Figure 6.5). This impact probably results from the contrast in hydraulic conductivity between the low hydraulic conductivity silt-smear and the beds of higher hydraulic conductivity (representing gravel conglomerates) in the model domain. Nevertheless, the substantial differences in head-drop across the fault zone resulting from two orders of magnitude difference in smear hydraulic conductivity, demonstrates that the specific contrast in hydraulic conductivity is important (e.g. Walsh *et al.*, 1998) in addition to smear thickness (e.g. Allan, 1989).

Similar to the modelled slip-surface cataclasites, where there were discontinuities in the fine-grained smear, flow vectors and streamtrace patterns showed fluid-flow was focused parallel to the dip of the smear and flowed through the mixed zone at the discontinuity (Appendix 5). Smear discontinuities are considered potential leak points for hydrocarbon reservoirs (Doughty, 2003), reducing the sealing capacity of faults (Caine and Minor, 2009; Faulkner *et al.,* 2010), yet similar to the discontinuities in slip surfaces, these discontinuities produced only marginal decreases in head-drop across the fault zones. This could be important for water resources since it suggests that leakage across fault zones may be possible even where there are significant head-drops across fault zones. Smear discontinuities also caused the rare combined conduit-barrier behaviour in the CC model set (Appendix 5). The absence of deflected sub-vertical fluid-flow in the CC models is probably because it is hindered by horizontal beds of low hydraulic conductivity in the model domain. Zones of mixed sediment are likely to have a similar, albeit smaller, hydraulic impact to fine-grained smears in these fault zones.

Applying anisotropy to the CC models with only a zone of mixed sediment dramatically reduced the head-drop across the fault zone, but did not increase along-fault fluid-flow in this case. The noticeable decrease in flow path tortuosity was also reported by Bense and Person (2006). In the CC models the effects of

anisotropy were minimal when combined with other fault zone elements. This contrast in the role of imposed anisotropy to PLG models probably results from the control of other fault zone elements dominating the fault zone, which were modelled as isotropic. There was also no straight forward relationship between lens characteristics and hydraulic impacts. This may result from the interplay of different controlling factors, including bulk fault zone hydraulic conductivity, lens connectivity, flow path tortuosity and mixed zone thickness. Structural heterogeneities are therefore also important controls on the hydraulic behaviour of the CC models.

The strong clustering of fault zone behaviour (Figure 6.5) suggests that despite the multiple possible fault zone heterogeneities modelled for the CC set, the overall hydraulic behaviour of faults is more predictable than those in poorly lithified gravels. This is likely in part due to the control of model fault throw/ bed configuration (e.g. Manzocchi *et al.*, 2007), since this impacted fluid-flow regardless of fault zone characteristics. Whilst in this case the specific configuration increased hydraulic connections between high hydraulic conductivity beds (Figure 6.6), alternative configurations could cause a range of different impacts (e.g. Bense and Person, 2006; Manzocchi *et al.*, 2007). Therefore, unlike faults in poorly lithified gravels, fault throw is primarily a key factor in controlling fault zone hydraulic conductivity in combination with sedimentological configuration, rather by controlling fault zone structure.

6.5.3 Fault zones juxtaposing fine and course-grained sediment

The hydraulic behaviour of fault zones in models in which fine and coarse-grained sediment are juxtaposed differed fundamentally from the previous model sets. The maximum head-drop occurred before the fault, along with an element of sub-vertical fluid-flow that resulted from streamtrace deflections, without inclusion of a mixed zone. This supports the finding from the CC models, and previous studies (e.g. Maclay and Small 1983; Haneberg, 1995; Mailloux *et al.*, 1999), that the juxtaposition of sediment of different hydraulic conductivity has a significant control on fault zone hydraulic behaviour.

Sub-vertical fluid-flow was significantly enhanced upwards through the fault zone in the zones of mixed sediment, and along the low hydraulic conductivity slip-

surface cataclasites and fine-grained smear. Sub-vertical fluid-flow was enhanced by discontinuities in slip surfaces and fine-grained smears, and fault zone anisotropies –similar to previous model sets. The irregular flow vector patterns in the mixed zones in a number of set J models occur under conditions favourable to high flow velocities – anisotropic, with low hydraulic conductivity structural elements to focus fluid-flow – thus it is possible that this reflects an unstable fluid-flow regime resulting from an increase in flow rate (Appendix 6). Importantly, this particular combination of structural elements is unlikely to occur in the faults of the other model sets (Chapter 4).

6.5.4 Hydraulic boundary conditions

Specific fault zone interactions with fluid-flow did not change under different hydraulic boundary conditions in the models, however the observable hydraulic impacts do differ (e.g. Eichhubl and Boles, 2000; Magri *et al.*, 2010). For example, in all of the models with shallow, unconfined flow conditions from south to north, fluid-flow is greatest towards the top of the fault zone, whereas under confined conditions it is largely equivalent across the length of the fault (Appendices 4 to 6). This characteristic occurs because the hydraulic boundary conditions impose different source and sink regions along the fault zone (e.g. Haneberg, 1995; Eichhubl and Boles, 2000; Gudmundsson, 2000; Eichhubl *et al.*, 2004). In CC models flow was additionally focused along the length of the fault zone in these conditions as it provided a vertical pathway for the enforced upwelling of fluid that did not exist within the rest of the model domain. This supports findings of Gudmundsson (2000) that hydraulic impacts are magnified the more closely aligned the orientation of fault zones and flow paths are. The consistent sub-vertical streamtrace distances across fault zones with maximum zone of mixed sediment hydraulic conductivity and a range of mixed zone thicknesses for PLG Sm 1 models indicates that the quantity of fluid transmitted by the fault zone is limited by flow supply (e.g. Haneberg, 1995). Establishing hydraulic boundary conditions are therefore central for determining the hydraulic impact of faults.

In the J models, the confined flow conditions from south to north require flow from the aquitard to the aquifer. This configuration is only likely to occur in rare

circumstances, since fluid-flow would preferentially occur within aquifers if there are aquifers in the wider region, and flow in the aquitard would be sub-vertical. Models in which fine and coarse-grained sediment is juxtaposed with confined flow from the north to the south represents a more likely scenario whereby flow occurs in the direction from the aquifer to aquitard. Under these boundary conditions, the hydraulic impacts of fault zones are similar to those described previously (e.g. Haneberg, 1995), resulting in significant upwelling along the fault zone as the flow reaches the impermeable barrier of the fine-grained sediment.

6.6 Fluid flow at outcrops

There was clear evidence for present day and previous fluid-flow surrounding fault zones in outcrop. The most prevalent precipitate within fault zones – micritic calcite – reflects the regional water type (Ca-HCO_3) (Pizzino *et al.*, 2003). Preferential precipitation of the micritic calcite cement along fault zones shows that fluid-flow has been focused along them. This micritic calcite cement differs to the coarse crystalline cement described in many of the larger fault zones in the region (e.g. Micarelli *et al.*, 2006b), reflecting its precipitation by water of meteoric origin in the vadose zone (Eichhubl and Boles, 2000), rather than the phreatic zone. This is supported by the presence of strong cementation along the top of some fault zones that crop out at the ground surface in the Loutraki and Mentourgianika outcrops (Figures 3.6 and 6.9a). These faults probably provided preferential flow pathways through the vadose zone due to the decrease in pore size (Chapter 5), which enabled pores to be wetted more easily, providing a hydraulic connection lacking in larger pores of the conglomerate (e.g. Flint *et al.*, 2001; Sigda and Wilson, 2003; Eichhubl *et al.*, 2004; Kelsen *et al.*, 2004). The capacity for these faults to behave as preferential fluid-flow paths in unsaturated hydraulic conditions suggests the decrease in fault zone pore-size is hydraulically significant, and in saturated conditions it is thus likely that fault zones will behave as barriers thus supporting the PLG model results. Importantly, the fault zone cements will dramatically decrease the fault zone porosity (Figures 5.3, 6.9c and d) and cause a reduction in fault zone hydraulic conductivity (Knipe, 1997; Caine and Minor, 2009).

The correlation of iron-oxide precipitate with apparent bed hydraulic conductivity at Voutsimos and Akrata (Figures 6.10 and 6.11) might imply that this was also formed from a post-depositional process (Eichhubl *et al.,* 2004). These precipitates commonly form by oxidation of reduced waters that contain iron. The proximity of these precipitates to fault zones suggests a process of formation whereby oxidised meteoric water flowing along fault zones seeped (or flowed) into adjacent high hydraulic conductivity beds, oxidising residual iron-rich waters within the pores of these beds, resulting in the precipitation of iron oxides (Figure 6.11) (e.g. Eichhubl *et al.,* 2004). These precipitation patterns indicate that in saturated conditions fault zones in poorly lithified gravels behaved as conduits to fluid-flow, possibly as a result of increased hydraulic conductivity or intrinsic anisotropy since none of these faults have slip- surface cataclasites. The configuration of beds of differing hydraulic conductivity appears to be integral to creating these precipitate patterns, reflecting fluid-flow characteristics in the set CC models. The complexity of cementation patterns reflects both fault zone behaviour and hydraulic boundary conditions combined.

The abundant vegetation and water source focused around the fault zones of juxtaposed fine and coarse-grained sediment at Voutsimos allude to the significant quantities of water that flow along these fault zones (e.g. Catchings *et al.,* 2009). These fault zones are unusual for the region because they dip antithetically to the crustal-scale Mamoussia-Pirgaki fault (Figure 2.7 and 2.8), reflecting the flow conditions from north to south (hangingwall to footwall). Therefore the model results suggesting high fluid-flow rates upwards along the mixed zone closely replicate reality for these fault zones (Figure 6.7).

It is difficult to compare the modelled fault zone hydraulic behaviours and those inferred from outcrop because of the primary control of hydraulic boundary conditions, and in particular aquifer saturation, that were not directly replicated. Modelled fault hydraulic behaviours appear to be reasonable approximations of reality. However, there is a possibility that key aspects of fault zone and fluid-flow interactions were absent from models due to simplification of fault zones, such as representation in two rather than three dimensions and consistent along-strike and dip mixed zone thickness, structural elements, hydraulic conductivity

and fault zone segmentation (Watterson *et al.*, 1996; Walsh and Watterson, 1998). In addition, damage zones and connecting fault networks have not been modelled but could also significantly impact fluid-flow properties (Antonellini and Aydin, 1995; Heynekamp *et al.*, 1999; Wu and Xu, 2003; Heffner and Fairley, 2006).

6.7 Summary

The hydraulic impacts of the modelled faults range from barriers through to conduit-barriers and conduits, with minor to significant impacts. Models of fault zones in poorly lithified gravels produced a considerable range of hydraulic behaviours whereas the majority of fault zones in sediment of contrasting competency behaved as comprehensive barriers. Models in which fine and coarse-grained sediments were juxtaposed across the fault zones commonly behaved as conduit-barriers. The diversity of fault zone hydraulic behaviour can be explained by differences in specific fault zone structure.

Fault zone barrier behaviour was found where bulk mixed zone hydraulic conductivity was lower than the protosediment. This was influenced by the combined hydraulic conductivity of structural elements. Slip-surface cataclasites and fine-grained smears had the greatest impact on fault zone fluid-flow properties, the geometry of which are important for fluid-flow pathways. Conduit-barrier behaviour resulted from intrinsic anisotropy representing grain rotation or sediment smears or, more significantly, from extrinsic anisotropies imposed by fault zone heterogeneities. Fault throw was a significant control on the hydraulic behaviour of fault zones in poorly lithified gravels, however, the configuration and juxtaposition relationships of high and low hydraulic conductivity sediment is as important in fault zones cutting sediment of contrasting competency. These beds may also reduce fault-adjacent sub-vertical fluid flow.

Outcrops show abundant evidence for fluid-flow around fault zones in the form of cementation and springs. The model results show some similarities with outcrop evidence of fluid-flow however the saturation state of the aquifer is a major control on fault zone hydraulic behaviour. The specific interactions of fault zones and fluid-flow was not influenced by hydraulic boundary conditions, however,

hydraulic boundary conditions have significant impact on the overall hydraulic impact of fault zones.

7. Thesis summary and conclusions

This chapter provides a summary and conclusion to this thesis. Key findings from the preceding data chapters are summarised in the context of the original research objectives specified in Chapter 1, followed by a brief discussion of the thesis hypothesis in light of this research. The contribution that this work makes to the field of fault zone hydrogeology and the broader implications of this research are then discussed. Limitations of the research are outlined and suggestions for further investigation into this topic proposed. The chapter ends with a brief concluding statement.

7.1 Summary of results

7.1.1 Objectives

The results of the three research objectives proposed in Chapter 1 that were intended to assist with evaluating the thesis hypothesis are summarised below:

1. Identify the structure and deformation processes of fault zones in poorly lithified sediment of the Gulf of Corinth rift.

Faults cutting the syn-rift sediment of the Gulf of Corinth rift are generally found as part of fault arrays in regions of high strain, proximal to crustal-scale faults (Figure 2.2). Investigation of the minor normal-fault array exposed north of Loutraki town in Chapter 3 enabled elucidation of the architectural and structural elements of fault zones and their evolution, in poorly lithified sediment and sediment in which poorly lithified and more cohesive beds are inter-bedded. These findings were corroborated and refined in Chapter 4 using evidence from faults outcropping at the remaining four study locations; Akrata, Pirgos, Mentourgianika and Voutsimos (Figure 2.2). These outcrops provided a greater range of lithological types, fault throws and settings.

Fault zone structure was found to differ somewhat to fault zones previously described cutting poorly lithified sediment. Fault zones described in this work comprise mixed zones, of variably deformed sediment that accommodate the majority of strain. Mixed zones are flanked by damage zones in just over half of the fault zones, though many were limited to fine-grained beds cut by the fault.

Damage zones primarily comprise antithetic or synthetic subsidiary faults that cut all lithologies, and sometimes disaggregation bands that cut fine-grained sediment.

Specific structural elements in mixed zones differ according to the lithology cut by the fault – in particular, the rheology and stratigraphic relationships – and the fault throw. Fault zone structure and evolution was analysed separately for three fault groups; those that cut only poorly lithified sediment, sediment of vertically contrasting competency, and those in which fine and coarse-grained sediments were juxtaposed. In the Gulf of Corinth rift these fault groups are found at different stratigraphic stages in the syn-rift sediment (see Figures 2.1 and 4.13).

Poorly lithified sediment cut by faults zones in the four southern Gulf of Corinth rift outcrops was coarse-grained Giant Gilbert-type gravel conglomerate (see Figure 4.1). In the Loutraki outcrop, the poorly lithified sediment was more heterogeneous, also originating from a delta setting (Figure 2.3). Mixed zones in these faults comprise beds cut by the fault that are rotated consistent to fault dip and smeared through the mixed zone (Figure 3.1a, 4.1 and 7.1). Sediment is entrained into the mixed zone, and accommodates mixed zone shear strain by distributed controlled particulate flow, whereby grains rotate and slide along their boundaries aided by incipient cataclasis.

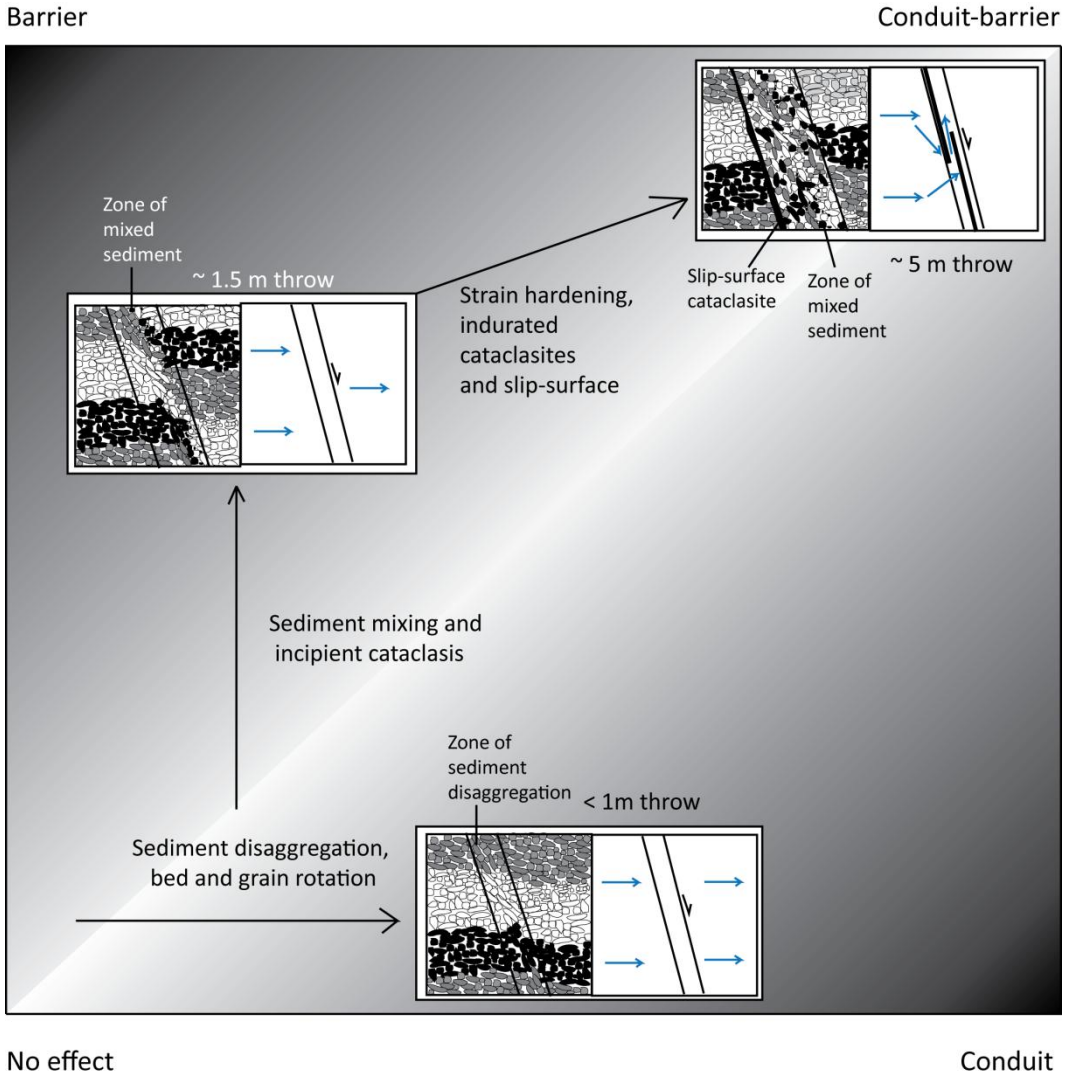

Figure 7.1 Summary of fault zone evolution and impacts on fluid-flow for poorly lithified sediment. Blue arrows indicate fluid flow. Shading refers to the hydraulic behaviour of faults as identified in the corners of the box.

Initial deformation of sediment in mixed zones (faults <~1 m throw) causes grain disaggregation, rotation, and possibly dilation. With further strain in the mixed zone, grain-scale mixing of sediment and cataclasis results in a decrease of grain-size, sorting and porosity (Figure 3.9b and 7.1). If fault throw exceeds bed thickness a zone of mixed sediment can form in the mixed zone from an amalgamation of surrounding beds. The positive relationship between fault throw and mixed zone thickness (Figures 4.10a to c) reflects steady incorporation of additional sediment into the mixed zone by particulate flow. Grain fabric development, and progressively decreasing porosity and grain-size in the mixed zone causes strain-hardening. Slip-surface cataclasites can be found in faults

with >1.5 m throw at the point of maximum strain hardening. Subsequent strain-weakening and localisation occurs along the slip-surfaces (Figure 4.12 and 7.1). Slip-surface cataclasite formation coincides with a discontinuity in the fault population distribution trend for poorly lithified sediment at ~1.5 m fault throw (Figure 4.11a). This suggests a hierarchy for faults cutting poorly lithified sediment in which the structure of fault zones differs for faults with throws above and below this size (Figure 7.1).

Poorly lithified sediment inter-bedded with cohesive marl or cemented beds produced vertical competency contrasts in sediment (see Figure 4.5). Sediment of contrasting competency was most commonly found in outcrops of the Giant Gilbert-type delta bottomsets or the Aiges Formation, comprising fine-grained marls inter-bedded with coarse sand to cobble debris flow deposits, or Giant Gilbert-type delta topsets of coarse-sand to gravel conglomerate with inter-bedded silt (Figures 2.1 and 7.2). The primary difference in the structure of fault zones cutting sediment of contrasting competency to poorly lithified sediment is strain localisation in competent beds. The transition of distributed to localised strain at the boundary between incompetent and competent beds causes fault tip bifurcation, and asperities at the mixed zone boundary. Blocks or lenses of relatively undeformed sediment are incorporated into mixed zones as asperities are sporadically removed with fault throw (Figure 3.9c). This process dominates evolution of mixed zones cutting sediment of contrasting competency, and is reflected in the weak relationship between fault throw and mixed zone thickness (Figure 4.10a to c). Fine-grained sediment (marl to fine-grained sand) cut by faults can form relatively continuous, un-mixed smears in mixed zones. The structure of mixed zones cutting sediment of contrasting competency is influenced by fault throw and mechanical stratigraphy of sediment cut by the fault.

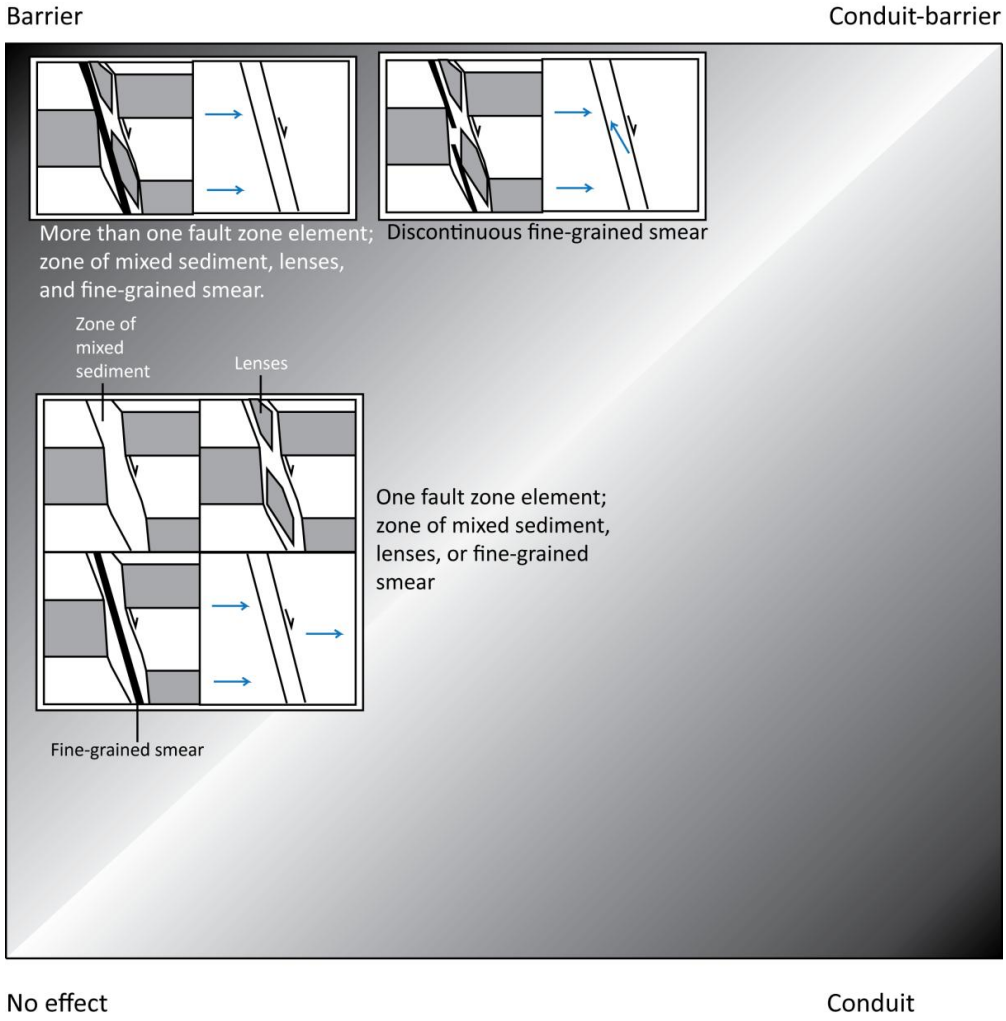

Figure 7.2 Summary of fault zones and impacts on fluid-flow for sediment of contrasting competency. Blue arrows indicate fluid flow. Shading refers to the hydraulic behaviour of faults as identified in the corners of the box.

Large faults exposed close to transitions from fine-grained silt and marl to coarse-grained gravel conglomerates cause large-scale juxtaposition of sediment across the fault zone. Mixed zones remain as distinct footwall and hangingwall sections separated by a discrete contact along fine-grained smears or localised shear zones, and even slip-surface cataclasites (Figures 4.9 and 7.3). Mixed zones in fine-grained sediment comprise localised shear zones and lenses or blocks of sediment, and occasionally rotated and smeared beds. In contrast, mixed zones in coarse-grained gravel conglomerate are dominated by rotated and smeared beds and zones of mixed sediment. Mixed zones evolve through mechanisms described for their respective sediment types in poorly lithified and sediment of contrasting competency.

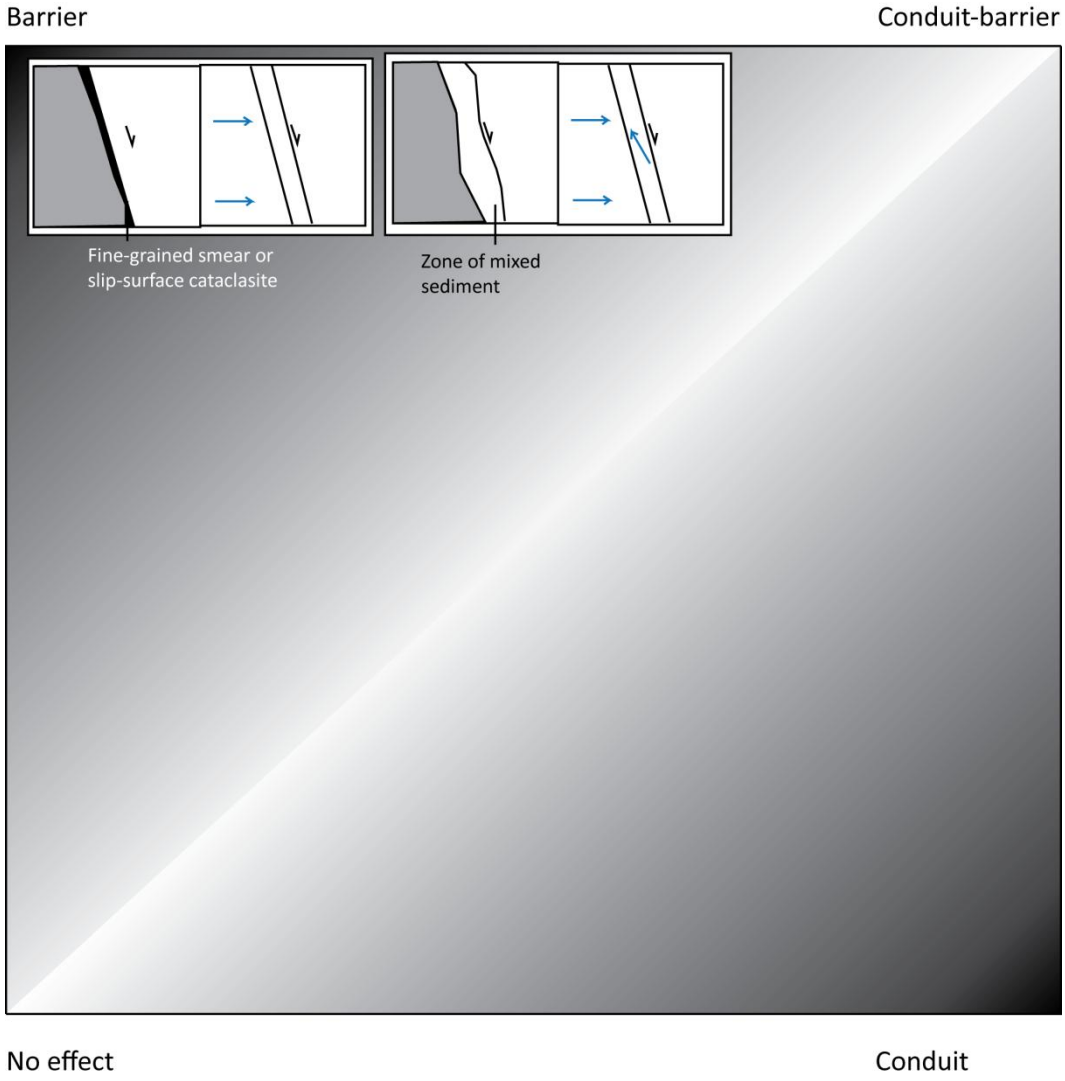

Figure 7.3 Summary of fault zone structure and impacts on fluid flow for faults juxtaposing fine and coarse-grained sediment. Blue arrows indicate fluid flow. Shading refers to the hydraulic behaviour of faults as identified in the corners of the box.

2. Ascertain the changes to the hydraulic conductivity of poorly lithified sediment in fault zones.

Porosity and hydraulic conductivity of mixed zones were estimated from thin section image analysis and the Kozeny-Carman equation, and compared with their protosediment. Variations in hydraulic conductivity were mapped across mixed zones and protosediment using grain-size distributions and the Krumbein-Monk equation.

Mean estimated porosity of zones of mixed sediment was 9% lower than the protosediment. Mean estimated hydraulic conductivity was up to an order of

magnitude lower than the protosediment. However, the estimated porosity and hydraulic conductivity alterations varied considerably for zones of mixed sediment, ranging between +2.8% and –19%, and an order of magnitude increase to four orders of magnitude decrease, respectively (Figure 5.3). Relationships between fault throw and zone of mixed sediment porosity and hydraulic conductivity suggests that fault throw influences hydraulic properties of mixed zones; total porosity has an apparent decrease in porosity of 3-4% with each order of magnitude fault throw, and hydraulic conductivity has an apparent decrease of an order of magnitude with each one and a half orders of magnitude fault throw (Figure 5.4). These results reveal that the most substantial alteration to mixed zone porosity and hydraulic conductivity occurs during the first 2 m of fault throw. Minor anisotropy, estimated from flow-path tortuosity, was re-orientated from horizontal in the footwall sediment to vertical in the mixed zone.

The estimated porosity and hydraulic conductivity of slip-surface cataclasites were the lowest of all structural elements; mean estimates were 19% and three orders of magnitude lower than the protosediment (Figure 5.3). The estimated porosity and hydraulic conductivity of fine-grained sediment smears were also very low, and could cause variation in hydraulic conductivity across the mixed zone of three orders of magnitude (Figure 5.8). A sample from a mixed zone containing cement indicates that cemented fault zones could reduce fault zone hydraulic conductivity more than primary fault zone processes.

Sediment smears and lenses or blocks of sediment introduce significant hydraulic heterogeneities and anisotropies across mixed zones, even without changes to grain-shape, size or porosity (Figures 5.5 to 5.8). Alteration of the spatial arrangement and geometry of beds in mixed zones of faults cutting beds of variable hydraulic conductivity causes juxtapositions and high variability in hydraulic conductivity across the mixed zone. However, in some fault zones natural sedimentary heterogeneities are greater than those resulting from sediment deformation.

3. Establish the ways in which fault zones in poorly lithified sediment influence fluid flow.

Numerical fluid-flow models of faults cutting poorly lithified sediment were constructed from characteristic fault zone structure and hydraulic conductivity of faults in the Gulf of Corinth rift. The suite of models represented a range of possible fault zone structures for the three identified fault sets; poorly lithified gravels (PLG), sediment of contrasting competency (CC) and faults across which fine and coarse-grained sediment is juxtaposed (J). Results show that fault zones cutting syn-rift sediment of the Gulf of Corinth rift are likely to impact fluid-flow but the magnitude and type of hydraulic behaviour is dependent on the fault zone structure.

Small (<1 m throw) (PLG Sm) and large (>5 m throw) (PLG Lg) faults cutting homogeneous poorly lithified gravels were modelled. Faults in PLG Sm models comprised smears or a zone of mixed sediment. Faults in PLG Lg models comprised a homogeneous zone of mixed sediment with or without a segmented 20 mm thick slip-surface cataclasite (Figure 6.2; Table 6.3). Domains of CC models represented alternating gravel conglomerate and silt beds, each 1 m thick, offset by a fault with 1 m throw. Mixed zones in CC models comprised different combinations of lenses, a fine-grained smear and a zone of mixed sediment (Figure 6.2; Table 6.3). In J models, silt in the footwall was juxtaposed against coarse-gravel conglomerate in the hangingwall. The mixed zone comprised combinations of a zone of mixed sediment, a fine-grained smear, and slip-surface cataclasite. In all sets models were run with both isotropic and anisotropic values for zones of mixed sediment and the model domain. Hydraulic boundary conditions were also varied for a few representative models.

The majority of the modelled faults in PLG models caused head-drops across the fault zone, behaving as varying degrees of barrier. Many faults also caused sub-vertical fluid flow. Conduit-only behaviour was found only in models where the hydraulic conductivity of the zone of mixed sediment was greater than the protosediment (Figure 7.1). Conduit-barrier behaviour resulted from anisotropies imposed on models representing grain rotation and sediment smears, and extrinsic anisotropy from elongate low hydraulic conductivity slip-surface cataclasites. The

most significant sub-vertical fluid-flow in models with slip-surface cataclasites was found in the hangingwall and footwall protosediment. Fluid-flow was deflected along the surface of the cataclasite towards the step-over where it was focused through this high hydraulic conductivity pathway. The magnitudes of hydraulic impacts were much greater for PLG Lg than PLG Sm models (Figure 7.1).

A significant proportion of faults in CC models behaved as virtually comprehensive barriers to fluid-flow (Figure 7.2). The most hydraulically significant structural element in these models was the fine-grained smear, although all fault zone structural elements included in these models caused the fault to behave as a barrier to fluid-flow. Sub-vertical fluid-flow was typically ~1 m in these models and was controlled by the configuration of high and low hydraulic conductivity beds and fault offset. Further conduit behaviour was induced only when discontinuities were included in the fine-grained smear, which caused preferential fluid-flow along the fault zone in order to cross the fault at the higher hydraulic conductivity discontinuities. Sub-vertical fluid-flow in the footwall and hangingwall was prevented by horizontal stratigraphy.

The juxtaposition of fine and coarse-grained sediment across the third model set (J) caused strong barrier behaviour regardless of whether fault zone structure was specified (Figure 7.3). Sub-vertical fluid-flow was common along these fault zones, particularly where slip-surface cataclasites and fine-grained smears were modelled.

Altering hydraulic boundary conditions did not influence specific fault-zone fluid-flow interactions, but it did influence the overall hydraulic impacts of fault zones. Models demonstrated that fault zones can enhance local fluid-flow conditions. The model results were largely substantiated by outcrop evidence of previous (cement) and current (springs and vegetation) fluid-flow that illustrate fault zone conduit-behaviour. Evidence of fluid-flow exposed in outcrops suggests preferential fluid-flow in the vadose zone, demonstrating the importance of lower-porosity mixed zones for providing preferential fluid-flow pathways in unsaturated conditions.

7.1.2 Hypothesis

"The structure of fault zones in poorly lithified sediment can explain the observed conduit-barrier behaviour from hydrogeological data"

Identification of new fault zone structures in poorly lithified sediment, sediment of contrasting competency and faults where fine and coarse-grained sediments are juxtaposed, and representation of these in numerical fluid-flow models has demonstrated that the observed conduit-barrier behaviour of faults in poorly lithified sediment can be explained by fault zone structure. All fault zones with a hydraulic conductivity lower than the protosediment behaved as barriers. The combined conduit-barrier behaviour was caused by anisotropies in the fault zone resulting from grain rotation, but more importantly, from structural elements, particularly slip-surface cataclasites, but also fine-grained smears. The geometry of structural elements is a key control on this behaviour. Conduit-barrier behaviour was primarily found in fault zones cutting poorly lithified sediment.

Despite this finding, a greater proportion of modelled fault zones behaved as barriers than conduit-barriers, particularly in faults cutting sediment of contrasting competency. This partly supports previous assertions that faults cutting poorly lithified sediment are most likely to behave as barriers (Heynekamp *et al*., 1999; Rawling *et al*., 2001; Caine and Minor, 2009; Balsamo and Storti, 2010). This barrier behaviour results from an overall reduction in porosity and hydraulic conductivity in fault zones and the re-arrangement of beds. Faults that behave only as conduits to fluid-flow are significantly less common, and the impacts are relatively minor. Specific hydraulic impacts of fault zones depend on their structure, and therefore lithology, stratigraphy and fault throw.

7.2 Context

7.2.1 Hydrogeological structure of fault zones in poorly lithified sediment

It was proposed from previous outcrop studies that clay-smears in fault cores and shear deformation bands would have the greatest influence on the hydrogeology of fault zones cutting poorly lithified sediment, causing the fault zones to behave as barriers to fluid-flow (Heynekamp *et al*., 1999; Sigda *et al*., 1999; Rawling *et al*., 2001; Bense *et al*., 2003; Sigda and Wilson 2003; Minor and Hudson, 2006;

Caine and Minor, 2009). The absence of these structural elements from fault zones in the Gulf of Corinth rift is probably due to differences in the physical properties of the sediment (generally coarser) and the stress conditions (possibly shallower burial and saturated) during deformation (e.g. Fossen *et al*., 2007). Numerical models of fluid-flow demonstrate that the majority of fault zones will behave as strong barriers to fluid-flow, confirming suggestions by Rawling and Goodwin (2006) and Caine and Minor (2009) that hydraulic conductivity reductions in mixed zones will also contribute to the barrier behaviour of fault zones, perhaps producing barriers as strong as those with clay smears (e.g. Sigda *et al*., 1999; Tueckmental, 2010). Low hydraulic conductivity heterogeneities within the fault zone – cataclasites, fine-grained smears and even fine-grained sediment lenses – have been shown to cause faults to behave as virtually comprehensive barriers. On this basis, algorithms for assessing seal capacity based on the proportion of clay in the protolith (e.g. Lindsay *et al*., 1993; Yielding *et al*., 1997; Sperrevik *et al*., 2002; Bense and Person, 2006) are not directly applicable to faults cutting the poorly lithified syn-rift sediment in the Gulf of Corinth rift since they do not account for other processes that influence fault zone hydraulic properties (e.g. Gibson, 1998). It is unlikely that the results in this thesis complete the suite of possible fault zone structures in poorly lithified sediment.

Consistent with the findings of Bense and Person (2006), numerical models presented here demonstrate that conduit-barrier behaviour of fault zones in poorly lithified sediment can be attributed to hydraulic anisotropies. Imposed anisotropy representing grain rotation in the fault zone was found to be less hydraulically significant than that resulting from extrinsic anisotropies from structural elements. Model results show that extrinsic anisotropy is primarily caused by sub-vertical fluid-flow along the boundaries of elements with low hydraulic conductivity that is enforced by preferential fluid-flow through high hydraulic conductivity flow pathways (e.g. Jourde *et al*., 2002; Lunn *et al*., 2008).

It is important that hydrogeological studies of fault zones in poorly lithified sediment account for sub-vertical fluid flow both within (e.g. Bense and Person, 2006) and adjacent to the mixed zone – despite it being largely disregarded in typical reservoir fault seal predictions (e.g. Manzocchi *et al*., 1999; Dockrill and

Shipton, 2010). The controls of geometry, spatial distributions and the hydraulic properties of fault zone heterogeneities on both along-fault and cross-fault fluid-flow in faults demonstrate the requirement for characterization of these parameters in fault zone models (Matthai *et al*., 1998; Manzocchi *et al*., 1999; Aydin, 2000; Jourde *et al*., 2002; Lunn *et al*., 2008). The fluid-flow path complexities and subsequent hydraulic impacts resulting from heterogeneities within fault zones, indicate that homogenisation of these properties across the thickness of the mixed zone (e.g. Manzocchi *et al*., 1999; Bense and Person, 2006) risks over-simplification of these processes. Statistical characterisation and explicit representation of structural elements within a fault zone volume, such as by the Fault Facies approach, may therefore be more suitable for this purpose (e.g. Fredman, 2007; Tveranger *et al*., 2007; Lunn *et al*., 2008; Braathen *et al*., 2009), though would require improved statistical and empirical relationship data and is, inevitably, more computationally intense.

7.2.2 Hydrological implications

The widespread barrier behaviour of most fault structures in the Gulf of Corinth rift indicates that in saturated aquifers, faults in poorly lithified sediment are likely to compartmentalise fluid flow (e.g. Bredehoeft *et al*., 1992; Sigda *et al*., 1999; Rawling *et al*., 2001; Rawling and Goodwin, 2003; Stamatis and Voudouris, 2003; Giurgea *et al*., 2004; Minor and Hudson, 2006; Caine and Minor 2009). Whilst larger faults will behave as stronger barriers due to the decrease in fault zone transmissivity with throw (e.g. Walsh *et al*., 1998; Sigda *et al*., 1999; Bense and Person, 2006; Balsamo *et al*., 2010; Childs *et al*., 2009; Manzocchi *et al*., 2010), the substantial decrease in hydraulic conductivity with the first 2 m of fault throw indicates that faults of most sizes will hinder cross-fault fluid flow (e.g. Balsamo *et al*., 2010). Owing to the high density fault arrays proximal to crustal scale faults in the Gulf of Corinth, and analogous rifts, regional compartmentalisation of aquifers even from sub-seismic scale faults could be significant (e.g. Grauch *et al*., 2004; Caine and Minor 2009) particularly when their cumulative effects are considered (e.g. Sternlof *et al*., 2006). In coastal settings such as the Gulf of Corinth rift, aquifer compartmentalisation could prove critical for maintaining a partition between marine and freshwater aquifers (e.g. Mohamed and Worden, 2006). However, the majority of faults have small throws

and therefore probably relatively small extents along strike and dip (e.g. Childs *et al.*, 1996a; Shipton *et al.*, 2006; Childs *et al.*, 2009; Torabi and Berg, 2011), leading to limited fault connectivity and allowing fluid-flow around fault terminations and potentially through the array, albeit on a more tortuous pathway (e.g. Micarelli *et al.*, 2006b; Bense and Van Balen, 2004).

Fault conduit behaviour can encourage the spread of contaminants, even between aquifers that would otherwise be hydraulically separated (e.g. Bense and Person, 2006; Bense *et al.*, 2008). This could explain the marine signature within the conglomerate aquifer landward of the main Aigion fault (Figure 2.1) reported by Giurgea *et al.* (2004). In coastal areas of the Gulf of Corinth rift, aquifer contamination by saline intrusion along fault zones is a serious concern (e.g. Giurgea *et al.*, 2004; Stamatis and Voudouris, 2003). Fluid-flow along fault zones from the ground surface may be an important mechanism by which aquifers are recharged in arid areas (e.g. Sigda and Wilson, 2003), but it could also lead to the transportation of pesticides, fertilisers, and other surficial contaminants into aquifers (Sigda and Wilson, 2003; Stamatis and Voudouris, 2003; Voudouris *et al.*, 2005). Where sub-vertical fluid-flow occurs in the protosediment adjacent to the fault zone, the presence of damage zones comprised of small-faults or disaggregation bands with increased porosity (Bense *et al.*, 2003) could act to focus up or down-welling fluid. Fault zones can also be sources of upwelling groundwaters (Bense *et al.*, 2003).

In addition to primary fault zone processes, a number of other factors have been shown to contribute to the hydraulic impact of faults in poorly lithified sediment. Lithostratigraphic configurations and juxtapositions resulting from fault offset were found to be as, and in some cases, more, important than changes to sediment hydraulic conductivity in fault zones, strongly influencing fluid-flow pathways across the fault zone (e.g. Sigda *et al.*, 1999; Bense and Person, 2006; Barnicoat *et al.*, 2009; Manzocchi *et al.*, 2010). The occurrence of horizontal beds with lower hydraulic properties in protosediment can prevent sub-vertical fluid flow adjacent to the fault zone.

Numerical fluid-flow models presented here have shown that hydraulic boundary conditions exert considerable control on the precise hydraulic impact of fault

zones (e.g. Haneberg, 1995; Eichhubl and Boles, 2000; Gudmundsson, 2000; Eichhubl *et al*., 2004). Fault zones enhance local flow conditions, particularly when they are favourably orientated with fluid-flow pathways (e.g. Gudmundsson, 2000). Altering hydraulic boundary conditions through excessive groundwater abstraction and pumping can therefore impact the fault zone hydraulic behaviour, potentially compelling additional cross or along-fault fluid-flow (e.g. Stamatis and Voudouris, 2003). Importantly, outcrop evidence of cements in fault zones supports the conclusions of Sigda and Wilson (2003) that the decrease in sediment porosity that causes fault zones to behave as hydraulic barriers in the phreatic zone will cause them to behave as preferential flow paths in the vadose zone.

Hand samples and thin sections have shown that cements preferentially precipitated in and around the pores of fault zones will significantly decrease fault zone hydraulic conductivity, which will increase the barrier behaviour of fault zones over time (e.g. Knipe, 1997; Bense *et al*., 2003; Micarelli *et al*., 2006b; Eichhubl *et al*., 2009). Cement precipitation will be enhanced in regions in which groundwater is over-saturated in minerals, though this process has proven difficult to quantify (Manzocchi *et al*., 1999). Low hydraulic conductivity structural elements in fault zones are the main cause of deflected sub-vertical fluid-flow, therefore a decrease in fault zone hydraulic conductivity resulting from cementation could also increase this component of sub-vertical fluid-flow over time. In addition, deformation in sediment stiffened by cementation can produce fractures from brittle deformation processes, resulting in an increase in fault zone hydraulic conductivity (Sibson, 1977; Woodcock *et al*., 2007; Balsamo *et al*., 2008).

Assuming a particular barrier, conduit or conduit-barrier behaviour for all fault zones in poorly lithified sediment risks wrongly predicting fault zone hydraulic behaviour. This could have profound consequences for groundwater management. Consequently, it would be prudent to assess likely fault zone hydraulic behavior by taking into account as many controlling factors as possible, including: mechanical and hydrogeological properties of the sediment and stratigraphy, fault size (throw) and evolution, fault array characteristics and hydraulic boundary

conditions. The large numbers of variables and difficulties constraining the multitude of fault zone parameters, suggests that deterministic prediction of fault zone structure and hydraulic behaviour will remain a challenge (e.g. Childs *et al*., 1997; Walsh *et al*., 1998; Manzocchi *et al*., 1999; Fredman, 2007).

7.2.3 Limitations of the research

There are various limitations with this work. The first limitation involves the structural data collected from outcrop. The number of faults, and outcrops assessed was limited by time and available exposures. Separating fault zone data into the three groups (faults in poorly lithified sediment, sediment of contrasting competency and those in which fine and coarse-grained sediment is juxtaposed) resulted in groups with fewer faults than would be needed for identifying very robust trends with which to analyse the fault zone structure and deformation processes. This limits confidence in the apparent trends, and may hinder identification of additional trends. The geometrical and thickness properties of heterogeneities such as fine-grained smears and slip-surface cataclasites were not routinely investigated in the field. Subsequent model results indicate that these parameters are critical to fault zone hydraulic behaviour therefore these should be better quantified for model inputs.

The second limitation concerns measurements of hydraulic parameters. It would have been preferable to conduct direct measurements of fault zone hydraulic conductivity using an air permeameter in the field or on core samples in the laboratory instead of estimating hydraulic conductivity from thin section image analysis and grain-size distributions combined with empirical equations, due to the uncertainties that exist with these methods. It was not possible to identify clear trends in porosity and hydraulic conductivity with fault throw from the number of samples collected from zones of mixed sediment therefore this trend remains relatively speculative. In addition, factors such as pore throat size and connectivity and 3D variations in hydraulic conductivity variability that will also influence fluid-flow were not accounted for.

The third major limitation concerns the numerical fluid-flow models with considerably simplified geometries of fault zone heterogeneities and mixed zone

thickness across the strike and dip of the fault zones. In addition, damage zones, which previously have been considered an important feature in fault zones in poorly lithified sediment (e.g. Rawling *et al.*, 2001), were not included in the models which could impact overall fault zone hydraulic behaviour. In general, the investigation of fault zone hydrogeological structure in two dimensions neglects the potentially important influence of three dimensional fault zone structures that have previously been shown to be important for focussing fluid-flow through pipe structures for example within fault zones (Eichhubl and Boles, 2004). While boundary conditions were designed to represent the regional flow conditions, the impact of specific boundary conditions on fault hydraulic behaviour limits the predictive capacity of each fault model.

7.3 Further research

This work has provided additional insight into the hydraulic behaviour of fault zones in poorly lithified sediment but there remain a number of uncertainties that would benefit from further investigation. The following list identifies those topics, though it is not exhaustive:

1. Validation of fault zone hydraulic behaviour predicted from numerical fluid-flow models with hydrogeological data from the southern flank of the Gulf of Corinth rift. Hydrogeological data could include geochemical data, tracer tests and pumping tests. An assessment of the regional role of faults in poorly lithified sediment, including their contribution to aquifer recharge, groundwater sources, aquifer compartmentalisation and contamination could aid in management of groundwater resources in Gulf of Corinth rift region.

2. Development of models or algorithms for predicting fault zone hydraulic behaviour in poorly lithified sediment. This could entail modification or calibration of existing fault seal algorithms to account for the hydraulic role of fine-grained smears, specifically their coarser grain-size and lower smearing efficiency along the fault zone in comparison to clays. The role of zones of mixed sediment should also be included, and the possibility of fault hierarchies in faults cutting poorly lithified sediment considered.

Such a model or algorithm should be transferable to regional scale models and include along-fault fluid-flow.

3. Continued collection of fault zone structural data in poorly lithified sediment. This would enable recognition of hydrogeological fault zone structures not yet reported – particularly from a range of different geological settings, and further elucidate the most common structural elements. Additional geological settings should include locations in which faults are locally known to rupture, and areas where crustal stress conditions are well established, in order to constrain fault zone structural evolution and contributing factors. Investigation of strike-slip or reverse-fault fault zone structures in poorly lithified sediment should also be undertaken and compared with structures of normal faults.

4. Further characterisation of fault zone structural elements such as slip-surface cataclasites, fine-grained smears, and lenses and blocks. This should include their continuity and extent, geometry, dimensions, numbers across the fault zone, connectivity and hydraulic properties. Recognition of these properties is likely to be aided by constraint of their evolution processes and trends with lithology, stratigraphy and fault size. Further investigation into deformation mechanisms, particularly particulate flow and the efficiency of mixing between sediments with various rheological properties in sediment smears and zones of mixed sediment would also be beneficial.

5. Spatial and temporal variability of fault zone hydraulic conductivity. Investigation of the hydraulic implications of three-dimensional fault zone structure in poorly lithified sediment, accounting for structural variability along-strike and dip. Constraint of changes to fault zone hydraulic conductivity with secondary processes such as cementation and subsequent fault deformation, and identification of the timescales on which these occur.

6. Improved characterisation of fault array attributes and occurrences in poorly lithified sediments to further understand fault interconnectivity and

regional hydraulic properties. Attributes should include fault population distribution characteristics and vertical and horizontal length and orientation of faults. In addition, the spatial distribution of fault arrays in relation to crustal scale faults and the geometrical relationships between faults in basement rocks and overlying sediment.

7. Further quantification of fault zone anisotropy resulting from fault zone heterogeneities and grain rotation. Development of a method that can represent the causes of anisotropy in fault zone fluid-flow models.

7.4 Concluding statement

This work has revealed additional diversity of fault zone hydrogeological structure in poorly lithified sediment and its dependency on lithology, stratigraphy, fault throw and evolution, and burial conditions. Combined outcrop studies and numerical fluid-flow models have been presented in poorly lithified sediment for the first time in this manner, and have shown that fault zone heterogeneities and anisotropies can explain the conduit-barrier behaviour observed from hydrogeological data. However, this work has demonstrated that faults in poorly lithified sediments can behave as barriers or conduits to fluid flow depending on their hydrogeological structure. Additional factors impacting fault zone hydraulic behaviour include stratigraphic unit configuration, aquifer saturation state and hydraulic boundary conditions. These factors should be taken into consideration when assessing the hydraulic impact of faults in poorly lithified rift sediments.

Faults in poorly lithified rift sediments may thus have the potential to significantly compartmentalise aquifers and provide preferential fluid flow pathways for recharge or contaminants. This diversity in possible fault zone behaviour indicates the importance not only of considering fault zones in regional hydrogeological models, but in understanding the relationships between the variables controlling fault zone hydraulic structure and hydraulic impacts.

Appendix 1 – Fault data

Fault ID	Throw (m)	Thickness (m)			Lithology category	Zone of mixed seidment	Localised shear zone	Disaggregation band	Fine-grained smear	Lenses	Damage zone	Structure	Grain orientation and figure	Broken clast counts and figure	Grain-size sample and figure	Hand sample
		Av	Max	Min												
F1A	7.00	0.84	1.15	0.63	PLS	y	y	n	n	n	y	3.1a	3.2		5.5	
F1B	5.27	2.05	2.87	1.76	PLS	n	y	y	n	n	y	3.1b				
F1C	5.90	1.05	1.05	0.02	CC	n	y	n	n	y	y	3.1c			5.6	
F2	1.30	0.38	0.50	0.24	CC	n	y	n	n	y	n					
F3	3.90	2.32	3.59	1.63	CC	y	y	y	n	y	y	3.5				
F4	1.00	0.42	0.46	0.34	CC	y	y	n	n	n	n	3.6				
F5	0.60	0.27	0.40	0.15	PLS	y	n	n	n	n	n	3.7			5.7	
F6	1.50	0.203	0.35	0.13	CC	n	y	y	n	y	y	2.3				
F1	0.50	0.21	0.22	0.16	PLS	y	n	n	n	n	n					Ak F1 MZ
F2a	2.00	0.37	0.45	0.32	CC	y	n	n	y	n	y	4.7			5.8	Ak F2a (S,P,MZ), Ak F2b MZ
F2b	0.30	0.16	0.19	0.11	PLS	n	n	n	n	n	n	4.7				
F3	7.00	0.26	0.64	0.13	PLS	y	y	n	n	n	y		4.2b	4.3a		Ak F3a FW, Ak F3b MZ, Ak F3c MZ (Figure 4.2a)
F4	8.00	1.14	1.64	0.95	CC	y	y	n	y	y	y	4.5c				
Segmented Fault	0.60	0.51	0.72	0.15	CC	n	y	n	y	y	n					
Small Fault	0.01	0.13	0.23	0.01	CC	y	y	y	n	y	y					Ak SF (FW, MZ, HW)
Big Fault 1	15.00	1.91	2.37	1.83	PLS	y	n	n	n	n	y					
Big Fault 1	23.00	2.60	2.88	2.12	J	n	y	y	y	y	y	4.b				
Big Fault 1 Antithetic	0.70	0.19	0.24	0.15	PLS	y	n	n	y	n	n					
Big Fault 2	17.30	0.59	0.76	0.49	J	y	y	n	y	y	n					
B-D 2	4.23	0.27	0.48	0.15	PLS	n	y	n	n	y	y					
B-D 3	5.00	3.97	4.84	3.00	PLS	n	n	n	n	n	y					
Disaggregation band fault	0.09	0.28	0.46	0.12	CC	y	y	y	n	y	y	4.8				V DB (FW, DB, HW)

Grey boxes indicate locations of hydraulic conductivity estimates from grain-size distributions or thin section image analysis. Av, Max and Min are average (mean), minimum and maximum mixed zone thicknesses. PLS is poorly lithified sediment, CC sediment of contrasting competency and J are faults where fine and coarse-grained sediment is juxtaposed across the fault zone. Faults highlighted in light grey were discounted from the fault throw/mixed zone thickness and fault population distribution analyses because their throw measurements were ambiguous.

Fault ID	Throw (m)	Thickness (m)			Lithology category	Zone of mixed seidment	Localised shear zone	Disaggregation band	Fine-grained smear	Lenses	Damage zone	Structure	Grain orientation and figure	Broken clast counts and figure	Grain-size sample and figure	Hand sample
		Av	Max	Min												
Gravel marl fault (C)	40.00	1.18	1.46	0.96	J	y	y	n	y	n	y	4.9c				M GMa SS, M GMb SS
West big fault (B)	7.00	1.09	1.66	0.75	PLS	y	n	n	n	n	n					
Terrace Fault (E)	80.00	1.31	1.64	0.89	PLS	y	y	n	n	n	y	4.3c		4.3b		M TF MZ (Figure 4.3b)
An	1.49	0.26	0.49	0.09	PLS	y	n	n	n	n	y	4.1b	4.2a			M An FW (a,b), M An MZ (a,b) (Figure 4.2a)
An antithetic	0.42	0.10	0.15	0.08	PLS	y	n	n	n	n	y					
Be	4.00	0.62	0.81	0.33	PLS	y	n	n	n	n	n					
Ch	1.78	0.38	0.59	0.25	PLS	n	n	n	n	n	n					
Cemented fault	1.88	1.30	1.43	1.11	PLS	y	y	n	n	n	y	4.2a				
Fault 6	5.00	0.88	1.20	0.62	PLS	y	n	n	n	n	n					
Fault 6 antithetic	0.24	0.25	0.44	0.16	PLS	y	n	n	n	n	n					
Af2 i	1.70	0.20	0.33	0.14	PLS	y	n	n	n	n	n					
AF 3	16.70	0.48	0.64	0.36	PLS	y	n	n	n	n	y					
Cemented Fault 2	1.00	0.30	0.59	0.17	PLS	y	n	n	n	n	y			4.3c	4.3c	M CF2a MZ, M CF2b MZ (Figure 4.3c)
Fault 10	5.05	2.78	9.45	0.95	CC	n	y	n	n	y	y					
Fault 11	4.79	0.90	1.38	0.66	CC	n	y	n	n	y	y	2.1				
Fault 11 Antithetic	0.01				PLS	y	n	n	n	n	n	2.10				M F11 An (FW, HW, MZ, FWb, DBb)
M1	1.20	0.07	0.16	0.04	CC	n	y	n	y	y	n					
M2	0.25	0.11	0.24	0.04	CC	n	n	n	y	y	y					
M3	1.00	0.11	0.14	0.04	CC	n	y	y	y	y	y	4.5b				
M4	1.80	0.03	0.08	0.02	CC	n	y	n	y	y	y					
G1	40.00	2.64	3.30	1.57	PLS	y	y	n	n	n	n	4.1c				P G1 SS (Figures 4.4a and b)

Grey boxes indicate locations of hydraulic conductivity estimates from grain-size distributions or thin section image analysis. Av, Max and Min are average (mean), minimum and maximum mixed zone thicknesses. PLS is poorly lithified sediment, CC sediment of contrasting competency and J are faults where fine and coarse-grained sediment is juxtaposed across the fault zone. Faults highlighted in light grey were discounted from the fault throw/ mixed zone thickness and fault population distribution analyses because their throw measurements were ambiguous.

Appendix 2 – Image analysis procedure using ImageJ

1. **Image acquisition:** *Choose magnification of the images based on grain and pore size in the thin section. Are random images are appropriate or should specific areas should be targeted.* Images acquired using Leica Software and camera attached to a petrographic microscope

↓

2. Pre-processing: Add scale to the image: select the line tool from the toolbar, draw a line of known length; "Analyze_Set scale". Enter parameters into "Known distance" and "units".

↓

3. Image selection: Select the area to be sampled: select the box tool from the tool bar and draw a box around an area that does not include the edge of the thin section "Image_Crop"

↓

4. Classification of grain and pore space: "Image_Adjust_Colour threshold_RGB". Select an area of pore space to classify using the box tool. Click "Sample" then "Threshold" and select the appropriate "pass" or "stop" for each wavelength. Pores and grains should now be divided.

↓

5. Image adjustments: Remove small holes and sharpen the image: "Process_Smooth" and "Process_Sharpen."

↓

6. Prepare image for analysis: Make binary image: "Process_Binary_Make Binary". Fill holes: Comparison of binary image with original, identification of wrongly classified regions. If there are, manually fill the holes in Adobe Illustrator. Import new image into ImageJ and convert to binary again.
Separate grains: "Process_Binary_Watershed"

↓

7. Grain analysis: Choose measurements: "Analyse_Set measurements" tick the measurements required. Run analysis: "Analyse_Analyse particles" and select the image output required leave "exclude on edges" box ticked. Key parameter; Feret for distributions: Analyse_Distributions". Select parameter (grain-size), number of bins, and range.

↓

8. Pore analysis: Set to analyse pores: Open original binary image "Edit_Invert Image". Choose measurements: "Analyse_Set measurements" tick the measurements required. Run analysis: "Analyse_Analyse particles" and select the image output required leave "exclude on edges" box ticked. Key parameter; Porosity.

Appendix 3 – Porosity and hydraulic conductivity of thin section samples

Location	Fault ID	Hand sample ID	Thin section ID	Sample number	Porosity (%)	Grain size (mm)	Sorting (Phi)	K (m s^{-1})
Akrata	Fault 1 (0.5 m throw)	Ak F1	Ak F1 MZ	1	25.70	1.46	0.47	2.72E-03
				2	23.10	2.19	0.25	4.15E-03
				Average	**24.40**	**1.82**	**0.36**	**3.44E-03**
				Range	**2.60**	**0.73**	**0.22**	**1.42E-03**
	Small fault (0.01 m throw)	Ak SF	Ak SF (FW)	1	31.20	1.56	0.33	6.53E-03
				2	22.20	1.57	0.34	1.85E-03
				Average	**26.70**	**1.56**	**0.34**	**4.19E-03**
				Range	**9.00**	**0.00**	**0.01**	**4.68E-03**
			Ak SF (MZ)	1	11.90	1.49	0.36	2.00E-04
				2	10.50	1.34	0.37	1.08E-04
				Average	**11.20**	**1.41**	**0.37**	**1.54E-04**
				Range	**1.40**	**0.14**	**0.01**	**9.11E-05**
			Ak SF (HW)	1	22.80	1.20	0.38	1.20E-03
				2	31.30	1.43	0.32	5.52E-03
				Average	**27.05**	**1.32**	**0.35**	**3.36E-03**
				Range	**8.50**	**0.22**	**0.06**	**4.32E-03**
	Fault 2 (2 m throw)	Ak F2a MZ	Ak F2a FZ (S)	1	11.00	0.61	0.32	2.62E-05
				2	5.10	0.52	0.31	1.65E-06
				Average	**8.05**	**0.57**	**0.32**	**1.39E-05**
				Range	**5.90**	**0.09**	**0.01**	**2.46E-05**
			Ak F2a MZ (M)	1	5.10	2.18	0.24	2.91E-05
				2	6.40	0.53	0.35	3.49E-06
				Average	**5.75**	**1.35**	**0.30**	**1.63E-05**
				Range	**4.75**	**1.65**	**0.11**	**2.56E-05**
			Ak F2a MZ (P)	1	25.30	0.66	0.33	5.25E-04
				2	14.60	0.72	0.34	9.12E-05
				Average	**19.95**	**0.69**	**0.34**	**3.08E-04**
				Range	**10.70**	**0.06**	**0.01**	**4.34E-04**
	Fault 2 (2 m throw)	Ak F2b MZ	Ak F2b FZ	1	9.90	1.68	0.33	1.41E-04
				2	5.70	1.36	0.39	1.60E-05
				Average	**7.80**	**1.52**	**0.36**	**7.86E-05**
				Range	**4.20**	**0.33**	**0.06**	**1.25E-04**
	Fault 3 (7 m throw)	Ak F3a FW	Ak F3a FW	1	10.10	3.29	0.22	5.74E-04
				2	20.40	2.35	0.25	3.07E-03
				Average	**15.25**	**2.82**	**0.24**	**1.82E-03**
				Range	**10.30**	**0.94**	**0.03**	**2.50E-03**
		Ak F3b MZ	Ak F3b MZ	1	3.70	1.89	0.35	8.11E-06
				2	13.10	2.62	0.35	8.49E-04
				Average	**8.40**	**2.25**	**0.35**	**4.29E-04**
				Range	**9.40**	**0.73**	**0.00**	**8.41E-04**
		Ak F3c MZ	Ak F3c FZ	1	6.30	1.84	0.16	4.03E-05
				2	9.70	1.43	0.34	9.50E-05
				Average	**8.00**	**1.64**	**0.25**	**6.77E-05**
				Range	**3.40**	**0.42**	**0.18**	**5.47E-05**
Voutsimos	Disaggregation band fault (0.09 m throw)	V DB	V DB (FW)	1	21.70	1.56	0.33	1.70E-03
				2	16.70	0.85	0.33	2.00E-04
				Average	**19.20**	**1.20**	**0.33**	**9.47E-04**
				Range	**5.00**	**0.72**	**0.00**	**0.00**
			V DB (DB)	1	39.80	1.49	0.32	1.60E-02
				2	45.10	1.34	0.37	2.28E-02
				Average	**42.45**	**1.41**	**0.35**	**1.94E-02**
				Range	**5.30**	**0.14**	**0.05**	**6.86E-03**
			V DB (HW)	1	18.70	1.20	0.38	5.98E-04
				2	26.70	1.43	0.32	3.01E-03
				Average	**22.70**	**1.32**	**0.35**	**1.80E-03**
				Range	**8.00**	**0.22**	**0.06**	**2.41E-03**

Location	Fault ID	Hand sample ID	Thin section ID	Sample number	Porosity (%)	Grain size (mm)	Sorting (Phi)	K (m s^{-1})
Mentourgianika	F 11 An (0.1 m)	M F11 An	M F11 An (FW)	1	20.70	1.52	0.38	1.35E-03
				2	24.40	3.18	0.18	1.07E-02
				Average	**22.55**	**2.35**	**0.28**	**6.02E-03**
				Range	**3.70**	**1.66**	**0.20**	**-0.01**
			M F11 An (HW)	1	18.30	2.22	0.25	1.88E-03
				2	23.10	2.71	0.43	6.39E-03
				Average	**20.70**	**2.47**	**0.34**	**4.14E-03**
				Range	**4.80**	**0.49**	**0.18**	**0.00**
			M F11 An (FZ)	1	13.70	2.08	0.25	6.24E-04
				2	15.70	2.38	0.27	1.28E-03
				Average	**14.70**	**2.23**	**0.26**	**9.54E-04**
				Range	**2.00**	**0.29**	**0.02**	**0.00**
			M F11 An (DB)	1	20.40	2.82	1.46	4.43E-03
				2	25.30	2.00	0.25	4.82E-03
				Average	**22.85**	**2.41**	**0.85**	**4.62E-03**
				Range	**4.90**	**0.82**	**1.21**	**3.89E-04**
			M F11 An (FW B)	1	11.10	1.52	0.38	1.66E-04
				2	9.70	3.18	0.24	4.70E-04
				Average	**10.40**	**2.35**	**0.31**	**3.18E-04**
				Range	**1.40**	**1.66**	**0.14**	**3.04E-04**
	Gravel/marl fault (40 m throw)	M GM SS a	M GM SS a	1	1.20	2.94	0.29	6.38E-07
				2	3.70	1.20	0.48	3.30E-06
				Average	**2.45**	**2.07**	**0.39**	**1.97E-06**
				Range	**2.50**	**1.74**	**0.19**	**2.66E-06**
	Gravel-marl fault (40 m throw)	M GM SS b	GM SS b	1	8.30	1.48	0.31	6.23E-05
				2	6.30	1.49	0.23	2.63E-05
				Average	**7.30**	**1.49**	**0.27**	**4.43E-05**
				Range	**2.00**	**0.00**	**0.08**	**3.61E-05**
	Terrace Fault 1 (80 m throw)	M TF MZ	M TF MZ	1	5.10	4.60	0.22	1.30E-04
				2	10.80	1.64	0.28	1.78E-04
				Average	**7.95**	**3.12**	**0.25**	**1.54E-04**
				Range	**5.70**	**2.95**	**0.06**	**0.00**
	An (1.49 m throw)	M An FW	M An FW a	Whole TS	20.10	8.53	0.22	3.86E-02
				1	14.30	2.84	0.19	1.34E-03
				2	33.70	1.44	0.22	7.51E-03
				Average	**22.70**	**4.27**	**0.21**	**1.58E-02**
				Range	**19.40**	**7.09**	**0.03**	**3.72E-02**
			M An FW b	Whole TS	29.70	3.50	0.32	2.71E-02
				1	10.50	2.09	0.36	2.63E-04
				2	24.80	2.80	0.29	8.82E-03
				Average	**21.67**	**2.80**	**0.32**	**1.20E-02**
				Range	**19.20**	**1.41**	**0.07**	**8.56E-03**
		M An MZ	M An MZ a	Whole TS	18.10	10.81	0.28	4.31E-02
				1	23.20	2.34	0.34	4.84E-03
				2	26.60	2.28	0.32	7.59E-03
				Average	**22.63**	**5.15**	**0.31**	**1.85E-02**
				Range	**8.50**	**8.53**	**0.06**	**3.82E-02**
			M An MZ b	Whole TS	27.50	10.46	0.24	1.80E-01
				1	9.50	2.19	0.29	2.09E-04
				2	10.40	2.71	0.34	4.30E-04
				Average	**15.80**	**5.12**	**0.29**	**6.04E-02**
				Range	**18.00**	**8.27**	**0.10**	**1.80E-01**
	Cement fault 2 (1 m throw)	M CF 2 MZ a	M CF 2a MZ	1	2.40	2.63	0.35	4.17E-06
				2	10.50	2.91	0.32	5.11E-04
				Average	**6.45**	**2.77**	**0.34**	**2.58E-04**
				Range	**8.10**	**0.29**	**0.03**	**5.07E-04**
	Cement fault 2 (1 m throw)	M CF 2 MZ b	M CF 2b MZ	1	0.90	2.49	1.48	1.92E-07
				2	0.60	3.77	1.32	1.30E-07
				Average	**0.75**	**3.13**	**1.40**	**1.61E-07**
				Range	**0.30**	**1.29**	**0.17**	**6.17E-08**
Pirgos	G1(40 m throw)	P G1 SS	P G1 SS	1	1.70	0.90	0.39	1.72E-07
				2	0.80	0.84	0.26	1.52E-08
				Average	**1.25**	**0.87**	**0.33**	**9.38E-08**
				Range	**0.90**	**0.07**	**0.13**	**1.57E-07**

Appendix 4 – PLG Model results

4.1 Model results and parameters for small faults in poorly lithified gravels (PLG Sm 1 and 2)

Model ID	Fault thickness			Zone of mixed sediment			Anis	Head drop (m)	Head contour type	Flow vector type	Streamtrace type	Streamtrace distance travelled (m)
	Min	Av	Max	Min	Av	Max						
CS No fault								0	Con A	Vec A	Str A	0
CS PLG Sm 1a								0	Con A	Vec A	Str A	0
CS PLG Sm 1b								0	Con A	Vec A	Str A	0
CS PLG Sm 1c								0	Con A	Vec A	Str A	0
CS PLG Sm 1d								0	Con A	Vec A	Str A	0
CS PLG Sm 1e								0	Con A	Vec A	Str A	0
CS PLG Sm 1f								0	Con A	Vec A	Str A	0
CS PLG Sm 2a								0.1	Con B	Vec B	Str A	0
CS PLG Sm 2b								0	Con A	Vec C	Str B	1.6
CS PLG Sm 2c								5.8	Con B	Vec B	Str A	0
CS PLG Sm 2d								0.1	Con B	Vec B	Str A	0
CS PLG Sm 2e								0	Con A	Vec C	Str B	1.2
CS PLG Sm 2f								6.4	Con B	Vec B	Str A	0
CS PLG Sm 2g								0.05	Con B	Vec B	Str A	0
CS PLG Sm 2h								0	Con A	Vec C	Str B	0.6
CS PLG Sm 2i								5	Con B	Vec B	Str A	0
CS PLG Sm 2j								0.05	Con Ci	Vec B	Str C	0.4
CS PLG Sm 2k								0	Con Ci	Vec C	Str B	2.1
CS PLG Sm 2l								0.5	Con Ci	Vec B	Str C	0.5
CS PLG Sm 2m								0.05	Con Ci	Vec B	Str C	0.6
CS PLG Sm 2n								0	Con C	Vec C	Str B	3.2
CS PLG Sm 2o								0.8	Con Ci	Vec B	Str C	0.7
CS PLG Sm 2p								0	Con Ci	Vec B	Str C	0.3
CS PLG Sm 2q								0	Con C	Vec C	Str B	2
CS PLG Sm 2r								0.6	Con Ci	Vec B	Str C	0.3
CN PLG Sm 2a								0.1	Con B (rev)	Vec B (rev)	Str A (rev)	0
CN PLG Sm 2a								N/a	Con E	Vec G	Str G	0
US PLG Sm 2j								0.05	Con Ci (rev)	Vec B (rev)	Str C (rev)	0.4
US PLG Sm 2j								N/a	Con F	Vec H	Str I	0.5

Light grey filled boxes indicates parameters that were applied to the model. Min, Av and Max refer to minimum, average and maximum values and Anis indicates anisotropy. Dark grey fill indicates parameters not relevant to the model. Con, Vec and Str refer to the head contour, vector and streamtrace types in Appendices 4.4 to 4.6. CS is confined flow from south to north, CN is confined flow from north to south and US is unconfined flow from south to north. Rev is reversed model output.

Appendix 4.2 Model results and parameters for large faults in poorly lithified gravels (PLG Lg 1)

Model ID	Fault thickness			Mixed zone			Anis	Head-drop (m)	Head contour type	Flow vector type	Streamtrace type	Streamtrace distance travelled
	Min	Av	Max	Min	Av	Max						
CS PLG Lg 1a								2.5	Con B	Vec B	Str C	0.4
CS PLG Lg 1b								0.4	Con Ci	Vec B	Str C	1.5
CS PLG Lg 1c								0	Con C	Vec C	Str B	2.2
CS PLG Lg 1d								8.4	Con B	Vec B	Str C	0.4
CS PLG Lg 1e								0	Con C	Vec C	Str B	4.5
CS PLG Lg 1f								2	Con Ci	Vec B	Str C	2
CS PLG Lg 1g								2.8	Con B	Vec B	Str C	0.7
CS PLG Lg 1h								1	Con Ci	Vec B	Str C	2.4
CS PLG Lg 1i								0	Con C	Vec C	Str B	4
CS PLG Lg 1j								8.8	Con B	Vec B	Str C	0.6
CS PLG Lg 1k								0	Con C	Vec C	Str B	4.5
CS PLG Lg 1l								2.5	Con Ci	Vec B	Str C	2.4
CS PLG Lg 1m								1.9	Con B	Vec B	Str C	0.4
CS PLG Lg 1n								0.4	Con Ci	Vec B	Str C	1.2
CS PLG Lg 1o								0	Con C	Vec B	Str B	2.2
CS PLG Lg 1p								6.9	Con B	Vec B	Str C	0.3
CS PLG Lg 1q								0	Con C	Vec C	Str B	4.5
CS PLG Lg 1r								1.8	Con Ci	Vec B	Str C	1.2
CN PLG Lg 1a								2.5	Con B (rev)	Vec B (rev)	Str C (rev)	0.4
CN PLG Lg 1b								0.4	Con Ci (rev)	Vec B (rev)	Str C (rev)	1.5
CN PLG Lg 1 a								N/a	Con E	Vec G	Str G	0
CN PLG Lg 1b								N/a	Con F	Vec H	Str J	2

Light grey filled boxes indicates parameters that were applied to the model. Min, Av and Max refer to minimum, average and maximum values and Anis indicates anisotropy. Con, Vec and Str refer to the head contour, vector and streamtrace types in Appendices 4.4 to 4.6. CS is confined flow from south to north, CN is confined flow from north to south and US is unconfined flow from south to north. Rev is reversed model output.

Appendix 4.3 Model results and parameters for large faults in poorly lithified gravels (PLG LG 2)

Model ID	Fault thickness			Zone of mixed sediment			Anis	Slip surface			Head-drop (m)	Head contour type	Flow vector type	Streamtrace type	Streamtrace distance travelled (m)
	Min	Av	Max	Min	Av	Max		Min	Av	Max					
CS PLG Lg 2a		■			■				■		5.9	Con D	Vec D	Str D	11*
CS PLG Lg 2b		■		■				■			9.2	Con Bi	Vec D	Str D	10*
CS PLG Lg 2c		■				■				■	0.4	Con C	Vec D	Str B	2.6
CS PLG Lg 2d			■		■				■		6.2	Con D	Vec D	Str D	10*
CS PLG Lg 2e			■	■				■			9.4	Con Bi	Vec D	Str D	7*
CS PLG Lg 2f			■			■				■	0.4	Con C	Vec D	Str B	4
CS PLG Lg 2g	■				■				■		6.4	Con Di	Vec D	Str E	1.5
CS PLG Lg 2h	■			■				■			9.2	Con Bi	Vec D	Str E	1
CS PLG Lg 2i	■					■				■	0.4	Con C	Vec D	Str B	2
CS PLG Lg 2j		■			■		■		■		7	Con D	Vec D	Str G	4.4
CS PLG Lg 2k		■		■			■	■			8.8	Con D	Vec D	Str E	10**
CS PLG Lg 2l		■				■	■			■	0	Con C	Vec E	Str F	4.5
CS PLG Lg 2m			■		■		■		■		4.2	Con D	Vec D	Str D	10 **
CS PLG Lg 2n			■	■			■	■			8.8	Con D	Vec D	Str D	13 **
CS PLG Lg 2o			■			■	■			■	0	Con C	Vec E	Str F	8
CS PLG Lg 2p	■				■		■		■		6.8	Con Di	Vec D	Str G	4.8
CS PLG Lg 2q	■			■			■	■			8	Con Di	Vec D	Str G	1.3
CS PLG Lg 2r	■					■	■			■	0	Con C	Vec E	Str F	4.2
CS PLG Lg 2s		■			■				■		5.9	Con D	Vec F	Str E	6*
CN PLG Lg 2a		■			■				■		5.9	Con D (rev)	Vec D (rev)	Str D (rev)	11*
CN PLG Lg 2j		■			■		■		■		7	Con D (rev)	Vec D (rev)	Str G (rev)	4.4
US PLG Lg 2a		■			■				■		N/a	Con G	Vec G	Str J	10*
US PLG Lg 2j		■			■		■		■		N/a	Con H	Vec I	Str K	7.5

Light grey filled boxes indicates parameters that were applied to the model. Min, Av and Max refer to minimum, average and maximum values and Anis indicates anisotropy. Con, Vec and Str refer to the head contour, vector and streamtrace types in Appendices 4.4 to 4.6. CS is confined flow from south to north, CN is confined flow from north to south and US is unconfined flow from south to north. * indicates deflected sub-vertical fluid flow. Rev is reversed model output.

Appendix 4.4 Head contour types for models of faults in poorly lithified gravels (PLG)

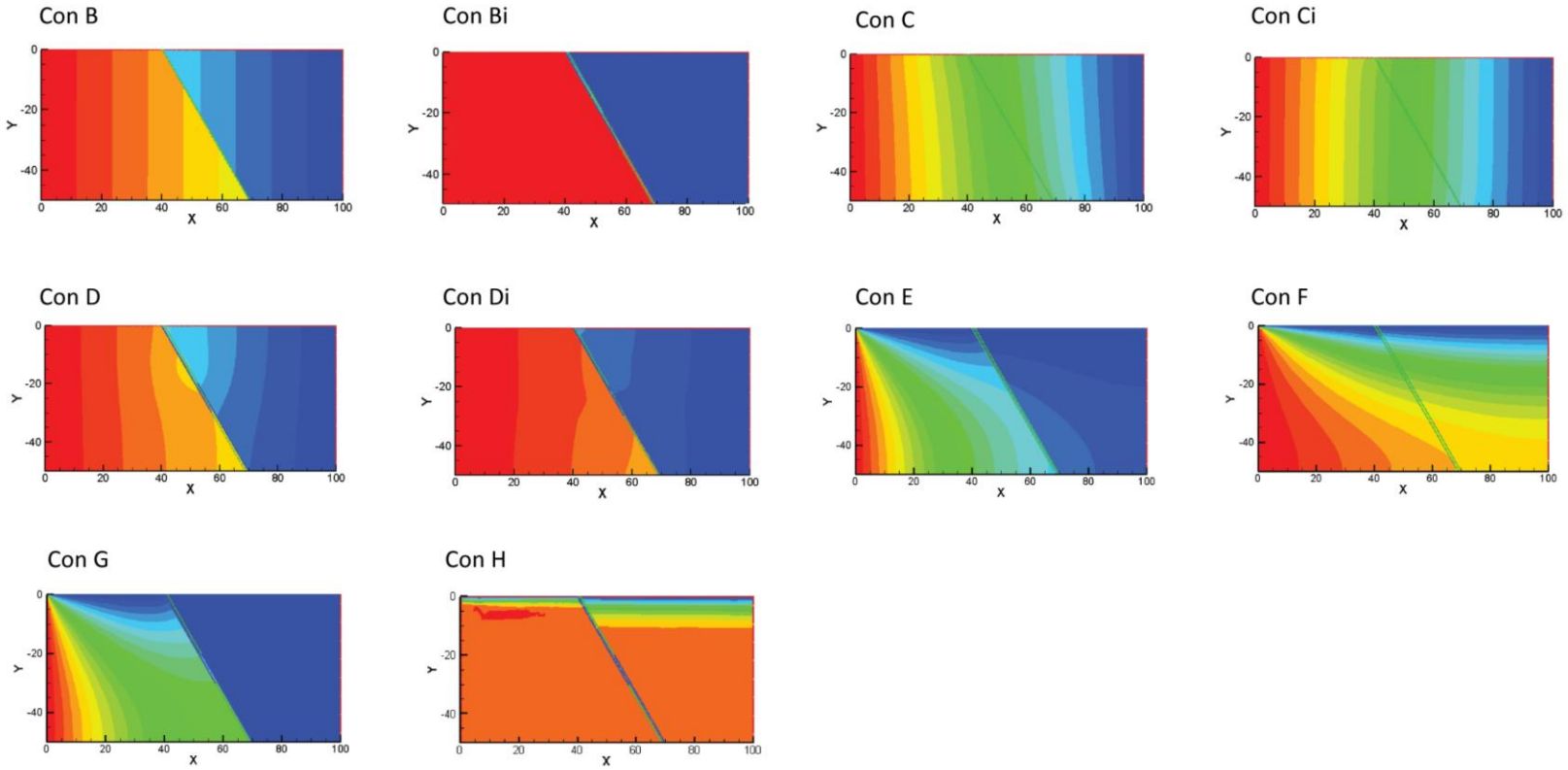

Head contour pattern "types" from PLG models. Con A is the pattern caused by confined flow from the south to north (CS), with no fault (Figure 6.1). Pattern types Con B to Di are also found under CS flow boundary conditions but with fault zones. The same boundary conditions with flow from north to south (CN) are not shown, but are the reverse of these. Pattern types Con E to H are found under unconfined boundary conditions with from south to north (US).

Appendix 4.5 Vector types for models of faults in poorly lithified gravels (PLG)

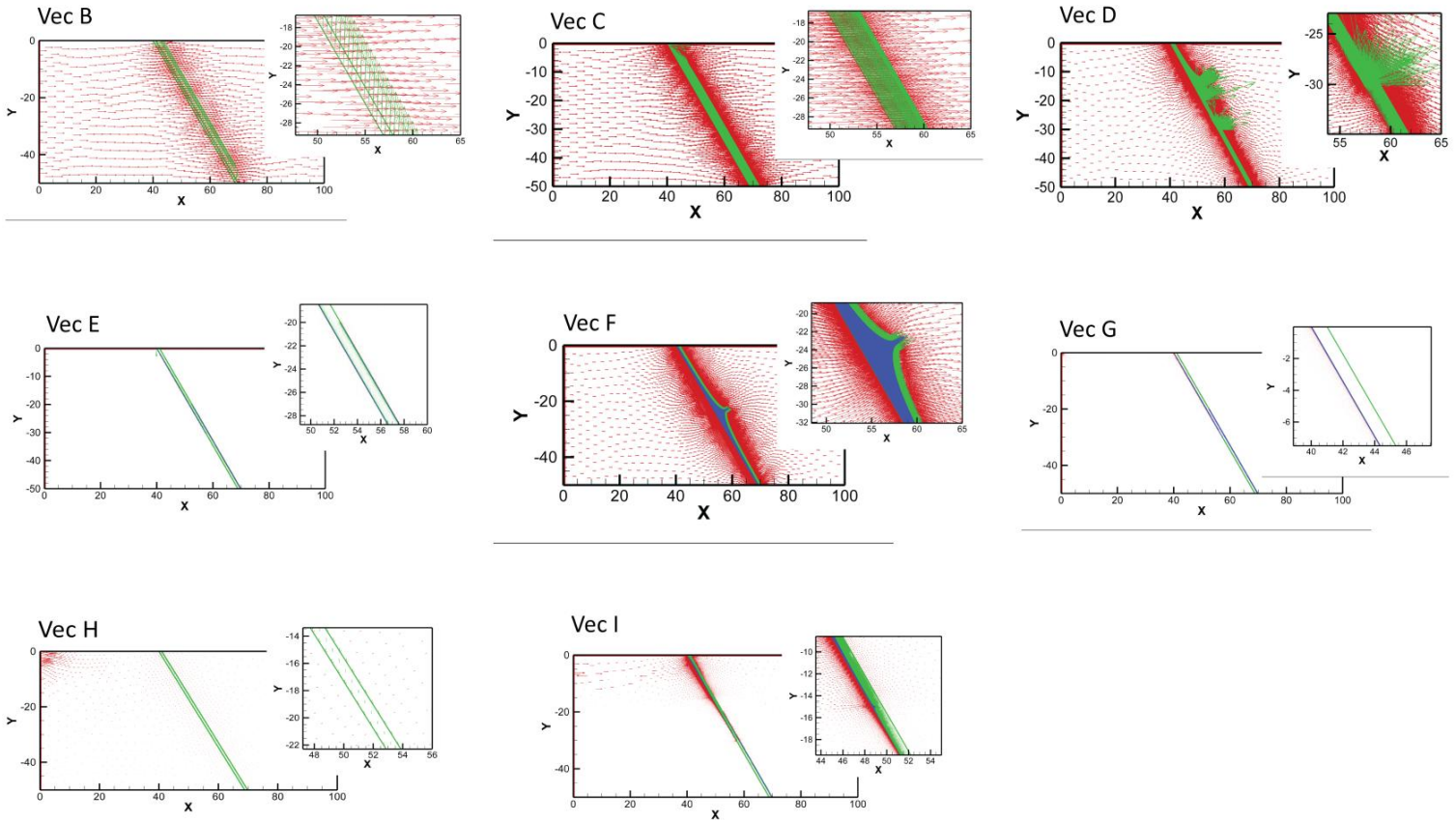

Vector pattern "types" patterns from PLG models. Vec A is the pattern caused by confined flow from the south to north (CS), with no fault (Figure 6.1). Pattern types Con B to G are also found under CS flow boundary conditions but with fault zones. The same boundary conditions with flow from north to south (CN) are not shown, but are the reverse of these. Pattern types Con H and I are found under unconfined boundary conditions with from south to north (US).

Appendix 4.6 Streamtrace types for models of faults in poorly lithified gravels (PLG)

Streamtrace pattern "types" from PLG models. Str A is the pattern caused by confined flow from the south to north (CS), with no fault (Figure 6.1). Pattern types Str B to G are also found under CS flow boundary conditions but with fault zones. The same boundary conditions with flow from north to south (CN) are not shown, but are the reverse of these. Pattern types Str H to J are found under unconfined boundary conditions with from south to north (US).

Appendix 5 – CC Model results

Appendix 5.1 Model results and parameters for faults cutting sediment of contrasting competency (CC)

Model ID	Mixed zone thickness	Lens	Zone of mixed sediment	Fine-grained smear	Head-drop (m)	Head contour type	Flow vector type	Streamtrace type	Streamtrace distance travelled (m)
CC CS 1	average				4.5	Con J	Vec K	Str O	0.7
CC CS 2	average	small			2.4	Con J	Vec K	Str O	0.6
CC CS 3	minimum				4	Con J	Vec K	Str O	0.8
CC CS 4	maximum				2.1	Con J	Vec K	Str O	0.6
CC CS 5	minimum				9.6	Con Jiii	Vec L	Str P	0.5
CC CS 6	average				9.4	Con Jiii	Vec L	Str O	1
CC CS 7	maximum				9.2	Con Jiii	Vec L	Str O	0.6
CC CS 8	minimum				9.5	Con Ji	Vec K	Str O	1
CC CS 9	average				9.2	Con Ji	Vec K	Str O	1
CC CS 10	maximum				8.4	Con Ji	Vec K	Str O	1
CC CS 11	minimum	both			8.4	Con J	Vec M	Str O	1
CC CS 12	average	both			5.6	Con J	Vec M	Str O	1
CC CS 13	maximum	both			7.8	Con Ji	Vec M	Str O	1
CC CS 14	minimum				5.4	Con Ji	Vec M	Str O	0.7
CC CS 15	average				5.6	Con Ji	Vec M	Str O	0.8
CC CS 16	maximum				5.6	Con Ji	Vec M	Str O	0.7
CC CS 17	minimum				9	Con Jiii	Vec L	Str O	0.5
CC CS 18	average				9	Con Jiii	Vec L	Str O	0.5
CC CS 19	maximum				8.8	Con Jiii	Vec L	Str O	0.4
CC CS 20	minimum				9.4	Con Jiv	Vec N	Str O	0.5
CC CS 21	average				9.7	Con Jiv	Vec N	Str O	0.5
CC CS 22	maximum				9.4	Con Jiv	Vec N	Str O	0.5
CC CS 23	minimum	both			9.2	Con Jiii	Vec L	Str O	0.5
CC CS 24	average	both			6.6	Con Jii	Vec L	Str O	0.8
CC CS 25	maximum	both			9	Con Jiii	Vec L	Str O	0.6
CC CS 26	minimum	both			9.6	Con Jiv	Vec N	Str O	0.8

Light grey filled boxes indicate parameters that were applied to the model. Con, Vec and Str refer to the head contour, vector and streamtrace types in Appendices 5.2 to 5.4. CS is confined flow from south to north. Both indicates both coarse and fine-grained sediment lenses and small indicates small lenses.

Model ID	Mixed zone thickness	Lens	Zone of mixed sediment	Fine-grained smear	Head-drop (m)	Head contour type	Flow vector type	Streamtrace type	Streamtrace distance travelled (m)
CC CS 28	maximum	both			9.8	Con Jiv	Vec K	Str Q	0
CC CS 29	minimum	both			8.4	Con J	Vec M	Str O	1
CC CS 30	average	both			5.4	Con J	Vec K	Str O	1
CC CS 31	maximum	both			7.8	Con J	Vec M	Str O	1
CC CS 32	minimum			thin	6	Con J	Vec L	Str O	0.5
CC CS 33	maximum			thin	5.6	Con J	Vec L	Str O	0.5
CC CS 34	average			thin	5.6	Con J	Vec L	Str O	0.5
CC CS 35	average			thick	9.6	Con Jiv	Vec L	Str O	0.5
CC CS 36	average	mult			2.4	Con J	Vec K	Str O	0.7
CC CS 37	average	mult			6.2	Con K	Vec M	Str O	1
CC CS 38	average	mult & both			8.4	Con Ji	Vec M	Str O	1
CC CS 39	average	mult & both			9.2	Con Jiii	Vec L	Str O	0.5
CC CS 40	average	mult & both			9.8	Con Jiv	Vec K	Str O	1.3
CC CS 41	average			low K	9.8	Con Jiv	Vec N	Str O	0.5
CC CS 42	average			high K	5.6	Con J	Vec L	Str O	0.4
CC CS 43	average			low K	10	Con Jiv	Vec N	Str O	0.8
CC CS 44	average			high K	9.4	Con Ji	Vec O	Str O	1
CC CS 45	minimum			low K	10	Con Jiv	Vec N	Str O	0.8
CC CS 46	maximum			high K	8.8	Con Ji	Vec N	Str O	0.8
CC CS 47	average			small dis	9.8	Con Ki	Vec O	Str O	5
CC CS 48	average			large dis	9.6	Con Ki	Vec O	Str R	5.4
CC CS 49	average			two small dis	8.6	Con Ki	Vec O	Str R	5
CC CS 50	average			two large dis	7.6	Con Ki	Vec O	Str R	5

Con, Vec and Str refer to the head contour, vector and streamtrace types in Appendices 5.2 to 5.4. CS is confined flow from south to north. Both indicates both coarse and fine-grained sediment lenses. Mult indicates multiple lenses. Thin and thick refer to the thickness of the fine-grained smear, and K the hydraulic conductivity. Dis indicates a discontinuity in the fine-grained smear.

Model ID	Mixed zone thickness	Lens	Zone of mixed sediment	Fine-grained smear	Head-drop (m)	Head contour type	Flow vector type	Streamtrace type	Streamtrace distance travelled (m)
CC CS 53	average			two small dis	9.4	Con Ki	Vec O	Str R	3
CC CS 54	average			two large dis	9.6	Con Ki	Vec O	Str O	0.9
CC CS 55	average			two large dis	9.4	Con Ki	Vec O	Str R	2.6
CC CS 56	average			two large dis	9.4	Con Ki	Vec O	Str R	4.2
CC CS 57	average	ev oth			6	Con Kii	Vec K	Str P	0.7
CC CS 58	average	ev oth			9.8	Con Jiv	Vec N	Str P	1
CC CS 59	average	ev oth & both			9.4	Con Kii	Vec M	Str O	1
CC CS 60	average	ev oth & both			9.4	Con Jiv	Vec L	Str O	0.8
CC CS 61	average		anisotropic		0	Con J	Vec P	Str O	0.8
CC CS 62	average		anisotropic		9.4	Con Ji	Vec P	Str O	1
CC CS 63	average	both	anisotropic		9.6	Con Ji	Vec P	Str O	1
CC CS 64	average		anisotropic		9.5	Con Kii	Vec Q	Str O	0.7
CC CS 65	average	both	anisotropic		9.6	Con Jiv	Vec M	Str O	0.8
CC CS 66	large				0	Con J	Vec K	Str O	1
CC CS 67	large	both			0	Con J	Vec K	Str O	1
CC CS 68	large				5.6	Con J	Vec K	Str O	0.8
CC CS 69	large		anisotropic		0.6	Con L	Vec P	Str O	1.5
CC CS 70	large				9.2	Con Jiv	Vec L	Str O	0.6
CC CS 71	large	both			7.2	Con J	Vec K	Str O	1
CC CS 72	large	both			9.4	Con Jiv	Vec K	Str O	1
CC CN 1	average				4.5	Con J (rev)	Vec K (rev)	Str O (rev)	0.7
CC CN 6	average				9.4	Con Jiii (rev)	Vec L (rev)	Str O (rev)	1
CC CN 61	average		anisotropic		0	Con J (rev)	Vec P (rev)	Str O (rev)	0.8

Con, Vec and Str refer to the head contour, vector and streamtrace types in Appendices 5.2 to 5.4. CS is confined flow from south to north, CN is confined flow from north to south and US is unconfined flow from south to north. Both indicates both coarse and fine-grained sediment lenses, ev oth indicates that every other lens was included. Anisotropic indicates that anisotropic conditions were used. Dis is discontinuity. Rev indicates reverse model outputs.

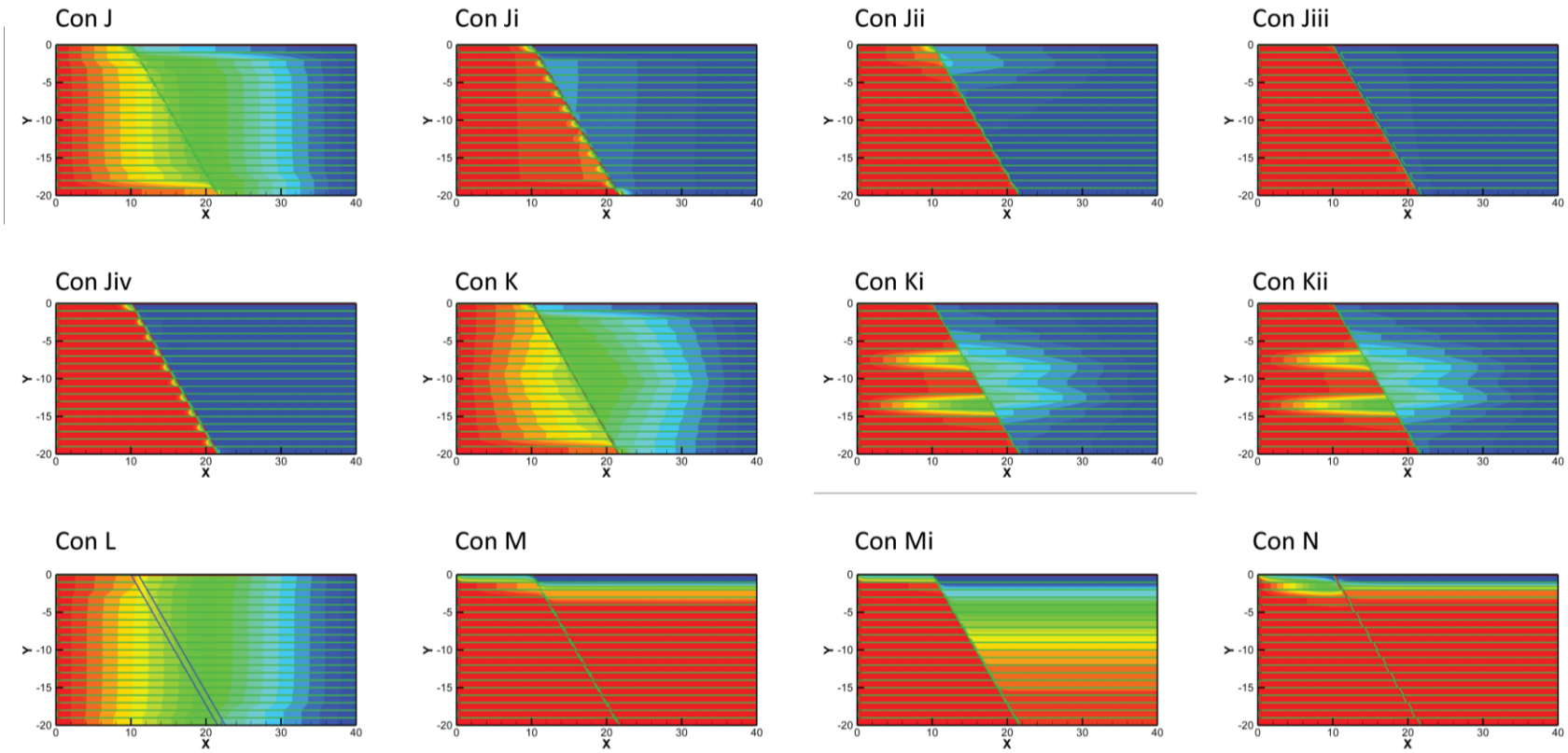
Con J
Con Ji
Con Jii
Con Jiii
Con Jiv
Con K
Con Ki
Con Kii
Con L
Con M
Con Mi
Con N
X
Y

Appendix 5.3 Vector types for models of faults cutting sediment of contrasting competency (CC)

Vector pattern "types" for CC models. Pattern types Vec K to Q are from confined flow boundary conditions from south to north (CS). The same boundary conditions with flow from north to south (CN) are not shown, but are the reverse of these. Pattern types Vec R to T are found under unconfined boundary conditions with from south to north (US).

Appendix 5.4 Streamtrace types for models of faults cutting sediment of contrasting competency (CC)

Streamtrace pattern "types" for CC models. Pattern types Str O to S are from confined flow boundary conditions from south to north (CS). The same boundary conditions with flow from north to south (CN) are not shown, but are the reverse of these. Pattern types Str T to Ui are found in unconfined boundary conditions with from south to north (US).

Appendix 6 – J model results

Appendix 6.1 Model results and parameters for faults cutting faults juxtaposing fine and coarse-grained sediment (J)

Model ID	Mixed zone thickness (m)	Zone of mixed sediment	Slip surface	Fine-grained smear	Head-drop	Head contour type	Flow vector type	Streamtrace type	Streamtrace distance travelled (m)
CS J 1	No fault zone					Con a	Vec a	Str a	2.2*
CS J 2	1	min K				Con a	Vec b	Str a	3*
CS J 3	1	av K				Con a	Vec b	Str a	3*
CS J 4	1	max K				Con a	Vec c	Str b	3* / 6.5
CS J 5	N/a		min			Con a	Vec d	Str c	3* / 2
CS J 6	N/a					Con a	Vec d	Str c	3* / 0.8
CS J 7	N/a		max K			Con a	Vec d	Str c	3* / 0
CS J 8	N/a		segmented			Con a	Vec e	Str d	3* / 2.2
CS J 9	N/a					Con a	Vec a	Str a	3*
CS J 10	N/a			segmented		Con a	Vec a	Str a	3*
CS J 11	1					Con a	Vec c	Str b	3* / 10
CS J 12	1				N/a	Con a	Vec c	Str b	3* / 9
CS J 13	1					Con a	Vec d	Str b	3* / 9
CS J 14	1	anisotropic				Con a	Vec f	Str e	0* / 0
CS J 15	1	anisotropic				Con a	Vec g	Str f	0* / 12
CS J 16	1	anisotropic				Con a	Vec g	Str f	0* / 4
CS J 17	1	anisotropic				Con a	Vec g	Str f	0* / 3
CN J 3	1					Con a (rev)	Vec b (rev)	Str a (rev)	3*
CN J 12	1					Con a (rev)	Vec h	Str g	2.5
CN J 16	1	anisotropic				Con a (rev)	Vec i	Str h	0
US J 3	1					Con a	Vec j	Str a	3*
US J 12	1					Con a	Vec k	Str i	8
US J 16	1	anisotropic				Con a	Vec l	Str j	18

Light grey filled boxes indicates parameters that were applied to the model. Min, Av and Max refer to minimum, average and maximum values. Con, Vec and Str refer to the head contour, vector and streamtrace types in Appendix 6.2 and 6.3. CS is confined flow from south to north, CN is confined flow from north to south and US is unconfined flow from south to north. Segmented indicates the structural element was segmented within the model and anisotropic indicates that the zone was assigned anisotropic parameters. * indicates deflected sub-vertical fluid flow.

Appendix 6.2 Vector types for models of faults juxtaposing fine and coarse-grained sediment (J)

Vector pattern "Types" from model set J. Pattern types Vec b to g are from confined flow boundary conditions from south to north (CS), Vec h and i are from the same boundary conditions with flow from north to south (CN). Pattern types Vec k to l are found under unconfined boundary conditions with from south to north (US).

Appendix 6.3 Streamtrace types for models of faults juxtaposing fine and coarse-grained sediment(J)

Vector pattern "Types" from model set J. Pattern types Str b to f are from confined flow boundary conditions from south to north (CS), Str g and h under the same boundary conditions with flow from north to south (CN). Pattern types Str i and j are from unconfined boundary conditions with from south to north (US).

Definitions

Abbreviation	Definition
CSP	Clay smear potential
SSF	Shale smear factor
SGR	Shale gouge ratio
k	Intrinsic permeability
CRL	Corinth rift laboratory
K	Hydraulic conductivity
ρ	Density
g	Acceleration due to gravity
μ	Fluid viscosity
D_{50}	Median grain-size
n	Percentage porosity
σØ	Grain-size sorting parameter
N_g	Total number of grains in class fraction
L	Fluid flow path length
L_T	Tortuous flow path length
T	Tortuosity
r	Mean pore radius

List of References

Agosta, F., and Kirschner, D.L. 2003. Fluid conduits in carbonate-hosted seismogenic normal faults of Central Italy. *Journal of Geophysical Research.* **108.** B4. 2221-2234.

Alfaro, C., and Wallace, M. 1994. Origin and classification of springs and historical review with current applications. *Environmental Geology*. **24** (2). 112-124.

Allan, U.S. 1989. Model for Hydrocarbon Migration and Entrapment within Faulted Structures. *AAPG Bulletin*. **73** (7). 803-811.

Anderson, E. I., and Bakker, M. 2008. Groundwater flow through anisotropic fault zones in multiaquifer systems. *Water Resources Research*. **44** (11). W11433.

Anderson, T. R., and Fairley, J.P. 2008. Relating permeability to the structural setting of a fault-controlled hydrothermal system in southeast Oregon, USA. *Journal of Geophysical Research*. **113** (B5). B05402.

Andrews, J.N., Burgess, W.G., Edmunds, W.M., Kay, R.L.F., and Lee, D.J. 1982. The thermal springs of Bath. *Nature*. **298**. 339-298.

Antonellini, M., and Aydin, A. 1994. Effect of faulting on fluid flow in porous sandstones: Petrophysical properties 1. *AAPG Bulletin*. **78** (3). 355-377.

Antonellini, M.A., Aydin, A., and Pollard, D.D. 1994. Microstructure of deformation bands in porous sandstones at Arches National Park, Utah. *Journal of Structural Geology*. **16** (7). 941-959.

Antonellini, M., and Aydin, A. 1995. Effect of faulting on fluid flow in porous sandstones: Geometry and spatial distribution. *AAPG Bulletin.* **79** (5). 642-671.

Arch, J., and Maltman, A. 1990. Anisotropic permeability and tortuosity in deformed wet sediments. *Journal of Geophysical Research.* **95** (B6). 9035-9045.

Armijo, R., Meyer, B., King, G. C. P., Rigo, A., and Papanastassiou, D. 1996. Quaternary evolution of the Corinth Rift and its implications for the Late Cenozoic evolution of the Aegean. *Geophysical Journal International*. **126** (1).11-53.

Armijo, R., Meyer, B., Hubert, A., and Barka, A. 1999. Westward propagation of the North Anatolian fault into the northern Aegean: Timing and kinematics. *Geology*. **27**(3). 267-270.

Avallone, A., Briole, P., Agatza-Balodimou, A., Billiris, H., Charade, O., Mitsakaki, C., Nercessian, A., Papazissi, K., Paradissis, D., and Veis, G. 2004. Analysis of eleven years of deformation measured by GPS in the Corinth Rift Laboratory area. *Comptes Rendus Geoscience.* **336** (4–5). 301-311.

Aydin, A., 1978. Small faults formed as deformation bands in sandstone. *Pure and Applied Geophysics*. **116**. 913-930.

Aydin, A. 2000. Fractures, faults, and hydrocarbon entrapment, migration and flow. *Marine and Petroleum Geology*. **17**(7). 797-814.

Aydin, A., Borja, R.I., and Eichhubl, P. 2006. Geological and mathematical framework for failure modes in granular rock. *Journal of Structural Geology***. 28** (1). 83-98.

Balsamo, F., Storti, F., Piovano, B., Salvini, F., Cifelli, F., and Lima, C. 2008. Time dependent structural architecture of subsidary fracturing and stress pattern in the tip region of an extensional growth fault system, Tarquinia basin, Italy. *Tectonophysics*. **454.** 54-69.

Balsamo, F., and Storti, F. 2010. Grain size and permeability evolution of soft-sediment extensional sub-seismic and seismic fault zones in high-porosity sediments from the Crotone basin, Southern Appenines, Italy. *Marine and Petroleum Geology*. **27**. 822-837.

Balsamo, F. Storti, F., Salvini, F., Silva, A.T., and Lima, C.C. 2010. Structural and petrophysical evolution of extensional fault zones in low-porosity, poorly lithified sandstones of the Barreiras Formation, NE Brazil. *Journal of Structural Geology*. **32** (11). 1806-1826.

Balsamo, F., and Storti, F., 2011. Size-dependent comminution, tectonic mixing, and sealing behavior of a "structurally oversimplified" fault zone in poorly lithified sands: Evidence for a coseismic rupture? *Geological Society of America Bulletin*. **123**. 613-619.

Barnicoat, A., Sheldon, H., and Ord, A. 2009. Faulting and fluid flow in porous rocks and sediments: implications for mineralisation and other processes. *Mineralium Deposita*. **44** (6). 705-718.

Bastesen, E., Braathen, A., Nøttveit, H., Gabrielsen, R. H., and Skar, T., 2009. Extensional fault cores in micritic carbonate - Case studies from the Gulf of Corinth, Greece. *Journal of Structural Geology*. **31**. 403-420.

Bear, J. 1972. *Dynamics of Fluids in Porous Media*. American Elsevier. New York.

Beard, D. C., and Weyl, P.K. 1973. Influence of texture on porosity and permeability of unconsolidated Sand. *AAPG Bulletin*. **57** (2). 349-369.

Bell, R.E., McNeill. L.C., Bull, J.M., Henstock, T.J., Collier, R.E.L., and Leeder, M.R. 2009. Fault architecture, basin structure and evolution of the Gulf of Corinth Rift, central Greece. *Basin Research*. **21**(6). 824-855.

Benedicto, A., Plagnes, V., Vergély, P., Flotté, N., and Schultz, R. A. 2008. Fault and fluid interaction in a rifted margin: integrated study of calcite-sealed fault-

related structures (southern Corinth margin). *Geological Society, London, Special Publications*. **299** (1). 257-275.

Bense, V. F., and Van Balen, R. T., 2003. Hydrogeological aspects of fault zones on various scales in the Roer Valley Rift System. *Journal of Geochemical Exploration*. **78-79**. 317-320.

Bense, V. F., Van den Berg, E. H., and Van Balen, R. T. 2003. Deformation mechanisms and hydraulic properties of fault zones in unconsolidated sediments; the Roer Valley rift system, the Netherlands. *Hydrogeology Journal*. **11**. 319-332.

Bense, V. F., and Van Balen, R.T., 2004. The effect of fault relay and clay smearing on groundwater flow patterns in the Lower Rhine Embayment. *Basin Research*. **16** (3). 397-411.

Bense, V.F., and Person, M.A. 2006. Faults as conduit-barrier systems to fluid flow in siliciclastic sedimentary aquifers. *Water Resources Research.* **42.** W05421

Bense, V. F., Person, M. A., Chaudhary, K., You, Y., Cremer, N., and Simon, S. 2008. Thermal anomalies indicate preferential flow along faults in unconsolidated sedimentary aquifers. *Geophysical Research Letters.* **35**. L24406.

Bense, V.F., Gleeson, T., and Loveless, S. Fault zone hydrogeology. *In review.*

Billi, A. 2005. Grain size distribution and thickness of breccia and gouge zones from thin strike-slip fault cores in limestone. *Journal of Structural Geology*. **27**(10). 1823-1837.

Bonson, C. G., Childs, C., Walsh, J. J., Schöpfer, M. P. J., and Carboni, V. 2007. Geometric and kinematic controls on the internal structure of a large normal fault in massive limestones: The Maghlaq Fault, Malta. *Journal of Structural Geology*. **29**(2). 336-354.

Borradaile, G. J., 1981. Particulate flow of rock and the formation of cleavage. *Tectonophysics*. **72**. 305-321.

Bouabid, R., Nater, E.A., and Barak, P. 1992. Measurement of pore size distribution in a lamella Bt horizon using epifluorescence microscopy and image analysis. *Geoderma.* **53.** 309-328.

Bouvier, J.D., Kaars-Sijpesteijn, C.H., Kluesner, D.F., Onyejekwe, C.C., and Van Der Pal, R.C. 1989. Three-dimensional seismic interpretation and fault sealing investigations, Nun River Field, Nigeria. *AAPG bulletin* **. 73**(11). 1397-1414.

Braathen, A., Tveranger, J. Fossen, H., Skar, T., Cardozo, N., Semshaug, S. E., Bastesen, E., and Sverdrup, E. 2009. Fault Facies and its application to sandstone reservoirs. *AAPG bulletin.* **93** (7). 891-917.

Brassington, R. 1998. *Field Hydrogeology*. John Wiley and Sons Ltd. Chichester.

Bredehoeft, J. D., Belitz, K., and Sharp-Hansen,S. 1992. The hydrodynamics of the Big Horn basin: A study of the role of faults. *AAPG Bulletin*. **76** (4).530-546.

Bredehoeft, J. D. 1997. Fault permeability near Yucca Mountain. *Water Resources Research.* **33** (11). 2459-2463.

Brown, K. M., and Moore, J.C. 1993. Anisotropic permeability and tortuosity in deformed wet sediments – comment. *Journal of Geophysical Research-Solid Earth.* **98** (B10). 17859-17864.

Bruhn, R. L., Parry, W.T., Yonkee, W. A., and Thompson, T. 1994. Fracturing and hydrothermal alteration in normal fault zones. *Pure and Applied Geophysics*. **42**(3). 609-644.

Caine, J. S., Evans, J. P., and Forster, C. B. 1996. Fault zone architecture and permeability structure. *Geology*. **24** (11). 1025-1028.

Caine, J. S., and Tomusiak, S. R. A. 2003. Brittle structures and their role in controlling porosity and permeability in a complex Precambrian crystalline-rock aquifer system in the Colorado Rocky Mountain Front Range. *Geological Society of America Bulletin*. **115** (11). 1410-1424.

Caine, J. S., and Minor, S. A. 2009. Structural and geochemical characteristics of faulted sediments and inferences on the role of water in deformation, Rio Grande Rift, New Mexico. *GSA Bulletin.* **121** (9-10). 1325-1340.

Carter, K. E., and Winter, C.L. 1995. Fractal nature and scaling of normal faults in the Española Basin, Rio Grande rift, New Mexico: implications for fault growth and brittle strain. *Journal of Structural Geology* .**17** (6). 863-873.

Cashman, S., and Cashman, K., 2000. Cataclasis and deformation-band formation in unconsolidated marine terrace sand, Humboldt County, California. *Geology*. **28**. 111-114.

Cashman, S. M., Baldwin, J. N., Cashman, K., Swanson, K., and Crawford, R. 2007. Microstructures developed by coseismic and aseismic faulting in near-surface sediments, San Andreas fault, California. *Geology*. **35** (7): 611-614.

Catchings, R. D., Rymer, M. J., Goldman, M. R., and Gandhok, G. 2009. San Andreas fault geometry at Desert Hot Springs, California, and its effects on earthquake hazards and groundwater. *Bulletin of the Seismological Society of America*. **99** (4). 2190-2207.

Chadwick, R. A., Noy, D. J., and Holloway, S. 2009. Flow processes and pressure evolution in aquifers during the injection of supercritical CO2 as a greenhouse gas mitigation measure. *Petroleum Geoscience*. **15** (1). 59-73.

Chester, F. M., and Logan, J. M. 1987. Composite planar fabric of gouge from the Punchbowl Fault, California. *Journal of Structural Geology*. **9** (5–6). 621-634.

Childs, C., Nicol, A., Walsh, J. J., and Watterson, J. 1996a. Growth of vertically segmented normal faults. *Journal of Structural Geology*. **18** (12). 1389-1397.

Childs, C., Watterson, J., and Walsh, J.J. 1996b. A model for the structure and development of fault zones. *Journal of the Geological Society of London.* **153**. 337-340.

Childs, C. Walsh, J. J., and Watterson, J. 1997. Complexity in fault zone structure and implications for fault seal prediction. In: P. Møller-Pedersen and Koestler, A. G. (Eds). *Hydrocarbon Seals – Importance for Exploration and Production.* Norwegian Petroleum Society Special Publications. Elsevier. **7.** 61-72.

Childs, C., Manzocchi, T., Walsh, J. J., Bonson, C. G., Nicol, A., and Schöpfer, M. P. 2009. A geometric model of fault zone and fault rock thickness variations. *Journal of Structural Geology*. **31** (2). 117-127.

Clarke, P. J. Davies, R. R. England, P. C. Parsons, B. Billiris, H. Paradissis, D. Veis, G. Cross, P. A. Denys, P. H. Ashkenazi, V. Bingley, R. Kahle, H. G. Muller, M. V., and Briole, P. 1998. Crustal strain in central Greece from repeated GPS measurements in the interval 1989–1997. *Geophysical Journal International.* **135** (1). 195-214.

Collier, R. E., 1990. Eustatic and Tectonic controls upon Quaternary coastal sedimentation in the Corinth Basin, Greece. *Journal of the Geological Society*. **147** (2). 301-314.

Craddock, J. P., Geary, J., and Malone, D. H. 2012. Vertical injectites of detachment carbonate ultracataclasite at White Mountain, Heart Mountain detachment, Wyoming. *Geology*. **40** (5). 463-466.

Cornet, F. H., Doan, M. L., Moretti, I., and Borm, G. 2004. Drilling through the active Aigion Fault: the AIG10 well observatory. *Comptes Rendus Geoscience.* **336** (4–5). 395-406.

Cowie, P. A., Knipe, R. J., and Main, I. G. 1996. Introduction to the special issue. *Journal of Structural Geology.* **18** (2-3). v-xi.

Crouch, D. P. 1996. Environmental geology of ancient Greek cities. *Environmental Geology*. **27**. 233-245.

Davies, S.N., and DeWeist, R.J.M. 1967. *Hydrogeology*. New York. John Wiley & Sons, Inc.

De Boever, E. Muchez, P. Swennen, R., and Dimitrov, L. 2011. Evolution of deformation and fault-related fluid flow within an ancient methane seep system (Eocene, Varna, Bulgaria). *Geofluids.* **11** (2). 166-183.

De Martini, P. M. Pantosti, D., Palyvos, N., Lemeille, F., McNeill, L., and Collier, R. 2004. Slip rates of the Aigion and Eliki Faults from uplifted marine terraces, Corinth Gulf, Greece. *Comptes Rendus Geosciences***. 336** (4-5). 325-334.

Dewhurst, D. N., Brown, K. M., Clennell, M. B., and Westbrook, G. K. 1996. A comparison of the fabric and permeability anisotropy of consolidated and sheared silty clay. *Engineering Geology.* **42** (4). 253-267.

Dewhurst, D.N., Aplin, A.C., and Yang, Y. 1999. Permeability and fluid flow in natural mudstones. In: Aplin, A.C., Fleet, A.J. and Macquaker, J.H.S. *Muds and mudstones:physical and fluid-flow properties.* Geological Society, London, Special Publications. **158.** 23-43.

Dia, A.N., Cohen, A.S., O'Nions, R.K., and Jackson, J.A., 1997. Rates of uplift investigated through ^{230Th} dating in the Gulf of Corinth (Greece). *Chemical Geology*. **138**. 171-184.

Doan, M., and F. H. Cornet. 2007. Thermal anomaly near the Aigio fault, Gulf of Corinth, Greece, maybe due to convection below the fault. *Geophysical Research Letters*. **34**. L06314.

Dockrill, B., and Shipton, Z. K. 2010. Structural controls on leakage from a natural CO2 geologic storage site: Central Utah, U.S.A. *Journal of Structural Geology***. 32**(11). 1768-1782.

Do Nascimento, A. F., Lunn, R. J., and Cowie, P. A. 2005. Modeling the heterogeneous hydraulic properties of faults using constraints from reservoir-induced seismicity. *Journal of Geophysical Research.* **110** (B9). B09201.

Dotsika, E. Poutoukis, D., and Raco, B. 2010. Fluid geochemistry of the Methana Peninsula and Loutraki geothermal area, Greece. *Journal of Geochemical Exploration.* **104** (3). 97-104.

Doughty, P. T. 2003. Clay smear seals and fault sealing potential of an exhumed growth fault, Rio Grande rift, New Mexico. *AAPG bulletin.* **87** (3). 427-444.

Doutsos, T. Pe-Piper, G. Boronkay, K., and Koukouvelas, I. 1992. Kinematics of the central Hellenides. *Tectonics*. **12** (4). 936-953.

Du Bernard, X., Eichbuhl, P., and Aydin, A., 2002. Dilation bands: A new form of localized failure in granular media. *Geophysical Research Letters.* **29** (4). 2176.

Egholm, D.L., Clausen, O.R., Sandiford, M., Kristensen, M.B., and Korstgård, J.A., 2008. The mechanics of clay smearing along faults. *Geology*. **36** (10). 787-790.

Eichhubl, P., and Boles, J. R. 2000. Focused fluid flow along faults in the Monterey Formation, coastal California. *Geological Society of America Bulletin.* **112** (11). 1667-1679.

Eichhubl, P., Taylor, W. L., Pollard, D. D., and Aydin, A. 2004. Paleo-fluid flow and deformation in the Aztec Sandstone at the Valley of Fire, Nevada—Evidence for the coupling of hydrogeologic, diagenetic, and tectonic processes. *Geological Society of America Bulletin* **.116** (9-10). 1120-1136.

Eichhubl, P., Davatz, N.C., and Becker, S.P. 2009. Structural and diagenetic control of fluid migration and cementation along the Moab fault, Utah. *AAPG bulletin.* **93** (5). 653-681.

Engelder, J.T. 1974. Cataclasis and the Generation of Fault Gouge. *Geological Society of America Bulletin*. **85** (10). 1515-1522.

Evans, J. P., Forster, C. B., and Goddard, J. V. 1997. Permeability of fault-related rocks, and implications for hydraulic structure of fault zones. *Journal of Structural Geology*. **19** (11). 1393-1404.

Exner, U., and Grasemann, B., 2010. Deformation bands in gravels: displacement gradients and heterogeneous strain. *Journal of the Geological Society, London.* **167**. 905-913.

Exner, U., and C. Tschegg. 2012. Preferential cataclastic grain size reduction of feldspar in deformation bands in poorly consolidated arkosic sands. *Journal of Structural Geology*. **43**. 63-72.

Faulkner, D. R., Lewis, A. C., and Rutter, E.H. 2003. On the internal structure and mechanics of large strike-slip fault zones: field observations of the Carboneras fault in southeastern Spain. *Tectonophysics*. **367**(3–4). 235-251.

Faulkner, D. R., Jackson, C.A.L., Lunn, R.J., Schlische, R.W., Shipton, Z.K., Wibberley, C.A.J., and Withjack, M.O. 2010. A review of recent developments concerning the structure, mechanics and fluid flow properties of fault zones. *Journal of Structural Geology*. **32**(11). 1557-1575.

Ferrill, D. A., and Morris, A.P. 2003. Dilational normal faults. *Journal of Structural Geology*. **25**(2). 183-196.

Ferrill, D. A., Sims, D.W., Waiting, D. J., Morris, A. P., Franklin, N. M., and Schultz, A. L. 2004. Structural framework of the Edwards Aquifer recharge zone in south-central Texas. *Geological Society of America Bulletin*. **116** (3-4). 407-418.

Finch, E., Hardy, S., and Gawthorpe, R. 2004. Discrete-element modelling of extensional fault-propagation folding above rigid basement fault blocks. *Basin Research***. 16** (4). 467-488.

Fisher, Q. J., and R. J. Knipe. 2001. The permeability of faults within siliciclastic petroleum reservoirs of the North Sea and Norwegian Continental Shelf. *Marine and Petroleum Geology***. 18** (10). 1063-1081.

Flint, A. L., Flint, L.E., Kwicklis, E.M., Bodvarsson, G.S., and Fabryka-Martin, J.M. 2001. Hydrology of Yucca Mountain, Nevada. *Reviews of Geophysics*. **39**(4). 447–470.

Ford, M., Rohais, S., Williams, E. A., Bourlange, S., Jousselin, D., Backert, N., and Malartre, F. 2012. Tectono-sedimentary evolution of the western Corinth rift (Central Greece). *Basin Research*. (Online).

Fossen, H., Schultz, R. A., Shipton, Z. K., and Mair, K. 2007. Deformation bands in sandstone: a review. *Journal of the Geological Society*. **164**. 755-769.

Fowles, J., and Burley, S. 1994. Textural and permeability characteristics of faulted, high porosity sandstones. *Marine and Petroleum Geology.* **11** (5). 608-623.

Foxford, K. A., Walsh, J.J., Watterson, J., Garden, I.R., Gusgott, S.C., and Burley, S.D. 1998. Structure and content of the Moab Fault Zone, Utah, USA, and its implications for fault seal prediction. *Geological Society, London, Special Publications*. **147** (1). 87-103.

Francus, P. 1998. An image-analysis technique to measure grain-size variation in thin sections of soft clastic sediments. *Sedimentary Geology.* **121.** 289-298.

Fredman, N. 2007. *Quantification of fault zone feature in siliciclastic rocks: Implications for 3D fault modelling and fluid flow*. Department of Earth Sciences. Bergen, University of Bergen. PhD Thesis**.**

Freeze, R.A., and Cherry, J.A. 1979. *Groundwater.* Prentice-Hall. Englewood Cliffs.

Fulljames, J.R., Zijerveld, J.J., and Franssen, R.C.M.W. 1997. Fault seal processes: systematic analysis of fault seals over geological and production time scales. In: In: P. Møller-Pedersen and Koestler, A. G. (Eds). *Hydrocarbon Seals – Importance for Exploration and Production.* Norwegian Petroleum Society Special Publications. Elsevier. **9**. 51-59.

Gibson, R. G. 1998. Physical character and fluid-flow properties of sandstone-derived fault zones. *Geological Society, London, Special Publications***. 127**(1). 83-97.

Gillespie, P. A., Howard, C.B., Walsh, J. J., and Watterson, J. 1993. Measurement and characterisation of spatial distributions. *Tectonophysics.* **226**. 113-141.

Giurgea, V., Rettenmaier, D., Pizzino, L., Unkel, I., Hötzl, H., Förster, A., and Quattrocchi, F. 2004. Preliminary hydrogeological interpretation of the Aigion area from the AIG10 borehole data. *Comptes Rendus Geoscience.* **336**(4–5). 467-475.

Glen, J. D., 1957. On the mechanism by which stones in till become orientated. *American Journal of Science*. **255** (3). 194-205.

Goldsworthy, M., Jackson, J., and Haines, J. 2002. The continuity of active fault systems in Greece. *Geophysical Journal International.* **148** (3). 596-618.

Goodwin, L.B., and Tikoff, B. 2002. Competency contrast, kinematics, and the development of foliations and lineations in the crust. *Journal of Structural Geology* **24**. 1065-1085.

Grauch, V. J., Hudson, M. R., and Minor, S. A. 2004. Aeromagnetic expression of faults that offset basin fill, Albuquerque basin, New Mexico. *Geophysics.* **66** (3). 707-720.

Gross, M. R., Gutie´rrez-Alonso, G., Bai, T., Wacker, M. A., Collinsworth, K. B., and Behl, R. J. 1997. Influence of mechanical stratigraphy and kinematics on fault scaling relations. *Journal of Structural Geology*. **19** (2). 171-183.

Gudmundsson, A. 2000. Active fault zones and groundwater flow. *Geophysical Research Letters*. **27**(18). 2993-2996.

Gumm, L. P. 2011. *A multi-tracer hydrochemical investigation of groundwater dynampics in the Lower Rhine Embayment, Germany.* School of Environmental Sciences. University of East Anglia. PhD Thesis.

Haneberg, W.C. 1995. Steady-state groundwater-flow across idealized faults. *Water Resources Research.* **31** (7). 1815-1820.

Heffner, J., and Fairley, J. 2006. Using surface characteristics to infer the permeability structure of an active fault zone. *Sedimentary Geology.* **184** (3-4). 255-265.

Heynekamp, M. R., Goodwin, L. B., Mozley, P. S., and Haneberg W.C. 1999. Controls on fault-zone architecture in poorly lithified sediments, Rio Grande Rift, New Mexico: Implications for fault zone permeability and fluid flow. In: Haneberg, P.S., Mozley, P.S., Moore, J.C., Goodwin, L.B. (Eds). *Faults and subsurface fluid flow in the shallow crust.* American Geophysical Union Monograph. **113**. 27-49

Hippler, S. J. 1993. Deformation microstructures and diagenesis in sandstone adjacent to an extensional fault: implications for the flow and entrapment of hydrocarbons. *AAPG bulletin.* **77**. 625-637.

Hiscock, K. 2005. *Hydrogeology: Principles and Practice*. Blackwell Publishing. Oxford.

Holcombe, R. J., 2010. GEOrient v9.4.2. Structural Geology - Mapping/GIS software. University of Queensland, Australia. http://www.holcombe.net.au/software/rodh_software_georient.htm [accessed 20/08/2010].

Hooke, R. L., and Iverson, N.R. 1995. Grain-size distribution in deforming subglacial tills: Role of grain fracture. *Geology*. **23** (1). 57-60.

Huang, W.-J., and Johnson, A. M. 2010. Quantitative description and analysis of earthwuake-induced deformation zones along strike-slip and dip-slip faults. *Journal of Geophysical Research.* **115**: B03408.

Ildefonse, B., Launeau, P. Bouchez, J-L., and Fernandez, A. 1992a. Effect of mechanical interactions on the developments of shape preferred interactions: a two-dimensional experimental approach. *Journal of Structural Geology*. **14** (1). 73-83.

Ildefonse, B., Sokoutis, D., and Mancktelow, N.S., 1992b. Mechanical interactions between rigid particles in a deforming ductile matrix. Analogue

experiments in simple shear flow. *Journal of Structural Geology*. **14** (10). 1253-1266.

Institute of Geology and Mineral Exploration (IGME). 1972. *Geological map of Greece, Korinthos Sheet.* **219**. IGME. Athens. 1: 50 000.

Institute of Geology and Mineral Exploration (IGME). 1989. *Geological map of Greece, Xylokastron Sheet.* **203**. IGME. Athens. 1: 50 000.

Institute of Geology and Mineral Exploration (IGME). 1993. *Geological map of Greece, Dhervenion Sheet.* **202**. IGME. Athens, 1: 50 000.

James, W. R. Fairchild, L. H. Nakayama, G. P. Hippler, S. J., and Vrolijk, P. J. 2004. Fault-seal analysis using a stochastic multifault approach. *AAPG bulletin.* **88** (7). 885-904.

Jolivet, L. 2001. A comparison of geodetic and finite strain pattern in the Aegean, geodynamic implications. *Earth and Planetary Science Letters.* **187**(1–2). 95-104.

Jourde, H., Flodin, E. A., Aydin, A., Durlofsky, L. J., and Wen, X-H. 2002. Computing Permeability of Fault Zones in Eolian Sandstone from Outcrop Measurements. *AAPG bulletin.* **86** (7). 1187-1200.

Kampman, N., Burnside, N.M., Shipton, Z.K., Chapman, H.J., Nicholl, J.A., Ellam, R.M., and Bickle, M.J. 2012. Pulses of carbon dioxide emissions from intracrustal faults following climatic warming. *Nature Geoscience*. **5** (5). 352-358.

Kearey, P. 2001. *Dictionary of Geology*. 2nd Edition. Penguin Reference. London.

Kelson, K.I., Bauer, P.W., Connell, S.D., Love, D.W., Rawling, G. C., and Mansell, M. 2004. Initial paleoseismic and hydrogeologic assessment of the southern sangre de cristo fault at the Taos Pueblo site, Taos County, New Mexico. *55th Field Conference, Geology of the Taos Region*. New Mexico Geological Society Guidebook**.** 289-299.

Keraudren, B., and Sorel, D. 1987. The terraces of Corinth (Greece) — A detailed record of eustatic sea-level variations during the last 500,000 years. *Marine Geology*. **77** (1–2). 99-107.

Kim, Y-S., and Sanderson, D. J. 2009. Inferred fluid flow through fault damage zones based on the observation of stalactites in carbonate caves. *Journal of Structural Geology*. **32** (9). 1305-1316.

Knipe, R. J. 1997. Juxtaposition and seal diagrams to help analyze fault seals in hydrocarbon reservoirs. *AAPG bulletin*. **87** (2). 187-195.

Knipe, R. J., Jones, G., and Fisher, Q.J. 1998. Faulting, fault sealing and fluid flow in hydrocarbon reservoirs: an introduction. In: Jones, G., Fisher, Q.J. and Knipe, R.J. (Eds). Faulting, Fault Sealing and Fluid Flow in Hydrocarbon Reservoirs. *Geological Society, London. Special Publication*. **147.** vii-xxi.

Kremer, Y. Lunn, R. J., Shipton, Z.K., and Wibberley, C. A. J. 2011. Heterogeneity is important for predicting the permeability of seismic scale faults. *American Geophysical Union Fall Meeting*. San Francisco, American Geophysical Union.

Kristensen, M. B., Childs, C. J., and Korstgard, J. A., 2008. 3D geometry of small-scale relay zones between normal faults in soft sediments. *Journal of Structural Geology*. **30**. 257-272.

Krumbein, W. C., and Monk. G.D. 1942. Permeability as a function of the size parameters of unconsolidated sand. Transactions of the AIME. **151** (1). 153-163.

Kurz, W., Imber, J., Wibberley, C.A.J., Holdsworth, R.E., and Collettini, C. 2008. The internal structure of fault zones: fluid flow and mechanical properties. In: Wibberley, C.A.J., Kurz, W., Imber, J., Holdsworth, R.E. and Colletini, C. *The internal structure of fault zones: Implications for Mechanical and Fluid-Flow Properties.* Geological Society Special Publication. **299.** Pp 1-3.

Labaume, P., Sheppard, S. M. F. Moretti, I. 2001. Fluid flow in cataclastic thrust fault zones in sandstones, Sub-Andean Zone, southern Bolivia. *Tectonophysics.* **340** (3–4). 141-172.

Lambrakis, N., and Kallergis, G. 2005. Contribution to the study of Greek thermal springs: hydrogeological and hydrochemical characteristics and origin of thermal waters. *Hydrogeology Journal*. **13** (3). 506-521.

Laubach, S. E. 1988. Subsurface fractures and their relationship to stress history in East Texas basin sandstone. *Tectonophysics.* **156**(1–2): 37-49.

Lee, H. K., and Kim, H. S. 2005. Comparison of structural features of the fault zone developed at different protoliths: crystalline rocks and mudrocks. *Journal of Structural Geology*. **27**(11). 2099-2112.

Leeder, M. R., McNeill, L. C., Collier, R. E., Portman, C., Rowe, P. J., Andrews, J. E., and Gawthorpe, R. L. 2003. Corinth rift margin uplift: New evidence from Late Quaternary marine shorelines. *Geophysical Research. Letters.* **30** (12). 1611.

Leeder, M. R., Portman, C., Andrews, J. E., Collier, R. E., Finch, E., and Gawthorpe, R. L. 2005. Normal faulting and crustal deformation, Alkonides Gulf and Perachora Peninsula, eastern Gulf of Corinth rift, Greece. *Journal of the Geological Society*. **162.** 549-561.

Leeder, M. R., Mack, G. H., Brasier, A. T., Parrish, R. R., McIntosh, W. C., Andrews, J. E., and Duermeijer, C. E. 2008. Late-Pliocene timing of Corinth (Greece) rift-margin fault migration. *Earth and Planetary Science Letters.* **274** (1–2). 132-141.

Leeder, M.R., Mark, D.F., Gawthorpe, R.L., Kranis, H., Loveless, S., Pedentchouk, N., Skourtsos, E., Turner, J., Andrews, J.E., and Stamatakis, M. 2012. A "Great Deepening": Chronology of rift climax, Corinth rift, Greece. *Geology*. G33360.

Le Pichon, X. L., and Angelier., J. 1979. The hellenic arc and trench system: A key to the neotectonic evolution of the eastern Mediterranean area. *Tectonophysics.* **60** (1–2). 1-42.

Lin, A. 1996. Injection veins of crushing-originated pseudotachylyte and fault gouge formed during seismic faulting. *Engineering Geology.* **43** (2–3). 213-224.

Lindanger, M., Gabrielsen, R.H., and Braathan, A. 2007. Analysis of rock lenses in extensional faults. *Norwegian Journal of Geology***. 87**. 361-372.

Lindsay, N.G., Murphy, F.C., Walsh, J.J., and Watterson, J., 1993. Outcrop studies of shale smears on fault surfaces. In: Flint, S.S., Bryant, I.D., (Eds). *The geological modelling of hydrocarbon reservoirs and outcrop analogues.* Blackwell Scientific Publications. Oxford. **15.** 11-123.

Long, J. J., and Imber, J. 2010. Geometrically coherent continuous deformation in the volume surrounding a seismically imaged normal fault-array. *Journal of Structural Geology.* **32** (2). 222-234.

Loveless, S., Bense, V., Turner, J. 2011. Fault architecture and deformation processes within poorly lithified rift sediments, Central Greece. *Journal of Structural Geology.* **33.** 1554-1568.

Lunn, R. J., Shipton, Z., and Bright, A.M. 2008. How can we improve estimates of bulk fault zone hydraulic properties? In: Wibberley, C. A. J., Kurz, W., Imber, J., Holdsworth, R.E., and Collettini, C. (Eds). *The Internal Structure of Fault Zones: Implications for Mechanical and Fluid-flow Properties.* Geological Society, London. Special Publications. **299**. 231-237.

Maclay, R. W., and Small, T.A. 1983. Hydrostratigraphic subdivisions and fault barriers of the Edwards aquifer, south-central Texas, U.S.A. *Journal of Hydrology.* **61**(1–3). 127-146.

Magri, F., Akar, T., Gemici, U., and Pekdeger, A. 2010. Deep geothermal groundwater flow in the Seferihisar–Balçova area, Turkey: results from transient numerical simulations of coupled fluid flow and heat transport processes. *Geofluids.* **10** (3). 388-405.

Mailloux, B.J., Person, M., Kelley, S., Dunbar, N., Cather, S., Straver, L., and Hundleston, P. 1999. Tectonic controls on the hydrogeology of the Rio Grande Rift, New Mexico. *Water Resources Research.* **35.** 2641-2659.

Malartre, F., Ford, M., Williams, E., 2004. Preliminary biostratigraphy and 3D geometry of the Vouraikos Gilbert-type fan delta, Gulf of Corinth, Greece. *Comptes Rendus Geoscience.* **336** (4–5). 269-280.

Maltman, A. J. 1988. The importance of shear zones in naturally deformed wet sediments. *Tectonophysics.* **145.** 163-175.

Manzocchi, T., Walsh, J. J., Nell, P., and Yielding, G. 1999. Fault transmissibility multipliers for flow simulation models. *Petroleum Geoscience.* **5** (1). 53-63.

Manzocchi, T., Walsh, J.J., Tomasso, M., Strand, J., Childs, C., and Haughton, P.D.W. 2007. Static and dynamic connectivity in bed-scale models of faulted and unfaulted turbidites. In: Jolley, S.J., Barr, D., Walsh, J.J. and Knipe, R.J. (Eds). *Structurally complex reservoirs.* Geological Society, London. Special Publications. **292.** 309-336.

Manzocchi, T., Childs, C., and Walsh, J.J. 2010. Faults and fault properties in hydrocarbon flow models. *Geofluids*. **10** (1-2). 94-113.

Marrett, R., and Allmendinger, R. W. 1991. Estimates of strain due to brittle faulting: sampling of fault populations. *Journal of Structural Geology*. **13**.6. 735-738.

Martel, S. J. 1990. Formation of compound strike-slip fault zones, Mount Abbot quadrangle, California. *Journal of Structural Geology*. **12** (7). 869-882.

Masch, F. D., and Denny, K. J. 1966. Grain size distribution and it's effect on the permeability of unconsolidated sands. *Water Resources Research.* **2** (4). 665-677.

Mathers, S., Zalasiewicz, J.A., and Davis, J. 1993. A guide to the sedimentology of unconsolidated sedimentary aquifers (UNSAs). *Overseas geology series*. BGS, ODA Technical report WC/93/32.

Mattei, M., D'Agostino, N., Zananiri, I., Kondopoulou, D., Pavlides, S., and Spatharas, V. 2004. Tectonic evolution of fault-bounded continental blocks: Comparison of paleomagnetic and GPS data in the Corinth and Megara basins (Greece). *Journal of Geophysical. Research*. **109** (B2). B02106.

Matthäi, S. K., Aydin, A., Pollard, D. D., and Roberts, S. G. 1998. Numerical simulation of departures from radial drawdown in a faulted sandstone reservoir with joints and deformation bands. In: Jones, G.A.K., Fisher, Q.J., and Knipe. R.J. (Eds). *Faulting, fault sealing and fluid flow in hydrocarbon reservoirs.* Geological Society, London. Special Publication. **147** (1). 157-191.

Micarelli, L., Benedicto, A., and Wibberley, C. A. J. 2006a. Structural evolution and permeability of normal fault zones in highly porous carbonate rocks. *Journal of Structural Geology*. **28** (7): 1214-1227.

Micarelli, L., Moretti, I., Jaubert, M., and Moulouel, H. 2006b. Fracture analysis in the south-western Corinth rift (Greece) and implications on fault hydraulic behaviour. *Tectonophysics*. **426**. 21-59.

Middleton, G. V., and Wilcock, P. R. 1999. Mechanics in the Earth and Environmental Sciences, Cambridge University Press, Cambridge.

Minor, S. A., and Hudson, M. R. 2006. Regional Survey of Structural Properties and Cementation Patterns of Fault Zones in the Northern Part of the Albuquerque Basin, New Mexico - Implications for Ground-Water Flow. *U.S. Geological Survey Professional Paper*. 1719.

Mohamed, E. A., and Worden, R.H. 2006. Groundwater compartmentalisation: a water table height and geochemical analysis of the structural controls on the subdivision of a major aquifer, the Sherwood Sandstone, Merseyside, UK. *Hydrology and Earth System Sciences.* **10**. 49-64.

Mozley, P. S., and Goodwin, L. B., 1995. Patterns of cementation along a Cenozoic normal fault: A record of paleoflow orientations. *Geology*. **23** (6). 539-542.

Murray, T., and Dowdeswell, J.A. 1992. Water throughflow and the physical effects of deformation on sedimentary glacier beds. *Journal of Geophysical Research- Solid Earth.* **97** (B6). 8993-9002.

Needham, T., Yielding, G., and Fox, R. 1996. Fault population description and prediction using examples from the offshore U.K. *Journal of structural geology.* **18** (2-3). 155-167.

Nicol, A., Walsh, J. J., Watterson, J., and Gillespie, P. A. 1996. Fault size distributions — are they really power-law? *Journal of Structural Geology.* **18** (2-3). 191-197.

Ori, G. G. 1989. Geologic history of the extensional basin of the Gulf of Corinth (?Miocene-Pleistocene), Greece. *Geology*. **17** (10). 918-921

PDE Solutions. FlexPDE 5.1.4. 2009. A Flexible Solution System for Partial Differential Equations. http://www.pdesolutions.com/index.html [accessed 2009].

Perry, C., and Taylor, K., 2007. *Environmental Sedimentology*. Blackwell Publishing. Oxford.

Person, M., Goodwin, L.B., Rawling, G., and Connell, S. 2000. The evolution of fault-zone permeabiility and groundwater flow patterns within the Albuquerque Basin of the Rio Grande Rift, NM. *Journal of Geochemical Exploration.* **69-70**. 565-568.

Piazolo, S., Bons, P.D., and Passchier, C.W., 2002. The influence of matrix rheology and vorticity on fabric development of populations of rigid objects during plane strain deformation. *Tectonophysics*. **351.** 315-329.

Pik, R., and Marty, B. 2009. Helium isotopic signature of modern and fossil fluids associated with the Corinth rift fault zone (Greece): Implication for fault connectivity in the lower crust. *Chemical Geology*. **266** (1–2). 67-75.

Pizzino, L., Quattrocchi, F., Cinti, D., and Galli, G. 2004. Fluid geochemistry along the Eliki and Aigion seismogenic segments (Gulf of Corinth, Greece). *Comptes Rendus Geoscience*. **336** (4–5). 367-374.

Rasband, W. 2011. ImageJ 1.43u. National Institutes of Health, USA. http://rsb.info.nih.gov/ij [accessed 2011].

Rath, A., Exner, U., Tshegg, C., Grasemann, B., Laner, R., and Draganits, E. 2011. Diagenetic control of deformation mechanisms in deformation bands in a carbonate grainstone. *AAPG Bulletin.* **95**. 1369-1381.

Rawling, G. C., Goodwin, L. B., and Wilson, J. L. 2001. Internal architecture, permeability structure, and hydrologic significance of contrasting fault-zone types. *Geology*. **29** (1). 43-46.

Rawling, G. C., and Goodwin, L. B., 2003. Cataclasis and particulate flow in faulted, poorly consolidated sediments. *Journal of Structural Geology.* **25**. 317-331.

Rawling, G. C., and Goodwin, L. B. 2006. Structural record of the mechanical evolution of mixed zones in poorly lithified sediments, Rio Grande rift, New Mexico, USA. *Journal of Structural Geology.* **28** (9). 1623-1639.

Rey, D., Rubio, B., Bernabeu, A.M., and Vilas, F. 2004. Formation, exposure, and evolution of a high-latitude beachrock in the intertidal zone of the Corrubedo complex (Ria de Arousa, Galicia, NW Spain). *Sedimentary Geology.* **169**. 93-105.

Roberts, G., and Stewart, I. 1994. Uplift, deformation and fluid involvement within an active normal fault zone in the Gulf of Corinth, Greece. *Journal of the Geological Society*. **151**(3). 531-541.

Rohais, S., Eschard, R., Ford, M., Guillocheau, F., and Moretti, I. 2007. Stratigraphic architecture of the Plio-Pleistocene infill of the Corinth Rift: Implications for its structural evolution. *Tectonophysics.* **440** (1–4). 5-28.

Rohais, S. Eschard, R., and Guillocheau, F. 2008. Depositional model and stratigraphic architecture of rift climax Gilbert-type fan deltas (Gulf of Corinth, Greece). *Sedimentary Geology*. **210** (3–4). 132-145.

Rowe, C., Moore, J. C., Meneghini, F., and McKeirnan, A.W. 2005. Large-scale pseudotachylytes and fluidized cataclasites from an ancient subduction thrust fault. *Geology*. **33** (12). 937-940.

Sammis, C., King, G., and Biegel, R. 1987. The kinematics of gouge deformation. Pure and Applied Geophysics. **125** (5). 777-812.

Shepherd, R.G. 1989. Correlations of permeability and grain size. Ground Water. **27** (5). 633-638.

Scholz, C. H., and Cowie, P.A. 1990. Determination of total strain from faulting using slip measurements. *Nature.* **346** (6287). 837-839.

Schulz, S. E., and Evans, J.P. 2000. Mesoscopic structure of the Punchbowl Fault, Southern California and the geologic and geophysical structure of active strike-slip faults. *Journal of Structural Geology*. **22** (7). 913-930.

Shipton, Z. K., and Cowie. P.A. 2001. Damage zone and slip-surface evolution over μm to km scales in high-porosity Navajo sandstone, Utah. *Journal of Structural Geology*. **23** (12). 1825-1844.

Shipton, Z. K., Evans, J. P., Kirschner, D., Kolesar, P. T., Williams, A. P., and Heath, J. 2004. Analysis of CO2 leakage through 'low-permeability' faults from natural reservoirs in the Colorado Plateau, east-central Utah. *Geological Society, London, Special Publications.* **233** (1). 43-58.

Shipton, Z.K., Soden, A.M., Kirkpatrick, J.D., Bright, A.M., and Lunn, R.J, 2006. How thick is a fault? Fault displacement-thickness scaling revisited in: Abercrombie, R. Earthquakes: Radiated Energy and the Physics of Faulting. *American Geophysical Union*. 193-198.

Sibson, R. H. 1977. Fault rocks and fault mechanisms. *Journal of the Geological Society.* **133**. 191-213.

Sibson, R. H., Robert, F., and Poulsen, K. H. 1988. High-angle reverse faults, fluid-pressure cycling, and mesothermal gold-quartz deposits. *Geology*. **16** (6). 551-555.

Sigda, J. M., Goodwin, L. B., Mozley, P. S., and Wilson, J. L. 1999. Permeability alteration in small-displacement faults in poorly lithified sediments: Rio Grande Rift, Central New Mexico in: Haneberg, P.S., Mozley, P.S., Moore, J.C., Goodwin, L.B. *Faults and Subsurface Fluid Flow in the Shallow Crust.* American Geophysical Union Monograph, Washington, D.C. **113**. 51-68.

Sigda, J. M., and Wilson, J.L. 2003. Are faults preferential flow paths through semiarid and arid vadose zones? *Water Resources Research.* **39**(8). 1225.

Similox-Tohon, D., Sintubin, M., Muchez, P., Verhaert, G., Vanneste, K., Fernandez, M., Vandycke, S., Vanhaverbeke, H., and Waelkens, M. 2006. The identification of an active fault by a multidisciplinary study at the archaeological site of Sagalassos (SW Turkey). *Tectonophysics.* **420** (3-4). 371-387.

Sperrevik, S., Færseth, R. B., and Gabrielsen, R. H. 2000. Experiments on clay smear formation along faults. *Petroleum Geoscience*. **6** (2). 113-123.

Sperrevik, S., Gillespie, P. A., Fisher, Q. J., Halvorsen, T., and Knipe, R.J. 2002. Empirical estimation of fault rock properties. In: Koestler, A.G., and Hunsdale. R. (Eds). *Hydrocarbon Seal Quantification.* Norwegian Petroleum Society Special Publications. Elsevier, New York. **11.** 109-125.

Stamatis, G., and Voudouris, K. 2003. Marine and human activity influences on groundwater quality of Southern Korinthos area (Greece). *Hydrological Processes*. **17.** 2327-2345.

Sternlof, K.R., Karimi-Fard, M., Pollard, D.D., and Durlofsky, L.J. 2006. Flow and transport effects of compaction bands in sandstone at scales relevant to aquifer and reservoir management. *Water Resources Research.* **42** (7). W07425.

Stewart, I., and Vita-Finzi, C. 1996. Coastal uplift on active normal faults: The Eliki Fault, Greece. *Geophysical Research Letters.* **23**(14). 1853-1856.

Torabi, A., and Berg, S.S. 2011. Scaling of fault attributes: A review. *Marine and Petroleum Geology.* **28** (8). 1444-1460.

Travè, A., Roca, E. Playá, E., Parcerisa, D., Gómez-Gras, D., and Martín- Martín, J. D. 2009. Migration of Mn-rich fluids through normal faults and fine-grained terrigenous sediments during early development of the Neogene Vallès-Penedès half-graben (NE Spain). *Geofluids*. **9** (4). 303-320.

Tueckmantel, C., Fisher, Q.J., Knipe, R.J., Lickorish, H., and Khalil, S.M. 2010. Fault seal prediction of seismic-scale normal faults in porous sandstone: A case study from the eastern Gulf of Suez rift, Egypt. *Marine and Petroleum Geology*. **27**(2). 334-350.

Tueckmantel, C. Fisher, Q. J., Manzocchi, T., Skachkov, S., and Grattoni, C. A. 2012. Two-phase fluid flow properties of cataclastic fault rocks: Implications for CO2 storage in saline aquifers. *Geology*. **40** (1). 39-42.

Turner, J.A., Leeder, M.R., Andrews, J.E., Rowe, P.J., Van Calsteren, P., and Thomas, L. 2010. Testing rival tectonic uplift models for the Lechaion Gulf in the Gulf of Corinth rift. *Journal of the Geological Society*. **167.** 1237-1250.

Tveranger, J., Braathen, A., Skar, T., and Skauge, A. 2007. Centre for Integrated Petroleum Research: Research activities with emphasis on fluid flow in fault zones. *Norwegian Journal of Geology.*179-187.

Van den Berg, E. H., Bense, V.F., and Schlager, W. 2003. Assessing textural variation in laminated sands using digital image analysis of thin sections. *Journal of Sedimentary Research*. **73** (1). 133.

Vita-Finzi, C. 1993. Evaluating Late Quaternary uplift in Greece and Cyprus. *Geological Society, London, Special Publications.* **76** (1). 417-424.

Voudouris, K.S., Daskalaki, P., and Antonakos, A. 2005. Water resources and groundwater quality in north Peloponnesus (Greece). *Global NEST***. 7** (3). 340-353.

Wada, Y., Van Beek, L.P.H., Van Kempen, C.M., Reckman, J.W.T.M., Vasak, S., and Bierkens, M.F.P. 2010. Global depletion of groundwater resources. *Geophysical Research Letters*. **37**. L20402.

Walker, R.J., Holdsworth, R.E., Imber, J., and Ellis, D. 2012. Fault-zone evolution in layered basalt sequences: A case study from the Faroe Islands, NE Atlantic margin. *Geological Society of America Bulletin*. **124** (7-8). 1382-1393.

Walsh, J., Watterson, J., and Yielding, G. 1991. The importance of small-scale faulting in regional extension. *Nature*. **351**. 391-393.

Walsh, J. J., Watterson, J., Heath, A.E. and Childs, C. 1998. Representation and scaling of faults in fluid flow models. Petroleum Geoscience. **4**. 241-251.

Watterson, J., Walsh, J.J., Gillespie, P.A., and Easton, S. 1996. Scaling systematics of fault sizes on a large-scale range fault map. Journal of Structural Geology**. 18** (2–3). 199-214.

Watterson, J., Childs, C., and Walsh, J.J., 1998. Widening of fault zones by erosion of asperities formed by bed-parallel slip. *Geology*. **26**. 71-74.

Wibberley, C. A. J., Yielding, G., and Di Toro, G. 2008. Recent advances in the understanding of fault zone internal structure: a review. In: Wibberley, C. A. J., Kurz, W., Imber, J., Holdsworth, R.E., and Collettini, C. (Eds). *The internal structure of fault zones.* Bath. Geological Society Special Publication. **299.** 5-33.

Wilkins, S. J., and Gross, M.R. 2002. Normal fault growth in layered rocks at split mountain, utah: influence of mechanical stratigraphy on dip linkage, fault restriction and fault scaling. *Journal of Structural Geology***. 24** (9). 1413-1429.

Wilson, J. E., Goodwin, L. B., and Lewis, C.J. 2003. Deformation bands in nonwelded ignimbrites: Petrophysical controls on fault-zone deformation and evidence of preferential fluid flow. *Geology*. **31** (10). 837-840.

Wilson, J. L., Goodwin, L. B., and Lewis, C. 2006. Diagenesis of deformation bands faults: Record and mechanical consequences of vadose zone flow and transport in the Bandelier Tuff, Los Alamos, New Mexico. *Journal of Geophysical Research*. **111**. B09201.

Wilson, P., Gawthorpe, R. L., Hodgetts, D., Rarity, F., and Sharp, I. R. 2009. Geometry and architecture of faults in a syn-rift normal fault array: The Nukhul half-graben, Suez rift, Egypt. *Journal of Structural Geology*. **31** (8). 759-775.

Wojtal, S. F. 1994. Fault scaling laws and the temporal evolution of fault systems. *Journal of Structural Geology*. **16** (4). 603-612.

Wojtal., S.F. 1996. Changes in fault displacement populations correlated to linkage between faults. *Journal of Structural Geology*. **18** (2-3). 265-279.

Woodcock, N. H., Dickson, J. A. D. and Tarasewicz, J. P. T. 2007. Transient permeability and reseal hardening in fault zones: evidence from dilation breccia textures. *Geological Society, London, Special Publications.* **270** (1). 43-53.

Wu, Q., and Xu, H. 2003. An approach to computer modeling and visualization of geological faults in 3D. Computers and Geosciences. **29** (4). 503-509.

Yang, J., Large, R. R., and Bull, S. W. 2004. Factors controlling free thermal convection in faults in sedimentary basins: implications for the formation of zinc–lead mineral deposits. *Geofluids*. **4** (3). 237-247.

Yielding, G., Needham, T. and Jones, H. 1996. Sampling of fault populations using sub-surface data: a review. *Journal of Structural Geology*. **18** (2-3). 135-146.

Yielding, G., Freeman, B., and Needham, T. 1997. Quantitative fault seal prediction. *AAPG bulletin*. **81** (6). 897-917.

Younger, P. L., Gluyas, J.G., and Stephens, W.E. 2012. Development of deep geothermal energy resources in the UK. *Energy*. **165** (En1). 19-32.

Zappa, G., Bersezio, R., Felletti, F., and Giudici, M. 2006. Modeling heterogeneity of gravel-sand, braided stream, alluvial aquifers at the facies scale. *Journal of Hydrology*. **325** (1-4). 134-153.

Zhang, S., and Tullis, T.E. 1998. The effect of fault slip on permeability and permeability anisotropy in quartz gouge. *Tectonophysics*. **295** (1–2). 41-52.

Zhang, S., and Cox, S. F. 2000. Enhancement of fluid permeability during shear deformation of a synthetic mud. *Journal of Structural Geology*. **22** (10). 1385-1393.

Zygouri, V., Verroios, S., Kokkalas, S., Xypolias, P., and Koukouvelas, I. K. 2008. Scaling properties within the Gulf of Corinth, Greece; comparison between offshore and onshore active faults. *Tectonophysics*. **453** (1-4). 193-210.